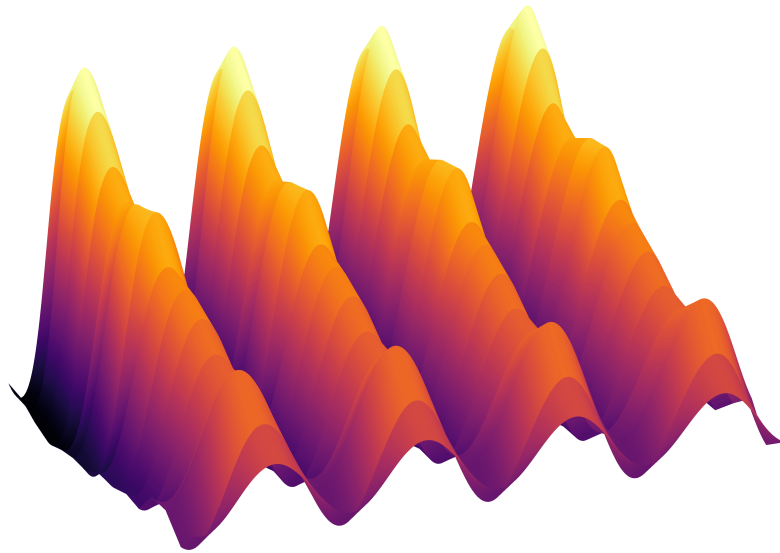


Investigation of efficient spin-photon interfaces for the realisation of quantum networks



Lukas Huthmacher

Cavendish Laboratory, University of Cambridge

This dissertation is submitted for the degree of
Doctor of Philosophy

Meinen Eltern.

Abstract

Quantum networks lie at the heart of distributed quantum computing and secure quantum communication - research areas that have seen a strong increase of interest over the last decade. Their basic architecture consist of stationary nodes composed of quantum processors which are linked via photonic channels. The key requirement, and at the same time the most demanding challenge, is the efficient distribution of entanglement between distant nodes.

The two ground states of single spins confined in self-assembled InGaAs quantum dots provide an effective two-level system for the implementation of quantum bits. Moreover, they offer strong transition dipole moments with outstanding photonic properties allowing for the realisation of close to ideal, high-bandwidth spin-photon interfaces. These properties are combined with the benefits of working in the solid state, such as scalability and integrability of devices, to form a promising candidate for the implementation of fast entanglement distribution.

In this dissertation we provide the first implementation of a unit cell of a quantum network based on single electron spins in InGaAs. We use a probabilistic scheme based on spin-photon entanglement and the erasure of which path information to project the two distant spins into a maximally entangled Bell state. The successful generation of entanglement is verified through a reconstruction of the final two-spin state and we achieve an average fidelity of $61.6 \pm 2.3\%$ at a record-high generation rate of 5.8 kHz.

One of the main constraints to the achieved fidelity is the limited coherence of the electron spin. We show that it can be extended by three orders of magnitude through decoupling techniques and develop a new measurement technique, allowing us to investigate the origins of the decoherence which has previously been obscured by nuclear feedback processes. Our results evidence that further extension of coherence is ultimately limited by intrinsic mechanisms closely related to local strain due to the growth method of self-assembled quantum dots.

After establishing the intrinsic limits to the electron coherence we investigate the coherence properties of the single hole spin as an alternative two-level system with the potential for higher coherence times. We show that the hole spin coherence is indeed superior to the one of the electron and realise the first successful dynamic decoupling scheme implemented in these

systems. We find that the decoherence at low external magnetic fields is still governed by coupling to the nuclear spins whereas it is dominated by electrical noise for fields exceeding a few Tesla. This noise source is extrinsic to the quantum dots and a better understanding offers the potential for further improvement of the coherence time.

The findings of this work present a complete study of the coherence of the charge carriers in self-assembled quantum dots and provide the knowledge needed to improve the implementation of a quantum-dot based quantum network. In particular, the combination of spin-spin entanglement and the hole coherence times enable further research towards multidimensional photonic cluster states.

Declaration

This dissertation is the result of my own work and includes nothing which is the outcome of work done in collaboration except as declared in the Preface and specified in the text.

It is not substantially the same as any that I have submitted, or, is being concurrently submitted for a degree or diploma or other qualification at the University of Cambridge or any other University or similar institution except as declared in the Preface and specified in the text. I further state that no substantial part of my dissertation has already been submitted, or, is being concurrently submitted for any such degree, diploma or other qualification at the University of Cambridge or any other University or similar institution except as declared in the Preface and specified in the text

It does not exceed the prescribed word limit of 60,000 words, including abstract, tables, footnotes and appendices.

Lukas Huthmacher

June 2018

Acknowledgements

This thesis is the result of more than 3.5 years of teamwork and a lot of people here and afar have contributed to the very enjoyable time during my PhD in Cambridge.

First and foremost, my thanks and gratitude go to Prof. Mete Atatüre who offered me the chance to join his amazing team and conduct research in his laboratories. Mete knows exactly how to create a stimulating and challenging atmosphere while keeping it sociable and fun. He always offered his support, both scientifically and as a friend (and fellow rower) and I am grateful for the freedom he gave me.

This work would not have been possible without the great quantum dot team. Special thanks go to Robert Stockill who worked with me on nearly all of the projects presented in this thesis and taught me everything I know about coherent rotations. He was always patient and willing to discuss about experimental details as well as music or politics and we shared quite a few pints. My gratitude also extends to Claire Le Gall who supported me throughout my PhD and played a part in all of my work. She has extensive knowledge and experience and is the good soul in our team who always takes time to listen to the problems of others. I would like to thank Clemens Matthiesen for introducing me to the work with quantum dots and the fabrication of our devices. And of course not to forget Megan Stanley who was an integral member of our team and significantly contributed to the entanglement experiment. Unfortunately I never succeeded in my quest of taking her to an Apocalyptica concert...

The other members of the quantum dot team might not have been part of the work presented here but they definitely contributed to its success. Gabriel, Dorian, Jonny and Constantin: Thank you for sharing the setups, all the stimulating discussions about physics and beyond and supporting me in my attempt to introduce python to the quantum dot experiments. My thanks extend to Carsten and Jack who were already writing up when I joined the team. I believe one of the keys to our success as a team is the strong social component at work, in the pub, and elsewhere and I am proud to call all of you my friends.

My time would not have been the same with the other members of our research group and I would like to thank Alejandro, Ben, Camille, Carmen, David, Dhiren, Gu, Helena, Jan, Jeff, Josh, Lucio, Matteo and Mustafa for the time inside and outside the laboratory.

My life in Cambridge would not have been the same without my College, Peterhouse, and my fellow students in the MCR, who created a welcoming and supportive environment. Through our boat club I got into rowing which soon became an essential part of my life here in Cambridge and I want to thank both Peterhouse Boat Club and the Cambridge University Lightweight Rowing Club for the great time I had on and off the water.

Finally, this thesis would not have been possible without the never-ending support of my friends and family. Especially I want to thank my parents and siblings for the support and encouragement from day one of my Bachelor up until today, no matter the distance between us. Above all, I thank Maria for being at my side these past 3.5 years and always giving me the space and support I needed pursuing my research. Thank you for being so understanding and patient throughout our time here.

Contents

Abstract	v
Declaration	vii
Acknowledgements	ix
Contents	xi
List of figures	xv
1 Introduction	1
2 InGaAs quantum dots as solid state qubits	5
2.1 Electronic level structure	6
2.1.1 Neutral exciton	7
2.1.2 Charged excitons	8
2.2 Experimental setup	9
2.2.1 Sample structure	9
2.2.2 Confocal microscope	12
2.2.3 Pulsed laser setup	14
2.3 Experimental techniques	15
2.3.1 Photoluminescence	15
2.3.2 Resonant excitation	16
2.3.3 Coherent rotations	24
2.4 Nuclear spin environment	29
2.4.1 Hyperfine interaction	29
2.4.2 Nuclear quadrupolar interaction	32
2.5 Conclusion	32

Contents

3	Elementary quantum network	35
3.1	Entanglement protocol	36
3.1.1	Single-photon entanglement scheme	37
3.2	Experimental realisation	40
3.2.1	Phase stabilisation	40
3.2.2	Interferometer setup	41
3.2.3	Experimental back end	43
3.2.4	Pulse sequence	44
3.2.5	Interferometer delay	46
3.3	Indistinguishable quantum dots	48
3.3.1	Optical mode matching	48
3.3.2	Hong-Ou-Mandel interference	49
3.4	Single spin projection	52
3.5	Measurement of spin-spin correlations	54
3.5.1	Correlation of spin population	54
3.5.2	Correlations in a transverse basis	56
3.5.3	Fidelity of entangled-state generation	60
3.5.4	Phase control	62
3.6	Data acquisition and post-processing	64
3.6.1	Data acquisition	64
3.6.2	Data post-processing	64
3.6.3	Ratio of Rayleigh scattering for post-processing	67
3.6.4	Correction for Stark shifts	69
3.7	Discussion of Results	69
4	Hong-Ou-Mandel interference of photons from two distant quantum dots	73
4.1	Intensity autocorrelation	73
4.1.1	Experimental method	74
4.1.2	Measurement of intensity autocorrelations	74
4.2	Hong-Ou-Mandel interference	76
4.2.1	Experimental method	76
4.2.2	Power-dependent HOM interference	77
4.2.3	HOM interference of distinguishable photons	78
4.2.4	Photon wave-packet area dependent HOM visibilities	78
4.3	Model of HOM interference	82
4.3.1	Second-order correlation function	83
4.3.2	Single-photon pulses	84

4.3.3	Calculation of HOM signatures	85
4.4	Discussion of Results	88
5	Electron Coherence	89
5.1	Inhomogeneous dephasing time	90
5.1.1	Experimental method	90
5.1.2	Nuclear feedback during Ramsey interferometry	91
5.1.3	Suppression of nuclear polarisation	93
5.1.4	Free induction decay	96
5.2	Coherence time	97
5.2.1	Experimental method	97
5.2.2	Hahn echo	99
5.3	Model of Hahn-echo visibility	100
5.3.1	Nuclear spectra	100
5.3.2	Delay-dependent Hahn-echo visibility	104
5.4	Discussion of results	105
6	Hole Coherence	109
6.1	Initial study of holes in our samples	109
6.1.1	Photocreation of holes	110
6.1.2	Charge lifetimes	112
6.1.3	Phonon-assisted processes	113
6.2	Inhomogeneous dephasing time	115
6.2.1	Experimental method	116
6.2.2	Magnetic-field-dependent inhomogeneous dephasing time	118
6.2.3	Electron FID in the same QD	120
6.3	Coherence time	122
6.3.1	Experimental method	122
6.3.2	Hahn-echo visibility decay	123
6.4	Measurement of the electrical noise	126
6.4.1	Intensity autocorrelation	126
6.5	Further extension of coherence	128
6.5.1	Experimental method	129
6.5.2	Scaling of dynamic decoupling with N_π	130
6.5.3	Periodic dynamic decoupling	136
6.6	Discussion of Results	136

Contents

7 Conclusion	139
Appendix A Python library	143
A.1 Measurement and compression of data	144
A.2 Clock-Channel correlations	146
A.3 Two-photon correlations	147
A.4 Extraction of three photon coincidences	148
A.5 Graphical user interface	149
References	151

List of figures

2.1	Band structure	7
2.2	InGaAs quantum dot energy level structure	8
2.3	Sample structure	10
2.4	Cryostat and confocal microscope	13
2.5	Pulsed laser setup	14
2.6	Photoluminescence spectra	16
2.7	Two-level system	18
2.8	Resonance fluorescence intensity	20
2.9	Three-level system	22
2.10	Readout and initialisation	24
2.11	Rabi oscillations	27
2.12	Ramsey interference	28
3.1	Single photon entanglement	38
3.2	Phase stabilisation	42
3.3	Entanglement setup	44
3.4	Pulse sequence	45
3.5	Pulse sequence fluorescence	46
3.6	Interferometer delay	47
3.7	Spectral and temporal mode matching	49
3.8	Second-order autocorrelation $g^2(\tau)$	51
3.9	Hong-Ou-Mandel interference	52
3.10	Single spin projection	54
3.11	Two-spin state population	55
3.12	Single-spin projection	58
3.13	Rayleigh-photon interference	59
3.14	Transverse basis measurement	60
3.15	Phase-tunable entangled state generation	63

List of figures

3.16	Post-processing of entanglement data	66
3.17	Ratio of Rayleigh scattering	68
3.18	Phase-dependent visibility for different post-processing window	68
3.19	Comparison of projective entanglement experiments	70
4.1	Autocorrelation pulse sequence	74
4.2	Intensity autocorrelations	75
4.3	HOM pulse sequence	76
4.4	Power dependent HOM	77
4.5	HOM of distinguishable photons	79
4.6	Photon area dependent HOM visibility	80
4.7	Optimising photon area	81
4.8	Post-selection on detection time difference	82
4.9	Fitting of HOM data	87
4.10	Modelling of HOM interference for different T_2^*	87
5.1	Energy level structure	91
5.2	Transition dependent Ramsey interference	92
5.3	Alternating pulse sequence	94
5.4	Ramsey dependence on inversion	95
5.5	Free induction decay	96
5.6	Hahn-echo sequence	98
5.7	Hahn-echo pulse sequence histogram and visibility	99
5.8	Hahn-echo visibility	101
5.9	Nuclear spin noise spectra	103
5.10	Hahn-echo decay components	105
6.1	Photocreation of holes	111
6.2	Gate-voltage dependent saturation of hole occupation	112
6.3	Power-dependent charge lifetime	114
6.4	Resonance fluorescence spectra	115
6.5	Photoluminescence spectrum	116
6.6	Hole spin Ramsey	118
6.7	Ramsey interference decay for different magnetic fields	119
6.8	Magnetic-field-dependent inhomogeneous dephasing time	120
6.9	Electron FID	121
6.10	Hahn-echo sequence and visibility	123
6.11	Hahn-echo visibility	124

6.12 Hahn-echo comparison	125
6.13 Magnetic-field-dependent coherence time	126
6.14 Normalised autocorrelation function of X^0 intensity fluctuations	127
6.15 Dynamic decoupling pulse sequence	129
6.16 Dynamic decoupling visibilities	131
6.17 T_2^{DD} with α as fitting parameter	133
6.18 Determination of the exponent α	133
6.19 Scaling of coherence with N_π	134
6.20 Reduction of visibility with N_π	135
6.21 Periodic dynamic decoupling	137
6.22 Scaling of coherence and visibility with N_π for PDD	137
A.1 Graphical user interface	149

Chapter 1

Introduction

"Might I say immediately, so that you know where I really intend to go, that we always have had (secret, secret, close the doors!) we always have had a great deal of difficulty in understanding the world view that quantum mechanics represents. At least I do, because I'm an old enough man that I haven't got to the point that this stuff is obvious to me. Okay, I still get nervous with it."

- Richard Feynman, [1]

The introduction of digital computing is certainly one of the greatest technological achievements of the last century. Its success was based on the fundamental theoretical work of Alan Turing, who introduced the mathematical concept of a programmable computing machine [2]: the Turing machine. The Church-Turing thesis states that the Turing machine can solve any problem that can be solved by an algorithm executed on any other machine. This characteristic is otherwise known as being universal. Soon after this achievement, the first physical implementations were built using basic electronic components such as vacuum tubes. However, the triumph of the computer as we know it today came with the invention of the transistor in 1947 [3], earning the inventors John Bardeen, Walter Brattain, and Will Shockley the Nobel price in 1956.

Not long after the first implementations of computers were available, the efficiency at which they were able to solve a problem became important and a probabilistic version of the Turing machine was developed in order to maintain the Church-Turing thesis. This thesis states that any algorithm can be efficiently simulated using such a machine, meaning a polynomial rather than exponential dependence of processing time on complexity will be obeyed. This inspired two physicists, Feynman and Deutsch, to think about ways to efficiently simulate systems which are governed by the laws of quantum physics.

Introduction

In 1981 Richard P. Feynman presented his thoughts to the audience of the First Conference on the Physics of Computation at the Massachusetts Institute of Technology [1]. He concluded that a computer with an architecture based entirely on classical physics is unable to efficiently simulate quantum mechanical systems. Instead, he proposed to build a computer based on the laws of quantum mechanics, capable of such simulations - the idea of a quantum computer was born.

A few years later, in 1985, David Deutsch published his work on a universal quantum computer [4], a machine that is not only capable of efficiently simulating the classical Turing machines, but also any arbitrary quantum computer. In his work he also gives the first example of an algorithm which offers a speed-up compared to its classical counterpart: the Deutsch algorithm, which determines whether a given one-dimensional function is constant or balanced. His idea is fundamentally based on the superposition principle of quantum mechanics.

In the following years, several algorithms were developed with the aim of providing more efficient solutions to specific problems. Famous examples are the Deutsch-Josza algorithm [5], a generalisation of the Deutsch algorithm to higher dimensions, or Grover's algorithm for searching unstructured databases [6], which provides a quadratic speed-up compared to the best known classical algorithm. The most renowned example is Shor's algorithm for the factorisation of integers [7]. Through the use of quantum Fourier transforms his algorithm can factorise integers in polynomial time. The fastest classical algorithm, the number field sieve, still takes sub-exponential time [8], meaning that the running time increases significantly slower than an exponential but still faster than any polynomial. This algorithm is of particular interest as today's public key cryptography utilises encryption schemes like RSA which rely on the difficulty of factorising large numbers [9].

Fortunately, quantum physics also offers new routes to secure communication through the incorporation of quantum mechanical principals in cryptography protocols. This way, secure key distribution via public channels can be guaranteed and no longer relies on limited computational power. Famous examples of these concepts are the BB84 [10] and the E91 [11] protocols. Further advances in the field of quantum computation led to the proposal of super dense coding [12] and quantum teleportation [13].

In the last decades the field of quantum computation and quantum communication has received an increasing amount of attention and a wide variety of physical systems compete for the large scale implementation of quantum computing architectures as well as secure quantum communication. Promising systems include trapped ions [14, 15], photons [16], NMR [17], superconducting qubits [18] and spins in the solid state such as nitrogen-vacancy centres in

diamond [19, 20] and quantum dots [21]. An important checklist for any implementation of a quantum computer are the so-called DiVincenzo criteria, a list of general requirements for the physical implementation of a quantum computer discussed by David DiVincenzo in 2000 [22]. Despite different levels of progress, no system yet has an unassailable advantage over the others. Instead, most systems focus on particular fields such as quantum computing [23], communication [24], simulation [25] or sensing [26].

Quantum computing is no longer solely an academic curiosity but attracts large companies who have started to invest significant resources into the goal of building an efficient, scalable quantum computer, including Google, IBM, Intel, Microsoft, Toshiba, HP and Hitachi.

In this work we will focus on single spins in InGaAs quantum dots [27], which are particularly interesting for the distribution of quantum information owing to their outstanding spin-photon interface [28–30]. Such an efficient light-matter interface lies at the heart of any quantum network [31] and the combination of scalable solid state devices with the possibility of operating at telecom wavelength [32] makes quantum dots a valuable candidate for the realisation of quantum networks.

In general, there are two areas of interest for quantum networks. On the one hand, they provide a solution for scalability through the implementation of clusters of powerful quantum processors, typically separated only by short distances. This type of architecture is often referred to as networked quantum computing and the idea is analogous to classical computer clusters. On the other hand, these networks can be used for communication purposes. In that case we can view it as a quantum internet [31] which can be used for secure communication through quantum key distribution [10, 11] or blind quantum computing [33]. The latter provides a way to securely delegate quantum computing to an untrusted device, without revealing the computation itself to the server. In this case, the nodes themselves only require relatively basic quantum processors - some of the protocols rely on a single quantum bit (qubit). While distributed quantum computing relies on short distances, allowing for a wide range of frequencies for the photonic links, a quantum network for communication purposes will rely on long-distance transmission of single photons and thus working at the telecom wavelength would be beneficial in terms of optical losses. Moreover, it would enable us to use the existing fibre network spanning the whole globe.

Here, we will present a fundamental implementation of such a network using InGaAs quantum dots and study the coherence properties of single electron and hole spins in these devices, providing an insight to the limits of the spin-photon interface performance.

Outline of the thesis

In **Chapter 2** we will give a brief introduction to self-assembled InGaAs quantum dots and the related experimental methods employed throughout this work together with the corresponding experimental setup. **Chapter 3** will cover the realisation of distant spin-spin entanglement, using single electrons confined to two quantum dots in separate cryostats. After a short review of the theoretical proposal, based on the projective measurement of a single photon, we introduce the experimental setup and identify two indistinguishable quantum dots. Subsequently, we verify the spin projection through measurement of a single photon and extract spin-spin correlations in the computational and transverse basis to confirm the successful generation of a phase-controlled entangled two-spin state. We include a brief discussion of limitations to the fidelity and identify the inhomogeneous dephasing of the electron spin as a key contribution and conclude the chapter with an overview of the complex data-analysis required for this experiment. **Chapter 4** presents a more detailed study on the indistinguishability of photons provided by two distinct quantum dots, including an analysis of behaviour for different areas of the photon wave packet. The results confirm that the indistinguishability is mainly limited due to the inhomogeneous dephasing of the spin. Following this, **Chapter 5** provides a detailed study of the electron-spin coherence in the presence of a dynamic nuclear spin bath. We introduce a new measurement technique, allowing us to suppress nuclear polarisation and access the coherence dynamics in free induction and Hahn-echo decay measurements. Our analysis shows that the electron-spin coherence is inherently limited owing to the strain-driven growth of self-assembled quantum dots. An alternative in our samples is the hole spin, which we study in **Chapter 6**. This is the first study of the hole spin in our laboratory and we, again, explore the coherence in order to quantify the performance of the spin-photon interface. We find that it provides superior coherence to the electron across a wide range of magnetic fields and that, in contrast to the electron, the limit is set by extrinsic, electrical noise. Finally, we summarise the results of the presented work in **Chapter 7** and provide a brief outlook on the implementation of our findings for future experiments.

Chapter 2

InGaAs quantum dots as solid state qubits

"There is no doubt that quantum mechanics has seized hold of a beautiful element of truth, and that it will be a test stone for any future theoretical basis, in that it must be deducible as a limiting case from that basis, just as electrostatics is deducible from the Maxwell equations of the electromagnetic field or as thermodynamics is deducible from classical mechanics."

- Albert Einstein, [34]

Today, quantum dots have become an established resource with a variety of applications including spintronics [35], medical applications [36, 37] and even for modern displays [38, 39]. However, it is the capability of hosting a single spin in combination with the optical properties that have led to an interest in using them for quantum information processing [40–43].

The field of quantum computation and quantum communication has seen tremendous progress in the past decades, both theoretically and experimentally. A full discussion of the fundamental concepts is beyond the scope of this thesis and the reader is referred to the book of M. A. Nielsen and I. L. Chuang [23] as an excellent resource for a basic introduction to the field. In this chapter, we will give a brief overview of the characteristics of InGaAs quantum dots in the context of quantum information processing and the essential experimental methods used throughout this work.

2.1 Electronic level structure

In general, we require a discrete, anharmonic energy level spectrum allowing us to address individual transitions and define computational ground states. Such a quantised energy spectrum can be achieved by confining a particle in a region smaller than the corresponding Bohr radius, analogous to the well known particle in a box model. A quantum dot provides three-dimensional confinement within a semiconductor crystal and is thus often viewed as being zero-dimensional. The resulting discrete energy levels can be filled with single electrons obeying the Pauli exclusion principle, leading to pseudo-atomic optical properties, which earned quantum dots the nickname 'artificial atoms'. In contrast to real atoms, quantum dots are mesoscopic systems and we can engineer their properties and incorporate them into more advanced photonic devices [44].

The band structure of InGaAs quantum dots can be derived from the underlying zinc-blende lattice characteristic for III-V semiconductors. There is a direct band gap at the Γ point and we can approximate the bands by parabolas, resulting in the band structure depicted in Fig. 2.1. The confinement is provided by the reduced band gap of InAs ($\Delta_g = 0.35$ eV) compared to the GaAs ($\Delta_g = 1.42$ eV) host crystal [45] and the lowest energy state of the conduction band has a s -shell symmetry and total angular momentum $J = 1/2$. In contrast, the highest valence band has a p -shell symmetry and supports four wavefunctions with total angular momentum $J = 3/2$ and two with $J = 1/2$. The latter contribution is lowest in energy due to the spin-orbit interaction and therefore often referred to as the split-off (so) band. As a result of the strong spin-orbit interaction in InAs and GaAs we can neglect the contributions of the so band to the quantum dot level structure. The degeneracy of the valence band is further lifted by the confinement and uniaxial strain, which results in heavy holes (hh) with $m_j = \pm 3/2$ and light holes (lh) with $m_j = \pm 1/2$, where the terminology stems from the different curvatures around the Γ point. In the following, we constrain the discussion to hh states since the strain in these quantum dots is sufficiently large to suppress most of the lh contribution.

Holes are created by exciting one of the valence-band electrons to the conduction band - the empty state is treated as a positively charged, spin carrying pseudo-particle with a modified mass and g -factor. Electron-hole pairs can form a bound state through the Coulomb interaction and the resulting quasiparticle is referred to as an exciton. The energy corresponding to the creation of such an exciton is typically engineered to be ~ 1.3 eV which leads to emission wavelengths in the range of 900-1000 nm. The choice of the wavelength is based on a trade-off between internal losses and detection efficiencies of widely-used silicon-based photodiodes.

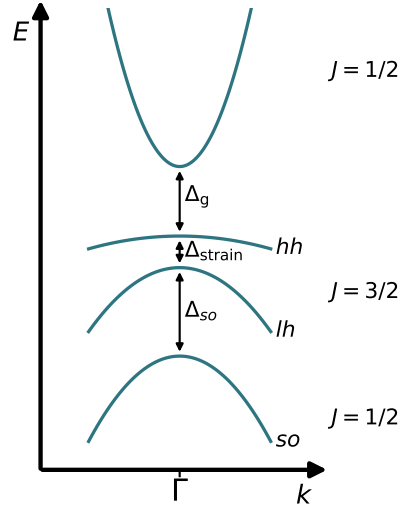


Fig. 2.1 **Band structure** Approximation of the band structure of a strained III-V semiconductor around the Γ point.

2.1.1 Neutral exciton

The most basic excitation in a quantum dot is the neutral exciton X^0 . There are four possible combinations of an electron spin ($|\uparrow\rangle, |\downarrow\rangle$) and a hh spin ($|\uparrow\rangle, |\downarrow\rangle$) to form an exciton: $|\uparrow\uparrow\rangle, |\downarrow\downarrow\rangle, |\uparrow\downarrow\rangle, |\downarrow\uparrow\rangle$. The first two states carry a total angular momentum of $J = \pm 2$, whereas the latter two only carry $J = \pm 1$. A single photon carries an angular momentum of $J = \pm 1$ and thus we have two optically dark and two optically bright states. Here, we focus only on the bright excitons. For a perfectly symmetric quantum dot and zero magnetic field we would obtain two degenerate optical transitions between the vacuum field ($|0\rangle$) and the two bright states. However, due to asymmetries in the confinement potential and the quantum dot shape, we obtain non-zero off-diagonal elements in the Hamiltonian resulting in two new eigenstates of the system [46]: $\frac{1}{\sqrt{2}}(|\downarrow\uparrow\rangle \pm |\uparrow\downarrow\rangle)$. These two states experience a fine-structure splitting, Δ_{FS} , due to the electron-hole interaction, which has been measured to be on the order of hundreds of μeV [46]. Through annealing of the sample this splitting can be reduced and even tuned through zero [47]. In our samples we typically measure a splitting of $\sim 20 - 30 \mu\text{eV}$. The angular momentum of the excited states leads to two optically allowed transitions with orthogonal linear polarisations and the resulting energy level scheme is depicted in Fig. 2.2 (a). Following the creation of an exciton we can measure a single photon emitted due to the electron-hole recombination; typical lifetimes measured for our samples are $\sim 700\text{ps}$.

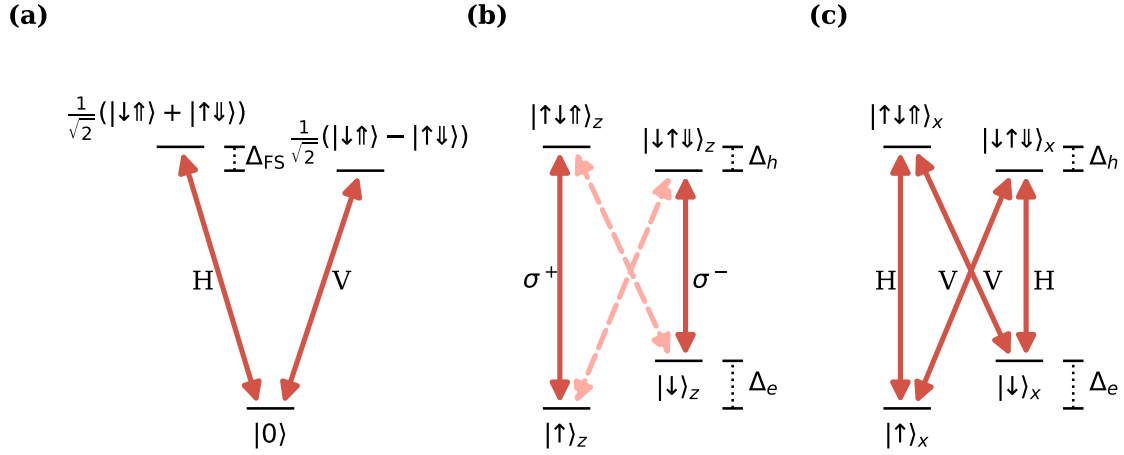


Fig. 2.2 **InGaAs quantum dot energy level structure** (a) Energy levels for the neutral exciton X^0 . Red arrows indicate linearly polarised transitions (H,V). (b) Energy levels and circularly polarised transitions for the negative trion X^- in Faraday geometry. Diagonal transitions are only weakly allowed due to finite $hh-lh$ mixing. (c) Energy levels and transitions for the negative trion X^- in Voigt geometry with four linearly polarised, equal-strength transitions.

2.1.2 Charged excitons

Quantum dots can also host a charge in the ground state which leads to the formation of charged excitons, often referred to as trions owing to the three contributing charges. Depending on the resident charge we distinguish between negative (X^-) and positive (X^+) trions.

Negative trion

In the case of a resident electron the trion consists of 2 electrons and a single heavy hole. The electrons form an anti-symmetric spin singlet, $\frac{1}{\sqrt{2}}(|\uparrow\downarrow\rangle - |\downarrow\uparrow\rangle)$, in short often denoted by $|\uparrow\downarrow\rangle$. The singlet has a net angular momentum of zero and thus the angular momentum of the trion is fully determined by the hh spin. Moreover, this prevents any exchange interaction with the hole and thus the trion does not experience any fine-structure splitting. Owing to the net angular momentum of ± 1 only the spin-conserving transitions are allowed, coupled by circularly polarised light. In this way it is possible to selectively excite one of the two degenerate trion states.

In our experiments we always work with an external magnetic field which lifts the degeneracy of ground and excited states due to the Zeeman splittings, Δ_e and Δ_h , respectively. In Faraday geometry, where the external magnetic field B_{ext} is aligned with the growth axis, the selection rules are maintained as depicted in Fig. 2.2 (b). The polarisation selectivity is slightly relaxed as a result of $hh-lh$ mixing and electron-nuclei interactions, which allows for spin initialisation fidelities of $> 99\%$ [48].

Applying a field perpendicular to the growth axis (Voigt geometry) changes the quantisation axis and thus the eigenstates of the system consist of superpositions of the basis states defined by the growth axis. Therefore, we get four optically allowed transitions which couple to linearly polarised light, shown in Fig. 2.2 (c). This system offers two Λ -systems with equal branching ratios and cross-polarised transitions. In this work, all experiments are carried out in Voigt geometry which allows for fast, high-fidelity spin initialisation [49, 50], coherent spin control (Sec. 2.3.3) and spin-photon entanglement [28–30]. Chapters 3-5 will focus on experiments utilising single electron spins and one of the Λ -systems provided in Voigt geometry.

Positive trion

The positive trion resembles an exact copy of the negative trion with the difference that electrons and holes swap their corresponding roles. Single hole spins have seen an increased interest due to their p -shell symmetry which enables strongly reduced hyperfine coupling to the nuclear spin bath [51, 52], resulting in longer coherence times [53–55] and we will take a closer look at single hole spins in Chapter 6.

2.2 Experimental setup

In this section we give a brief overview of the most important components of our experiments. More detailed descriptions will be given in the corresponding chapters.

2.2.1 Sample structure

The samples are grown using molecular beam epitaxy (MBE), a technique developed in the 1960s which allows for very clean layer-by-layer growth of semiconductor crystals [56]. A schematic of the different layers of our samples is shown in Fig. 2.3.

In order to lift the Fermi level close to the energy of the conduction band we grow a 40 nm thick layer of heavily n -doped GaAs with a free charge carrier density of $4 \times 10^{18} \text{ cm}^{-3}$, where the electrons are provided by Silicon doping of the GaAs [57]. A 35 nm layer of

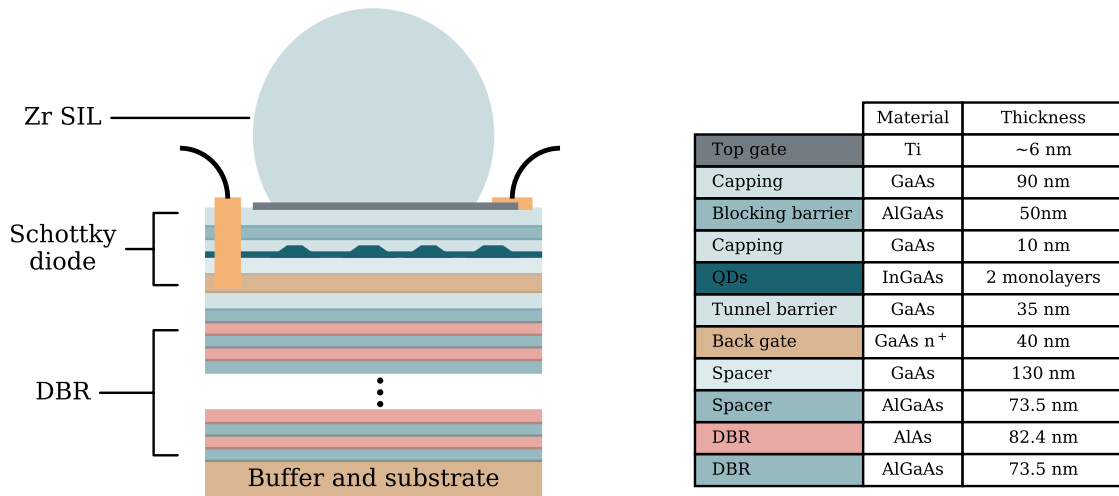


Fig. 2.3 **Sample structure** Schematic of the quantum dot device grown by MBE and further processed in our clean room facilities to enable charge control. A DBR and cubic-zirconia SIL are used to improve the light outcoupling efficiency. A description of the layer function together with the corresponding material and thickness are summarised in the table on the right-hand side.

undoped (001) oriented GaAs is deposited as tunnel barrier before the growth of the quantum dot layer. The self assembly of the quantum dots is achieved through Stranski-Krastanov growth: After the initial growth of a wetting layer of InAs (~ 1.6 monolayers), the strain due to the lattice mismatch of about 7% is relaxed through nucleation and small islands form randomly on top of the wetting layer. The quantum dot layer is subsequently capped with 10 nm GaAs which serves to prevent oxidation and minimises interactions with surface states. Moreover, the capping blue-shifts the transition frequency which can be further tuned through careful annealing of the sample [47]. A blocking barrier of 50 nm AlGaAs minimises charge leakage owing to the larger band gap and the sample is capped with a further 90 nm of GaAs.

The wafers used throughout my PhD were grown in the EPSRC National Centre for III-V Technologies in Sheffield.

Charge control

In order to allow for deterministic charge control of our quantum dots and to suppress noise due to electrical charges we embed the quantum dot layer into a Schottky-diode structure. This is achieved by further processing the two-inch, MBE-grown wafer in our clean room

facilities. In a first step we cleave the wafer into small squares with a length of ~ 5 mm. We then use photolithography and wet etching to etch a hole down to the n -doped layer which we fill with a gold-germanium-nickel alloy (AuGeNi) through thermal evaporation and annealing. The top-gate is provided by a semi-transparent, 5 – 6 nm thick layer of titanium which is deposited through electron-beam evaporation.

This structure allows us to tune the energy of the quantum dot states relative to the Fermi level through application of a voltage bias across the sample. For the correct bias, the ground-state energy of a bound electron is below the Fermi level and a single electron tunnels into the quantum dot. Further tunneling is prevented due to the Coulomb-interaction which repels additional electrons, an effect known as Coulomb blockade [58]. Therefore, the stable charge configuration of the quantum dot is directly related to the voltage bias and we can find different charge stability regions, a process that we will see in bias dependent measurements of photoluminescence (Sec. 2.3.1).

Another effect that will be apparent in those PL measurements is the quantum-confined Stark shift [59]. The large electric field, \mathbf{F} , applied across the sample also affects the energies of the excitonic states, which are shifted by:

$$\Delta E_{Stark} = -\mathbf{p}\mathbf{F} + \beta\mathbf{F}^2, \quad (2.1)$$

where \mathbf{p} denotes the permanent dipole of the exciton and β is the polarisability. In our samples we measure a linear shift of the transition wavelength with applied DC bias of about 250MHzmV^{-1} .

Light extraction

The collection of the emitted photons directly affects the efficiency of our measurements and various strategies have been developed in order to increase the overall outcoupling efficiency. Here, we apply a minimalistic approach which ensures a low noise sample with charge control. We only collect the light at the top of the sample and thus introduce a highly reflective distributed Bragg reflector (DBR) below the sample to also collect the emission below the quantum dot layer. The DBR consists of 20 layers of AlGaAs/AlAs which are grown directly on top of the substrate via MBE (Fig. 2.3) and we optimise the thickness of the layers to achieve the highest reflectivity around 960 nm where we expect the emission of our quantum dots.

The outcoupling efficiency at the top of our sample is mainly limited by total internal reflection due to the large mismatch of refractive indices. Here, we introduce a super-hemispherical cubic-zirconia solid immersion lens (SIL) which is placed in direct contact

to the sample surface (sub wavelength). In the ideal case, we would use a SIL where the refractive index is matched to suppress any total internal reflection. However, good quality GaAs SILs are hard to get and here we rely on cubic zirconia which has a refractive index of $n \sim 2.2$, compared to $n = 3.44$ for GaAs.

The SILs used in this work have a diameter of 1-2 mm, sufficiently large to ensure that we can find a good quantum dot in the working area. In order to mount the SIL we immerse it in a water droplet on the sample surface which is then evaporated by heating the sample to about 60°C. The resulting suction is enough to provide good contact to the sample surface and we further secure the SIL with mounting wax.

For quantum dots with an emission wavelength around 970 nm we estimate the total outcoupling efficiency to be on the order of 10%.

2.2.2 Confocal microscope

The exact requirements for the measurement setup will vary for different experiments, but at the core of each experiment is the cryostat-mounted confocal microscope setup.

In order to achieve control over the discrete energy-level spectrum of the quantum dot we place the sample inside a liquid Helium bath cryostat, reducing the thermal energy $k_B T$ to about 0.36 meV at 4.2 K. This way, we ensure that the charge carriers are in their ground state and incoherent, phonon-assisted transitions are suppressed [60]. The experimental configuration is shown in Fig. 2.4 (a), where the sample is placed in a low pressure Helium atmosphere at the bottom of an insert to allow for good thermal contact to the Helium bath whilst ensuring optical access from the top of the cryostat. Nanoscale positioning in all three dimensions is provided by piezoelectric stages and a superconducting electromagnetic coil surrounds the insert to provide external magnetic fields of up to 9 Tesla along the direction of optical access. Operation in Voigt geometry is achieved by mounting the sample at a 90 degree angle as shown in Fig. 2.4 (a) and DC-wiring ensures control of the bias voltage.

Optical access is provided by a home-built confocal microscope mounted on top of the bath cryostat in combination with an 0.5 NA aspheric lens mounted a few millimetres away from the sample to provide focussing of the collimated beam. The moderate NA is sufficient in combination with the surface-mounted SIL. The microscope shown in Fig. 2.4 (b) provides two inputs and one output and is operated in a dark-field configuration [61]. Excitation and collection are coupled to the optical access path of the cryostat using an imbalanced beam splitter, which transmits 90% of the collected photons to the output of the microscope whilst directing 10% of the excitation to the sample. A photo diode (PD) is used to monitor the transmitted excitation power which can be used as an error signal for a PID to stabilise the input power with an acousto-optic modulator (AOM).

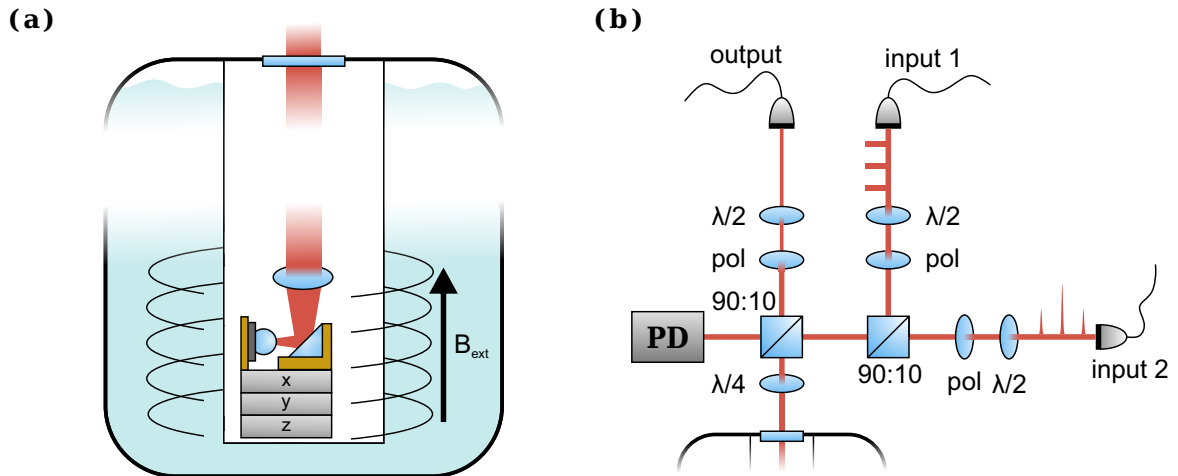


Fig. 2.4 **Cryostat and confocal microscope** (a) Schematic of the liquid Helium bath cryostat used to cool the sample to 4.2 K. The sample is mounted in Voigt geometry on top of piezoelectric positioners based at the bottom of the cryostat insert and surrounded by a superconducting magnet. (b) Confocal microscope in dark-field configuration with fibre coupled in- and outputs. A 90:10 beam splitter ensures that most of the outgoing light is directed towards the output.

A combination of polariser and half-wave plate is used to control the polarisation in each arm and suppress the laser scattering through cross-polarisation in the output. The exact performance of this method is highly frequency dependent and through careful tuning of beam position, angle and polarisation we achieve suppression of the laser scattering by a factor 10^7 , resulting in signal-to-background ratios > 100 . An additional quarter-wave plate just before the cryostat window ensures circularly polarised light which is needed for the coherent control of the ground-state spins and provides one more tuning knob for the optimisation of laser background suppression.

The two input arms are designated for different tasks: One input is used for high-power laser pulses for coherent control (Sec. 2.3.3), while the other arm carries all the light derived from CW-lasers used for readout and initialisation. The latter typically contains frequencies resonant with the quantum dot transitions and we thus have to optimise the cross-polarised suppression for this arm specifically. The amount to which the off-resonant, high-power laser pulses used for coherent rotations can be suppressed with this method is limited due to the strong frequency dependence of the background suppression. Therefore, we typically use a holographic diffraction grating after the output fibre of the microscope to filter any remaining background from the pulsed laser.

The fibre coupled in- and outputs make this setup very flexible and allow us to easily switch between different sources and detection devices. The excitation is typically provided

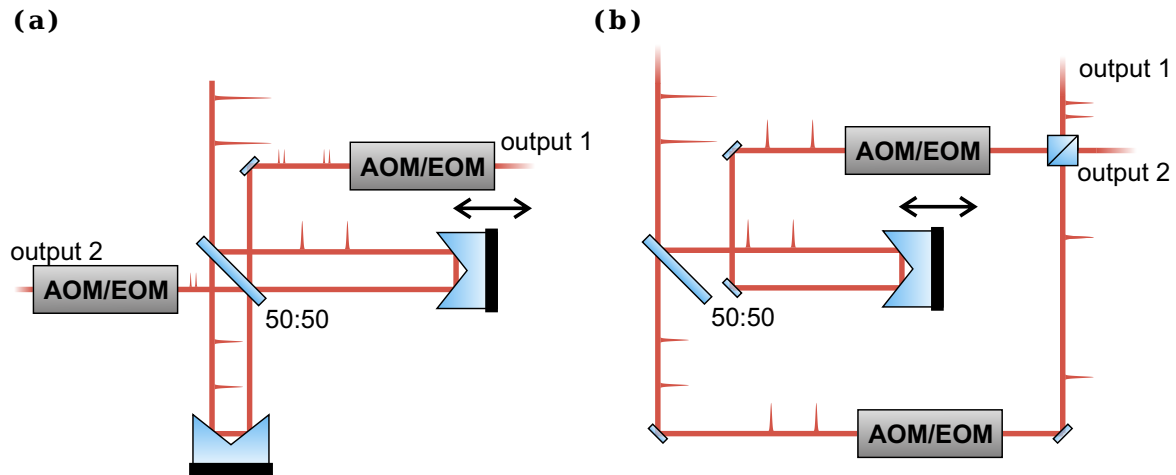


Fig. 2.5 **Pulsed laser setup** (a) Interferometer configuration the derivation of pairs of pulses with a tunable inter-pulse delay. (b) Configuration for the generation of more complicated multipulse schemes, allowing for an arbitrary combination of pulses from both arms, where the relative delay between the two arms can be controlled using the delay stage.

by external-cavity diode lasers operated in CW mode with active frequency stabilisation through a wavemeter and pulses are derived using AOMs and electro-optic modulators (EOMs). The coherent rotations are derived from a mode-locked Ti:sapphire laser and the setup to selectively pick pulses will be described in the next section. Depending on the experiment we detect the quantum dot fluorescence using a spectrometer, silicon based avalanche photodiodes (APDs) or superconducting nanowire single photon detectors (SNSPDs) optimised for the quantum dot wavelength.

2.2.3 Pulsed laser setup

In order to realise coherent optical rotations of the spin state, we need a powerful source for ps-laser pulses. In our experiments we use a mode-locked Ti:sapphire laser with a repetition rate of 76 MHz to provide us with ~ 3 ps long pulses. Experimentally, we need a different repetition rate most of the time which means that we need to have the ability to isolate certain pulses, a process referred to as pulse picking. Moreover, we often need to vary the delay between two pulses in the sub-nanosecond range. This is achieved through the implementation of an unstabilised Michelson interferometer. Depending on the experimental requirements we work with the two different configurations presented in Fig. 2.5.

For experiments which require small inter-pulse delays for equally strong pulses, we use the configuration shown in Fig. 2.5 (a). The train of pulses is split by a 50:50 beam splitter and the two interferometer arms are reflected using retroreflectors. Subsequently both beams

are recombined on the same beam splitter. This way, we get two identical outputs with about a quarter of the initial power which we can then further pulse pick and send to two different quantum dots. One of the retroreflectors is mounted on a piezoelectric delay stage which is used to control the inter-pulse delay over a range of 1.2 ns with an accuracy of $\ll 1$ ps.

For sequences where the inter-pulse delay needs to be > 1.2 ns or for more complicated multipulse schemes we need to be able to introduce more flexibility in terms of the pulse picking. This is achieved by removing the stationary retroreflector as shown in Fig. 2.5 (b). In this configuration we get two trains of pulses at about half the initial power. Through the motorised delay stage we can vary the relative delay between the two arms and individually pulse pick from each train of pulses before recombining them.

In general, the pulse picking is performed by passing the pulses either through an EOM or a 350 MHz AOM which are controlled through voltage pulses that are generated in synchronisation to the repetition rate of the mode-locked laser. The final rotation is dependent on the pulse area and we can use additional 80 MHz AOMs to stabilise the average power at the microscope through a PID controlled feedback loop.

2.3 Experimental techniques

This section gives a short overview of the optical methods used to interact with the quantum dot and the spin of the resident charge carrier.

2.3.1 Photoluminescence

Photoluminescence (PL) is a term for the light that is emitted subsequent to the absorption of photons, in our case through the recombination of electron-hole pairs. In order to generate electron-hole pairs we non-resonantly drive our system with above band gap excitation, typically at 780 nm. This way, we create free charge carriers that form excitons in the wetting layer. Through non-radiative decay channels these excitons populate the lowest energy states before they radiatively recombine. If there is a quantum dot in close proximity they will populate its lowest energy state and subsequently recombine emitting a photon at the transition frequency. By recording the PL emission with a spectrometer we can therefore identify the general features of a quantum dot, such as transition frequencies and charging plateaus.

Figure 2.6 shows a PL map where we record spectra at different gate voltages to recover a two-dimensional map of the charging plateaus. The gate voltage dependence can be used to identify the different charging configuration of the quantum dot and we can identify the

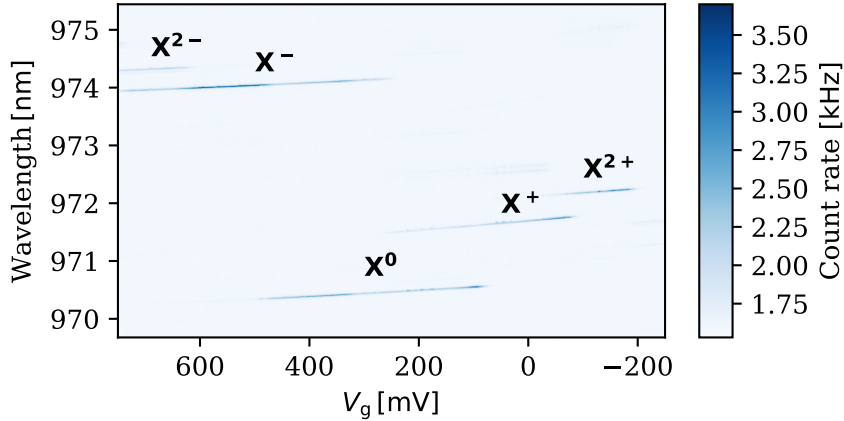


Fig. 2.6 **Photoluminescence spectra** Photoluminescence as a function of applied gate voltage. We can identify different charge states of the quantum dot which shift in wavelength with applied electrical field. This is a clear signature of the DC-Stark shift.

neutral exciton, X^0 as well as the two trions, X^\pm and even higher charge states, $X^{2\pm}$. We cannot observe the fine-structure splitting of the neutral exciton as the resolution of the spectrometer is limited to 10 GHz. The overlap of the different charge states can be explained due to the optically created charges which allow for different charge configurations at a fixed gate voltage. This behaviour depends on the tunneling probability which is controlled by the relatively thick tunnel barrier in our samples. A result of the overlap of different charge states is fast, second-order cotunneling across the tunnel barrier, which randomises the spin orientation in nanoseconds [62, 63]. Typically, we are interested in a long spin lifetime and thus work far away from these regions. However, the mechanism can be used to thermalise the nuclear spin bath [64], erasing any parasitic nuclear spin polarisation. The non-zero gradient of the charging plateaus is a direct result of the quantum-confined Stark shift discussed earlier.

This technique is used to find a suitable quantum dot for our experiments and determine its wavelength. Furthermore, we can use the emission spectrum to align our microscope optics through optimisation of the position and angle of the excitation and collection beam. Experiments are then carried out using the resonant transitions, which we can identify using the PL spectrum.

2.3.2 Resonant excitation

Resonance fluorescence (RF) is the light that is scattered if we drive a transition close to the resonance condition, a technique that is key to our experiments. The basic principle can be

understood by considering a simple two-level system interacting with a classical light field, which can subsequently be generalised to multi-level systems.

Hamiltonian for resonant interaction with a two-level system

We assume an idealised system with a single ground $|g\rangle$ and excited state $|e\rangle$ as depicted in Fig. 2.7 (a), which is described by the Hamiltonian:

$$\hat{H}_0 = \hbar\omega_e |e\rangle \langle e|. \quad (2.2)$$

The system is perturbed by the introduction of an oscillation electric field, which we assume to be linearly polarised along the x -axis, $\mathbf{E}(t) = E_0 \cos(\omega t) \mathbf{e}_x$. The resulting interaction Hamiltonian is given by:

$$\hat{H}_1(t) = -\hat{\mathbf{d}} \cdot \mathbf{E}(t), \quad (2.3)$$

where $\hat{\mathbf{d}} = q\hat{\mathbf{r}}$ denotes the electric dipole operator for a charge q which couples the two states [65]:

$$\hat{\mathbf{d}} = q \langle e | \hat{x} | g \rangle |e\rangle \langle g| + q \langle g | \hat{x} | e \rangle |g\rangle \langle e|. \quad (2.4)$$

Through going to a frame rotating at the laser frequency and applying the rotating wave approximation, where we neglect fast oscillating terms, we find that $\hat{H} = \hat{H}_0 + \hat{H}_1$ is given by:

$$\hat{H} = -\hbar\Delta |e\rangle \langle e| + \frac{\hbar\Omega}{2} (|e\rangle \langle g| + |g\rangle \langle e|). \quad (2.5)$$

Here, Δ denotes the detuning of the laser frequency from the transition and we can see that the two level system is now coupled via the Rabi frequency $\Omega = -E_0 q \langle e | \hat{x} | g \rangle / \hbar$. For simplicity, we assume $\Omega \in \mathbb{R}$ in the following discussion.

AC-Stark effect

Before taking a look at the population transfer between the ground and excited state, we can diagonalise the Hamiltonian and see the effect of the light field on the transition energies. The two eigenenergies are given by:

$$E_{\pm} = \frac{\hbar}{2} \left[-\Delta \pm \sqrt{\Delta^2 + \Omega^2} \right] \quad (2.6)$$

and the corresponding eigenstates are:

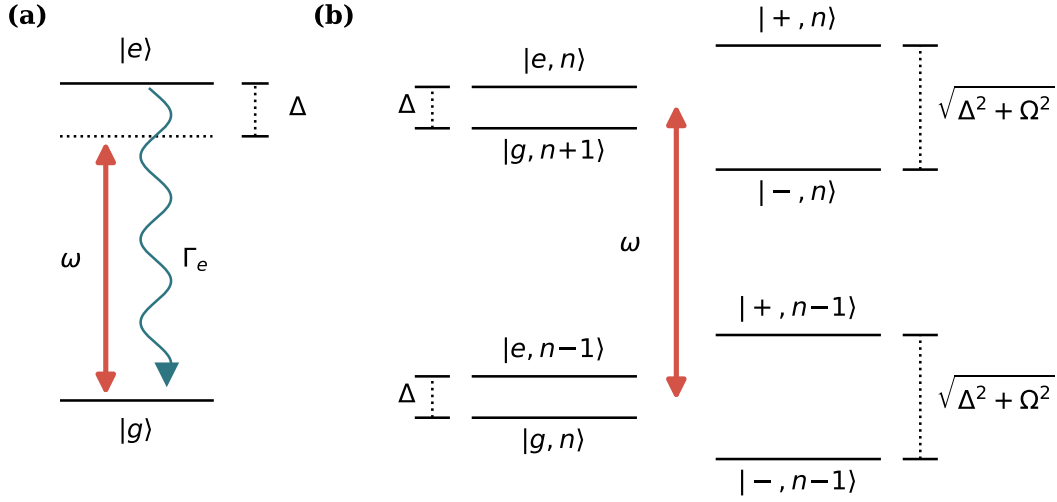


Fig. 2.7 **Two-level system** (a) Schematic of energy levels of a two-level system, indicating the spontaneous emission rate Γ_e , the driving laser light field ω and its detuning Δ from the excited state. (b) Schematic of the bare (left) and dressed (right) states and photon numbers $n, n \pm 1$ for a driven two-level system.

$$|+\rangle = \sin \theta |g\rangle + \cos \theta |e\rangle \quad (2.7)$$

$$|-\rangle = \cos \theta |g\rangle - \sin \theta |e\rangle, \quad (2.8)$$

where $\tan \theta = \Omega / (\Delta + \sqrt{\Delta^2 + \Omega^2})$. This shift of the ground- and excited-state energies is known as AC-Stark shift and the corresponding eigenvectors are called dressed states. The level scheme of the bare and dressed eigenstates is shown in Fig. 2.7 (b). At resonance ($\Delta = 0$) the bare states would be degenerate, but instead they are coupled by the classical light field dressing the system. This dressing results in an anti-crossing of the bare states with a splitting which is proportional to the Rabi-frequency. Experimentally this so-called Autler-Townes splitting can be observed in the absorption spectrum. If we scan a weak probe across the transition to a third energy level whilst strongly driving the bare transition of the two-level system, we recover two peaks in the absorption spectrum which are separated by Ω [66–68]. Equally, the dressing of the system through a strong drive leads to the formation of a Mollow triplet in the emission spectrum, where one observes a central peak at the bare resonance frequency and two satellite peaks at $\pm\Omega$ [65, 69–71].

Dynamics of the system - optical Bloch equations

In order to get a more realistic picture of the population transfer we have to introduce the spontaneous decay of the excited state population at a rate $\Gamma_e = 1/T_1$. The coherence of the state will then decay following the dephasing time T_2 :

$$\frac{1}{T_2} = \frac{1}{2T_1} + \gamma, \quad (2.9)$$

where we have included a pure dephasing rate γ . For a transform-limited linewidth, i.e. in the absence of pure dephasing, the time evolution of the system under this incoherent relaxation and the Hamiltonian in Eqn. 2.5 is described by the optical Bloch equations [72]:

$$\dot{\rho}_{ee} = -\dot{\rho}_{gg} = i\frac{\Omega}{2}(\rho_{eg} - \rho_{ge}) - \frac{\rho_{ee}}{T_1} \quad (2.10)$$

$$\dot{\rho}_{ge} = (\dot{\rho}_{eg})^* = i\frac{\Omega}{2}(\rho_{gg} - \rho_{ee}) - \rho_{ge}\left(\frac{1}{T_2} + i\Delta\right), \quad (2.11)$$

where the density matrix is defined as $\rho_{ij} = |i\rangle\langle j|$.

Excited state population - steady state solution

In the case of our experiments the excitation typically takes place on timescales much longer than the excited state lifetime T_1 and we can assume that the system reaches a steady state between coherent transfer of population and incoherent decay of the excited state. Therefore, we can set $\dot{\rho}_{ee} = \dot{\rho}_{ge} = 0$ and we find that the population of the excited state is given by:

$$\rho_{ee} = \frac{1}{2} \frac{\Omega^2}{(T_1 T_2)^{-1} + \Delta^2 T_2 T_1^{-1} + \Omega^2}. \quad (2.12)$$

The maximum population of the excited state on resonance is $\rho_{ee} = 1/2$ and we approach this value asymptotically for increasing laser intensity $I \propto \Omega$. In the laboratory it is useful to describe the strength at which we drive a transition in terms of the so called saturation intensity I_{sat} which corresponds to $\rho_{ee} = 1/4$. This way, we can define the dimensionless saturation parameter $s = I/I_{sat} = T_1 T_2 \Omega^2$ and rewrite Eqn. 2.12 as:

$$\rho_{ee} = \frac{1}{2} \frac{s}{1 + s + \Delta^2 T_2^2}. \quad (2.13)$$

Multiplying the excited state population with its decay rate we obtain the scattering rate of the excited state $\Gamma_{RF}(s, \Delta) = \Gamma_e \rho_{ee}(s, \Delta)$. The intensity of the fluorescence we detect is directly related to Γ_{RF} allowing us to determine I_{sat} through a measurement of the resonant

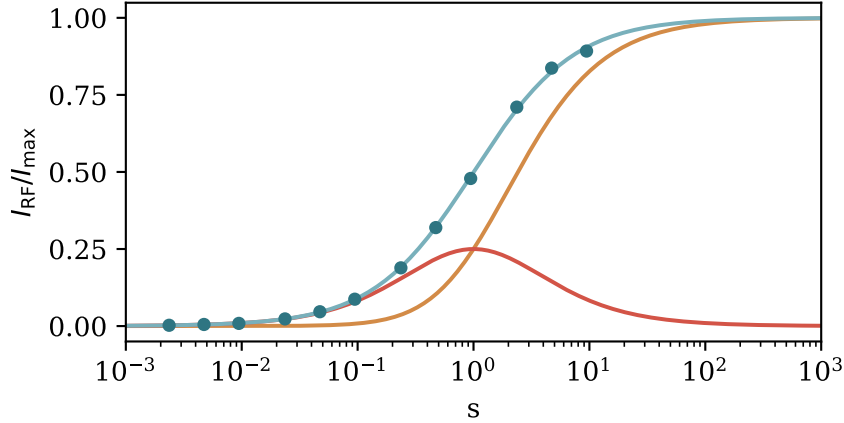


Fig. 2.8 **Resonance fluorescence intensity** Measurement of the saturation of I_{RF} , blue curve represents fit to the data points. The red (orange) curves represent the coherent (incoherent) fraction of the RF intensity, assuming no pure dephasing.

quantum dot emission for different laser intensities. An example of such a measurement is shown in Fig. 2.8 where the data are fitted with $I_{RF}(s) = I_{max}s/(1 + s)$ (blue curve) to extract the saturation intensity.

The absorption has a Lorentzian line shape with a full width at half maximum (FWHM) $\Delta_{FWHM} = \sqrt{4T_2^{-2}(1 + s)}$. At low driving intensity ($s \ll 1$) the width of the transition is set by the natural linewidth $\Gamma_e = 1/T_1 = 2/T_2$ whereas at high intensity the emission is power broadened: while the absorption close to the resonance is saturated, it is nearly unaffected at larger detunings.

Emission properties

The scattered light has two contributions: a coherent part owing to the interaction with the transition dipole, I_{coh} , as well as an incoherent part owing to the spontaneous decay of excited state population, I_{incoh} . The coherent scattering does not change the energy of the photon and is thus often also referred to as elastic scattering. Accordingly, the incoherent scattering is called inelastic scattering. The fraction of elastically scattered light is given by [73]:

$$\frac{I_{coh}}{I_{tot}} = \frac{1}{2} \frac{T_2^3 T_1^{-1} \Delta^2 + T_2 T_1^{-1}}{T_2^{-2} \Delta^2 + 1 + s}, \quad (2.14)$$

where $I_{tot} = I_{coh} + I_{incoh}$. If we consider the case where we drive the system on resonance the expression simplifies to:

$$\frac{I_{\text{coh}}}{I_{\text{tot}}} = \frac{1}{2} \frac{T_2 T_1^{-1}}{1 + s} \quad (2.15)$$

and we can see that the fraction of coherently scattered light is determined by the strength of the driving light field. The corresponding fractions of coherently and incoherently scattered light in the absence of pure dephasing are shown in Fig. 2.8. For low driving powers ($s \ll 1$) and in the absence of pure dephasing the light is mainly scattered elastically and the spectrum is centered around the drive frequency [73, 74], following its linewidth [75]. In fact, the scattered light carries the coherence of the drive field, which can be used to shape the waveform of the emitted photons [76]. As a consequence, elastically scattered light offers protection against small spectral wandering of the resonance frequency, even though its phase will still be susceptible to the changing frequency. At high driving powers ($s > 1$) the incoherent decay of excited-state population starts to dominate and the elastic scattering is strongly suppressed, leading to an emission spectrum determined by the dephasing time and power broadening of the transition.

Independent of the excitation intensity, the two-level system can only support a single excitation at a time, leading to highly non-classical behaviour of the autocorrelation, $g^{(2)}(\tau)$ of the emitted photons around $\tau = 0$. For a coherent light source the autocorrelation is pinned to 1 independent of the delay. In contrast, a two-level system can only emit one photon at a time and therefore we observe antibunching for $g^{(2)}(\tau = 0)$. This is true for both elastically and inelastically scattered light [73] and is clear evidence that the system acts as a single photon source [77].

Three-level system

We have seen that InGaAs quantum dots provide three or four energy levels depending on the charge state. These additional levels give rise to a variety of phenomena that do not exist for the basic two-level system. The experiments presented in this work rely on isolating a Λ -system within the energy levels of the positive or negative trion. In Fig. 2.9 we show such a Λ -system including two detuned light fields and spontaneous decay rates of the excited state.

Following the approach we used to describe the two level system, we find that the Hamiltonian of the system is given by:

$$\begin{aligned} \hat{H} = & -\hbar\Delta_1 |e\rangle \langle e| - \hbar(\Delta_1 - \Delta_2) |g_2\rangle \langle g_2| \\ & + \frac{\hbar\Omega_1}{2} (|e\rangle \langle g_1| + |g_1\rangle \langle e|) + \frac{\hbar\Omega_2}{2} (|e\rangle \langle g_2| + |g_2\rangle \langle e|) \end{aligned} \quad (2.16)$$

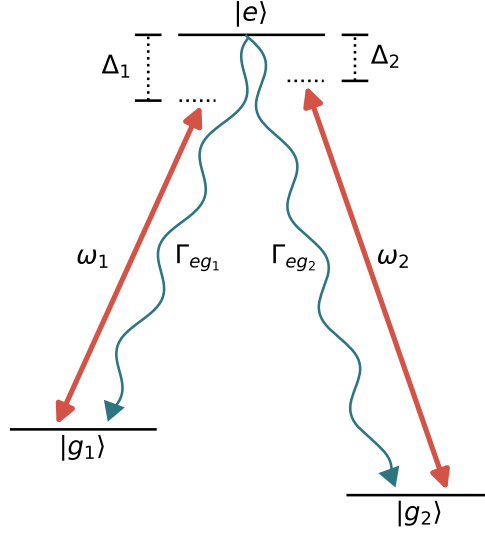


Fig. 2.9 **Three-level system** Schematic of energy levels of a three-level system, indicating the spontaneous emission rates ($\Gamma_{eg_1}, \Gamma_{eg_2}$), the driving laser light fields (ω_1, ω_2) and corresponding detunings from the excited state (Δ_1, Δ_2).

The eigenstates of this Hamiltonian, assuming two-photon resonance ($\Delta_1 = \Delta_2 = \Delta$) are given by [78]:

$$|+\rangle = \sin \theta \sin \phi |g_1\rangle + \cos \phi |e\rangle + \cos \theta \sin \phi |g_2\rangle \quad (2.17)$$

$$|0\rangle = \cos \theta |g_1\rangle - \sin \theta |g_2\rangle \quad (2.18)$$

$$|-\rangle = \sin \theta \cos \phi |g_1\rangle - \sin \phi |e\rangle + \cos \theta \cos \phi |g_2\rangle, \quad (2.19)$$

where the mixing angles are given by:

$$\tan \theta = \frac{\Omega_1}{\Omega_2} \quad (2.20)$$

$$\tan 2\phi = \frac{\sqrt{\Omega_1^2 + \Omega_2^2}}{\Delta}. \quad (2.21)$$

The $|0\rangle$ state has no contribution of the bare excited state and does not experience a shift in energy, whereas the $|\pm\rangle$ states are shifted by:

$$E_{\pm} = \frac{\hbar}{2} \left(\Delta \pm \sqrt{\Delta^2 + \Omega_1^2 + \Omega_2^2} \right). \quad (2.22)$$

In the limit of $\Delta = 0$ and $\Omega_2 \ll \Omega_1$, i.e. we strongly drive the first transition to dress the system while weakly probing the second transition, we recover the Autler-Townes splitting discussed earlier.

The $|0\rangle$ state, is a so-called dark state since it cannot lead to spontaneous emission owing to the absence of any contribution of the excited state. This results in a number of interesting phenomena, one of which involves pumping the population into the dark state, known as coherent population trapping (CPT) [79, 80]. In the limit of $\Omega_1 \ll \Omega_2$, $|0\rangle \rightarrow |g_1\rangle$ and resonant absorption of the incident light field is frustrated - a process known as electromagnetically induced transparency (EIT) [78, 81]. The narrow EIT resonance results in a large gradient of the refractive index which can be used to strongly reduce the group velocity of a light pulse and create slow light [82]. In fact, the velocity can be slowed down to zero, allowing the storage of a light pulse for example in an atomic vapor [83]. Finally, the dark state can also be used to coherently transfer population between the two ground states without population of the excited state. This technique is known as stimulated Raman adiabatic passage (STIRAP) [84, 85].

In our experiments we work with a Λ -system in Voigt geometry where the two ground states form the computational basis. Typically, we only drive one of the two transitions in order to read out and initialise the spin state. The corresponding level scheme including the drive field is depicted in Fig. 2.10 (a). In this configuration, we only get photons if the spin is initially in the $|\uparrow\rangle$ state. Owing to the 50% branching ratio of the excited state ($\Gamma_{e\downarrow} = \Gamma_{e\uparrow} = \Gamma$), we get on average two photons before the spin population is transferred to the $|\downarrow\rangle$ state. This way, we can use the spin pumping to probabilistically read out and initialise the spin with a single resonant laser pulse.

Figure 2.10 (b) shows the measured fluorescence during a readout pulse for different driving powers. The exponential decay of the signal scales with the power of the resonant drive and we can initialise the spin in nanoseconds with fidelities $> 98\%$ [49, 50]. The fidelity of the initialisation can be estimated by the residual fluorescence at the end of the readout pulse, shown in the inset, compared to the maximum of the readout pulse. For the measurement presented here we obtain a residual population of the $|\downarrow\rangle$ state of $11 \pm 3\%$, $2.1 \pm 0.9\%$ and $0.8 \pm 0.04\%$ with increasing power.

The decay of the high-power measurements does not follow a single exponential decay but shows additional oscillations which are a signature of Rabi oscillations between the ground and excited state owing to the strong resonant drive.

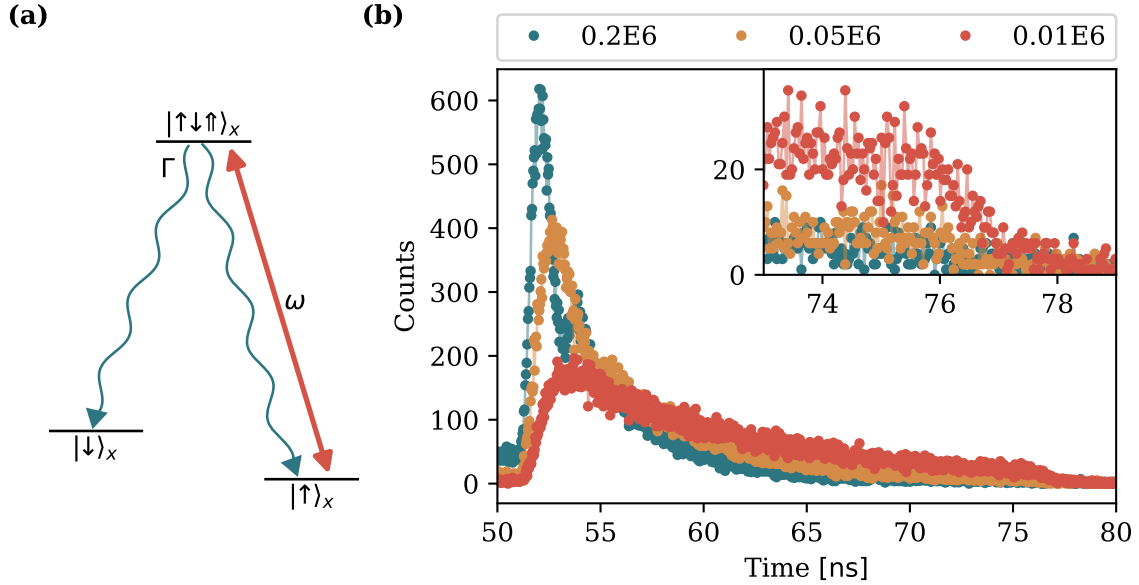


Fig. 2.10 **Readout and initialisation** (a) Schematic of a Λ -system within the energy-level structure of a trion used for readout and initialisation of the spin state. (b) Measurement of spin pumping within a 25 ns readout and initialisation pulse for different laser powers. The inset shows a zoom in on the fluorescence at the end of the readout pulse.

2.3.3 Coherent rotations

So far we have seen how we can identify quantum dots through PL and resonantly drive the optical transitions, which allows us to initialise and read out the spin state in a charged quantum dot. For the implementation of any quantum information protocol we require one more key ingredient: full coherent control of the spin state [22].

In general, we can achieve coherent control by resonantly driving the transition between the two ground states with microwave-frequency pulses [86, 87]. However, this process typically requires tens of nanoseconds and is therefore not compatible with the spin dephasing time in our quantum dots. Instead, there have been a number of proposals to use ultrafast optical pulses to manipulate the spin state [41, 88–92], followed by the experimental realisation of full coherent control for the electron [93] and hole spin [94].

In order to work with coherent rotations we have to align our external magnetic field perpendicular to the growth axis, resulting in the energy-level structure introduced in Fig. 2.2 (c). We follow the convention that the growth axis is along the z -direction and the external magnetic field, defining the eigenstates of the system, is applied along the x -axis. The process allowing for the rotation of the ground-state spin can be understood as a Raman process [88,

92, 95] or equivalently by considering the AC-Stark shift [94, 96]. Here, we view the process in the AC-Stark shift picture.

The optical axis is aligned with the growth axis and the application of a short, high-intensity laser pulse can best be viewed in the corresponding z -basis. The pulse length of 2-4 ps is much shorter than the Larmor precession in the external magnetic field and we can therefore approximate the ground states to be degenerate on the relevant time scales, i.e. we are going to neglect the external magnetic field.

The two transitions in this basis are selectively driven by circularly polarised light, leading to polarisation dependent amplitudes of the Rabi frequencies Ω_{\pm} . In the case of a large detuning $\Delta \gg \Omega_{\pm}$ the pulse will not create any excited state population and we can adiabatically eliminate the excited states. However, the two ground states will experience a time-dependent AC-Stark shift (Sec. 2.3.2) given by:

$$\delta_{\pm}(t) = \frac{1}{2} \sqrt{\Delta^2 + |\Omega_{\pm}(t)|^2} - \frac{\Delta}{2}. \quad (2.23)$$

We denote the two ground states in the z -basis as $|\leftarrow\rangle$ & $|\rightarrow\rangle$, which can be written in terms of the eigenstates of the system defined by the external magnetic field, $|\uparrow\rangle$ & $|\downarrow\rangle$:

$$|\leftarrow\rangle = \frac{1}{\sqrt{2}} (|\downarrow\rangle + |\uparrow\rangle) \quad (2.24)$$

$$|\rightarrow\rangle = \frac{1}{\sqrt{2}} (|\downarrow\rangle - |\uparrow\rangle) \quad (2.25)$$

Due to the AC-Stark shift these states will acquire a relative phase shift, depending on the pulse area of the applied rotation pulse. The resulting rotation angle is given by the difference of the time-dependent Stark shifts integrated over the duration of the rotation pulse:

$$\theta = \int [\delta_{+}(t) - \delta_{-}(t)] dt. \quad (2.26)$$

More specifically, a spin initialised in the $|\downarrow\rangle$ can be written as:

$$|\downarrow\rangle = \frac{1}{\sqrt{2}} (|\leftarrow\rangle + |\rightarrow\rangle) \quad (2.27)$$

and the application of a rotation pulse will result in the final state:

$$\begin{aligned} \frac{1}{\sqrt{2}} \left(e^{i\theta} |\leftarrow\rangle + |\rightarrow\rangle \right) &= \frac{1}{2} \left(e^{i\theta} |\downarrow\rangle + e^{i\theta} |\uparrow\rangle + |\downarrow\rangle - |\uparrow\rangle \right) \\ &= \frac{1}{2} \left[\left(e^{i\theta} + 1 \right) |\downarrow\rangle + \left(e^{i\theta} - 1 \right) |\uparrow\rangle \right], \end{aligned} \quad (2.28)$$

so in the case of $\theta = \pi$ we indeed transfer the spin population to the $|\uparrow\rangle$ state.

Equation 2.26 shows that the angle depends on the relative AC-Stark shift of the two ground states. Therefore, we choose the polarisation of the laser pulse such that we mainly drive one of the two transitions; due to imperfect selection rules and experimentally limited control of the polarisation we always have residual coupling the other transition. For mostly σ_+ polarised light we can assume that $\Omega_+ \gg \Omega_-$, maximising the efficiency of the rotation in terms of required laser power.

The picture presented here is of course only an approximation, since we neglect any effect of the external magnetic field, and we will discuss the effect of a non-zero field along the x -axis at the end of this section.

In our experiments the ultra-short laser pulses are provided by the mode-locked laser (Sec. 2.2.3) which we typically operate at detunings of ~ 3 nm. We choose to work at energies below the resonant transition (red detuned) in order to avoid phonon assisted population of the excited state [97, 98].

Measurement of Rabi oscillations

For every experiment involving coherent spin rotations we have to first calibrate the pulse area to match the desired rotation angle. In our case, we tune the pulse area by modifying the total power as the length of the pulses is fixed to ~ 3 ps.

The sequence used to measure Rabi oscillations is depicted in Fig. 2.11 (a). We apply a constant resonant drive to the high energy transition which serves to initialise and read out the spin state. Every 13.14 ns we introduce a ps-rotation pulse to transfer the spin population. Using an AOM, we tune the average power and thus the rotation angle. Figure 2.11 (b) shows the count rate recorded for such a measurement with respect to the average power measured at the cryostat input. The recorded fluorescence is a direct measure of the spin population after the rotation pulse and we recover spin-Rabi oscillations with increasing pulse area. The count rate for a 2π -rotation is a good measure for the coherence of the process and the low values we recover show that we indeed transfer the population without introducing significant decoherence. The main source for decoherence during this process is provided by excitation-induced dephasing due to coupling to acoustic phonons [99]. However, our data

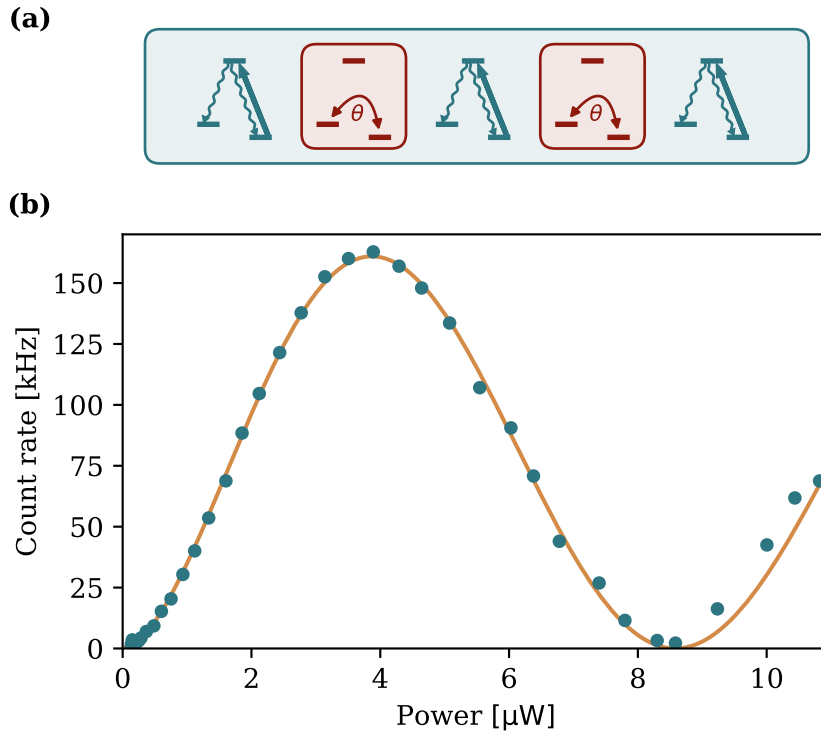


Fig. 2.11 **Rabi oscillations** (a) Pulse sequence for a Rabi measurement. The spin state is continuously read out while we introduce a rotation every 13.14 ns. The rotation angle is set by the pulse area. (b) Count rate for the readout depending on the pulse area (power). The solid curve represents a sinusoidal fit with a sublinear power dependence.

indicate that this effect has only an insignificant contribution on the single pulse level and we will consider our rotations as coherent for the rest of this work.

Measurement of Ramsey interference fringes

Full control over the spin state requires rotations around an arbitrary axis of the Bloch sphere. In the case of quantum dots we can achieve this by using a combination of rotations around the z -axis using coherent rotation pulses and the free evolution of the spin in the external magnetic field which effectively realises a rotation around the x -axis. Combining these two mechanisms allows for full control of the spin state through careful timing of the applied rotations. This control is demonstrated through a Ramsey interference measurement.

The pulse sequence for such an experiment is presented in Fig. 2.12 (a). We apply two $\pi/2$ -rotations with a varying delay, τ , followed by a readout and initialisation pulse resonant with the high energy transition. Experimentally, the two pulses are derived from the pulsed laser using an interferometer as discussed in Sec 2.2.3 and we use the delay stage to control

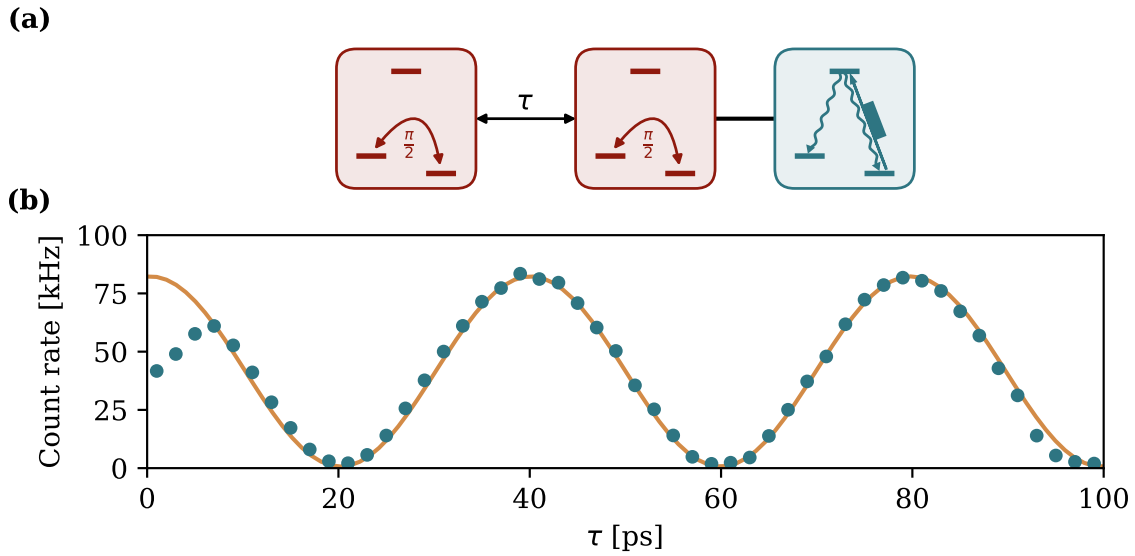


Fig. 2.12 **Ramsey interference** (a) Pulse sequence for the measurement of Ramsey interference fringes. Two $\pi/2$ rotations with variable inter-pulse delay, τ , are followed by a readout and initialisation pulse. (b) Recorded count rate at 4 T external magnetic field. Through fitting the data with a sine (solid curve) we extract a Larmor frequency of 25.16 ± 0.06 GHz and a visibility of $98 \pm 2\%$.

the separation τ . The pulse area is calibrated through a Rabi measurement and controlled by setting the average power using a filter wheel or an AOM. For the readout and initialisation we derive a pulse from a continuous wave (CW) laser using an EOM.

Through changing τ we are able to observe the precession of the spin in the magnetic field, evidenced by oscillations of the fluorescence count rate we recover. Such a measurement performed at an external magnetic field of 4 T is shown in Fig. 2.12 (b). The sinusoidal oscillation is a direct measure of the Larmor frequency and by fitting a sine curve to the data (solid line) we extract a precession frequency of 25.16 ± 0.06 GHz and a visibility of $98 \pm 2\%$. Here, the deviation of the data from the fit for $\tau < 8$ ps is caused by overlap of the two rotation pulses.

Within one Larmor precession we achieve rotation fidelities $> 99\%$, ultimately limited by the spin dephasing. If we sweep the delay for times longer than one Larmor precession, we can measure the fluctuations of the spin splitting resulting in a reduced average visibility. The decay of visibility with increasing delay provides a way of measuring the inhomogeneous spin dephasing time, as we will see in Chapter 5 and 6.

Compound pulses

As previously mentioned, neglecting the spin evolution due to the external magnetic field is only strictly valid for delta-like pulses and thus we apply it as an approximation. However, our pulses have a finite length of ~ 3 ps and we have seen that in a 4 T magnetic field a full Larmor precession takes about 40 ps. Therefore, we have a significant contribution of the spin precession in the externally applied magnetic field. This competition between the external magnetic field and the effective field due to the AC-stark shift results in a rotation axis which is not fully transverse to the growth axis but slightly tilted [95].

The tilt of the rotation axis will prevent us from fully inverting the spin with a π pulse and thus limit our rotation fidelity. We can counteract this error, by using composite (or compound) pulses [100, 101]. The basic idea is that we split a π rotation into two $\sim \pi/2$ rotations separated by about one Larmor precession. Through fine-tuning the exact delay and amplitude of the pulses we can significantly increase the fidelity of the state inversion.

In general, the pulse fidelities are sufficient for our experiments. However, complex pulse schemes with multiple successive π rotations as well as high-fidelity state tomography require very precise rotations. In Sec. 3.4 we will see that the implementation of such composite rotations results in an increase in rotation fidelity of about 5%.

2.4 Nuclear spin environment

In self-assembled InGaAs quantum dots the charge carrier is trapped in a mesoscopic environment where it interacts with $10^4 - 10^5$ nuclear spins as every atomic site carries a non-zero spin component. This so-called central spin problem leads to a number of interesting phenomena, as well as experimental challenges [102].

2.4.1 Hyperfine interaction

The two main interactions between the nuclear spin bath and the charge carrier are the Fermi-contact hyperfine interaction and the direct dipole-dipole hyperfine coupling. The former interaction dominates for the s -type state of the electron, whereas the p -type heavy-hole states have a vanishing wavefunction at the nuclear sites and mainly experience dipole-dipole coupling, which is found to be an order of magnitude weaker [51, 52].

Fermi-contact hyperfine interaction

The Fermi-contact hyperfine interaction for the electron is described by the following Hamiltonian [103]:

$$\hat{H}_{fc} = v_0 \sum_j A_j^e |\Psi(\mathbf{r}_j)|^2 \left(\hat{I}_z^j \hat{S}_z^e + \frac{1}{2} [\hat{I}_+^j \hat{S}_-^e + \hat{I}_-^j \hat{S}_+^e] \right), \quad (2.29)$$

where v_0 is the unit cell volume and we sum over all nuclear sites j , with a nuclear spin \hat{I}^j and hyperfine coupling constant A_j^e which is on the order of $\sim 50 \mu\text{eV}$ for In, Ga and As [103, 104]. The normalised charge carrier wavefunction at site j is given by $|\Psi(\mathbf{r}_j)|^2$ and \hat{S}^e denotes the electron spin.

In general we observe two types of interactions: the $\hat{I}_z^j \hat{S}_z^e$ term alters the precession frequencies along a well defined axis, whereas the $\hat{I}_\pm^j \hat{S}_\mp^e$ terms enable flip-flop interactions around the other two axes. The latter interaction can be suppressed by applying an external magnetic field, which leads to a large mismatch in the splittings of the charge carrier and the nuclear spins.

In a semi-classical picture we can approximate the interaction as an effective field acting on the host spin, the Overhauser field [103]:

$$\mathbf{B}_{\text{OH}} = \frac{v_0}{g_e \mu_B} \sum_j A_j^e |\Psi(\mathbf{r}_j)|^2 \langle \hat{\mathbf{I}}^j \rangle. \quad (2.30)$$

In the absence of an external magnetic field the nuclear spins are randomly polarised and on average the Overhauser field is zero. However, as a result of the mesoscopic nature of our system the fluctuations of the field, σ_{OH} , are non-negligible: the nuclear spin operators along the three orthogonal axes do not commute and thus cannot be determined simultaneously and due to the limited number of nuclear spins the contribution of each site is finite, i.e. $|\Psi(\mathbf{r}_j)|^2 > 0$. The dispersion of the Overhauser field can be described by a three dimensional Gaussian distribution:

$$W(\mathbf{B}_{\text{OH}}) \propto \exp \left[-\frac{3(\mathbf{B}_{\text{OH}})^2}{2\sigma_{\text{OH}}^2} \right]. \quad (2.31)$$

If we approximate the electron wavefunction as a uniform distribution across all lattice sites, $\Psi(\mathbf{r}_j) \propto 1/\sqrt{N}$, the variance scales with the number of nuclei and can be approximated by $\sigma_{\text{OH}} \approx B_{\text{OH}}^{\text{max}}/\sqrt{N}$, where $B_{\text{OH}}^{\text{max}}$ denotes the Overhauser field corresponding to 100% nuclear spin polarisation, resulting in fluctuations of $\sim 30 \text{ mT}$ [103].

The nuclei experience an analogous field produced by the electron spin: the Knight field. The interaction is proportional to the electron wavefunction and thus its strength shows a

strong spatial dependence. Overall this interaction is much weaker as it is the result of a single spin compared to N nuclear spins. Therefore, the corresponding Overhauser field dynamics are much slower compared to the precession of the electron spin and we can assume the electron precesses around a constant field with random magnitude and direction distributed according to Eqn. 2.31 - often referred to as frozen fluctuation model [105]. However, in our system we often find that the Overhauser field dynamics are dominated by other processes related to the quadrupolar interaction of the nuclei discussed at the end of this section.

We typically work with a few-Tesla external magnetic field to suppress the electron-nuclear spin flip-flop interaction, allowing us to define a quantisation axis for the electron. In the presence of an externally applied field, the electron precesses in the effective field $\mathbf{B}_{\text{tot}} = \mathbf{B}_{\text{ext}} + \mathbf{B}_{\text{OH}}$ and the Overhauser field fluctuations result in variations of the electron spin splitting which leads to dephasing of the spin state. We further investigate the electron spin dephasing due to the coupling to the Overhauser field components in Chapter 5.

Dipolar hyperfine interaction

The dipolar hyperfine interaction that dominates for the hole spin takes a similar form to H_{fc} and is described by the following Hamiltonian [103]:

$$\hat{H}_{dd} = v_0 \sum_j \frac{A_j^h}{1 + \beta^2} |\Psi(\mathbf{r}_j)|^2 \left(\hat{I}_z^j \hat{S}_z^h + \frac{\alpha}{2} [\hat{I}_+^j \hat{S}_-^h + \hat{I}_-^j \hat{S}_+^h] \right), \quad (2.32)$$

where β denotes the hh - lh mixing and is typically on the order of ~ 0.1 in our quantum dots. \hat{S}^h now represents the pseudospin $\frac{1}{2}$ operator for the heavy hole. The dipole-dipole interaction is highly anisotropic and in the case of a pure heavy-hole state the anisotropy factor α is in fact zero, i.e. only the z component of the nuclear spins contributes to the hyperfine coupling [104]. The small but significant hh - lh mixing in our samples suppresses the anisotropy resulting in $\alpha = 2|\beta|/\sqrt{3}$. The main difference to \hat{H}_{fc} apart from this anisotropy are the strongly reduced hyperfine coupling constants A_j^h which are about an order of magnitude weaker [51, 52].

In a similar fashion to our electron model, we can describe this interaction as a semi-classical field, this time taking into account the anisotropy of the interaction which leads to highly anisotropic Overhauser field fluctuation [103]:

$$W(\mathbf{B}_{\text{OH}}) \propto \exp \left[-\frac{(\mathbf{B}_{\text{OH},z})^2}{2(\sigma_{\text{OH},\parallel})^2} \right] \exp \left[-\frac{(\mathbf{B}_{\text{OH},x})^2 + \mathbf{B}_{\text{OH},y}^2}{2(\alpha\sigma_{\text{OH},\parallel})^2} \right]. \quad (2.33)$$

This combination of anisotropy and reduced hyperfine interaction strength has motivated experiments using single hole instead of electron spins as they promise longer dephasing times [51]. We will investigate the coherence of a single hole in a dynamic nuclear environment in more detail in Chapter 6.

2.4.2 Nuclear quadrupolar interaction

Owing to the strain-driven growth process of self-assembled InGaAs quantum dots in combination with the random alloying of indium and gallium, the nuclei experience strong inhomogeneous electric-field gradients across the quantum dot [106]. The coupling to these electric-field gradients is enabled through the non-spherical charge distribution of the nuclei with a nuclear spin $> 1/2$ [103]; in our samples this condition is true for all isotopes. The quadrupolar coupling leads to a mixing of the eigenstates defined by the external magnetic field [107] and we will see in Chapter 5 and 6 that this interaction strongly influences the spin coherence at external magnetic fields of a few Tesla.

Moreover, this process enables charge-spin preserving nuclear spin flips through the hyperfine interaction, owing to the fact that the nuclear spin eigenstates are now a mixture of \hat{I}_z eigenstates [108]. This interaction leads to one of the most surprising effects in InGaAs quantum dots: the (anti-)dragging of optical resonances observed when driving the high (low) energy Zeeman transition with a detuned probe and at finite external magnetic fields [107, 109]. As a result the effect of electrical noise on the high energy transition can be strongly reduced, whereas the low energy transition is unstable and even small detunings will push the transition off resonance (anti-dragging). This effect is present for all our experiments and needs to be taken into consideration when designing an experiment.

Another interesting consequence of the quadrupolar fields is the suppression of nuclear diffusion due to the local shift of nuclear transition energies. As a result the strained nuclear bath preserves coherence for longer than the unstrained bath [110, 111] and for temperatures below 1 K the bath polarisation can potentially be maintained for hours [64].

2.5 Conclusion

In this introductory chapter, we have provided an overview of the most important concepts and experimental techniques required for the understanding of the experiments with InGaAs quantum dots presented in the remainder of this thesis.

By now, InGaAs quantum dots are a well-studied system and there are, of course, many more interesting concepts and experimental results to explore. Current areas of research

reach from fundamental optics experiments about the squeezing of resonance fluorescence [112] and efficient single photon sources [113] over the incorporation of quantum dots into photonic structures [44] and electrically gated micropillars [114] to the demonstration of spin-photon entanglement [28–30] and recently also quantum correlations between distant hole spins [115]. The latter work is closely linked to the experiment presented in the next chapter where we will demonstrate distant spin-spin entanglement for electrons [116]. More details about the fundamental concepts as well as the recent progress in the field of InGaAs quantum dots can be found in textbooks (e.g. [117, 118]) and review articles [27, 44, 103, 113].

Chapter 3

Elementary quantum network

"I would not call that one but rather the characteristic trait of quantum mechanics, the one that enforces its entire departure from classical lines of thought. By the interaction the two representatives (or ψ -functions) have become entangled."

- Erwin Schroedinger, [119]

Previously, we have given a broad overview of the attractions of quantum networks and the basic constituents needed for their realisation. We have also discussed the outstanding and unique properties offered by a single electron spin in a self-assembled InGaAs quantum dot, together with the recent progress in utilising them as a fully controllable qubit. Here, we will use two independent quantum dots linked through photonic channels as a test bed for the realisation of a quantum network.

In this Chapter, we demonstrate the successful generation of distant entanglement between two electron spins in separate cryostats. We first briefly discuss different ways of generating entanglement, before we introduce the probabilistic single photon scheme implemented in this work. We then present the details of the experimental setup and discuss the physical implementation of the protocol. Following this, we assess the quality of the two quantum dots chosen for this work and provide evidence that they meet the requirements of the employed protocol. Finally, we confirm the creation of an entangled two-spin state through measurements of three-photon correlations and discuss the limitations and experimental bounds to the achieved fidelity.

This experiment has been highly demanding, both on the time commitment as well as the physical setup and it has been a collaborative effort of the whole quantum dot team. Everyone has contributed significantly to the preparation, implementation and operation of the experiment. However, such a complex endeavour requires distribution of forces and

thus, Megan Stanley initially was in charge of the optical setup and phase stabilisation of the interferometer, while Robert Stockill took the lead in design and implementation of the pulse sequence including spin control and I focussed on the software for the acquisition and analysis of the data. We all have been supported by Claire Le Gall and Clemens Matthiesen, the postdocs who worked with us on the experiment and were essential to its success.

3.1 Entanglement protocol

There are several ways to generate entanglement between two distinct solid state qubits. Theoretically, the most straightforward way would be to use a combination of 1- and 2- qubit gates in order to directly entangle two qubits [120, 121] an approach which has been realised in different systems [122–124]. However, this usually requires the two systems to be in close proximity in order to initiate an interaction between them. Here, we are more interested in generating entanglement in the context of a quantum network, linking distant nodes through quantum channels. This can be achieved through entangling one of the nodes with a flying qubit (i.e. a single photon) and subsequently transferring the entanglement to the second node upon arrival of the flying qubit [125–127]. This protocol has the advantage that it provides deterministic entanglement but it comes at the cost of being susceptible to photon loss which scales exponentially with the length of the photonic channel [128]. However, single photons generally only interact weakly with their environment (which is why they are excellent flying qubits in the first place) and the qubits at the nodes usually need to be placed inside a cavity to enhance the interaction. There has been impressive progress in the field of quantum-dot micro-pillar cavities, including ultra-high extraction efficiencies [129], deterministic placement [130] and incorporation of electrical gates allowing stabilisation of the electrical environment and tuning of the transitions [114]. However, there is still some progress lacking in terms of incorporating spin initialisation, control and readout in those structures to the extent that is available in more basic structures like the ones used in this work.

Another approach is to use a probabilistic scheme where we generate the entanglement through projective measurements of either one or two photons. The advantage of such a scheme is that it is robust against losses in photonic channels, but it comes at the cost of being inherently probabilistic and it scales with the single photon detection efficiency. Here, we can distinguish between schemes relying on the detection of a single photon [131] opposed to schemes that rely on the detection of two photons [132, 133]. In the latter case both nodes are deterministically prepared in a superposition state which is entangled with a property of a corresponding photon (e.g. polarisation or time). The which-path information

is erased through interference of the two photons on a beam splitter and a photonic Bell state is created. Subsequently a careful measurement of the Bell state will project the two nodes into a well defined entangled state. Such two-photon schemes have successfully been implemented in experiments using atoms and ions [134, 135], as well as Nitrogen vacancy centers (NVs) [136] and recently superconducting qubits [137]. However, the need to detect two single photons means that this method scales quadratically with the collection and detection efficiency of single photons. In contrast, a scheme relying only on the detection of a single photon will scale linearly with these efficiencies and is thus favourable for a system such as ours, where the collection efficiency is estimated to be about 2%. Of course, we will see that such a scheme comes at a cost, namely a trade-off between the fidelity of the entanglement generation and the corresponding generation rate, but remains still more likely to succeed for collection efficiencies below 20%.

3.1.1 Single-photon entanglement scheme

Entanglement through the detection of a single photon was first discussed in a pioneering paper by Cabrillo *et al.* [131] in 1999 and has been realised using trapped ions [138] and heavy-hole spins in quantum dots [115]. The basic setup, outlined in Fig. 3.1 (a), resembles a Mach-Zehnder interferometer (MZI) where the two mirrors are replaced by two identical Λ -systems (A and B), representing the nodes to be entangled. In our case, we will use quantum dots which are deterministically loaded with a single electron. The corresponding level scheme is presented in Fig. 3.1 (b). By applying a magnetic field in Voigt geometry we achieve a significant Zeeman splitting (Δ_e) of the electron-spin states ($|\downarrow\rangle$ and $|\uparrow\rangle$) which serve as computational basis in our experiment. The Λ -scheme is completed by choosing one of the two excited states of the negative trion, which we can isolate due to the significant excited state splitting.

We start with both systems initialised in a well-defined ground state $|\downarrow\rangle$. Subsequently, we simultaneously excite both systems with a weak resonant drive, creating a small excited state population which will decay back to either of the two computational states with equal probability. The emitted photons are well separated in frequency and thus the population of the state-changing Raman mode will be entangled with the electron spin state [28–30]:

$$|\Psi_i\rangle = \sqrt{1-p}|\downarrow_i\rangle|0_i\rangle + \sqrt{p}e^{i\phi_i}|\uparrow_i\rangle|1_i\rangle, \quad (3.1)$$

where $|0\rangle$ and $|1\rangle$ represent the photon number in the Raman mode and p is the probability of an inelastic scattering process, which is the combination of excitation probability and the 50:50 branching ratio. The phase ϕ_i is inherited from the excitation pulse as a result of the

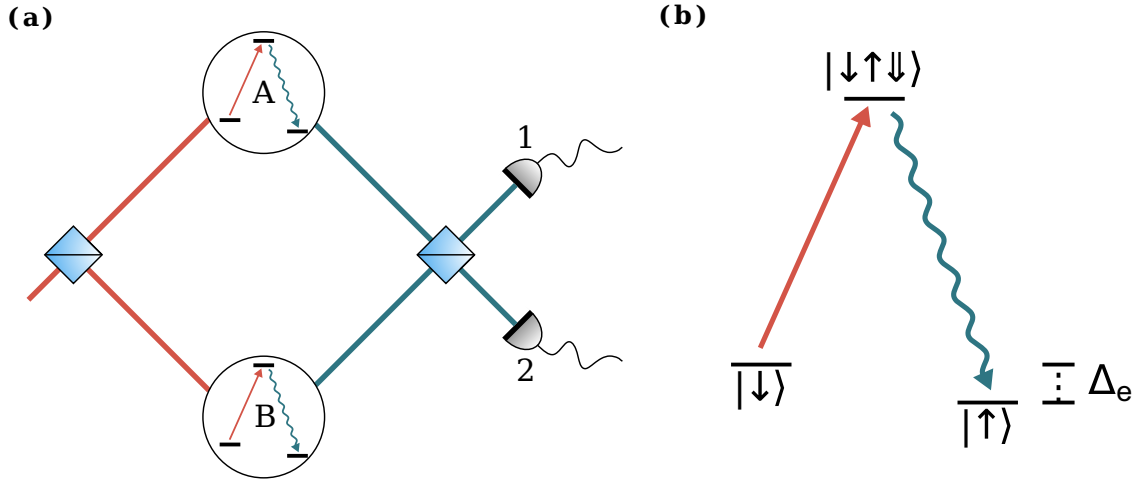


Fig. 3.1 **Single photon entanglement** (a) Schematic of the fundamental setup for the realisation of entanglement through single photon projection. A Mach-Zehnder interferometer with two identical Λ -systems (A & B) replacing the mirrors and single photon-detection after the second beam splitter. The system is excited with a laser (red) and subsequently any emission on the high-frequency transition (blue) is detected to project the system in the entangled state. (b) Zoom in of the Λ -system provided by the electron spin. The ground-states are split by Δ_e and we can neglect the second excited state due to the significant excited-state splitting.

coherent excitation process [76]. Thus, the combined state of the system after excitation and subsequent emission can be described as:

$$\begin{aligned}
 |\Psi\rangle &= |\Psi_A\rangle \otimes |\Psi_B\rangle \\
 &= (1-p) |\downarrow_A \downarrow_B\rangle |0_A 0_B\rangle \\
 &\quad + \sqrt{p(1-p)} \left(e^{i\phi_A} |\uparrow_A \downarrow_B\rangle |1_A 0_B\rangle + i e^{i\phi_B} |\downarrow_A \uparrow_B\rangle |0_A 1_B\rangle \right) \\
 &\quad + i p e^{i(\phi_A + \phi_B)} |\uparrow_A \uparrow_B\rangle |1_A 1_B\rangle.
 \end{aligned} \tag{3.2}$$

Here we include the relative phase shift of the excitation laser, due to the first beam splitter. The effect of the second beam splitter on a single photon will depend on the input mode; a reflected photon will acquire an additional $\frac{\pi}{2}$ phase shift. The two input modes transform as:

$$|1_A 0_B\rangle = \frac{1}{\sqrt{2}} (i |1_1 0_2\rangle + |0_1 1_2\rangle) \tag{3.3}$$

$$|0_A 1_B\rangle = \frac{1}{\sqrt{2}} (|1_1 0_2\rangle + i |0_1 1_2\rangle), \tag{3.4}$$

3.1 Entanglement protocol

where we distinguish between the photon modes going to detector 1 or 2. In the case where both quantum dots emit a photon simultaneously we observe Hong-Ou-Mandel (HOM) interference [139] at the second beam splitter, namely bunching of the photons:

$$|1_A 1_B\rangle = \frac{1}{\sqrt{2}} (|2_1 0_2\rangle - |0_1 2_2\rangle). \quad (3.5)$$

This is of course assuming that the two quantum dots are truly indistinguishable, which directly places a limit on the fidelity of the created state. If we now combine all equations we get the final state after the second beam splitter and just before the detectors:

$$\begin{aligned} |\Psi\rangle = & (1-p) |\downarrow_A \downarrow_B\rangle |0_1 0_2\rangle \\ & + \sqrt{\frac{p(1-p)}{2}} i \left(e^{i(\phi_A + \varepsilon_A)} |\uparrow_A \downarrow_B\rangle + e^{i(\phi_B + \varepsilon_B)} |\downarrow_A \uparrow_B\rangle \right) |1_1 0_2\rangle \\ & + \sqrt{\frac{p(1-p)}{2}} \left(e^{i(\phi_A + \varepsilon_A)} |\uparrow_A \downarrow_B\rangle - e^{i(\phi_B + \varepsilon_B)} |\downarrow_A \uparrow_B\rangle \right) |0_1 1_2\rangle \\ & + \frac{ip}{\sqrt{2}} e^{i(\phi_A + \varepsilon_A + \phi_B + \varepsilon_B)} |\uparrow_A \uparrow_B\rangle (|2_1 0_2\rangle - |0_1 2_2\rangle). \end{aligned} \quad (3.6)$$

Here, ε_i denotes the phase the emitted photons acquire before they interfere on the second beam splitter. It is apparent that the which-path information has successfully been removed and we can see another caveat of this entanglement protocol: with a probability of p^2 both spins will undergo a spin flipping Raman process leading to two photons in a single mode after the second beam splitter. In the absence of number resolving detectors and due to optical losses this contribution cannot be distinguished from the single-photon contribution and therefore presents an error inherent to the protocol. This is the reason why we can only weakly excite the system ($p \ll 1$) resulting in the highly probabilistic nature of our scheme.

The detection of a single photon however will map the spin-photon entanglement onto the two spins and we end up with a maximally entangled state between the two electron spins. The relative phase of the state depends on the detector the photon is measured on. For a single photon in the first output mode of the beam splitter we get:

$$|\Psi_1\rangle = |\uparrow_A \downarrow_B\rangle + e^{i\Delta\phi} |\downarrow_A \uparrow_B\rangle, \quad (3.7)$$

whereas detection of a single photon in the second beam splitter collapses the waveform into:

$$|\Psi_2\rangle = |\uparrow_A \downarrow_B\rangle - e^{i\Delta\phi} |\downarrow_A \uparrow_B\rangle. \quad (3.8)$$

The phase $\Delta\phi$ accounts for the difference in the phase accumulated by the two interferometer arms, accounting for differences in path length before and after the quantum dots as well as slight frequency deviations. As we can see, this phase difference between the photons is mapped onto the final spin state once the photon is detected and therefore imposes some requirements on the setup: first of all we need fully indistinguishable Raman photons and phase-coherent excitation of the systems. Any deviation from perfectly indistinguishable photons, will lead to a reduction in state fidelity. Moreover, we need to stabilise the phase of the interferometer in order to get a well defined, stationary relative phase [140], which will also allow us to deterministically choose the phase and therefore produce any desired entangled state.

3.2 Experimental realisation

Starting from the very simplistic picture given in Fig. 3.1 (a) we will now discuss the technical requirements for the experiment in more detail. We will see that this experiment is technically very demanding and we had to combine all the experience and equipment gathered in our laboratory over the last decade in order to be able to perform this challenging experiment.

3.2.1 Phase stabilisation

First of all, in order to control the relative phase of the entangled spin state we need to implement an active phase stabilisation of the interferometer. Essentially, we need to be able to keep the path length difference of the two interferometer arms fixed, ensuring that we do not get drifts in the propagation time of the photons. Theoretically, stabilising an interferometer is a straightforward process. Experimentally, however, it quickly becomes quite challenging and involved - especially when the interferometer involves several meters of fibre and two liquid Helium bath cryostats. Despite active stabilisation of the temperature in the laboratory, the experiment experiences drifts of about $\pm 0.5^\circ\text{C}$, which in turn alters the length and the refractive index of the optical fibres. During a 20-minute cycle of our air conditioning system we measure the drift of the interferometer delay to be on the order of hundreds of femtoseconds.

The phase stabilisation requires several additions to the basic setup presented in Fig. 3.1 (a). First of all, we introduce another laser to monitor the phase of the interferometer. This laser is far detuned from the optical resonances in order to avoid any excitation and is introduced at the first beam splitter of the interferometer. In our case we work at a wavelength

which is blue detuned from the resonant laser by ~ 12 nm. This large detuning allows us to easily isolate and measure the corresponding signal by utilising refractive gratings in our filtering stage after the second beam splitter. Furthermore, due to the highly chromatic nature of our background suppression through cross polarisation, it also ensures that we measure a strong signal with low shot noise. The photons corresponding to the stabiliser frequency are detected using silicon-chip based APDs. Pulse counters subsequently convert the count rates into analogue signals for each output separately and in a final step the difference of those two signals is electrically generated and used as the error signal for two proportional-integral-derivative (PID) controllers. This method is advantageous as the difference is less susceptible to intensity noise due to fluctuations in the laser intensity. The first PID controller compensates for the slow, thermal drifts up to 10 Hz by controlling the position of a retroreflector mounted on a piezoelectric stack, whereas the second PID controller focusses on the audio-frequency range (10 – 1500 Hz) through application of an offset voltage to a fibre-based phase electro-optic modulator (EOM). A 10 Hz low-pass filter is used to avoid high-frequency components in the error signal for the PID controller of the piezoelectric stack. We operate the stabilisation at the midpoint of the fringes, corresponding to equal signal strength in each detector. This provides a linear error signal for the PID controllers and attenuates uncorrelated intensity drifts of the individual cryostat outputs due to fluctuations of the background suppression. An updated schematic of the setup, containing all components for the phase stabilisation is given in Fig. 3.2 (a).

In Fig. 3.2 (b) we present two measurements showcasing the performance of the stabilisation through active feedback, where the light green data was taken without any stabilisation and the dark green data corresponds to the case where both PID controllers stabilise to the midpoint. Through mapping the voltage to an angle distribution, calibrated by the data of the free running interferometer, we can extract the full width at half maximum (FWHM) for the phase distribution in the stabilised case, which we find to be 6.8° .

3.2.2 Interferometer setup

The actual interferometer of course needs to be further extended beyond the basic setup presented in Fig. 3.2 (a) and in the following we will discuss the additional requirements and their implementation, resulting in the full setup schematically outlined in Fig. 3.3.

First of all, in our case the two Λ -systems are provided by two quantum dots on samples mounted in separate liquid Helium bath cryostats, with the external magnetic fields provided by superconducting magnets housed inside the cryostats. Each cryostat is fitted with one of our home-built confocal microscopes which incorporate two input modes and a single output, as well as a cross-polarisation setup to suppress the laser background in resonant

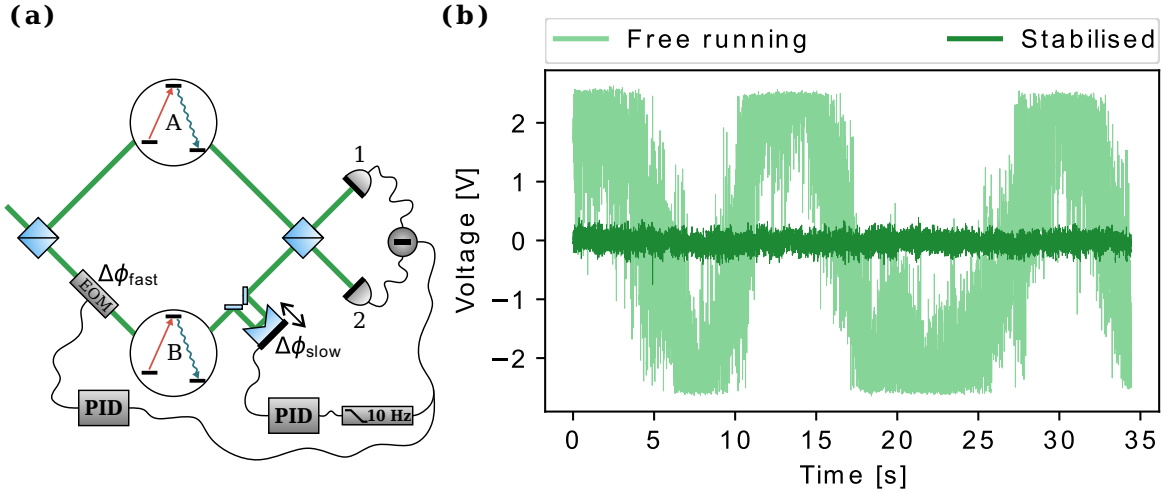


Fig. 3.2 **Phase stabilisation** (a) Schematic of the experimental setup including the components for stabilisation of the interferometric phase. The difference signal of the phase reference measured at the two outputs of the MZI is used as an error signal for the PIDs controlling a phase EOM for fast ($\Delta\phi_{\text{fast}}$) and a piezo-mounted retroreflector for slow ($\Delta\phi_{\text{slow}}$) phase drifts. (b) Measurement of the free running (light green) and stabilised (dark green) interferometer. We extract a FWHM of 6.8° for the phase distribution of the stabilised interferometer.

excitation [71]. The two cryostats replace the mirrors of a large, fibre based interferometer which also incorporates the piezo-stack mounted retroreflector and phase EOM for the phase stabilisation. The phase reference laser is introduced on one of the input modes of the first beam splitter and separated from the other emission in the filtering setup after the final beam splitter.

Implementation of the entanglement scheme and confirmation of the final spin state requires the use of several laser pulses, which need to be incorporated prior to the cryostats. We use the second input of the first beam splitter to introduce the weak excitation pulse, in the following also referred to as 'entanglement pulse'. This way we can ensure a stable relative phase between the Raman modes at the second beam splitter. We also need to be able to separately read out and initialise the two electron spins. Therefore, we introduce the laser pulses for readout and initialisation individually in each interferometer arm through two additional beam splitters and offset the arrival times by 8 ns. Finally, we use the second input of the confocal microscopes to introduce the ps-laser pulses for individual coherent control of the two electron spins.

In order to run the experiment we need to be able to distinguish between the different frequencies in our detection setup. This is achieved through two identical filtering setups after the second beam splitter. We first use a holographic grating with 1200 grooves/mm to

separate the phase reference laser from the quantum dot emission. Furthermore, the grating filters residual background from the coherent rotation pulses needed for the selection of the readout basis, as well as the incoherent emission of the phonon sideband [141, 142]. While the phase reference laser is directly detected by two APDs and processed as described in 3.2.1, the quantum dot emission requires further filtering since we need to isolate the state-projection Raman photons from the Rayleigh scattering. The second filtering step is provided by a Fabry-Pérot etalon with a FWHM of 5 GHz and free spectral range of 250 GHz. The etalon is arranged such that the Raman mode is transmitted while the Rayleigh photons and any residual laser background of the entanglement pulse are reflected. This ensures a highly purified Raman mode at the point of detection. We detect the photons in the Raman and the Rayleigh mode on 4 different SNSPDs and we use a time-to-digital converter (TDC) to transform every single-photon detection to a unique timestamp associated with the channel on which it was registered.

3.2.3 Experimental back end

The components described so far are at the core of the experiment, i.e. directly related to the interferometer and the detection of single photons. However, the setup involves many more components for the generation of the pulse sequence for the experiment. At the heart of the generation is an arbitrary waveform generator (AWG) which provides signals with sampling rates up to 25 GS/s and provides a common timer to ensure synchronisation of different components of the sequence.

Readout and initialisation, as well as entanglement pulses, are derived from CW diode lasers using fibre-based amplitude EOMs with a bandwidth of 1.7 GHz and 20 GHz, respectively. The required voltage pulses are directly generated by the AWG and amplified using high-bandwidth amplifiers in order to reach the voltage required for maximal contrast at the EOM output. We use beam pick-offs to measure the mean intensity at the output of the EOMs and supply an active feedback to the DC-offset in order to compensate for thermal drifts. This way, we reliably reach on-off ratios exceeding 300.

The laser pulses for the coherent rotations are derived from a mode-locked Ti:sapphire laser with a repetition rate of 76 MHz. For this experiment we work about 3 nm red-detuned from the quantum dot transitions, using compound pulses (2.3.3). We use free-space acousto-optic modulators (AOMs) operating at 350 MHz to isolate the pulses required for the experiment. Different rotation angles are achieved by changing the pulse area through different heights of the voltage pulses which are supplied by digital delay generators triggered by the AWG. During the course of a measurement constant rotation angles are ensured by stabilising the average power at the input of each cryostat with a PID controlled 80 MHz

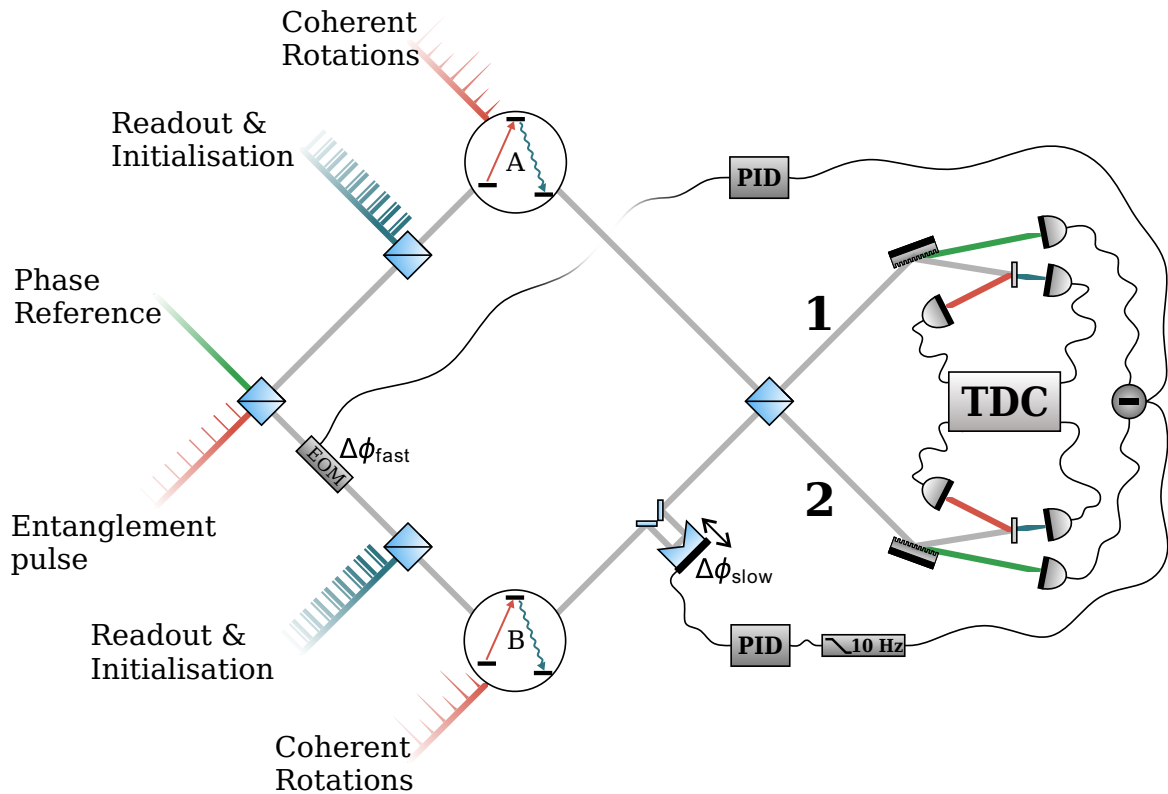


Fig. 3.3 **Entanglement setup** Schematic of the measurement setup consisting of a fibre-based MZI where each arm incorporates a quantum dot sample mounted in a liquid Helium bath cryostat. One arm includes the phase EOM and piezo-mounted retroreflector for the phase stabilisation. The detection after the MZI includes two identical filtering stages based on a grating and an etalon to separate the relevant frequencies. Single photons from the quantum dot emission are time tagged by a time-to-digital converter (TDC). All inputs required to entangle and readout the electron spins are depicted at their corresponding inputs to the MZI.

AOM. Due to its fixed repetition rate, the mode-locked laser also plays the role of the metronome for our experiment, providing the clock for the AWG and a trigger for the start of each measurement run. This way we can ensure that our pulse picking is always synchronised to the repetition rate.

Finally, the AWG also provides a voltage pulse every 56 measurement cycles as a timing reference for the TDC.

3.2.4 Pulse sequence

The pulse sequence of the experiment is depicted in Fig. 3.4. We start by driving the higher frequency transition with a 20 ns pulse in order to initialise the spin in the $|\downarrow\rangle$ state with $\sim 97\%$ fidelity. Subsequently the entanglement pulse, resonant with the low-frequency

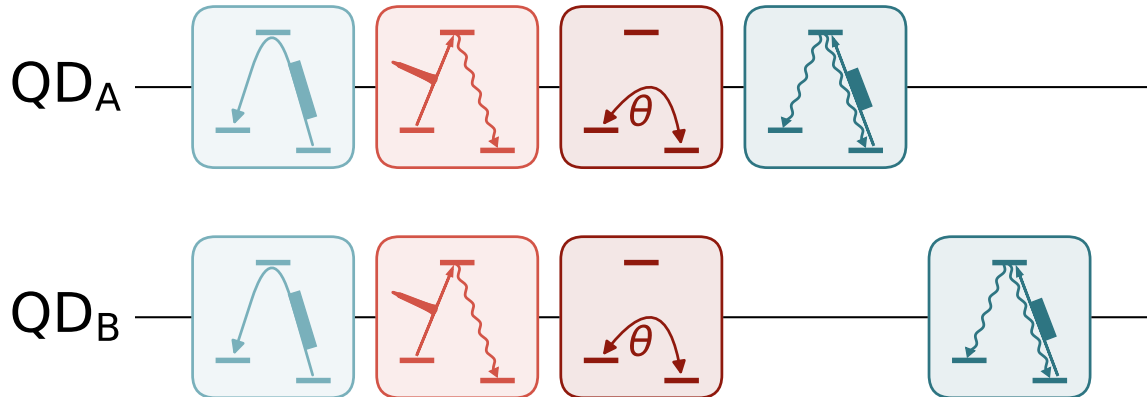


Fig. 3.4 **Pulse sequence** Experimental pulse sequence for the generation and verification of entanglement. First, the spins are simultaneously initialised to the $|\downarrow_A\downarrow_B\rangle$ state (light blue), followed by the entanglement pulse (light red). Subsequently we apply coherent rotations to determine the readout basis (dark red) before we finally read out the two spins individually (dark blue). We continuously cycle through the 4 possible readout-basis states and check for three-photon correlations.

transition, weakly excites the system. This pulse has a duration of only 160 ps, which ensures a lifetime-limited emission window for the Raman photons. We send the coherent rotations, which determine the measurement basis, 1.2 ns after the entanglement pulse in order to limit the effect of spin dephasing. The angle of rotation is chosen such that the desired measurement-basis state is mapped onto the $|\uparrow\rangle$ state, which we read out in the final part of the pulse sequence by successively applying a 7 ns pulse to each quantum dot on the low-frequency transition. We drive each quantum dot at saturation intensity in order to maximise the signal-to-background ratio, generating on average about 1.6 photons for a $|\uparrow\rangle$ state within the detection window. Here, we benefit from the fact that we measure both the Rayleigh and the Raman photons in our setup. A single run of this pulse sequence takes 78.9 ns, corresponding to 6 repetitions of the pulsed laser.

We choose to implement a pulse sequence which cycles through all four basis states repeatedly, taking 315.6 ns to finish one cycle. Due to technical limitations of our pulse-generating electronics we need to add a 52.6 ns break at the end of each cycle to account for the dead time of our digital delay generators. Therefore, a full cycle of measuring all four basis states takes 368.2 ns and we can run the experiment at an attempt rate of 10.9 MHz. Also, the initialisation step actually happens after the readout, i.e. the last initialisation happens at

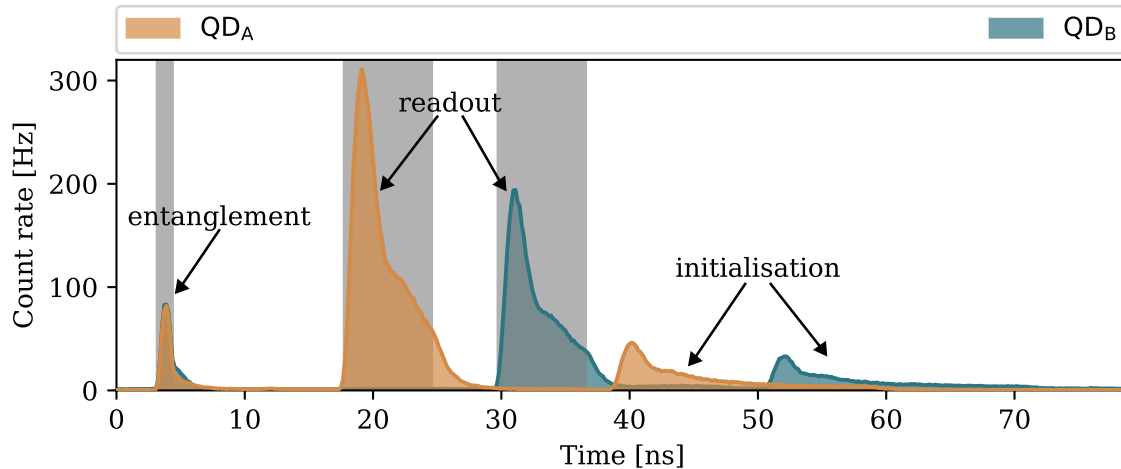


Fig. 3.5 **Pulse sequence fluorescence** Superimposed histograms of the quantum dot fluorescence recorded while running the pulse sequence. The bin size is 162 ps, identical to the final experiment. The regions of interest used for the extraction of three-photon correlations are indicated in grey. The readout and initialisation pulses are clearly offset whereas the Raman photons due to the entanglement pulse overlap in time.

the end of the cycle and not at the beginning. However, due to the strong suppression of the weak excitation laser this does not influence the outcome of the measurement.

By correlating the clock to the quantum dot fluorescence measured independently for each quantum dot and superimposing them, we can obtain the signature of the pulse sequence in the quantum dot emission. Figure 3.5 shows the quantum dot fluorescence based on the pulse sequence, where orange (blue) represents fluorescence from QDA (QDB). One can clearly distinguish the fluorescence due to the two readout pulses as well as the initialisation, whereas the Raman emission of course overlaps. The rotation pulses are not visible here as they are off-resonant and do not produce any fluorescence, but the shape of the entanglement pulse is altered due to the presence of rotations which shift the emission outside of the frequency detection window. The grey areas indicate the regions of interest (ROI) used later to extract three photon coincidences.

3.2.5 Interferometer delay

Active stabilisation allows us to protect the state against short-term drifts of the interferometer. However, in order to ensure simultaneous excitation and rotation of the spin states we need to set the initial interferometer delay to zero.

In a first step, we use the 160 ps long weak excitation pulse by reducing the suppression of the excitation laser frequency such that we can record the arrival time of the pulses and

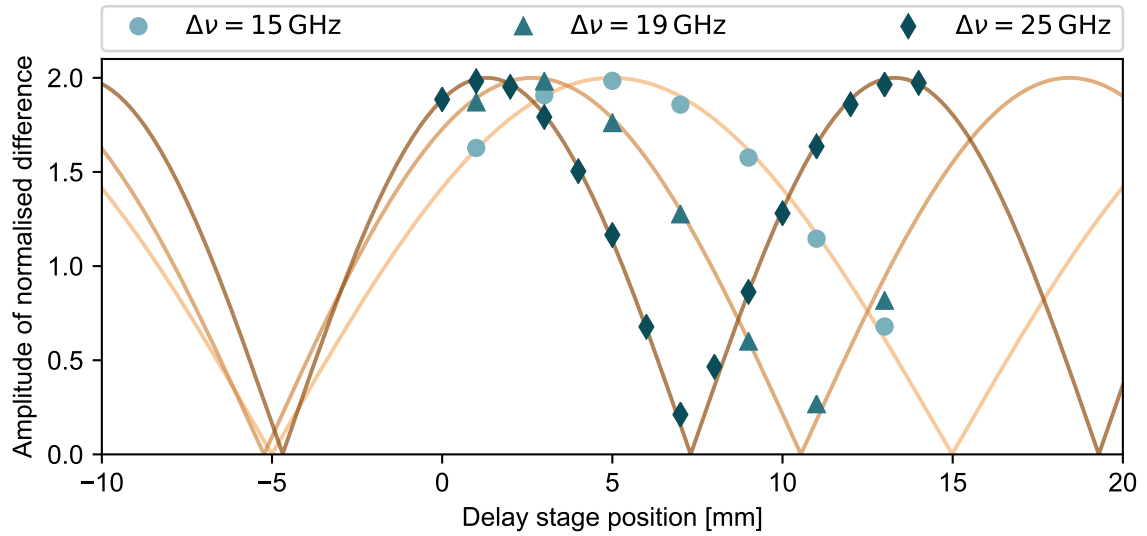


Fig. 3.6 **Interferometer delay** Amplitude of the normalised difference of interferometer interference at different frequency separations $\Delta\nu$ and delay stage positions. Solid curves represent fits to extract the zero-delay position which we find to be -4.77 ± 0.02 mm.

correct the relative delay to ensure overlapping arrival times. Due to the limited timing resolution of our detection system, which is on the order of 200 ps, this only serves as a first step as we require single picosecond accuracy.

The final fine tuning of the relative delay is achieved using a manual delay stage included in one of the interferometer arms. The correct position of the delay stage is determined through interference of different frequencies in our interferometer. In our experiment we use two frequencies separated by the ground-state splitting of 25 GHz, which we can detect separately using the etalons. For a relative delay of zero, the interference fringes of all frequencies will have the same phase. Therefore, by measuring the amplitude of the normalised difference between the two interference signals for different positions of the manual delay stage, we can determine points where the relative phase between those two frequencies is zero. For $\Delta\nu = 25$ GHz the signal will rephase every 40 ps. Repeating the measurement with $\Delta\nu = 19$ GHz and $\Delta\nu = 15$ GHz allows us to accurately determine the zero-delay position of the manual delay stage. Such a measurement is presented in Fig. 3.6 where we show the data for all $\Delta\nu$ and the corresponding fits. By combining the results of the three fits we can determine the zero-delay position to be -4.77 ± 0.02 mm.

3.3 Indistinguishable quantum dots

As pointed out earlier, the two indistinguishable Λ -systems are crucial to the success of the protocol employed here. Therefore, we have to identify two quantum dots with near-identical characteristics and good spectral quality. The two samples used in this work were processed from the same wafer, increasing the chance of finding two matching candidates. After identifying a good quantum dot on the sample with slightly lower density we scan across the second sample, recording PL spectra in order to identify a quantum dot with a similar charge-stability plateau. This allows us to Stark-shift both quantum dots into resonance while remaining sufficiently centered on the charge-stability plateau in order to reduce the effect of cotunneling which will limit the electron spin life time T_1 [143].

3.3.1 Optical mode matching

We choose two quantum dots (QD_A & QD_B) which are Stark-shifted to a common resonance at 967.9 nm. The ground-state splitting is measured using Ramsey interferometry and matched through fine tuning of the external magnetic field applied to QD_B . We operate the experiment at 4 T (3.85 T) for QD_A (QD_B) which results in an electron spin splitting of $2\pi \times 25.2 \pm 0.1$ GHz ($2\pi \times 25.3 \pm 0.1$ GHz). The measurement is performed under the same conditions as the final experiment, ensuring a similar degree of nuclear polarisation which could otherwise significantly change the spin splitting [103]. Figure 3.7 (a) shows the measured data (points) together with the fit (solid curves) used to extract the spin splitting. Matching the splitting not only ensures the spectral overlap of the Raman mode but also that the entangled state we generate is static in the laboratory frame.

Good optical mode matching further requires that the photon wave packets overlap in time which we can confirm by measuring the radiative lifetime of both quantum dots individually. This measurement basically covers the first two steps of the entanglement protocol: initialisation and weak excitation. After preparing the system in the ground state $|\downarrow\rangle$ we weakly drive the red (low frequency) transition of the Λ -system. We then perform a time-resolved measurement of the emitted Raman photons which are separated from any spin-preserving Rayleigh scattering and laser background in our filtering setup. The measurements are presented in Fig. 3.7 (b) and show that both quantum dots have closely matched excited-state lifetimes: We measure a radiative lifetime of 727 ± 10 ps for QD_A and 742 ± 10 ps for QD_B .

Finally, it is important to note that InGaAs quantum dots typically possess a few-nanometer broad phonon sideband [141, 142], which constitutes up to 10% of the emission. Being

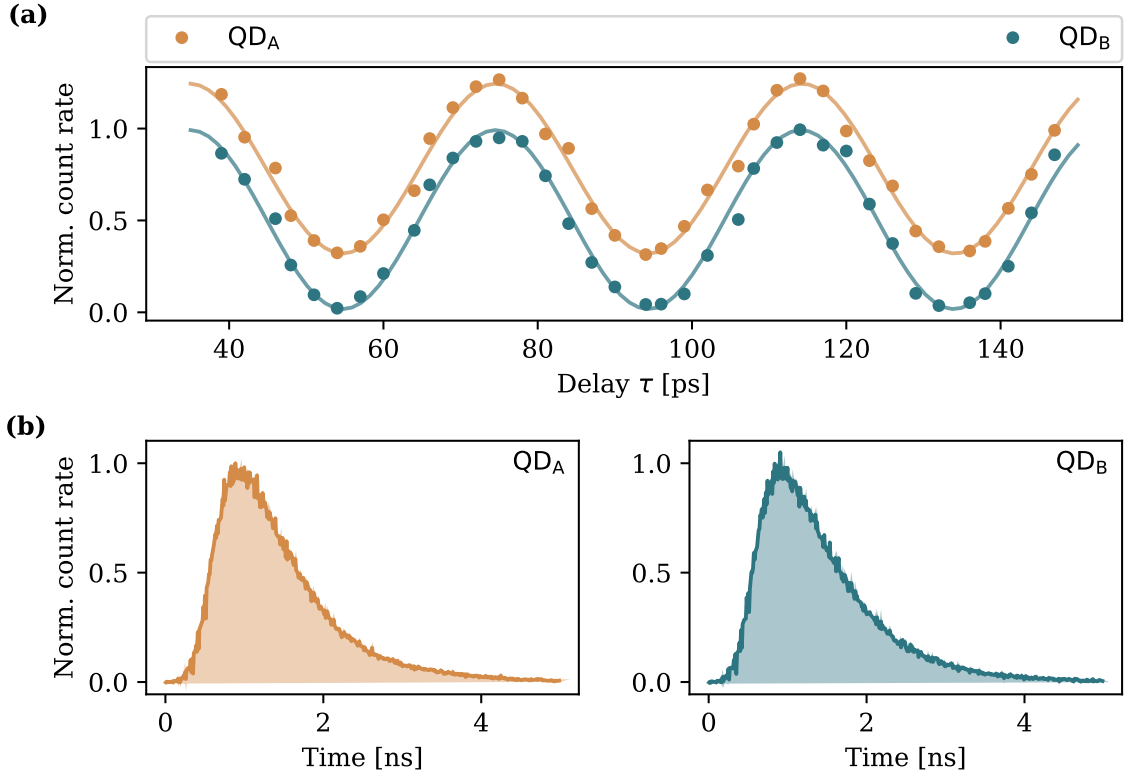


Fig. 3.7 **Spectral and temporal mode matching** (a) Measurement of the Larmor frequency through a Ramsey-type interference measurement. By fitting the data with a sine curve (solid curves) we extract 25.2 ± 0.1 GHz (25.3 ± 0.1 GHz) for QDA (QDB). The data is offset for clarity. (b) Lifetime measurements for QDA (left panel) and QDB (right panel), we extract a lifetime of 727 ± 10 ps (QDA) and 742 ± 10 ps (QDB) by fitting the exponential decay.

inherently incoherent this would of course dramatically reduce the indistinguishability of the photons and is thus removed through filtering.

3.3.2 Hong-Ou-Mandel interference

The experimental verification of photon indistinguishability is a measurement of the HOM interference [139] at the second beam splitter. Two indistinguishable photons that simultaneously arrive at the two input ports of a beam splitter will interfere and exit at the same port as described by Eqn. 3.5. Before measuring the HOM interference we have to check the quality of our emitters and confirm that they are close to ideal single-photon sources by measuring the second-order autocorrelation ($g^2(\tau)$) of the Raman emission. The measured anti-bunching will set a limit on the visibility of the HOM interference [113].

Elementary quantum network

The sequence is identical with the one presented in Sec. 3.2.4 and we just block one interferometer arm in order to perform the measurement separately for each quantum dot. The second-order autocorrelation presented in Fig. 3.8 is calculated from two-photon coincidences within the detection window of the Raman mode. Due to the pulsed emission we measure well separated peaks of two-photon coincidences, where the separation of the peaks is commensurate with the repetition rate of the experiment. In other words, every peak corresponds to the correlation of two photons from repetitions n and $n+i$ where $i \in \mathbb{Z}$, as indicated in Fig. 3.8. The absence of a peak for $\tau = 0, (n, n)$, is a clear proof that we have high-quality single-photon emitters. We record 0 (2) counts leading to $g^2(0) = 0.0$ ($g^2(0) = 0.01$) for QD_A (QD_B). This near-perfect antibunching is a result of the close to background-free detection in combination with the fact that the Raman scattering transfers the spin to the $|\uparrow\rangle$ ground state, where it remains until it is reinitialised - only limited by the spin lifetime which can be on the order of milliseconds [144]. The two events registered during the measurement for QD_B can be attributed to the background count rate of ~ 10 Hz in the detection window - a result of detector dark counts and residual background. This measurement not only confirms that we have high-quality single-photon sources but also showcases the advantage of a Λ -system over a simple two-level system where this process would be limited by the optical lifetime of the excited state, which is typically < 1 ns (see 3.3.1).

Now that we have confirmed the quality of our single photon sources we can directly measure their indistinguishability. For this measurement we now unblock the second interferometer arm to simultaneously excite both quantum dots and check for correlations between the two detectors. In the case of perfect indistinguishability and ideal experimental conditions, namely a perfect 50:50 beam splitter and complete mode overlap, we expect to get zero coincidences between the two detectors within the same experimental cycle [139, 145] - a clear signature of photon bunching. In our system, the indistinguishability will ultimately be limited by the inhomogeneous dephasing time T_2^* [146, 147]. For the electron spin in our quantum dots we measure $T_2^* \approx 1.7$ ns, which means that for the combined system of the two quantum dots we have an inhomogeneous dephasing time of about 1.2 ns, comparable to the radiative lifetime. Therefore, we postselect only photons that have been emitted within the first 1.2 ns after the excitation, leaving us with roughly 60% of the emission. The result of the measurement is presented in Fig. 3.9 and shows a clear suppression of the central peak. In order to quantify the degree of indistinguishability we ideally require a calibration measurement with completely distinguishable photons. The textbook method to calibrate our measurement would be a measurement where we rotate the polarisation in one arm by $\pi/2$, providing fully distinguishable photons. However, our setup contains gratings for the filtering

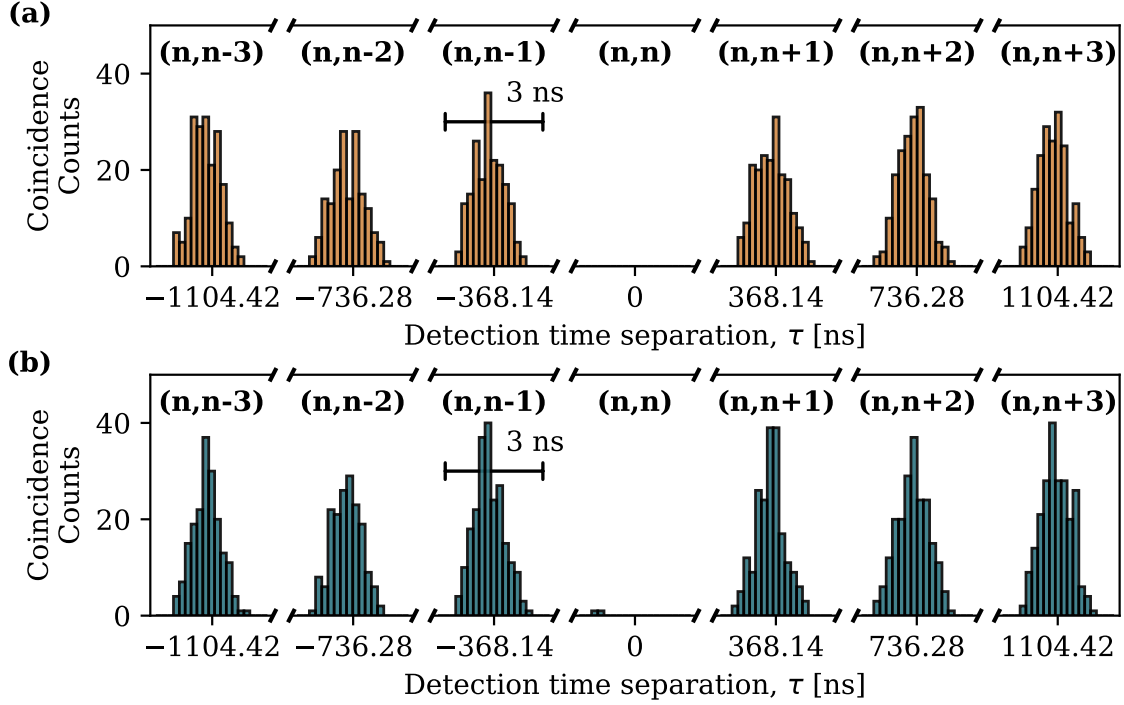


Fig. 3.8 **Second-order autocorrelation $g^2(\tau)$** (a) & (b) Measurements of $g^2(\tau)$ for QD_A (orange) and QD_B (blue), respectively. The correlations are calculated from 3 min long measurements of the quantum-dot emission following the entanglement pulse and presented with a bin width of 162 ps. Tuples (i, j) label the peaks, indicating the origin of the contributing photons. The central peak contains 0 (2) counts leading to $g^2(0) = 0.0$ ($g^2(0) = 0.01$) for QD_A (QD_B).

of the emission which require polarisation matching and thus prevent such a measurement. In order to still quantify the indistinguishability of our photons, we compare the height of the central peak (n, n) with its satellite peaks $(n, n + i)$ where $i \in \mathbb{Z}_{\neq 0}$. If we consider classical light without any single-photon character we would expect all peaks to have the same height. However, if we include the fact that we have close to perfect single-photon sources, we expect the center peak to only contain 50% of the coincidences registered in the satellite peaks since we can never get two photons from the same input within the same experimental cycle and we can estimate the HOM visibility as:

$$V_{\text{HOM}} = 1 - \frac{2N_{n=m}}{N_{n \neq m}}, \quad (3.9)$$

where $N_{n=m}$ denotes the number of coincidences in the central peak and $N_{n \neq m}$ is given by the mean of the coincidence counts in the satellite peaks.

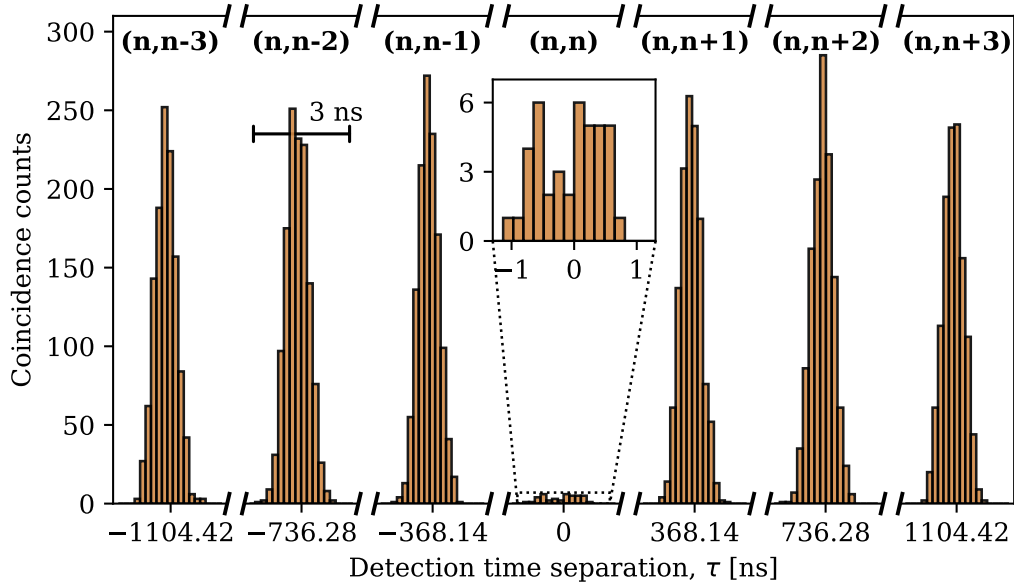


Fig. 3.9 **Hong-Ou-Mandel interference** Coincidence counts measured in a pulsed HOM measurement within the entanglement sequence presented with a bin width of 162 ps. Tuples $(n, n \pm i)$ indicate the origin of the photons contributing to the labeled peak. Inset shows a zoom of the strongly suppressed central peak and we extract an visibility of $V_{\text{HOM}} = 93 \pm 1\%$.

In our case, we find $V_{\text{HOM}} = 93 \pm 1\%$ which directly corresponds to the indistinguishability in the case of a perfect 50:50 beam splitter [113]. While higher indistinguishabilities of up to 99.5% have been reported in recent years [114, 129, 148], those measurements are performed with a single quantum dot using an unbalanced MZI. This restricts the noise timescales which can be accessed and does not capture slowly varying, environmental noise [147]. Experiments utilising two independent quantum dots include the full noise spectrum and have so far only reported low indistinguishabilities [145, 149] and our experiment certainly sets a new benchmark close to the state of the art for single devices. A more detailed discussion and further measurements of HOM interference going beyond the simple proof of high indistinguishability can be found in Chapter 4.

3.4 Single spin projection

So far we have introduced the entanglement scheme that we want to realise and provided evidence that we have two highly indistinguishable single-photon sources. Moreover, we discussed the requirements of a phase-stable interferometer and provided evidence that we can stabilise the phase of our fibre-based interferometer through active feedback. In a final

step we verify that the measurement of a single Raman photon indeed projects the electron spin into the $|\uparrow\rangle$ ground state.

Experimentally, we will confirm that a Raman photon emitted due to the weak excitation correlates with a photon in the readout only if we measure the population of the $|\uparrow\rangle$ state. The measurement is again performed by using the entanglement pulse sequence (Fig. 3.4), with one arm of the interferometer blocked. The basis of the readout is alternated between subsequent measurements by optically applying a π -rotation to the spin population every other sequence. The result is presented in Fig. 3.10: we achieve fidelities of 96.4% and 97.3% for QD_A and QD_B respectively.

Theoretically, the detection of a single Raman photon always projects the spin into the $|\uparrow\rangle$ ground state. The small, but significant reduction of fidelity can be understood considering measurement imperfections. Namely, it quantifies the combined performance of the filtering of the Raman mode, through grating and etalon, the residual background due to laser leakage and detector dark counts, and the fidelity of spin-rotations. The first two will both result in false detection events during both the Raman emission as well as the readout, an effect that we estimate to contribute $\lesssim 1\%$ of the measured reduction. Imperfect rotations will lead to an artificial increase of measured $|\downarrow\rangle$ population and are the main limitation to the measured fidelity. This measurement showcases the increase of spin-rotation fidelity of compound pulses (see 2.3.3): similar measurements with a single π -rotation pulse were bound to fidelities $\leq 92\%$. It is worth noting, that unintentional spin pumping from $|\uparrow\rangle$ to $|\downarrow\rangle$ between the spin rotation and readout due to limited suppression of the EOM will slightly reduce the overall number of correlations. However, this effect is small and has no impact on the fidelity of spin-state reconstruction.

This measurement puts most of the entanglement pulse sequence to a test, including weak excitation, spin rotation, and readout of the final spin state. However, the degree of initialisation does not interfere with the outcome of this measurement, but will limit the fidelity of the spin-spin entanglement. From measurements of our spin pumping we estimate the fidelity of the spin initialisation to be 97%. Thus, this measurement sets a boundary for our capability of recovering the spin-state populations, which ultimately limits the extent to which we are able to reconstruct the state in the process of determining the degree of entanglement. A full discussion of the limitations to the fidelity of the reconstructed entangled two-spin state is given at the end of Sec. 3.5.3.

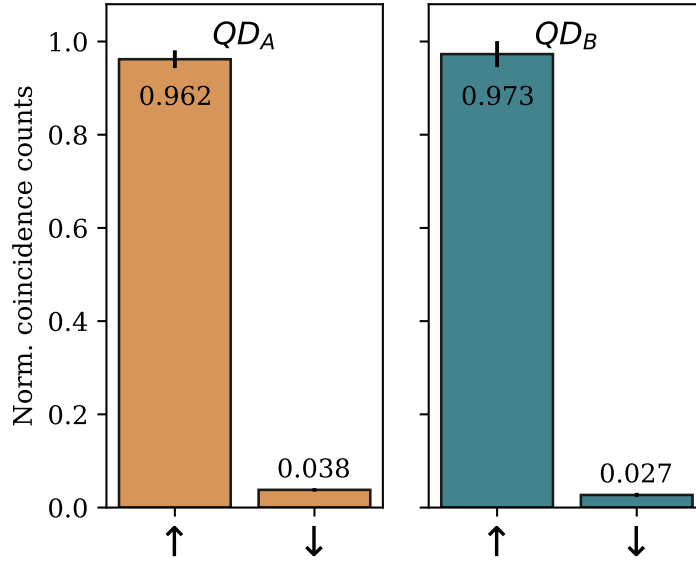


Fig. 3.10 **Single spin projection** Measured two-photon correlations between a Raman photon and subsequent spin-state readout for QDA (orange) and QDB (blue) in the population basis. Error bars indicate uncertainty due to shot noise.

3.5 Measurement of spin-spin correlations

Having provided experimental evidence that we can indeed project the spin state through measurement of a single photon in the Raman mode and that we have met all other experimental requirements necessary for the implementation of the desired entanglement protocol, we will now move to the generation of distant spin-spin entanglement and quantify the corresponding fidelity.

3.5.1 Correlation of spin population

In order to confirm the non-classical nature of the created two-spin state we need to reconstruct the state after successful projection through measurement of a single Raman photon. In a first step we check the correlations in the population basis, aligned with the externally applied magnetic field. We run the measurement sequence introduced in Sec. 3.2.4 and cycle through the four possible basis states $\{|\downarrow_A\downarrow_B\rangle, |\downarrow_A\uparrow_B\rangle, |\uparrow_A\downarrow_B\rangle, |\uparrow_A\uparrow_B\rangle\}$ repeatedly, by applying independent spin rotations to each quantum dot. The power of the weak excitation is chosen such that the overall state-projection probability amounts to $p \approx 4.4\%$, leading

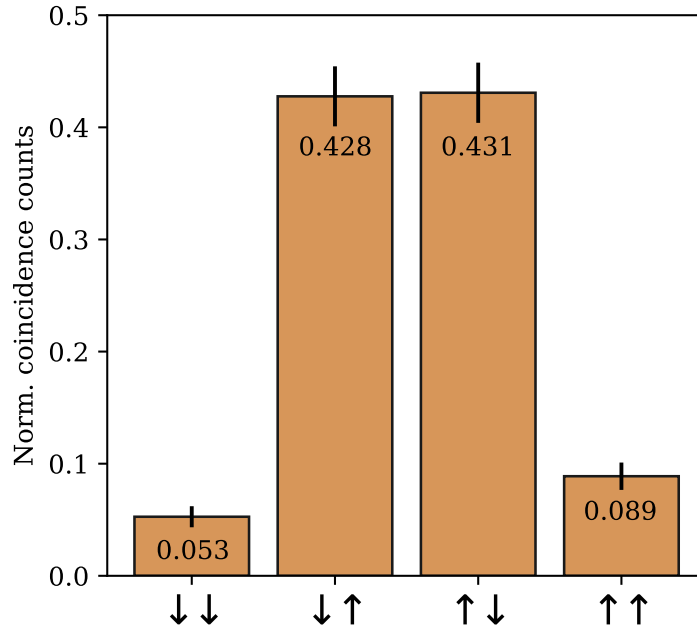


Fig. 3.11 **Two-spin state population** Measurement of three-photon correlations between a projecting Raman photon and subsequent readout photons from each quantum dot. With a fidelity of $85.8 \pm 3.8\%$ we measure the expected anticorrelated spin population. Error bars indicate the shot noise of the contributing events. In total, this measurement consists of 603 three-photon correlations.

to an entanglement generation rate of about 5.8 kHz for a repetition rate of 10.9 MHz¹. In order to avoid any which-path information we need to ensure that both quantum dots emit Raman photons at similar rates. Therefore, the excitation power is set individually for each quantum dot to account for differences in collection efficiencies.

We recover the joint spin population conditioned on a successful state projection by looking for three-photon correlations between a state-projecting Raman photon and a readout photon for each quantum dot within the same run of the measurement sequence. The results presented in Fig. 3.11 show that we recover the desired antisymmetric spin population with a probability of $85.8 \pm 3.8\%$, where the uncertainty is given by the shot noise due to the 603 three-photon coincidences that contribute to the data. The similar probability of measuring either antisymmetric spin-state is evidence that we have set the excitation powers correctly and which-path information is successfully removed. Deviations from the perfectly antisymmetric state can be understood considering the entanglement scheme as well as previously provided measurements. The $|\uparrow_A \uparrow_B\rangle$ population is intrinsic to the single-

¹In the original publication [116] we have mistakenly quoted a rate of 7.3 kHz and a projection probability of 7%.

photon entanglement scheme and follows the set spin-flip probability p . The slightly higher population probability we measured is likely due to imperfect initialisation of the initial spin state. The population of $|\downarrow_A \downarrow_B\rangle$ relates to the imperfections in the readout quantified through the two-photon correlations presented in Sec. 3.4. From those measurements we can infer that we expect to measure $|\downarrow_A \downarrow_B\rangle$ instead of either antisymmetric population with an average probability of 3.3% comparable to the measured 5.3%. As discussed, this error is mainly due to imperfect spin rotations and uncorrelated background counts.

The measurement in the population basis only provides information about the diagonal elements of the joint spin-state density matrix. Thus, it does not provide proof of any non-classical correlations. It merely is a proof that we are projecting the spins into an anti-correlated spin-state through detection of a single Raman photon and provides insight into the performance of our measurement setup. The non-classical nature can only be confirmed through measurements of the phase of the entangled state.

3.5.2 Correlations in a transverse basis

In order to confirm that we indeed measure a well-defined entangled state and not only a classical mixture of the antisymmetric spin states, we need to find a way to access the phase of the entangled state. Assuming the ideal case where we project our system into a maximally entangled state, $|\Psi_{1,2}\rangle = \frac{1}{\sqrt{2}} (|\uparrow_A \downarrow_B\rangle \pm e^{i\Delta\phi} |\downarrow_A \uparrow_B\rangle)$, we can write the density matrix as:

$$\rho_{1,2} = |\Psi_{1,2}\rangle \langle \Psi_{1,2}| = \frac{1}{2} \begin{bmatrix} 0 & 0 & 0 & 0 \\ 0 & 1 & \pm e^{i\Delta\phi} & 0 \\ 0 & \pm e^{-i\Delta\phi} & 1 & 0 \\ 0 & 0 & 0 & 0 \end{bmatrix}, \quad (3.10)$$

where we chose the basis $\{|\downarrow_A \downarrow_B\rangle, |\downarrow_A \uparrow_B\rangle, |\uparrow_A \downarrow_B\rangle, |\uparrow_A \uparrow_B\rangle\}$. In our measurement we can only access the population of the spin states, namely the diagonal elements of the density matrix. Therefore, we need to change to a transverse basis by rotating both spins by $\pi/2$ around a well-defined axis in order to measure the phase. Experimentally, we can introduce a rotation around the x -axis through picosecond-laser pulses. For a single spin this is mathematically expressed through:

$$\hat{X}_\theta = e^{i\theta\sigma_x} = \begin{bmatrix} \cos \frac{\theta}{2} & i \sin \frac{\theta}{2} \\ i \sin \frac{\theta}{2} & \cos \frac{\theta}{2} \end{bmatrix}, \quad (3.11)$$

3.5 Measurement of spin-spin correlations

$\Delta\phi$	output 1	output 2
0	$\frac{1}{\sqrt{2}} (\leftarrow_A \leftarrow_B\rangle + \rightarrow_A \rightarrow_B\rangle)$	$\frac{1}{\sqrt{2}} (\leftarrow_A \rightarrow_B\rangle - \rightarrow_A \leftarrow_B\rangle)$
π	$\frac{1}{\sqrt{2}} (\leftarrow_A \rightarrow_B\rangle - \rightarrow_A \leftarrow_B\rangle)$	$\frac{1}{\sqrt{2}} (\leftarrow_A \leftarrow_B\rangle + \rightarrow_A \rightarrow_B\rangle)$

Table 3.1 **Relation between output mode and spin population** The choice of $\Delta\phi$ will determine which state we detect on which output.

where σ_x denotes the Pauli matrix and θ the angle of rotation. By applying this operator to the two basis states $\{|\downarrow\rangle, |\uparrow\rangle\}$ we rotate our basis to the equatorial plane of the Bloch sphere and the basis states are given by:

$$|\leftarrow\rangle = \frac{1}{\sqrt{2}} (|\downarrow\rangle + i|\uparrow\rangle) \quad (3.12)$$

$$|\rightarrow\rangle = \frac{1}{\sqrt{2}} (|\downarrow\rangle - i|\uparrow\rangle) \quad (3.13)$$

This transverse basis now allows us to access the phase of the entangled state, which is even more apparent when we apply this basis transformation to the density matrix of the two-spin state:

$$\begin{aligned} & (\hat{X}_{\pi/2} \otimes \hat{X}_{\pi/2}) \rho_{1,2} (\hat{X}_{\pi/2} \otimes \hat{X}_{\pi/2})^\dagger \\ &= \frac{1}{4} \begin{pmatrix} 1 \pm \cos \Delta\phi & \mp \sin \Delta\phi & \pm \sin \Delta\phi & 1 \pm \cos \Delta\phi \\ \mp \sin \Delta\phi & 1 \mp \cos \Delta\phi & \pm \cos \Delta\phi - 1 & \mp \sin \Delta\phi \\ \mp \sin \Delta\phi & \pm \cos \Delta\phi - 1 & 1 \mp \cos \Delta\phi & \pm \sin \Delta\phi \\ 1 \pm \cos \Delta\phi & \mp \sin \Delta\phi & \pm \sin \Delta\phi & 1 \pm \cos \Delta\phi \end{pmatrix}. \end{aligned} \quad (3.14)$$

The spin population of this state is correlated with the phase of the entangled state and we maximise the contrast by choosing $\Delta\phi = 0$ or π . There is a phase difference of π between the two beam-splitter outputs (see Eqn. 3.6), due to which we will always measure both correlated and anticorrelated spin populations, corresponding to a projection on $|\Psi^+\rangle$ and $|\Psi^-\rangle$, respectively. The relation between output mode and spin population depends on the choice of $\Delta\phi$ and is summarised in Tab. 3.1.

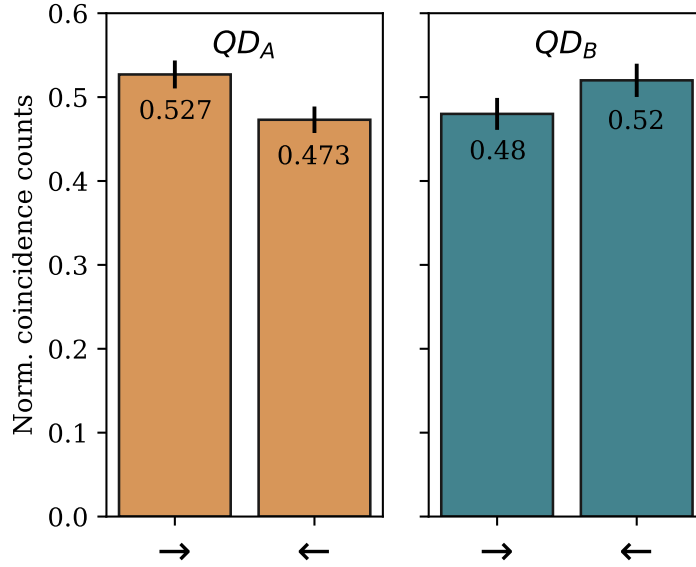


Fig. 3.12 **Single-spin projection** Measured two-photon correlations between a Raman photon and subsequent spin-state readout for QD_A (orange) and QD_B (blue) in the transverse basis. Error bars indicate uncertainty due to shot noise.

The successful basis transformation is confirmed by measuring two-photon correlation similar to the measurement presented in Sec. 3.4, but including the additional $\pi/2$ rotation. Thus, we still prepare the system in the $|\downarrow\rangle$ state, but measure it in the transverse basis, where we expect equal coincidence rates. The results are presented in 3.12 and show that we indeed project onto the $|\leftarrow\rangle$ and $|\rightarrow\rangle$ basis states with nearly equal probability. Analogous to before, the small deviation can be attributed to imperfect rotations as well as residual background counts and presents a limit to the fidelity of our measurement.

While the measurement in the population basis did not require a phase stable interferometer, we now need to ensure that the interferometer is stabilised with a relative phase, $\Delta\phi$, of either 0 or π and that this phase is kept constant over the course of the measurement. We can monitor and set the phase by utilising the Rayleigh scattering during the weak excitation pulse. Such a measurement is presented in Fig. 3.13, where we show the count rate integrated of the 1.2 ns ROI measured by the two detectors recording the light reflected from the etalon. In the first part of the measurement, the interferometer is left free running and we can see interference fringes as the relative path length varies over time. The reduction in visibility can mainly be attributed to the incoherent fraction of Rayleigh scattered light, which reduces the visibility by about 15%. Further contributions are high-frequency electrical noise, imperfect mode overlap, which both will also affect the visibility in the transverse basis, and

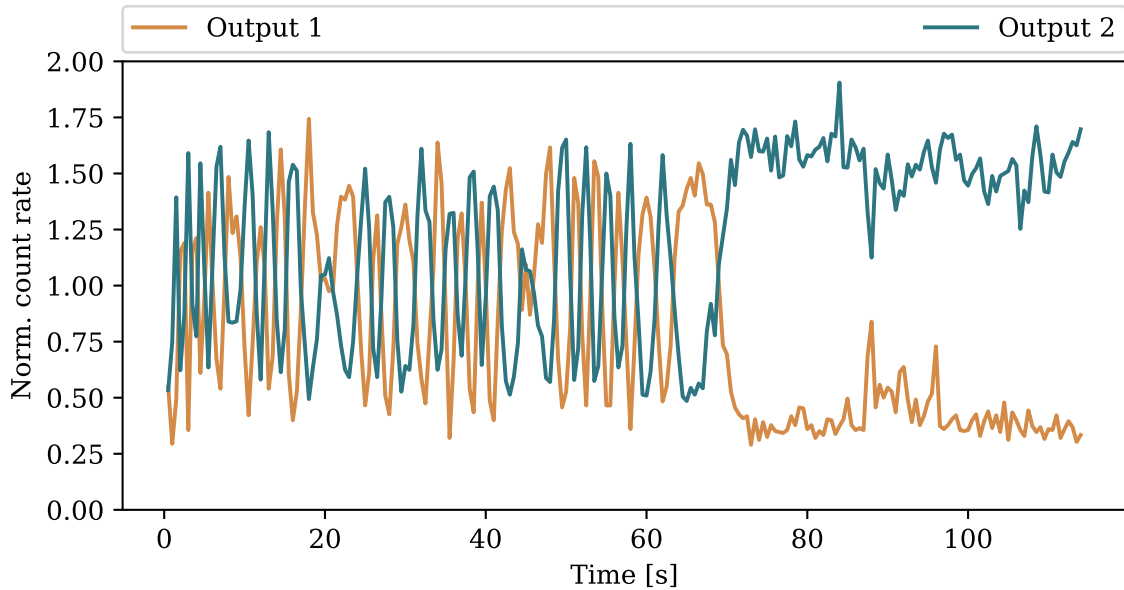


Fig. 3.13 **Rayleigh-photon interference** Normalised count rates for Rayleigh photons detected within the state projection window at output 1 (orange) and 2 (blue). The interferometer stabilised from ~ 70 s onwards, clearly evidenced by the absence of interference fringes past this point.

laser background from rotation and weak-excitation pulses in the reflection of the etalon. The second part of the measurement shows the signature of the stabilised interferometer where we do not observe any interference fringes, but instead measure relatively constant count rates on each detector. The desired phase of 0 or π corresponds to maximum contrast of the two outputs, i.e. the Rayleigh photons will interfere constructively on one output and destructively on the other. In the presented measurement the stabilisation was switched on at 70 s and the phase was chosen to be π , resulting in constructive interference at the first beam-splitter output. The relative phase is chosen by introducing a sub-picosecond delay between the two arms.

The extracted three-photon coincidences presented in Fig. 3.14 are distinguished by the beam-splitter output on which the state-projecting Raman photon was detected. According to the relations summarised in Table 3.1 a detection on the output mode with constructive Rayleigh interference results in correlated spins, whereas we expect to measure anticorrelated spins in the destructively interfering case. The results clearly follow the expected behaviour and show strong deviations from the classical mixed state, identified by equal contributions in all measurement bases. We define the visibility $V = p_c - p_a$, where p_c (p_a) denotes the relative population of the (anti-)correlated spin states. For our measurement we find

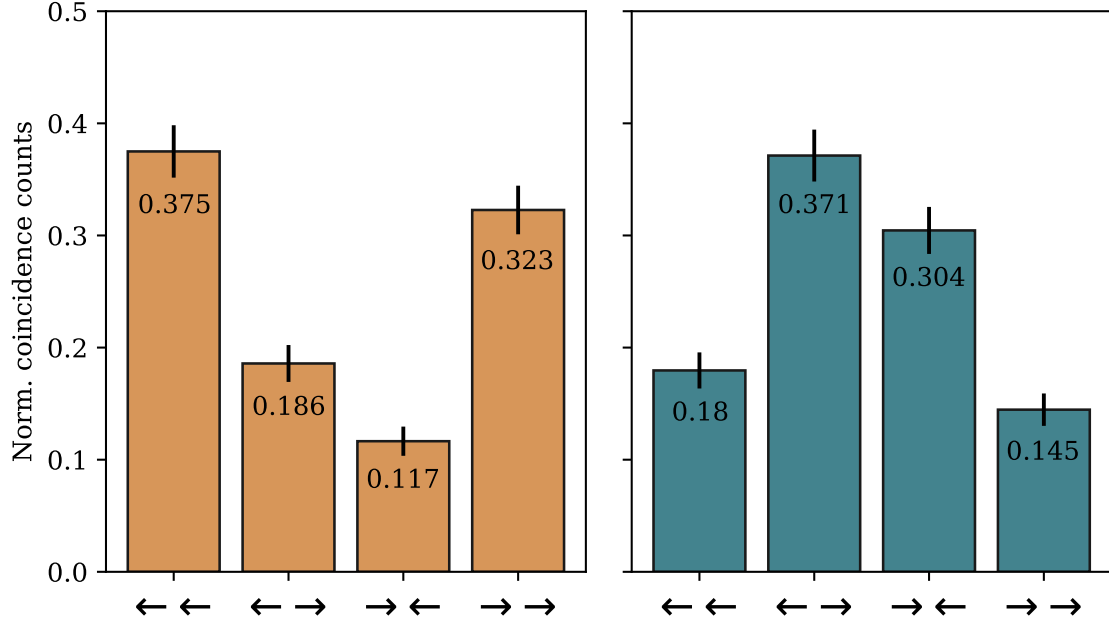


Fig. 3.14 **Transverse basis measurement** Measurement of three-photon correlations between a projecting Raman photon and subsequent readout photons from each quantum dot after projecting the state into the transverse basis. For an interferometer phase of $\Delta\phi = 0, \pi$ we measure $|\Psi^+\rangle$ (orange) and $|\Psi^-\rangle$ (blue) depending on the beam-splitter output and recover visibilities of $39.5 \pm 3.8\%$ and $-35.1 \pm 3.8\%$, respectively. Error bars indicate the shot noise of the contributing events. In total, these measurements consists of 905 (orange) and 745 (blue) three-photon correlations.

$V = 39.5 \pm 3.8\%$ for $|\Psi^+\rangle$ (correlated spins) and $V = -35.1 \pm 3.8\%$ for $|\Psi^-\rangle$ (anticorrelated spins), evidencing the presence of a non-classical two-spin state.

3.5.3 Fidelity of entangled-state generation

In order to quantify the fidelity of our entanglement generation we need to relate the measured visibilities to the overall fidelity. The fidelity of a measured two-spin state (ρ) with respect to the maximally entangled Bell states $|\Psi^\pm\rangle$ is given by:

$$F = \langle \Psi^\pm | \rho | \Psi^\pm \rangle = \frac{1}{2} (\rho_{\downarrow\uparrow, \downarrow\uparrow} + \rho_{\uparrow\downarrow, \uparrow\downarrow} \pm \Re(\rho_{\downarrow\uparrow, \uparrow\downarrow})). \quad (3.15)$$

The spin populations $\rho_{\downarrow\uparrow, \downarrow\uparrow} + \rho_{\uparrow\downarrow, \uparrow\downarrow}$ are directly given by our population basis measurement and amount to 0.857 ± 0.038 . The last term of Eqn. 3.15 can be related to the visibility, V , measured in the transverse basis:

$$V = 2\Re(\rho_{\downarrow\uparrow,\uparrow\downarrow}) + 2\Re(\rho_{\downarrow\downarrow,\uparrow\uparrow}). \quad (3.16)$$

Here, we also have a contribution from $\rho_{\downarrow\downarrow,\uparrow\uparrow}$, which we have not accessed in our measurements. However, the contributing spin states are not stationary in our laboratory frame, but instead precess with twice the Zeeman splitting of the spin ground states. In other words, they evolve at ~ 50 GHz. Our measurements are ultimately limited by the timing accuracy which is determined by the jitter on the time passing between the state projection and the mapping of the phase onto the population basis through optical rotations. While the rotations are accurate to < 3 ps, the state projection is ultimately limited by the jitter of our single-photon detection which is > 80 ps. Thus, we cannot resolve those fast precessing states and their contribution is averaged out over the course of the measurement. We can therefore assume that for our measured density matrix $\Re(\rho_{\downarrow\downarrow,\uparrow\uparrow}) = 0$ and we can directly identify $2\Re(\rho_{\downarrow\uparrow,\uparrow\downarrow})$ with the visibility extracted from the transverse basis measurement.

Averaging the two transverse basis measurements we arrive at an overall average fidelity of $61.6 \pm 2.3\%$ for the generation of a maximally-entangled Bell state - the maximum fidelity for an anticorrelated classical state is 50%. This means, that we confirm the non-classical nature of the two-spin state by 5 standard deviations of the mean.

Understanding the limitations to the fidelity

The deviation from a perfectly entangled state can be understood taking into account experimental limitations, some of which we have mentioned before. In the following, we will examine contributions to the reduction of the maximally achievable fidelity.

The first source of error are the double-spin flips, which are inherent to the employed single-photon scheme. The error scales with the excitation probability p and leads to a reduction of fidelity to 95.6%.

Another contribution stems from the imperfect initialisation of the spins at the beginning of the measurement. Starting the measurement with one of the spins in the $|\uparrow\rangle$ state will affect the fidelity in the same way as the double-spin flip since the detection of a Raman photon projects the system in the $|\uparrow\uparrow\rangle$ state. From the fluorescence remaining at the end of the spin initialisation pulse, we estimate our spin initialisation to be 97%, resulting in a reduced fidelity of 92.6%.

The residual distinguishability, extracted from the HOM experiment in Sec. 3.3.2, will hinder the erasure of which-path information. Instead of generating a Bell state, the detection of a photon that still carries information about its origin will project the system in to a product state. Thus, it will still resemble an antisymmetric spin population, but the visibility of the

transverse basis measurement will be reduced due to the lack of coherence, limiting the fidelity to 89%.

The limitations discussed so far mean that we will be able to generate a Bell state with 89% fidelity, however the verification through measurement will impose further limits to the fidelity. Readout imperfections will result in erroneous three-photon coincidences, reducing the visibility for both measurement bases. The effect is characterised by the two-photon correlation measurement (3.4) and amounts to a 6% reduction of fidelity.

For the measurement in the transverse basis we are also limited by the joint spin dephasing of about 1.2 ns. The electron spins will dephase during the time between the emission of the Raman photon and the optical rotation which maps the phase onto the population, resulting in a reduced coherence of the two-spin state. We estimate a reduction by a factor of 0.87 by assuming a Gaussian decay of coherence due to dephasing of the spins.

All the effects combined set an upper bound of 78% to the measurable fidelity. The discrepancy to the fidelity observed in our experiment is most likely due electrical noise in the sample, which is hard to quantify directly. On the one hand, slow electrical noise will lead to variations in the Larmor frequency, leading to an increased distinguishability of the Raman photons as well as a non-stationary final state in the laboratory frame. On the other hand, fast electrical noise can alter the relative phase of the photons scattered from the two quantum dots which will be directly mapped onto the final state.

3.5.4 Phase control

At first, it might appear that the phase sensitivity of the employed single photon scheme is one of its biggest weaknesses as it requires phase stabilisation of the interferometer and is directly related to a large fraction of the limitations of fidelity. However, it also presents one of the biggest strengths of this scheme: we can directly map the phase of the interferometer onto the generated two-spin state.

So far, we have chosen to operate with $\Delta\phi$ set to either 0 or π in order to maximise the contrast of our measurement. Here, we will demonstrate the phase tunability by measuring the visibility in the transverse basis for $\Delta\phi \in \{0, \frac{\pi}{4}, \frac{\pi}{2}, \frac{3\pi}{4}, \pi\}$. The results are presented in Fig. 3.15, where we show the relative coincidences rates alongside with their corresponding visibilities. The phase is set by monitoring the Rayleigh interference during the weak-excitation and we distinguish between the two output modes of the beam splitter. We start with $\Delta\phi = 0$ which projects the spins into $|\Psi^+\rangle$ ($|\Psi^-\rangle$) for a detection on output 1 (2), corresponding to a measurement of a correlated (anticorrelated) spin population in the transverse basis measurement. For a phase of $\Delta\phi = \frac{\pi}{2}$ we project the system into $\frac{1}{\sqrt{2}}(|\Psi^+\rangle \pm |\Psi^-\rangle)$ - a state which does not possess any transverse spin-spin correlations.

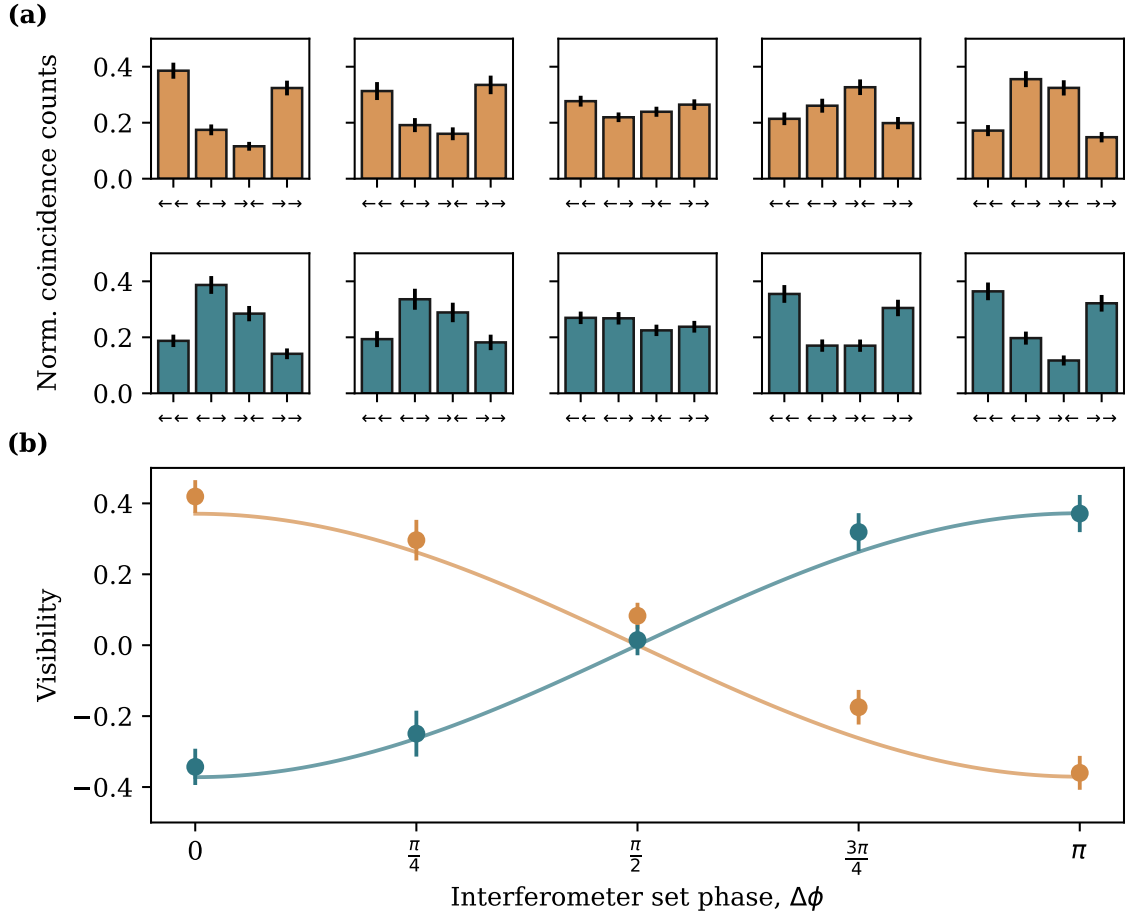


Fig. 3.15 **Phase-tunable entangled state generation** (a) Extracted three-photon coincidences in the transverse basis for 5 different set points of the interferometer phase: 0 , $\pi/4$, $\pi/2$, $3\pi/4$, π (left to right). The results are sorted according to outputs 1 (orange) and 2 (blue). Error bars extracted from shot noise. (b) Visibilities extracted from the three-photon correlations presented above. Solid curves are a guide to the eye. In total this measurement consists of 4246 three-photon events.

Consequently, our measurement confirms close to zero visibility. Finally, for $\Delta\phi = \pi$ the relation between the two output modes is reversed and we recover the visibility corresponding to $|\Psi^-\rangle$ and $|\Psi^+\rangle$, respectively. While it is of course possible to transform Bell states into one another through local gates, we show that we can *a priori* control the phase of the state that is generated. This measurement showcases the principle of the scheme proposed by Cabrillo *et al.* [131] where quantum erasure is used to project the phase of the Raman modes onto the nonlocal two-spin state.

3.6 Data acquisition and post-processing

The experiment produces a substantial amount of raw data and for an efficient running of the experiment we need to ensure fast acquisition and post-processing of the data in order to ensure its correct running.

So far, experimental control for the quantum dot experiments in our laboratory was mainly achieved through programs written in LabVIEW, owing to the great support of instruments and the natural inclusion of a graphical interface. However, the required high data stream in combination with a fast analysis cannot be provided by LabVIEW which is designed for experimental control and only supports basic analysis functionality. Furthermore, the necessary data post-processing required full timing information of the registered events which is not supported by the combination of our TDC (quTAU) and LabVIEW. Thus, we have chosen to use Python 3.6 for the implementation of data taking and processing. In the following, we briefly summarise the data acquisition and discuss the post-processing necessary to extract valid three-photon coincidences from the data, while some technical details of the library written for this experiment can be found in Appendix A.

3.6.1 Data acquisition

In our experiment, all single photon events are converted to unique timesteps using a TDC from qutools (quTAU). This 8 channel TDC provides a minimum bin width of 81 ps and a deadtime of 5.5 ns for events occurring on the same channel. We operate the device in time tagging mode, where it can process up to 3 Mevents/s. The data are saved in a binary file containing 10 bytes for every timestamp where the first 8 define the 56 bit timestamp and the last two indicate the channel number.

During the entanglement experiment we typically deal with an overall photon count rate of $\sim 190\text{kHz}$ in addition to the 200kHz reference clock, which results in a data rate of $\sim 3.9\text{MB s}^{-1}$. In order to contain the file size we save the timestamps in intervals of 60 s. An efficient running of the experiment can only be ensured if the analysis of the data scales linearly with the measurement time and through optimisation of the analysis procedure and implementation of multiprocessing we are able to analyse each 60s measurement within 2 minutes after the data is taken.

3.6.2 Data post-processing

Typically a measurement of 60 seconds contains about 5-6 three-photon correlations and only ~ 2 fulfil all the criteria of the post processing - this shows how rare the events are and

3.6 Data acquisition and post-processing

the high demand we have on efficient filtering of the data. Owing to the offset in analysis, the experiment does not provide real-time feedback and we typically restrict the measurement time to 20 minutes before checking the correct setting of all experimental parameters. Once a measurement is finished and all three-photon coincidences have been extracted we further process the data in order to post-select on the correct experimental conditions. The post-processing is based on the count rates extracted during the analysis, which returns the count rates within a pre-defined time interval for all ROIs and readout basis separately. For the analysis of our measurement we choose an interval of one second.

During our experiment we observe low-frequency charge fluctuations (< 1 Hz) in the vicinity of our quantum dots which occasionally causes one of them to wander off resonance, resulting in a prominent drop of the entanglement rate. Therefore, we first compare the measured entanglement rate, i.e. the rate of Raman photons during the experiment, to a threshold set for the post-processing which is based on the value initially set for the experiment. We note that during the setup of the experiment we check the rate using one of the standard LabVIEW programs, relying on a different ROI than the analysis. Therefore, we extract the Raman-photon rate for a ROI length of 1.62 ns compared to the 1.215 ns used for the photons contributing to the three-photon rate, resulting in an average rate of 7.3 kHz. The Raman-photon rate for an exemplary 20-minute measurement is shown in Fig. 3.16 (a), where each point corresponds to the rate of a one-second interval of the measurement. The set threshold is indicated by the grey line and we can clearly see that one of the quantum dots is off resonance from about 800 s onwards. All intervals that fall below the threshold are shown in light blue and any three-photon events within these intervals are not considered for the final results. For the measurement in the computational basis, this represents the only post-processing step since it is phase-insensitive.

For the measurements in the transverse basis we include two more post-processing steps. First, we assess the quality of the additional $\pi/2$ rotations which is achieved by monitoring the ratio of the readout photons in the $|\uparrow\rangle$ and $|\downarrow\rangle$ states for each QD individually. In the case of perfect rotations this ratio is 1 and indeed the measured value only rarely shows a significant deviation, a confirmation that we have good control of our rotation angles. As a result, this step has only a negligible effect on the final results.

In a final step, we check how well the set phase is maintained throughout the measurement. This is achieved by comparing the ratio of the Rayleigh-scattered photons between the two beam-splitter outputs measured within the entanglement ROI. The extracted ratio is shown in Fig. 3.16 (b) for the same measurement as presented in (a). Here, the grey area represents the acceptance window for the phase ratio, based on the desired phase and the initial ratio of Rayleigh scattering, which is measurement dependent. A more detailed discussion of the

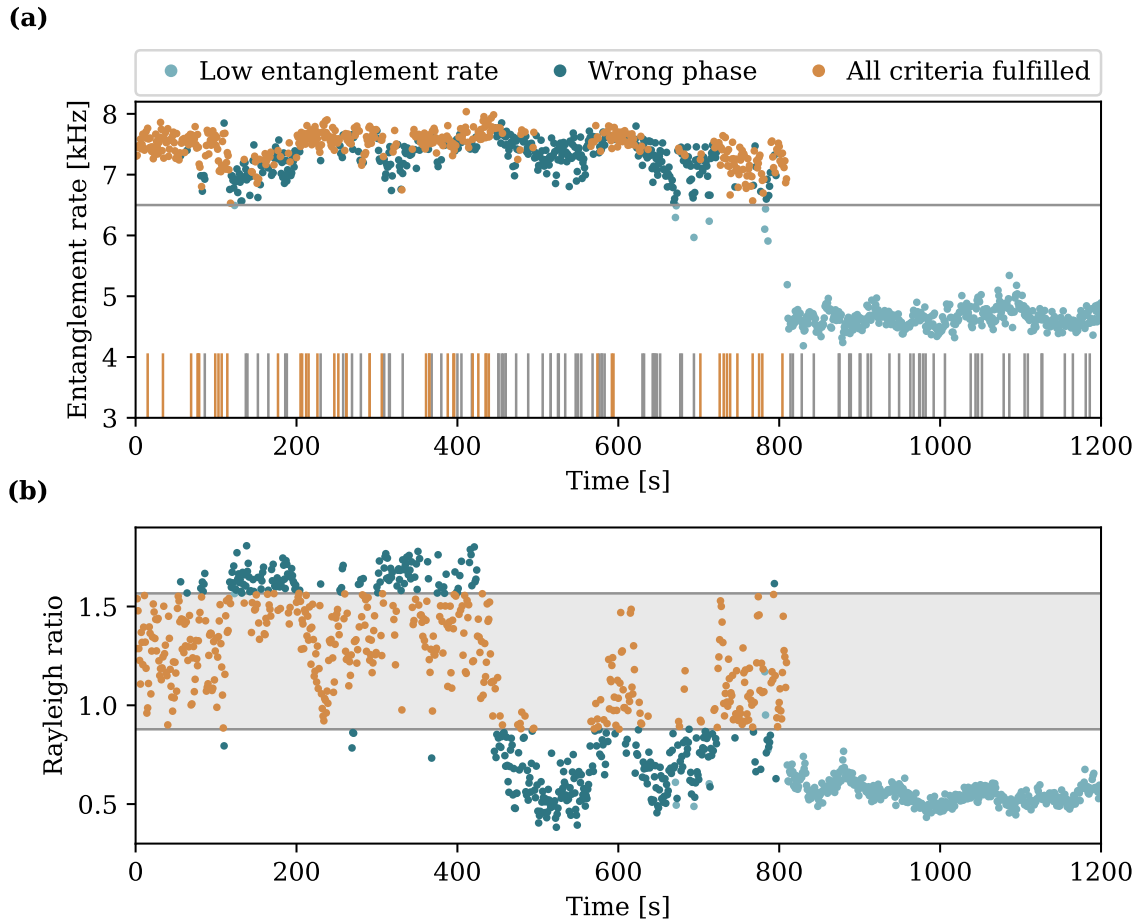


Fig. 3.16 **Post-processing of entanglement data** (a) Exemplary 20-minute measurement showing the most important post-processing steps. Every point corresponds to the Raman-photon rate during a 1 s interval of the measurement where colors represent the employed post-processing steps: light blue points are below the Raman-photon rate threshold indicated by the grey line, dark blue points are outside the interval for the phase ratio and orange points are measurement intervals that fulfil all post-processing criteria. The bars at the bottom indicate all three-photon events during this measurement (N=136), where orange bars mark events fulfilling all post-selection criteria (N=47). (b) Rayleigh ratio for the same measurement as presented in (a). The grey area indicates the $\pm 25^\circ$ interval used for the selection of valid intervals.

derivation of the acceptance window is presented below. All intervals that have passed the initial post-processing steps, but do not have the correct phase ratio are shown in dark blue. The orange points represent intervals which have passed all post-processing steps and we therefore only consider three-photon events that were registered during these intervals. The bars at the bottom of Fig. 3.16 (a) represent all three-photon events registered during this measurement and the orange bars correspond to events registered during intervals which fulfil all post-processing criteria.

3.6.3 Ratio of Rayleigh scattering for post-processing

In order to determine the theoretically expected ratio of the Rayleigh-scattered photon rates between the two beam-splitter outputs we make use of measurements like the one presented in Fig. 3.13, where we have data corresponding to the free running interferometer as well as data where the interferometer is stabilised with a phase difference of either 0 or π . These measurements allow us to extract a value for the mean count rate on each beam-splitter output, given by the average of the interference fringes as well as an estimate for the amplitude of the fringes from the signal of the stabilised interferometer. Therefore we can calculate the theoretical ratio of the Rayleigh-scattering and define an acceptance window for the post-processing.

The corresponding curve for the exemplary measurement presented in this section is shown in Fig. 3.17. The measurements corresponds to an interferometer phase of $\frac{3\pi}{4}$ and the acceptance window is set to $\pm 25^\circ$ indicated by the gray shaded region below the curve. The histogram on the y-axis indicates the distribution of the 47 three-photon events. We note, that for a measurement where the phase is set to 0 (π) we only consider an upper (lower) bound.

The choice of a relatively large acceptance window is based on the fact that the Rayleigh scattering is also subject to intensity fluctuations and noise which will lead to fluctuations of the ratio which do not correspond to actual change of phase. Consequentially, the obtained visibilities shown in Fig. 3.15 present a lower bound due to the averaging over a broad phase distribution. As a comparison Fig. 3.18 shows the same data, but this time with an acceptance window of $\pm 10^\circ$ (a) and $\pm 20^\circ$ (b). As a result of the stricter post-processing the overall visibility is higher, but the behaviour with changing phase still approximates the expected sine curve. The increase in visibility comes at the cost of lower statistics and thus higher uncertainty represented by the error bars. The total number of three-photon evens is reduced from 4246 for the data presented in the last chapter to 2027 ($\pm 10^\circ$) and 3541 ($\pm 20^\circ$).

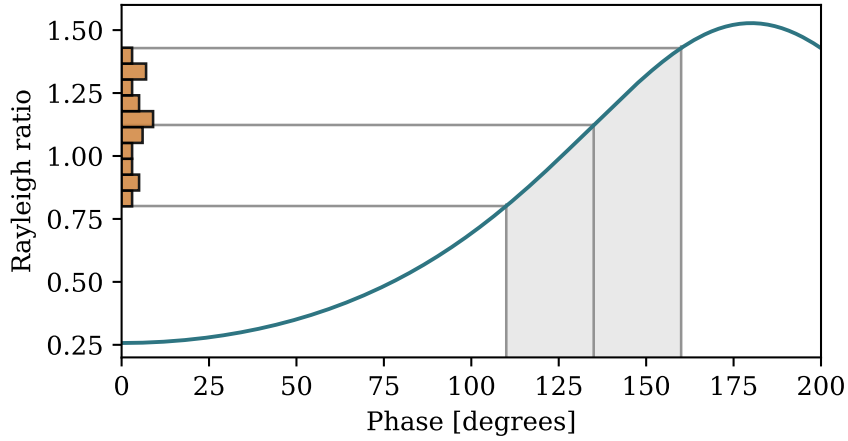


Fig. 3.17 **Ratio of Rayleigh scattering** Calculated ratio of the Rayleigh-scattered photons at the two beam-splitter outputs for the same measurement as presented in Fig. 3.16. The grey area indicates the acceptance window of $\pm 25^\circ$ around the desired phase, which defines the boundaries for the ratio used for post-processing. The distribution of the 47 three-photon events within the acceptance window is given by the histogram on the y-axis.

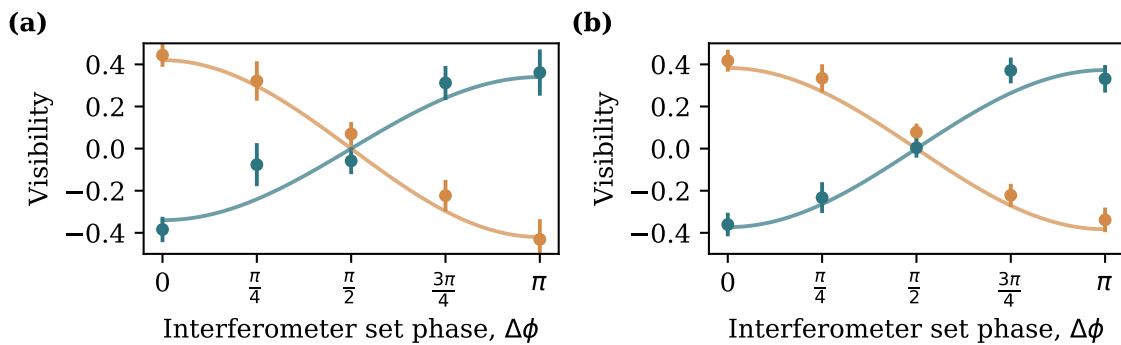


Fig. 3.18 **Phase-dependent visibility for different post-processing window** (a) & (b) Data for the phase-tunable entangled state with an acceptance window of $\pm 10^\circ$ and $\pm 20^\circ$, respectively.

3.6.4 Correction for Stark shifts

We have seen before that the presence of the off-resonant rotation pulses can alter the decay shape of the fluorescence following the entanglement pulse due to the induced Stark shifts. Depending on the readout basis there are different numbers of rotations with different pulse areas and by comparing the relative count rates within the ROI of the Raman photons for the four measurement basis we can correct for the small imbalances caused by the rotations. We perform this correction independently for the computational basis and each interferometer set point in the transverse basis and find that the overall deviation is on the order of $\lesssim 1\%$. Once we have applied this final correction we can calculate the ratios of the events in different readout bases which naturally define the visibilities of our measurements.

3.7 Discussion of Results

In order to put our results into perspective, we summarise the fidelities that have been reported thus far for experiments realising distant entanglement through projective measurements of either one or two photons. These implementations cover a variety of systems: atomic qubits [134, 135, 138, 150, 151], Nitrogen-vacancy centers [136, 152, 153], superconducting qubits [137], and quantum dot hole spins [115]. In Fig. 3.19 (a) we show the reported fidelity with respect to the entanglement generation rate, where we distinguish between one- and two-photon schemes (blue and yellow data points). In general terms we can see that two-photon schemes tend to report higher fidelities, whereas one-photon schemes generally report higher entanglement-generation rates. This behaviour can be explained considering that the successful projection of a state will scale either linearly (one photon) or quadratically (two photon) with the detection efficiency and that the one-photon scheme has an inherent error proportional to p and is inherently phase sensitive.

With an entanglement generation rate of 5.8kHz we are setting a new benchmark for fast distribution of entanglement between distant systems. The fidelity of our state directly depends on the choice of p and thus, the generation rate and we can increase the fidelity by lowering the rate until we are ultimately limited by the detector dark counts. It is worth noting that we report our bare, measured fidelity of $61.6 \pm 2.3\%$ and do not correct for experimental imperfections during the state reconstruction.

Another interesting measure is the relation between fidelity and success probability reported in Fig. 3.19 (b). Here, we take into account the rate at which entanglement generation is attempted in order to calculate the probability of success per attempt. Therefore, we factor out experimental conditions like the requirement for intermittent cooling or reloading of traps in atomic systems as well as the intrinsic timescales of the physical systems. In our

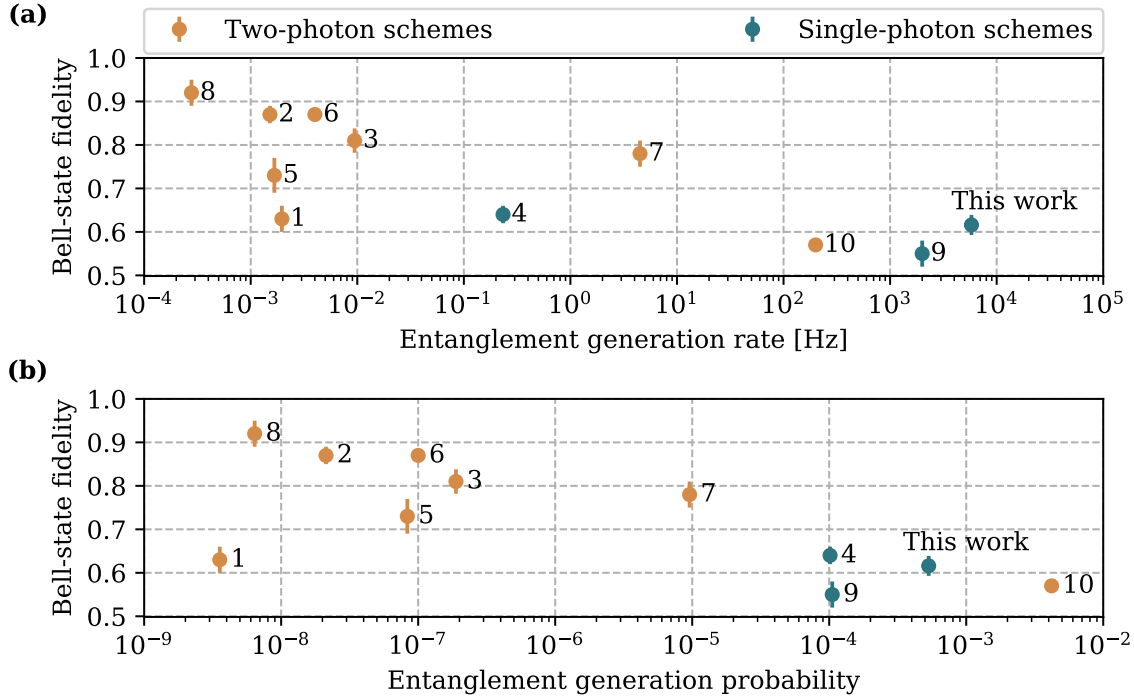


Fig. 3.19 Comparison of projective entanglement experiments (a) Comparison of Bell-state fidelity and entanglement generation rate to other realisations of distant entanglement via projective measurements. Numbered points represents results from the following references: 1 [134], 2 [150], 3 [135], 4 [138], 5 [152], 6 [153], 7 [151], 8 [136], 9 [115], and 10 [137]. (b) Comparison of Bell-state fidelity and generation probability for the same experiments.

experiment we are able to operate continually at an attempt rate of 10.9 MHz, which does not present an intrinsic limit but is rather set by the capability of the experimental setup. With a resulting success probability of 5.3×10^{-4} we are still reporting the highest value for optically linked systems and are only outperformed by superconducting qubits which are only separated by a few centimetres, linked through microwave channels, and make use of on-chip detectors.

It is important to note that our experiment is limited by the inhomogeneous dephasing of the electron spin which necessitates the readout of the spin state to be prior to the state projecting detection of the Raman photon. Currently it takes ~ 100 ns for the Raman photons to reach the detector and thus we are looking to improve the dephasing time by about two orders of magnitude. This can be achieved through the addition of a single spin-echo pulse, extending the coherence up to the microsecond regime [93, 154], which will be discussed in more detail in Chapter 5. Another promising route to improve the coherence of the electron spin is active stabilisation of the nuclear-spin bath through coherent population trapping [155], which provides an extension of T_2^* to tens of nanoseconds. Finally, we can

also utilise the hole spin which has been shown to have suppressed interaction with the nuclear-bath [51, 52] and coherence times superior to the electron (see Chapter 6). In fact, the hole spin has been used to generate heralded entanglement between two distant spins [115], but the implementation is lacking the phase control required to deterministically generate a desired two-spin state.

Improving the coherence time not only allows for the realisation of heralded entanglement but also results in an increase of both fidelity and entanglement-generation rate. The reduced spin dephasing leads to a higher visibility in the phase-sensitive transverse basis and thus an improvement of the overall fidelity. Furthermore, it allows us to delay the coherent rotations for the selection of the readout basis which are currently limiting our entanglement ROI to 57% of the photon, offering a potential increase of the entanglement rate by a factor ~ 1.75 .

In terms of the data post-processing one of the main limitations is the slow electrical noise which can cause the transition of one of the quantum dots to wander off resonance. In principle, real-time monitoring of the count rates relevant for the post-processing could be achieved through the implementation of fast, designated electronics which could enable a direct feedback to the experiment. Ideally, this would allow for measurements without the need for any post-processing, which could be relevant for long-term applications of entanglement distribution.

Chapter 4

Hong-Ou-Mandel interference of photons from two distant quantum dots

"In every branch of knowledge the progress is proportional to the amount of facts on which to build, and therefore to the facility of obtaining data. "

- James Clerk Maxwell, [156]

One of the key ingredients for the successful realisation of distant spin-spin entanglement presented in Chapter 3 is the high indistinguishability of Raman photons emitted by the two quantum dots. In this chapter we further investigate the indistinguishability of Raman photons from two distinct quantum dots and present a detailed analysis of the HOM visibility for different areas of the emitted single-photon wave packet defined by a time window $[t_1, t_2]$. In other words, in contrast to common post-selection techniques we use our time-tagged data to directly select time windows within the photon wave packet and calculate the corresponding visibility.

The measurements were performed directly after the spin-spin entanglement and rely on the setup and techniques developed by everyone involved in that experiment. The data was taken with the support of Claire Le Gall.

4.1 Intensity autocorrelation

The single-photon purity of the source used for a HOM experiment sets an upper bound to the HOM visibility since any multi-photon emission contributes to the central peak around $\tau = 0$ [113]. We can characterise this contribution through measurements of the intensity autocorrelation for each quantum dot.

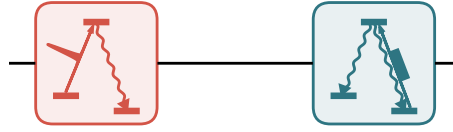


Fig. 4.1 **Autocorrelation pulse sequence** Pulse sequence for the $g^2(\tau)$ measurements used to characterise the single-photon purity of the quantum dots. A weak excitation pulse on the low-energy transition generates Raman photons followed by a 30 ns pulse on the high-energy transition to reinitialise the spin state.

4.1.1 Experimental method

The further investigation of indistinguishability of Raman photons is a follow-up of the entanglement experiment and makes use of the setup introduced in Sec. 3.2. Furthermore, we work with the same quantum dots as in the previous chapter and at a field of $B_{\text{ext}} = 4\text{ T}$, which allows us to isolate one of the two Λ -systems.

For the measurement of the intensity autocorrelation $g^2(\tau)$ we use the pulse sequence shown in Fig. 4.1. Following a weak 160ps excitation on the low-energy transition we collect the fluorescence at the Raman frequency using the filtering setup of the entanglement experiment. Subsequently, the spin is reinitialised in the $|\downarrow\rangle$ state using a 30 ns pulse resonant with the high-energy transition. The intensity autocorrelation is calculated from the recorded timestamps of the measurement, where we post-select only the Raman photons emitted following the weak excitation.

4.1.2 Measurement of intensity autocorrelations

The measurements are presented in Fig. 4.2 (a) & (b), where we show the central peak and the first satellite peak on each side. In contrast to the measurements shown in Fig. 3.8 we include the full fluorescence signal measured after the weak excitation pulse for the calculation of the correlations. Considering the averaged integrated counts of the satellite peaks corresponding to $(n, n \pm i)$ with $i \in \{1, 2, 3\}$ we find $g^2(0) = 0.046 \pm 0.006$ and $g^2(0) = 0.016 \pm 0.003$ for QD_A and QD_B , respectively. The number of residual coincidence counts around $\tau = 0$ agrees with our estimate for residual background and detector dark counts within the fluorescence signal. The difference in total coincidence counts can be attributed to dissimilar Raman-photon rates caused by a difference in both collection efficiency and coupling to the quantum dots.

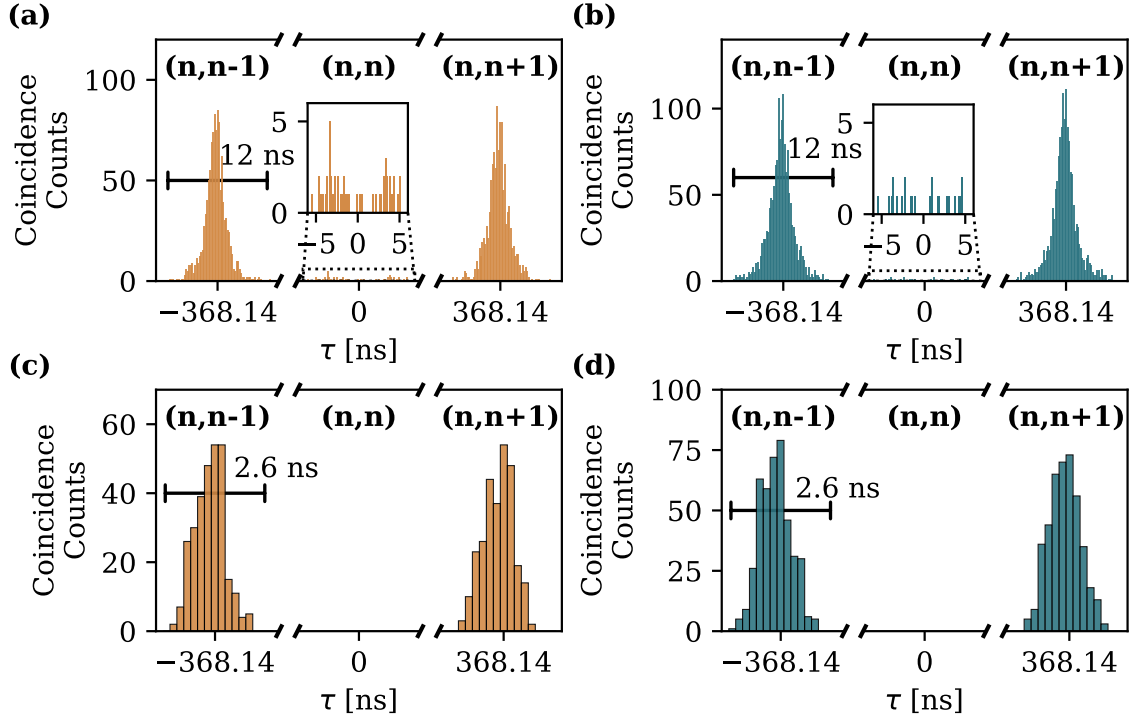


Fig. 4.2 **Intensity autocorrelations** (a) & (b) $g^2(\tau)$ extracted from measurements of the quantum dot emission following a weak excitation for QD_A (orange) and QD_B (blue), respectively. We find $g^2(0) = 0.046 \pm 0.006$ ($g^2(0) = 0.016 \pm 0.003$) for QD_A (QD_B). (c) & (d) Extracted $g^2(\tau)$ if only the first 1.2 ns of the photon are included, resulting in $g^2(0) = 0$ for both quantum dots.

The two measurements in Fig. 4.2 (c) & (d) are based on the same data as (a) and (b), however this time we only analyse the first 1.2 ns of the photon analogous to the measurements taken during the entanglement experiment. The data show perfect anti-bunching of the quantum dot emission, compatible with a prediction of ≤ 4 coincidence counts in the central peak based on the background and dark-count rate of the detectors.

These background-limited measurements confirm the high quality of our single-photon emitters and in the following we approximate both quantum dots as perfect single-photon sources. Therefore, we expect the HOM visibility to be only limited by the distinguishability of the photons.

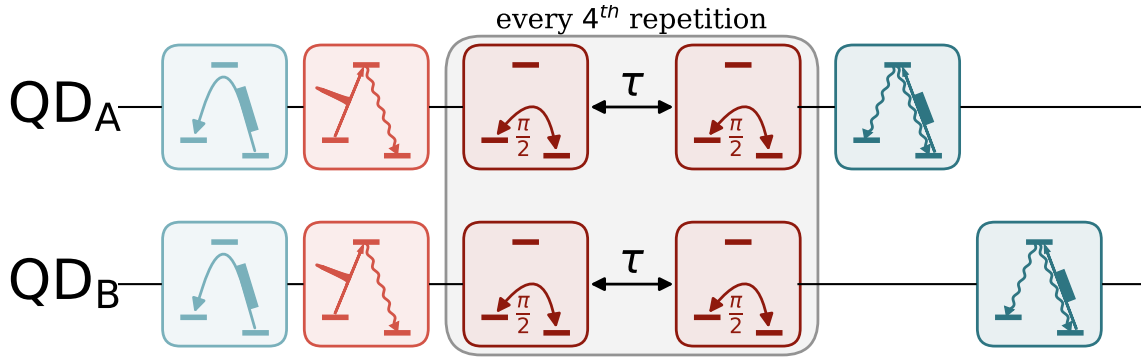


Fig. 4.3 **HOM pulse sequence** Experimental pulse sequence for the measurement of HOM interference. Both quantum dots are simultaneously initialised in the $|\downarrow\rangle$ state (light blue) and subsequently excited by a weak 160 ps pulse on the low energy transition (light red). Every fourth repetition we introduce two $\pi/2$ rotations implementing a Ramsey measurement sequence (grey box) followed by individual readouts of the spin states (dark blue).

4.2 Hong-Ou-Mandel interference

For the entanglement experiment we only considered $\sim 57\%$ of the photon to minimise the effect of dephasing. Here, we study the indistinguishability for different driving powers and provide a detailed analysis of its dependence on the selected area of the photon wave packet.

4.2.1 Experimental method

For the measurements of HOM interference visibility we extend the basic $g^2(\tau)$ measurement sequence in order to allow for a simultaneous measurement of the spin splitting of the two quantum dots. The pulse sequence is shown in Fig. 4.3 and follows the structure of the sequence used during the entanglement experiment. Both quantum dots are simultaneously initialised and excited in order to generate single photons. Every fourth repetition of the experiment we introduce two $\pi/2$ pulses, implementing a Ramsey-interference measurement. In preparation for a measurement we use the measured Larmor frequency to fine-tune the spin-splitting of the two quantum dots and ensure spectral overlap of the Raman photons. Finally, both spin states are read out individually, which is only needed for the Ramsey measurements and otherwise serves as part of the initialisation.

The inclusion of the Ramsey measurement into the overall measurement sequence is necessary due to the AC-Stark shift induced by the rotation pulses which would otherwise alter the resonance condition and thus the spin splitting. We note that in contrast to the entan-

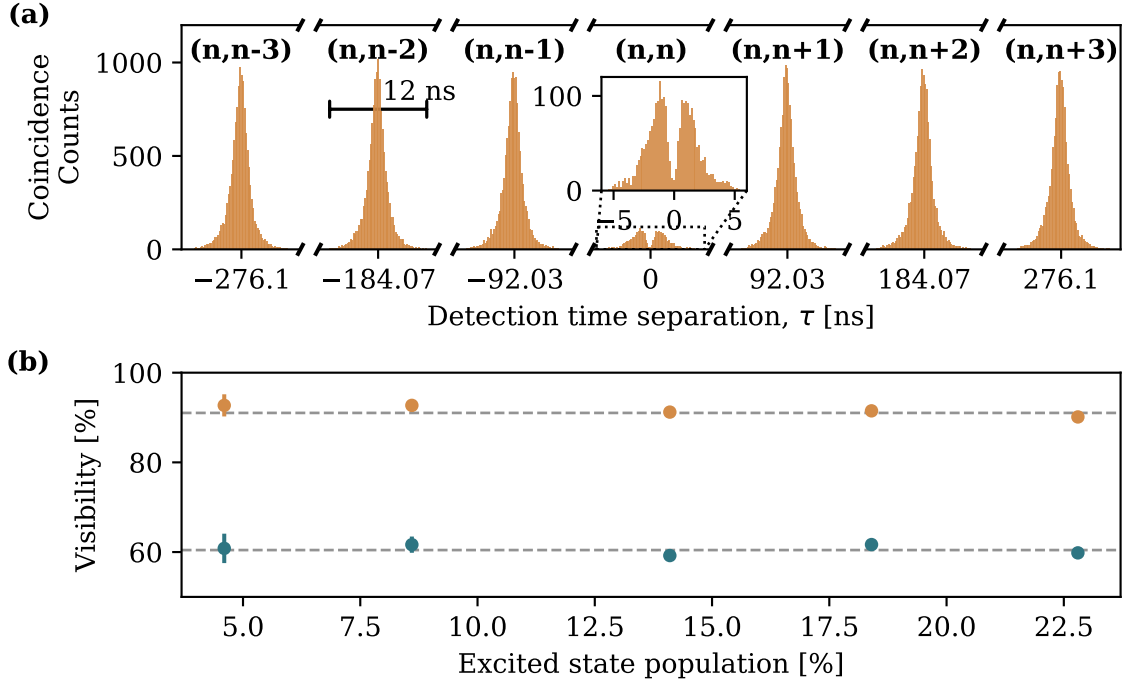


Fig. 4.4 **Power dependent HOM** (a) Measured HOM interference for an excited-state population of 18.4%. The central peak is strongly suppressed showing a prominent dip around $\tau = 0$ and we extract $V_{\text{HOM}} = 61.7 \pm 0.8$. (b) Extracted visibilities for different drive strength indicated by the excited-state population (blue data). The orange data show the visibilities corresponding to the HOM interference of the first 1 ns of the single photon pulse. The two dashed lines indicate the average visibility and error bars represent ± 1 standard deviation.

gument experiment, the coherent rotations are introduced 6.5 ns after the weak excitation and thus do not overlap with the quantum dot emission.

Each measurement is taken for a duration of 30 minutes and we save the timestamps of all registered single-photon events allowing us to look at different areas of the emitted Raman photon during the post-processing of the data.

4.2.2 Power-dependent HOM interference

We measure the Hong-Ou-Mandel interference for different excitations powers, corresponding to different excited-state populations. A measurement representing $\sim 18.4\%$ population of the excited state is shown in Fig. 4.4 (a), where we observe Lorentzian-shaped side peaks and a strongly suppressed central peak at $\tau = 0$.

As discussed in the last chapter, we cannot repeat the measurement with cross-polarised photons and thus estimate the visibility based on the assumption that for distinguishable

Hong-Ou-Mandel interference of photons from two distant quantum dots

photons the central peak has exactly half the height of the satellite peaks. The visibility given by:

$$V_{\text{HOM}} = 1 - \frac{2N_{n=m}}{N_{n \neq m}} \quad (4.1)$$

is then a direct measure of the indistinguishability assuming a 50:50 beam splitter. For the remainder of this chapter $N_{n \neq m}$ is given by the average over the satellite peaks ($n, n \pm i$) with $i \in \{1, 2, 3, 4\}$.

For the measurement presented in Fig. 4.4 (a) we find $V_{\text{HOM}} = 61.7 \pm 0.8\%$ which is shown in (b) alongside the visibilities extracted for different excited-state populations. Here, we also show the visibility corresponding to the first 1.2 ns of the photon, analogous to the entanglement experiment. These measurements show a significantly higher visibility due to the suppressed effect of spin-state dephasing. In both cases, the visibility shows no significant decrease across the range of excited-state populations and we find an average visibility of $V_{\text{HOM}} = 60.4 \pm 0.4\%$ and $V_{\text{HOM}} = 91.0 \pm 0.4\%$. For all measurements the power is below saturation (i.e. 25%) and the results show that the contribution of possible two-photon emission through re-excitation during the finite excitation pulse is negligible at these powers.

4.2.3 HOM interference of distinguishable photons

In order to validate our approach of calculating the visibility, we perform a HOM measurement where we introduce distinguishability in the spectral domain. Single photons which are far detuned in energy do not show any interference and thus we expect to recover zero visibility [149, 157].

We tune the external magnetic field of QD_A to 4.4 T while keeping QD_B at 4 T to detune the two quantum dot transition frequencies. Further, the applied gate voltage is used to fine tune the detuning and ensure stable resonance conditions. The corresponding Ramsey interference measurements are shown in Fig. 4.5 (a) & (b) where we extract a ground-state splitting of 26.2 ± 0.1 GHz and 23.0 ± 0.3 GHz for QD_A and QD_B , respectively. Therefore, the emitted photons are detuned by 3.2 ± 0.3 GHz and the corresponding HOM measurement in Fig. 4.5 (c) indeed shows no suppression of the central peak around $\tau = 0$; we extract $V_{\text{HOM}} = -0.5 \pm 2.0\%$. The measurement shows that we recover a peak containing 50% of the coincidence counts in the satellite peaks validating our method of estimating the visibility.

4.2.4 Photon wave-packet area dependent HOM visibilities

The data presented in Fig. 4.4 (b) show that the indistinguishability is closely related to the photon area considered for the calculation of the coincidence counts, which is a direct

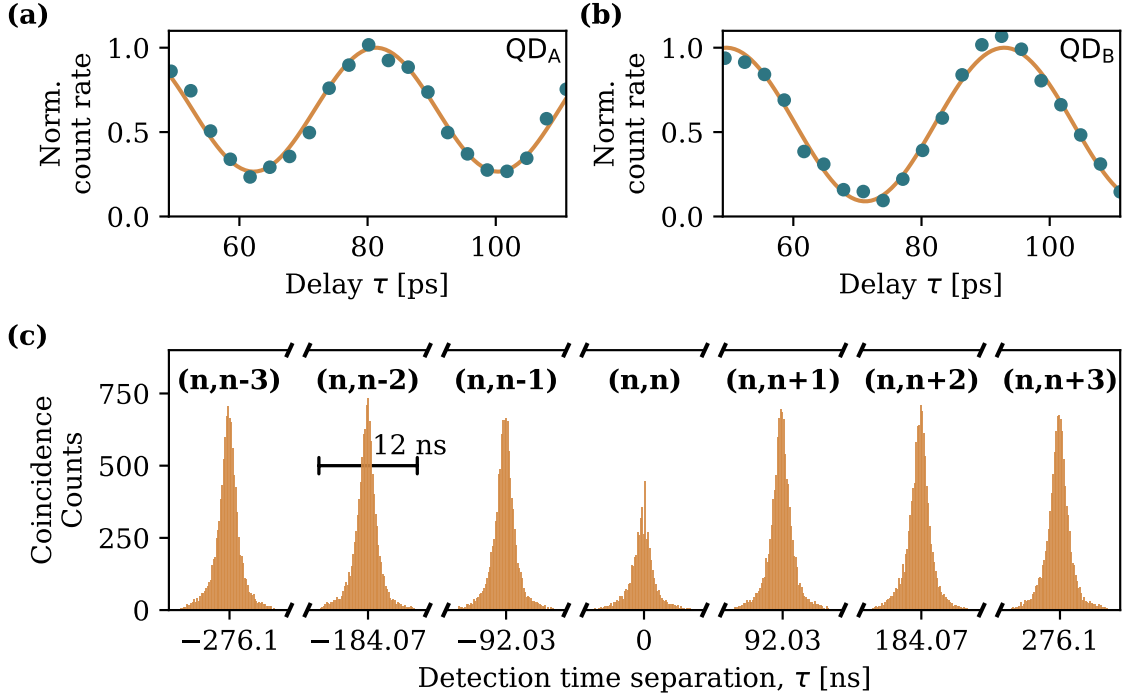


Fig. 4.5 **HOM of distinguishable photons** (a) & (b) Measurement of electron-spin splitting through Ramsey interference. We extract 26.2 ± 0.1 GHz (23.0 ± 0.3 GHz) for QD_A (QD_B). (c) HOM interference of distinguishable photons resulting in $V_{\text{HOM}} = -0.5 \pm 2.0\%$.

consequence of T_2^* being on the order of the radiative lifetime of the excited state. Here, we perform a detailed analysis of the data shown in Fig. 4.4 (a) to investigate the effect of selecting different areas of the photon wave packet on the indistinguishability.

The results are summarised in Fig. 4.6, where we show a two-dimensional density plot of the extracted HOM visibilities for different areas of the photon wave packet, specified through the interval $[t_1, t_2]$. In other words, we only consider detection events with a time tag t , where $t_1 \leq t \leq t_2$. Here, $t = 0$ is defined as the start of the photon as can be seen in the histogram in the top right panel. In theory, we would expect to get data for the whole triangle where $t_2 > t_1$. However, for small intervals, where t_1 & t_2 are either right at the beginning of the photon wave packet or well beyond the radiative lifetime, the statistics can be too low to extract any meaningful data, resulting in missing data points. This is especially prominent for $t_1 > 2.5$ ns.

The top panel shows the data of two vertical line cuts corresponding to $t_1 = 0.486$ ns (dark blue) and $t_1 = 1.215$ ns (light blue). In both cases the initial indistinguishability is greater than 98% which is continuously reduced as we include more and more area of the photon wave packet, approaching about 60% for $t_2 = 5.994$ ns. The increased distinguishability is a

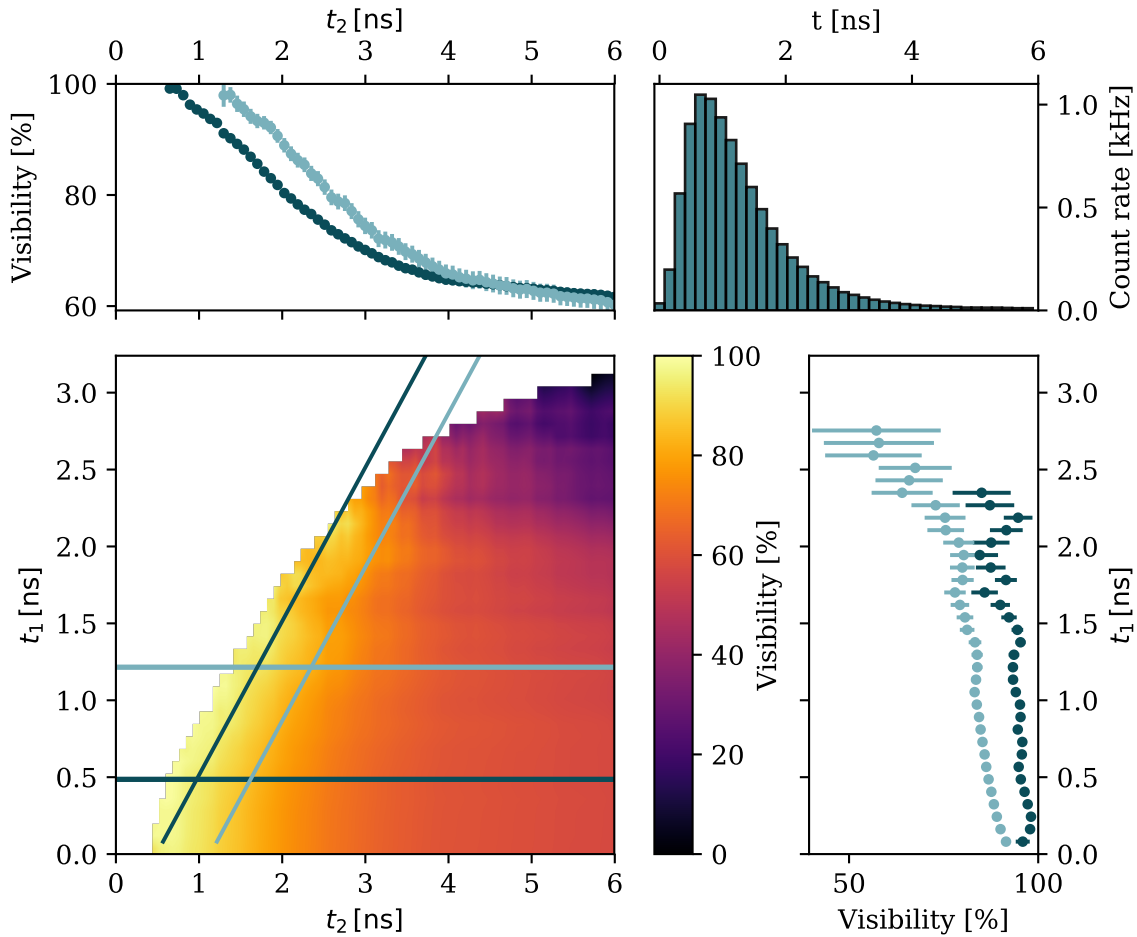


Fig. 4.6 **Photon area dependent HOM visibility** Visibility of the HOM interference for different parts of the photon wave packet characterised by t_1 and t_2 . The top panel shows the data corresponding to the line cuts for $t_1 = 0.486$ ns (dark blue) and $t_1 = 1.215$ ns (light blue). The left panel shows line cuts for a fixed-length interval, Δt , with increasing t_1 for $\Delta t = 0.567$ ns (dark blue) and $\Delta t = 1.215$ ns (light blue). The photon is shown in the top right panel for reference and error bars represent ± 1 standard deviation.

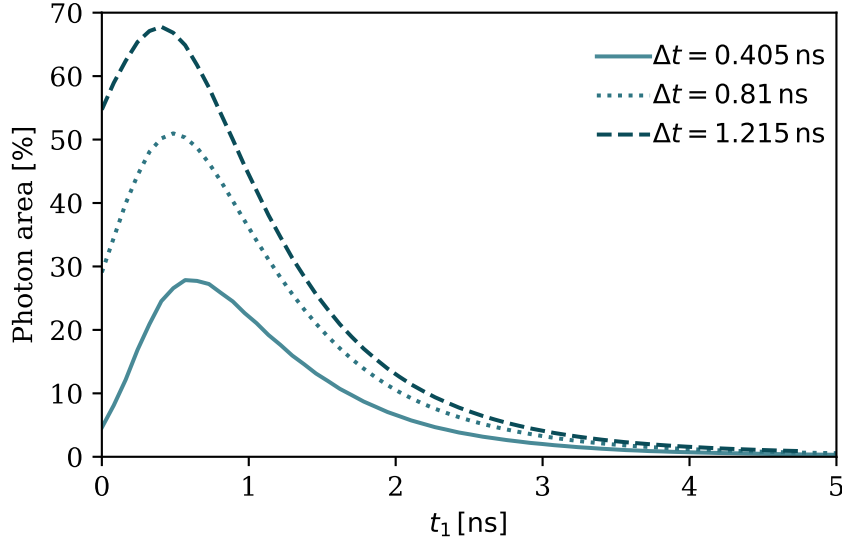


Fig. 4.7 **Optimising photon area** The curves show the dependence of area of the photon wave packet within the selected time interval on the starting point t_1 . There is a clear maximum indicating an optimal value for the choice of t_1 .

direct result of the dephasing of the spins due to the combined inhomogeneous dephasing of about 1.2 ns [146, 147], as well as electrical noise which modifies the transition energy.

The panel on the right of the density plot shows the data along two diagonal line cuts, corresponding to $\Delta t \equiv t_2 - t_1 = 0.567$ ns (dark blue) and $\Delta t = 1.215$ ns (light blue), i.e. visibilities where the length of the considered interval is constant for increasing t_1 . Here, we observe a slow decrease of visibility for $t_1 \leq 1.5$ ns, while for $t_1 > 1.5$ ns the visibility shows a further decay accompanied by fluctuations. The latter part suffers from the lower statistics due to the small probability of detecting a photon at delays where t_1 & t_2 are well beyond the radiative lifetime, also evidenced in the increasing error bars. Whereas the slow decay of the former part is an indication of the dephasing of the photon due to electrical noise.

The increase of visibility with decreasing Δt can be understood by considering the effect of this filtering of the data: By reducing Δt we set a time filter that allows for a greater frequency mismatch between the two quantum-dot photons. Thus, the visibility is higher for $\Delta t = 0.567$ ns compared to $\Delta t = 1.215$ ns as shown in the right panel of Fig. 4.6.

For the design of an experiment these results provide a method to determine the best area of the photon wave packet as a trade-off between the indistinguishability of the photons and the rate that can be obtained. While a small time interval Δt leads to a high indistinguishability it also reduces the area of the photon wave packet that is considered. Moreover, due to finite rise time of the photon envelope the choice of t_1 , i.e. the starting point of the considered

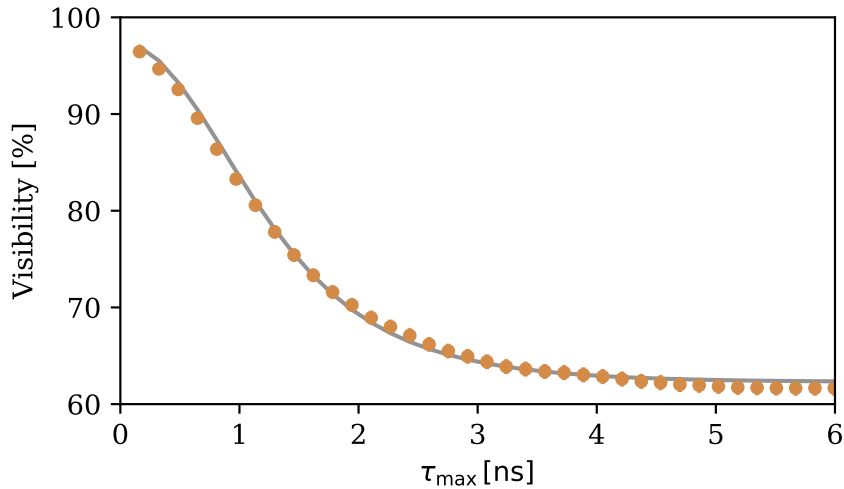


Fig. 4.8 **Post-selection on detection time difference** Post-selection through decreasing of the maximum considered detection time difference, τ_{\max} (orange points). The solid curve is a fit to the data. Error bars represent ± 1 standard deviation.

interval, has an optimum value which depends on Δt . Figure 4.7 shows three exemplary curves which can be used to determine the best estimate of t_1 depending on the choice of Δt .

Typically, HOM experiments directly calculate the coincidences and subsequently post-select events which correspond to a detection time separations within a certain bound, τ_{\max} . In other words, once the coincidence counts are extracted we post-select the events based on their separation: $\tau < \tau_{\max}$. In principle this method is similar to the analysis above, as it also relies on the definition of a time filter which reduces the effect of a frequency mismatch between the photons. However, it does not allow to consider specific areas of the photon wave packet which can be used to determine the optimum area for experiments like the entanglement experiment presented in the previous chapter.

The results of this post-selection on τ are shown as orange data points in Fig. 4.8. Again, we can see that the visibility is increasing with decreasing τ_{\max} , allowing for a larger frequency mismatch. The solid curve represents a fit to the data, which is based on a model assuming Lorentzian-shaped photons and includes inhomogeneous dephasing as well as the detector response. The details and fit parameters are discussed in the next section.

4.3 Model of HOM interference

The measurement signal of the HOM experiment corresponds to the second-order correlation function, which we will calculate using a model based on the works of Legero *et al.* [158]

and Woolley *et al.* [159]. Here, we will briefly outline its derivation and discuss the results obtained in combination with our data.

4.3.1 Second-order correlation function

The effect of a balanced beam splitter on two dimensionless, time-dependent input modes \hat{a}_{in} and \hat{b}_{in} is described by [23]:

$$\begin{bmatrix} \hat{a}_{\text{out}} \\ \hat{b}_{\text{out}} \end{bmatrix} = \frac{1}{\sqrt{2}} \begin{bmatrix} 1 & -1 \\ 1 & 1 \end{bmatrix} \begin{bmatrix} \hat{a}_{\text{in}} \\ \hat{b}_{\text{in}} \end{bmatrix}, \quad (4.2)$$

where \hat{a}_{out} and \hat{b}_{out} denote the corresponding modes of the beam-splitter outputs. In the following, we will focus on the photon statistics at the output of the beam splitter and for the ease of notation we will drop the subscript of the field operators, i.e. the output fields will be labelled \hat{a} and \hat{b} . The number of photons in the output modes is given by the number operator $\hat{n}_c = \hat{c}^\dagger(t)\hat{c}(t)$ and we are interested in the corresponding normally ordered correlation functions [159]:

$$\langle : \hat{n}_c(t + \tau) \hat{n}_d(t) : \rangle = \langle \hat{d}^\dagger(t) \hat{c}^\dagger(t + \tau) \hat{c}(t + \tau) \hat{d}(t) \rangle, \quad (4.3)$$

with $c, d \in \{a, b\}$. In the case of $c = d$ this expression gives us the output intensity autocorrelation function, whereas for $c \neq b$ we obtain the output intensity cross-correlation function. Here, the former corresponds to the signal expected for a classical field, whereas the latter represents the output expected for a quantum field. In the following we focus on the calculation of the cross-correlation function.

If we evaluate this expression in terms of the input fields we find sixteen fourth order moments. However, by assuming that the two sources are not entangled (i.e. the fields are separable) and that we can neglect the phase-dependent moments we can reduce the expression to only six relevant terms. The latter assumption is justified by the fact that all phase-dependent moments evaluate to zero for single photons and are otherwise averaged out through repeated measurements [159]. The output intensity correlation functions are then given by:

$$\begin{aligned} \langle : \hat{n}_a(t + \tau) \hat{n}_b(t) : \rangle &= \frac{1}{4} \sum_{(\hat{c}, \hat{d}) \in \Pi(\hat{a}_{\text{in}}, \hat{b}_{\text{in}})} \langle \hat{c}^\dagger(t) \hat{c}^\dagger(t + \tau) \hat{c}(t + \tau) \hat{c}(t) \rangle \\ &\quad + \langle \hat{c}^\dagger(t) \hat{c}(t) \rangle \langle \hat{d}^\dagger(t + \tau) \hat{d}(t + \tau) \rangle - \langle \hat{c}^\dagger(t + \tau) \hat{c}(t) \rangle \langle \hat{d}^\dagger(t) \hat{d}(t + \tau) \rangle \end{aligned}, \quad (4.4)$$

Hong-Ou-Mandel interference of photons from two distant quantum dots

where $\Pi(\hat{a}_{\text{in}}, \hat{b}_{\text{in}}) = \{(\hat{a}_{\text{in}}, \hat{b}_{\text{in}}), (\hat{b}_{\text{in}}, \hat{a}_{\text{in}})\}$. The three terms of Eqn. 4.4 contain the intensity correlation function of the input (first term), the product of the input intensities (second term) and the product of the first order correlation functions (third term). At $\tau = 0$ the second and third term cancel which is evidence for two-photon interference.

In order to obtain the second-order correlation function we need to eliminate t , which can be achieved by either integrating or taking the limit. We define the first- and second-order correlation functions, $G_c^{(1)}(\tau)$ and $G_{cd}^{(2)}(\tau)$, respectively, as [159]

$$G_c^{(1)}(\tau) = \int dt \langle \hat{c}^\dagger(t) \hat{c}(t+\tau) \rangle \quad \text{or} \quad G_c^{(1)}(\tau) = \lim_{t \rightarrow \infty} \langle \hat{c}^\dagger(t) \hat{c}(t+\tau) \rangle \quad (4.5)$$

$$G_{cd}^{(2)}(\tau) = \int dt \langle : \hat{n}_c^\dagger(t+\tau) \hat{n}_d(t) : \rangle \quad \text{or} \quad G_{cd}^{(2)}(\tau) = \lim_{t \rightarrow \infty} \langle : \hat{n}_c^\dagger(t+\tau) \hat{n}_d(t) : \rangle. \quad (4.6)$$

If we now further make the assumption that both sources have identical statistics, we can rewrite Eqn. 4.4:

$$G_{ab}^{(2)}(\tau) = \frac{1}{2} \left[G^{(2)}(\tau) + [G^{(1)}(0)]^2 - |G^{(1)}(\tau)|^2 \right], \quad (4.7)$$

where $G^{(2)}(\tau) = G_{cc}^{(2)}(\tau)$ and $G^{(1)}(\tau) = G_c^{(1)}(\tau)$ for $c \in \{a_{\text{in}}, b_{\text{in}}\}$. Again, the two-photon interference is evidenced in the cancellation of the last two terms for $\tau = 0$.

4.3.2 Single-photon pulses

During the experiment we work with pulsed excitation of the quantum dots and thus pulsed single-photon emission. In order to incorporate this into the formalism developed so far we consider temporal mode functions:

$$\zeta(t) = \frac{1}{\sqrt{2\pi}} \int d\omega \Phi(\omega) e^{-i\omega t}. \quad (4.8)$$

Here, $\Phi(\omega)$ is the spectral density of the single-photon pulse [158, 159]. Using this formalism we can write $\hat{c}(t) = \zeta_c(t) \hat{c}_0$, where \hat{c}_0 is the corresponding annihilation operator of the temporal mode.

Assuming perfect single photon sources, i.e. $g^{(2)}(0) = 0$, we can now rewrite Eqn. 4.4 as:

$$\langle : \hat{n}_a(t+\tau) \hat{n}_b(t) : \rangle = \frac{1}{4} |\zeta_a(t+\tau) \zeta_b(t) \pm \zeta_b(t+\tau) \zeta_a(t)|^2. \quad (4.9)$$

While the cross-correlation function clearly vanishes for $\tau = 0$, the exact behaviour for $\tau \neq 0$ will depend on the temporal mode of the single photon.

Here, we consider a Lorentzian mode based on the line shape observed in the coincidence counts of the HOM experiment. The temporal mode function is determined by the decay rate, γ , and the photons have an exponential shape. The two mode functions are represented by:

$$\zeta_{a(b)}(t) = \sqrt{2\gamma}e^{-\gamma t}H(t)e^{-i(\omega_0 \pm \Delta/2)t}, \quad (4.10)$$

where Δ denotes the carrier frequency difference centred around ω_0 and $H(x)$ denotes the Heaviside step function.

Using this mode function in Eqn. 4.9 and assuming $\tau > 0$, we find [159]:

$$\langle : \hat{n}_a(t + \tau) \hat{n}_b(t) : \rangle = 4\gamma^2 e^{-2\gamma(2t+\tau)} H(t) \sin^2(\tau\Delta/2). \quad (4.11)$$

In a final step we then integrate over t in order to obtain the second-order correlation functions of the output:

$$G_{ab}^{(2)}(\tau) = \gamma e^{-2\gamma\tau} \sin^2(\tau\Delta/2). \quad (4.12)$$

In order to normalise our data and calculate the HOM visibility we also require an expression for the satellite peaks. These peaks correspond to the non interfering case and are given by the non-coherent addition of the two input modes (Eqn. 4.10), leading to:

$$G_S^{(2)}(\tau) = \gamma e^{-2\gamma\tau}. \quad (4.13)$$

4.3.3 Calculation of HOM signatures

In our experiment, the frequency detuning between the two sources is relatively small and well controlled through simultaneous measurements of the Larmor frequencies. However, we use the dependence of the signal on the detuning to incorporate the effect of inhomogeneous dephasing, by integrating over a Gaussian distribution of detunings with a width of $\sqrt{2}/T_2^*$ [55, 158]:

$$G_{ab(S)}^{(2)}(\tau, \gamma, T_2^*) = \frac{T_2^*}{2\sqrt{\pi}} \int_{-\infty}^{\infty} d\Delta G_{ab(S)}^{(2)}(\tau, \gamma, \Delta) e^{-\frac{1}{4}(\Delta T_2^*)^2}. \quad (4.14)$$

In a second step we also include the jitter of our detection:

$$G_{ab(S)}^{(2)}(\tau, \gamma, T_2^*, J) = \frac{1}{2\sqrt{2\pi}J} \int_{-\infty}^{\infty} dt G_{ab(S)}^{(2)}(t, \gamma, T_2^*) e^{-\frac{1}{2}((\tau-t)/J)^2}. \quad (4.15)$$

Hong-Ou-Mandel interference of photons from two distant quantum dots

In the following we set $J = 180$ ps, which roughly corresponds to our system response.

Now we can calculate the HOM visibility, V_{HOM} , according to Eqn. 4.1:

$$V_{\text{HOM}} = 1 - 2 \frac{\int_{-\tau_b}^{\tau_b} d\tau_b G_{ab}^{(2)}(\tau_b, \gamma, T_2^*, J)}{\int_{-\tau_b}^{\tau_b} d\tau_b G_S^{(2)}(\tau_b, \gamma, T_2^*, J)}. \quad (4.16)$$

By changing τ_b we can model the post-selection process described at the end of the previous section and fit the corresponding curve to the measured values using the least squares formalism. This way, we have generated the solid curve in Fig. 4.8, which corresponds to values $\gamma = 2\pi \times 91.5$ MHz and $T_2^* = 1.108$ ns and is reproduced in Fig. 4.9 (a). We can also calculate the envelope of the suppressed HOM interference around $\tau = 0$ as shown in Fig. 4.9 (b), which is in good agreement with the measurement data. Here, we use the area of the satellite peak to determine the correct scaling factor between the model and the measured data.

The fitted decay rate, γ , corresponds to an excited state lifetime of $T_1 = 1.74$ ns, which is significantly longer than the measured lifetimes of about 0.74 ns. This extended excited-state lifetime can be attributed to the shape of the photon wave packet which includes a finite rise time due to the non-negligible length of the excitation pulse (see Fig. 4.6), while the model is based on a truncated exponential decay, leading to an overestimate of T_1 .

In contrast, the inhomogeneous dephasing time is shorter than expected from measurements through Ramsey interference. However, these measurements are performed on the ground state of the electron and thus exclude any influence of electrical noise. In our samples, we expect this noise to cause significant alternations of the transition energy, which will result in a reduction of indistinguishability. The shorter T_2^* extracted from a model can thus be attributed to the presence of electrical noise, posing a limit to the achievable visibility of the HOM interference. A more precise quantification of the electrical noise requires further measurements.

We can use the model to visualise the effect of the strong nuclear-spin induced inhomogeneous dephasing in our system. The calculated HOM visibility and the central peak are shown in Fig. 4.10 (a) & (b) for different values of T_2^* . The solid curve corresponds to the values obtained from the fit to the HOM visibility ($\gamma = 2\pi \times 91.5$ MHz and $T_2^* = 1.108$ ns). The other two curves correspond to calculations for the same γ and $T_2^* = 5$ ns (dotted curve), and $T_2^* = 10$ ns (dashed curve). We can clearly see the dramatic effect this relatively moderate improvement has on the indistinguishability, which is further evidence that the entanglement experiment would benefit from an improved inhomogeneous dephasing time. However, we would potentially still be limited by the electrical noise which is not included in the model.

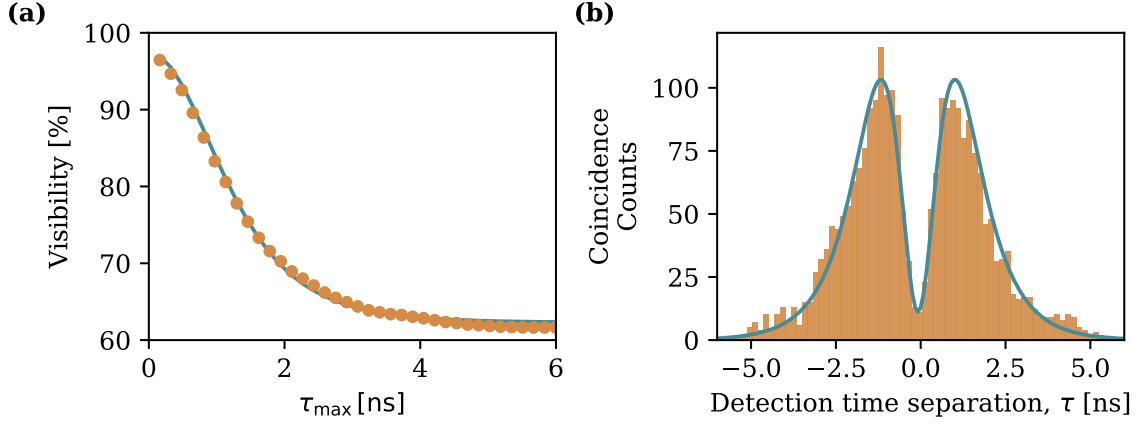


Fig. 4.9 **Fitting of HOM data** (a) Data reproduced from Fig. 4.8 (orange points) alongside the fit (solid line) corresponding to $\gamma = 2\pi \times 91.5$ MHz and $T_2^* = 1.108$ ns. (b) Central peak of the HOM interference measurement and calculated two-photon interference for the same parameters as in (a).

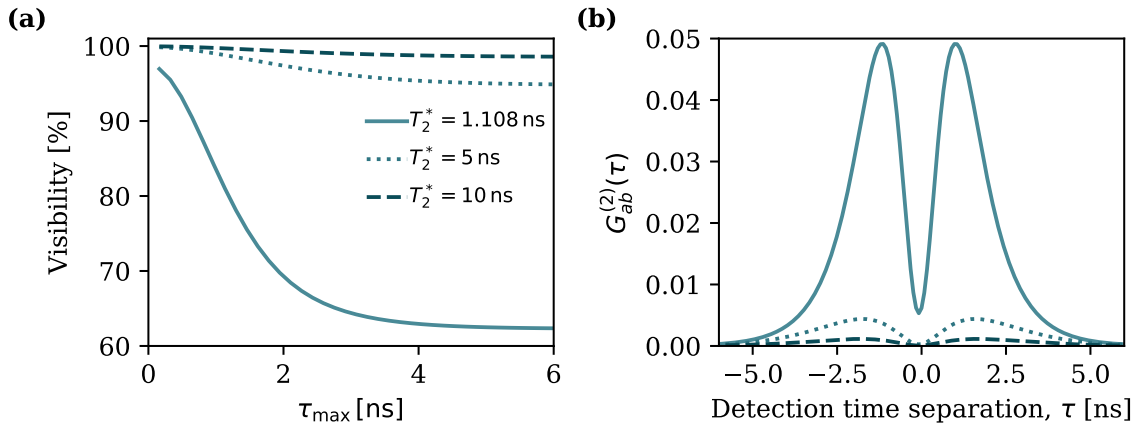


Fig. 4.10 **Modelling of HOM interference for different T_2^*** (a) Dependence of the post-selected HOM visibility on the inhomogeneous dephasing time. (b) Model of the central peak of the HOM-interference signal for the same values of T_2^* as in (a).

4.4 Discussion of Results

In this chapter we have further investigated the indistinguishability of two distinct quantum dots in separate cryostats as a follow-up to the entanglement experiment. Compared to previously reported experiments with separate quantum dots [145, 149] and molecules [157] our results show an improvement of the indistinguishability, especially for post-selected data, where we are able to reach nearly perfectly indistinguishable photons.

We have shown that the indistinguishability is not significantly affected for different powers below P_{sat} , which is an important result regarding any application where we would like to maximise the count rates extracted from the devices while maintaining their quality. In contrast, the influence of the inhomogeneous dephasing time is clearly demonstrated by the drastic difference of visibilities when comparing coincidences from the first 1.2 ns and to the full photon.

This observation is further supported by the detailed analysis of HOM visibilities for different areas within the photon wave packet which shows that the indistinguishability decays with increasing time intervals and is mainly limited by photons which are separated by $\tau \gtrsim 1$ ns. Our results also point towards the fact that the only relevant parameter is the detection time difference τ , whereas the position of the two events within the envelope of the photon appears to only have a minor influence, i.e. the indistinguishability is dominated by the frequency mismatch of the quantum dot photons.

Owing to the fact that our setup does not support measurements in a cross-polarised basis, we have chosen to detune the two quantum dot transitions in frequency in order to perform a HOM measurement with two distinguishable sources. The dependence on the detuning has been investigated before [149, 157] and the results justify our method for extracting the HOM interference visibility.

Even though the basic model of HOM interference based on previous works [158, 159] is able to describe the overall behaviour of our data, it is an overestimate of the excited state lifetime which could potentially be resolved by extending the model to include a more realistic photon shape, including a finite rise time.

From the measurements and the model we conclude that the combination of a short inhomogeneous dephasing time with electrical noise in the sample is limiting the indistinguishability of the photons. While a longer T_2^* can be achieved for example with hole spins (see Chapter 6) we ultimately also need electrically clean samples to achieve perfectly indistinguishable photons.

Chapter 5

Electron Coherence

"The goal is nothing other than the coherence and completeness of the system not only in respect of all details, but also in respect of all physicists of all places, all times, all peoples, and all cultures."

- Max Planck, [160]

The performance of our elementary unit cell of a quantum network was partially limited by the joint spin dephasing time of the two electron spins. In order to extend our entanglement scheme to a fully heralded version we need to prolong the coherence time of the electron spin: the dephasing time of ~ 1.2 ns corresponds to about 35 cm in terms of distance and realistically we would need about two orders of magnitude improvement of the coherence time taking into account the distance to our detectors and the propagation delay of the electronics. More generally, the spin coherence is essential for any quantum information processing or quantum communication protocols as dephasing will ultimately set the timescales on which we can still recover the encoded information.

In this chapter, we will take a closer look at the electron coherence and its limitations in an external magnetic field applied in Voigt geometry. We start with an investigation of the inhomogeneous dephasing time, which can be extracted from a measurement of the free induction decay (FID) of the electron spin. Here, we introduce a new measurement technique in order to prevent the build-up of nuclear polarisation which has up until now obscured the inhomogeneous dephasing time through strong back action on the measurement signal. Having measured the full electron FID utilising this new technique, we turn towards extending the available coherence through decoupling of the electron from the noise spectrum. We explore the limitations to the coherence through implementations of a Hahn echo decoupling sequence and use the measured signal as a spectroscopic tool in order to gain insight into the underlying noise spectrum. Finally, we use the obtained data to determine the mechanism

governing the electron spin coherence in this type of quantum dots through the development of a basic model.

The data presented in this chapter have been measured in collaboration with Robert Stockill as well as Clemens Matthiesen and Claire Le Gall who have also performed the modelling of the nuclear spectra. The work presented here has been published in a peer-reviewed journal [161].

5.1 Inhomogeneous dephasing time

In order to determine the inhomogeneous dephasing time, T_2^* , we need to apply a Ramsey-type interference measurement as introduced in Sec. 2.3.3. By measuring the full FID we can extract T_2^* from the decay envelope of the measured interference fringes and gain knowledge about the Overhauser field fluctuations.

5.1.1 Experimental method

As before, our quantum dot sample is placed in a liquid Helium bath cryostat and optical access is provided through our home-built confocal microscope. The superconducting magnet inside the cryostat is used to apply a 4 T external magnetic field perpendicular to the growth axis, resulting in the level structure depicted in Fig. 5.1. The ground and excited states are split by Δ_e and Δ_h , respectively, resulting in four linear polarised transitions of equal strength at 969 nm.

For the experimental realisation of a Ramsey interference measurement we first calibrate the pulse area of our ps-laser pulses to match a $\pi/2$ rotation of the electron-spin state. The area is controlled through an AOM, where we control the amount of light diffracted into the first order through the applied voltage. This measurement is calibrated through a Rabi curve taken before the measurement. The basic Ramsey interference measurement can be carried out within the repetition rate of our mode-locked laser and we therefore do not need to pick pulses. The relative delay, τ , of the two rotation pulses is controlled with the piezoelectric stage as discussed in Sec. 2.2.3. We work with pulses that are red detuned from the quantum dot transition by ~ 3 nm.

The readout and initialisation of the electron is provided by driving one of the four transitions resonantly. We drive the transition for about 80% of the time and only suppress the resonant laser for a window of 2.5 ns where we apply the spin rotations. For the laser suppression we use an EOM stabilised against thermal drifts through active feedback on the DC offset. The voltage pulse for the EOM is supplied by a pulse pattern generator which

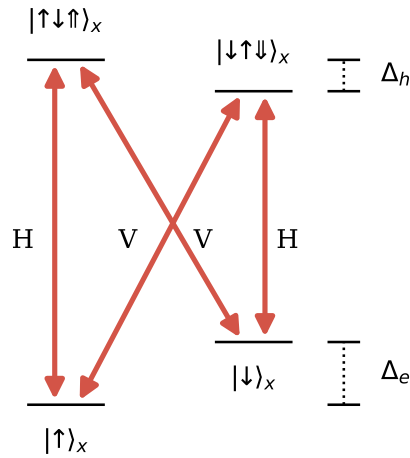


Fig. 5.1 **Energy level structure** The four energy levels of a negatively charged quantum dot in Voigt geometry are shown together with the optically allowed transitions (red arrows) and their corresponding polarisation (H, V).

is triggered by the mode-locked laser in order to ensure perfect synchronisation with the rotation pulses.

The Ramsey interference fringes are recovered by plotting the integrated readout counts against the corresponding delay τ .

5.1.2 Nuclear feedback during Ramsey interferometry

For a Ramsey interference measurement we expect to observe a sinusoidal beating at the precession frequency of the electron spin, experiencing a continuous decay of visibility due to the inhomogeneous dephasing. Instead, we observe strong deviations from this behaviour depending on the probed transitions. In Fig. 5.2 we show data measured for all four allowed optical transitions, as well as scans with increasing and decreasing delay between the $\pi/2$ rotations. For the two high frequency transitions (top row, Fig. 5.2) we initially recover the expected signal. We observe a beating corresponding to a spin splitting of 24.9 GHz with a 99% fringe visibility independent of the scanning direction. However, for $\tau > 150$ ps the signal starts to significantly deviate from a sine curve and completely vanishes for delays exceeding 250 ps. In contrast, we observe quite a different behaviour on the low energy transitions (bottom row, Fig. 5.2), where we recover a direction-dependent sawtooth-shaped signal roughly at the frequency of the spin splitting.

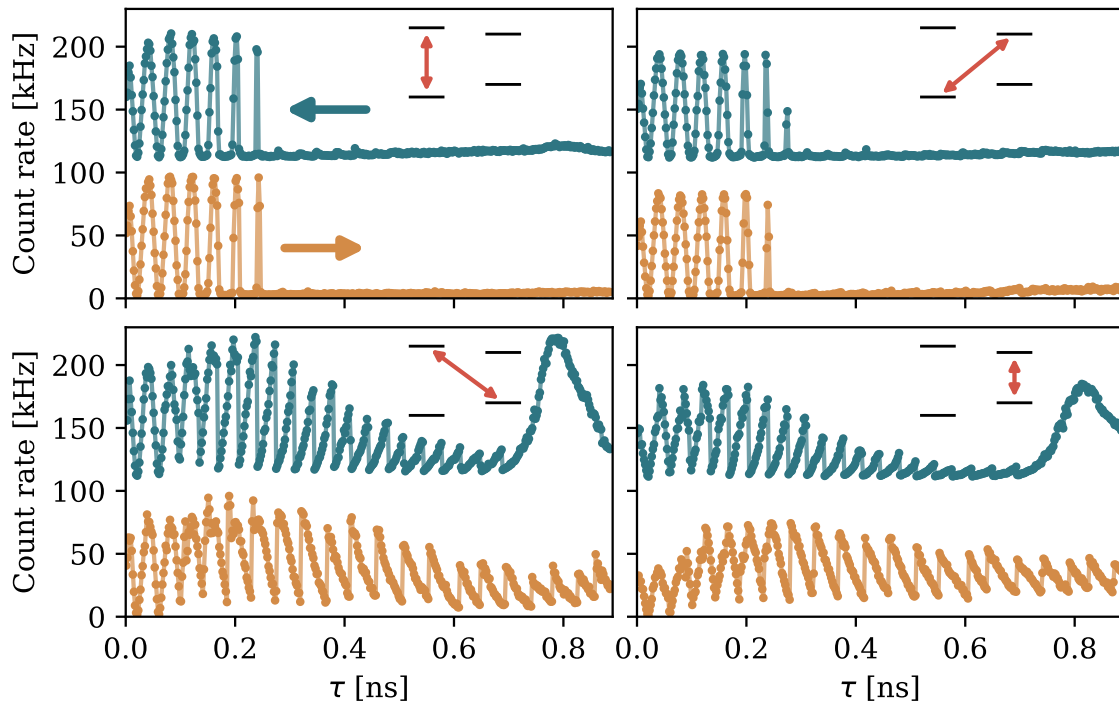


Fig. 5.2 **Transition dependent Ramsey interference** Measurement of Ramsey inference for all four transitions and both scanning directions at 4 T. The probed transition is indicated by the simplified schematics of the energy levels in each panel and the scanning direction of the relative pulse delay τ is displayed by the two arrows in the top left panel. The backwards scanning data (blue) has been offset for clarity.

Both behaviours have been encountered before [29, 162] and originate from the dynamic polarisation of the nuclear spins (DNSP) as a result of resonantly driving the optical transitions [109]. A non-zero polarisation of the nuclear spin bath will result in a change of the Overhauser field, which will change the transition frequency as well as the spin splitting. Therefore, our readout laser will be detuned and we drive the system less efficiently resulting in lower count rates and reduced fidelity for the initialisation of the spin. Furthermore, the initialisation of the spin state will also be influenced by the final spin population of the Ramsey sequence which is intimately linked to the changing spin splitting.

We observe that the different system responses are linked to the ground-state spin of the read-out transition similar to the case of (anti-)dragging of the resonance [107]. This shows that it is the electron spin that is causing the nuclear feedback and not the hole in the excited state. The signal shows signs of dragging when the readout is on the low energy transition while it appears to be ant dragged for the high energy transition. At first sight this behaviour is opposite to the one observed in experiments which resonantly drive one

of the trion transitions [107]. However, it can be explained by considering the effective two-level system in the ground-state manifold: the readout resembles a finite linewidth for one of the two electron-spin ground states, rendering it the effective excited state and the coherent rotations are driving the transition within this quasi two-level system. Now, the ladder picture introduced by Hoegle *et al.* [107], where we consider a detuning-induced imbalance in the bidirectional nuclear spin diffusion, fully explains the observed behaviour in the same fashion as (anti-)dragging.

In general, the signals we recover show that the electron picks up a non-trivial phase, closely linked to DNSP and the finite transition linewidth. For increasing τ the electron spin becomes increasingly sensitive to sub-linewidth nuclear polarisation and a feedback loop between electron spin and nuclear spin polarisation is formed. In their study of feedback between the nuclear bath and the electron spin, Ladd *et al.* [162] have developed a model based on the interplay of this mechanism and nuclear spin diffusion which is able to capture the sawtooth behaviour of the lower energy transitions, but does not explain the signature observed for the high energy transition.

5.1.3 Suppression of nuclear polarisation

Dynamic nuclear spin polarisation is an interesting effect specific to these mesoscopic systems and a research area in its own right. However, for our experiments it is an undesirable effect keeping us from accessing the coherent dynamics of the spin.

One way we can access the whole FID without any disturbance due to DNSP is to reset the polarisation of the nuclear bath for every measurement. This is a method that has been investigated by Robert Stockill and Claire Le Gall and has been proven to be very successful. The depolarisation of the nuclear spins is achieved through modulation of the DC bias applied to the gated sample. By going to the cotunneling region of the charging plateau a significant speedup of nuclear depolarisation can be achieved [64]. However, this method is still very time consuming as the depolarisation takes tens of milliseconds, whereas we will lose the signal for longer delays within hundreds of microseconds. A successful measurement of the FID required a measurement sequence where the readout window accounted for $\ll 1\%$ of the measurement time, reducing the integrated count rate to single Hz instead of tens of kHz. This reduction in photon counts results in larger errors of the extracted quantities, a problem that will be even more pronounced for more complicated multipulse decoupling sequences which require lower repetition rates.

It would thus be advantageous to avoid the polarisation of the nuclear spin bath to begin with. We introduce a new measurement method allowing us to strongly suppress any build-up of nuclear polarisation, enabling an efficient measurement of the full electron FID.

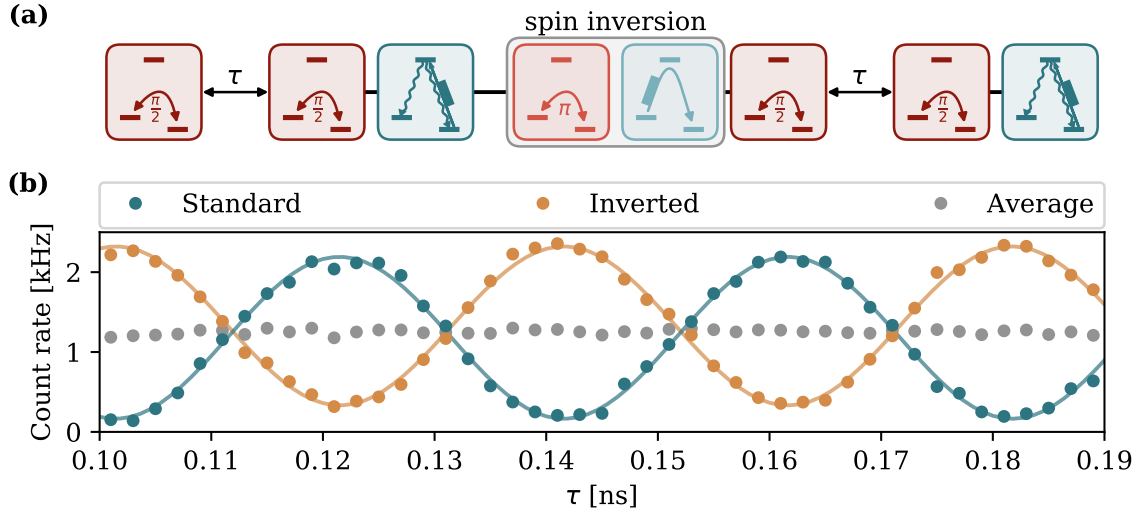


Fig. 5.3 **Alternating pulse sequence** (a) Schematic of the Ramsey sequence with alternating initial spin state. The inversion (grey box) is realised by using a π rotation (light red), spin-pumping via the excited state (light blue) or a combination of both. (b) Count rates from a time-resolved measurement. The average (grey) is clearly independent of τ , whereas we recover the full visibility by selecting the data corresponding to the either initial spin state.

We have seen that the polarisation of the nuclear bath depends on the initial electron spin state. However, the nuclear bath dynamics are slow compared to the repetition rate of our experiment and the nuclear spins are affected by the time-averaged signal only. Here, we introduce a measurement sequence where we invert the initial spin population every other repetition. The two spin states precess 180° out of phase and thus the average signal does not acquire any phase.

Experimentally, this is realised through the pulse sequence depicted in Fig. 5.3 (a). The standard Ramsey sequence consisting of two $\pi/2$ pulses (dark red) separated by a variable delay τ and a readout and initialisation pulse (dark blue) on the high-energy transition is followed by a second Ramsey sequence with an initial spin-state inversion (grey rectangle). The inversion can be realised through a coherent π rotation (light red), incoherent spin-pumping via the excited state (light blue) or a combination of both. In this way we will run the experiment with alternating initial spin states and the average signal will be independent of τ . Here, we are only considering one of the two Λ -systems and neglect the second excited state which is well detuned in energy. Through time-resolved measurements we can extract the count rates corresponding to the two initial spin states separately and thus recover the Ramsey fringes as presented in 5.3 (b). We can see that both signals are indeed completely out of phase and the average signal is independent of the delay. The count rate is lower compared to the measurements presented in Fig. 5.2 since the implementation of this slightly

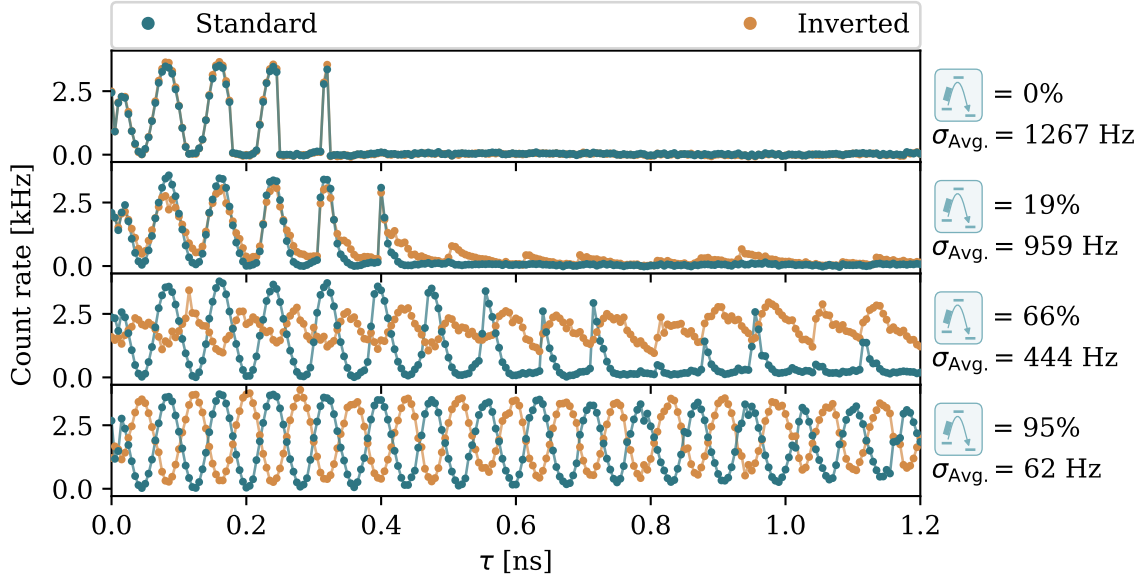


Fig. 5.4 **Ramsey dependence on inversion** Ramsey interference fringes for increasing amount of spin inversion (top to bottom) through changing the laser intensity on the low-energy transition. An estimate of the amount of spin inversion is given on the right-hand-side together with the standard deviation of the average signal for the first full fringe.

more involved pulse sequence requires a reduction of the repetition rate. In contrast to the earlier measurements, we are now pulse picking the mode-locked laser and only work with part of the available rotation pulses. Furthermore, we introduce a second laser resonant with the lower-energy transition in order to invert the electron spin to the $|\uparrow\rangle$ state. All voltage pulses for the pulse-picking and derivation of pulses from the CW lasers are now provided by a combination of digital delay generators triggered by the mode-locked laser.

The effect of this alternating sequence is showcased in Fig. 5.4, where we vary the intensity of the laser driving the low-energy transition and thus the amount of spin inversion. The four panels show the measured Ramsey fringes with increasing laser intensity, where estimates of the corresponding amount of spin inversion are given on the right-hand-side, alongside the standard deviation of the average signal, $\sigma_{\text{Avg.}}$. As expected, we recover the trace measured in Fig. 5.2 when the inversion laser turned off (top panel). As the laser intensity increases, we start to recover the Ramsey fringes for longer delays and at 95% spin inversion we get equal and opposite fringes across the whole range of τ , evidenced by the strongly reduced standard deviation of the mean. This is clear evidence that we can suppress the formation of nuclear polarisation and recover the electron spin dynamics.

We still recover signatures of a small amount of residual nuclear polarisation for long delays, $\tau > 1$ ns, where the signal starts to deviate from a sine curve. This can be understood

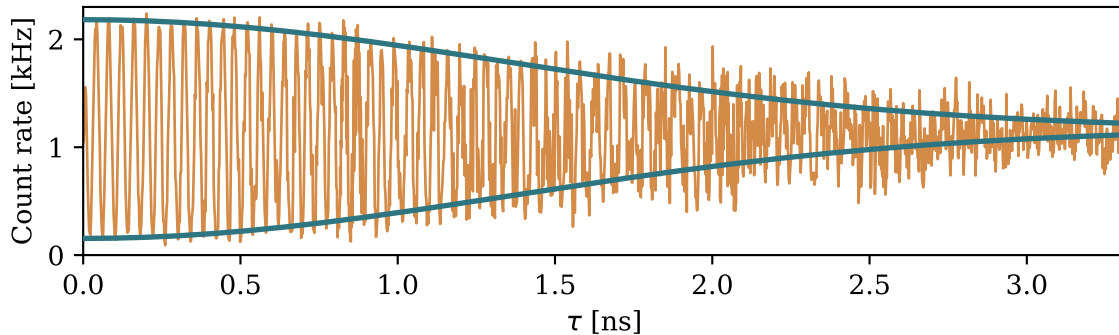


Fig. 5.5 **Free induction decay** Full electron spin FID recorded with an alternating Ramsey sequence (orange). Here, we only show the data without spin inversion. Blue solid curves represent a Gaussian decay envelope with $T_2^* = 1.93 \pm 0.03$ ns, extracted from a Fourier analysis of the data.

considering that the spin-inversion laser is driving the low-energy transition which is unstable under DNSP [107], ultimately limiting the spin-inversion fidelity.

5.1.4 Free induction decay

In order to recover the full electron-spin FID, we combine the spin pumping with a coherent π rotation. The fidelity of the coherent rotation is limited mainly due to the external field (Sec. 2.3.3) and the subsequent spin pumping will transfer any residual spin population. Here, we benefit from the fact that most of the population is transferred by the coherent rotation and we thus drive the low-energy transition much less, leading to a more stable resonance condition. This way, we obtain a spin-inversion fidelity high enough to sufficiently suppress nuclear polarisation on the relevant timescales and recover the FID.

Figure 5.5 shows the result of our measurement and we extract the inhomogeneous dephasing time through a moving Fourier transform method. The fast Fourier transform (FFT) of the data contains a strong component at the Larmor-precession frequency (24.9 GHz). Through extraction of the integrated power of this component for a 0.5 ns window moving in steps of 50 ps across the whole data range, we recover the decay envelope of the Ramsey fringes. The decay of the integrated power can be fitted to $Ae^{-(\tau/T_2^*)^\alpha}$ and we extract $\alpha = 2.03 \pm 0.11$ and $T_2^* = 1.96 \pm 0.03$ ns. Correcting for a slight overshoot of the decay time introduced by the moving-window method we find $T_2^* = 1.93 \pm 0.03$ ns. This method allows us to accurately extract the dephasing time despite the residual nuclear polarisation for long delays, evidenced in the non-sinusoidal behaviour of the data. The small build-up of nuclear polarisation for $\tau > 1.2$ ns is most likely caused by low-frequency electrical noise in the

sample which leads to changes in the transition frequency. These changes are counteracted by nuclear polarisation since we are driving the dragged transition.

The Gaussian decay we observe is evidence for the quasi-static, large-amplitude noise of the nuclear spin bath. For the course of a single run of the sequence, the Overhauser field can be considered frozen, but the averaging of millions of runs means that we sample the whole spread of the Overhauser field distribution. Therefore, the measurement of the FID allows us to get a good estimate of the Overhauser field standard deviation, σ_{OH} [105, 154]:

$$\sigma_{\text{OH}} = \sqrt{6} \frac{\hbar}{g_e \mu_B T_2^*}, \quad (5.1)$$

where the prefactor of $\sqrt{6}$ is due to the Gaussian decay envelope ($\sqrt{2}$) and the fact that we consider the three-dimensional width of the Overhauser field ($\sqrt{3}$). Here we assume that the sensitivity of the electron spin is limited to the noise along the externally applied magnetic field. From the Larmor precession we extract an electron g-factor of $g_e = 0.44$ and we find $\sigma_{\text{OH}} = 32.3 \pm 0.05$ mT, consistent with previous measurements in similar samples [154, 163, 164].

5.2 Coherence time

The coherence time, T_2 , is obscured by the quasi-static noise that is dephasing our electron spin during the FID. Thus, we implement a Hahn-echo sequence [93, 165] which decouples the spin from the quasi-static components of the noise spectrum. The recovered electron coherence is now limited by the dynamics of the underlying noise spectrum and therefore serves not only as a probe of the electron coherence but also provides a valuable spectroscopic tool, which we can use to understand the dynamics of the nuclear spin bath.

5.2.1 Experimental method

The measurement is in close analogy to the Ramsey measurements performed before. However, we introduce an additional π rotation in the center of the two $\pi/2$ pulses [93]. This additional pulse will invert the spin state after an evolution of $T/2$ and therefore refocus any dephasing of the spin due to quasi-static noise which is correlated on time scales $\gtrsim T$. A schematic of the pulse sequence is given in Fig. 5.6. The two $\pi/2$ rotations are separated by T and encapsulate the additional refocussing pulse at $T/2$. The sequence is terminated by a pulsed readout on the high-energy transition (blue). As before, the initial spin-inversion step will only be applied for every other repetition of the pulse sequence and prevents the

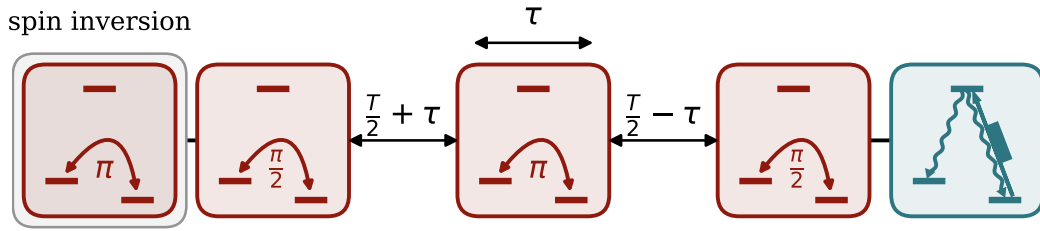


Fig. 5.6 **Hahn-echo sequence** Schematic of the alternating Hahn-echo pulse sequence. The spin inversion (grey box) is provided every other run of the sequence by a coherent π rotation. The Hahn-echo sequence consist of a π rotation separated between two $\pi/2$ rotations which are separated by T . At the end of the sequence the spin population is read out and initialised by driving the high-energy transition. We observe fringes by scanning the refocussing π pulse by $\tau \ll T_2^*$.

build-up of nuclear polarisation. In order to extract the coherence at each time T we vary the position of the central refocussing pulse by a delay $\tau \ll T_2^*$ leading to oscillation of the readout signal at twice the Larmor frequency. The fringe visibility follows a direct mapping of the coherence in the case of perfect rotations and thus, provides a good measure for a lower bound of the coherence. The external magnetic field, B_{ext} , is varied to investigate the field dependence of the coherence.

Experimentally, we split the output of the mode-locked laser and calibrate the pulse areas such that one arm corresponds to a $\pi/2$ rotation, whereas the other output provides π pulses. The pulses for the sequence are isolated using AOMs and we can scan the position of the π pulses using the motorised delay stage. The relative delay between the two outputs can be manually set to 0 or 6.6 ns, allowing us to record visibilities at even and odd multiples of the laser repetition rate; the separation of the $\pi/2$ pulses, T , is limited to multiples of the repetition rate. In order to avoid unintentional spin pumping during the Hahn-echo sequence, we derive the readout and initialisation pulse using a combination of an EOM centred within an AOM pulse, this way we are able to improve the on-off suppression ratio from ~ 300 to ~ 6300 . All voltage pulses are generated using digital delay generators which are synchronised to the repetition rate of the mode-locked laser.

Due to the decoupling sequence, the overall phase accumulated by the electron spin is smaller than in a FID measurement. Therefore, it is sufficient for these measurements to work with a single π rotation to provide the state inversion for the alternating sequence. This reduces the technical overhead and erases any errors due to unintentional excitation of the low-energy transition.

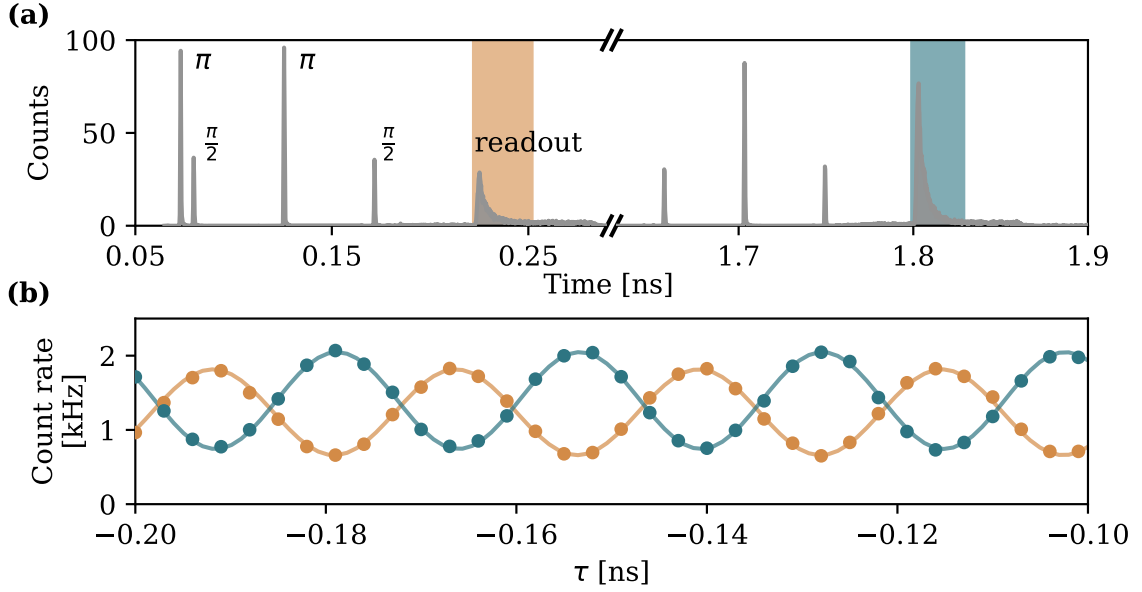


Fig. 5.7 **Hahn-echo pulse sequence histogram and visibility** (a) Histogram of the counts recorded for a measurement at $B_{\text{ext}} = 3\text{T}$ for $T = 91.2\text{ns}$. Due to laser leakage we can see the coherent-rotation pulses with different pulse areas, replicating the applied pulse sequence. The two coloured ROIs indicate the integration windows of the readouts. (b) Fringes recovered from the measurement shown in (a), colours match the ROIs. For the non-inverted signal (blue) we extract $V = 46.7 \pm 0.6\%$.

The detected photons are again recorded by a TDC, allowing us to distinguish between the two initial spin states. Figure 5.7 (a) shows a histogram of the recorded counts for $T = 91.2\text{ns}$ at $B_{\text{ext}} = 3\text{T}$. We can clearly see the residual laser leakage of the rotation pulses followed by the quantum dot fluorescence illustrating the pulse sequence. The coloured rectangles indicate the ROIs used to extract the count rates plotted in Fig. 5.7 (b). Here we recover the sinusoidal signal which oscillates at twice the Larmor frequency. The solid curves represent fits to the data which are used to extract the visibility. Here, we recover $V = 46.7 \pm 0.6\%$ for the non-inverted signal (blue).

5.2.2 Hahn echo

We investigate the decay of visibility in the Hahn-echo measurements by varying the inter-pulse delay, T , between 13.14ns and $1.2\mu\text{s}$ at external magnetic fields of 2-5 Tesla. The results are summarised in Fig. 5.8. The figure shows the full decay curves on the LHS and a zoom into the first 350ns on the RHS. The data are recorded in multiple scans of T at each field and the data points represent the average visibility recorded.

The coherence for $B_{\text{ext}} \geq 3$ T shows a linear increase with the external magnetic field up to $T_2 = 1709 \pm 24$ ns for $B_{\text{ext}} = 5$ T. The sub-unity visibility we recover even at $T \rightarrow 0$ can mainly be attributed to a field-dependent tilt of the spin-rotation axis, limiting the fidelity of our coherent rotations (Sec. 2.3.3). This reduces the visibility we can extract, which is no longer a direct mapping of the coherence, and limits the fidelity of the decoupling mechanism provided by the refocussing pulse. The inversion fidelity can be estimated through the ratios of the readout visibilities obtained for the two initial spin-states in the sequence and decreases with increasing magnetic field as the Larmor frequency rises accordingly. However, we can still extract T_2 from the decay of visibility with increasing T . The behaviour for $B_{\text{ext}} = 2$ T deviates strongly from the observations at higher fields as the visibility vanishes almost completely within the first 20 ns, followed by a weak revival around 125 ns.

Due to our alternating pulse sequence, we can rule out DNSP as cause for this behaviour and in fact, we observe similar, yet strongly suppressed signatures at higher fields, shown in the right panels of Fig. 5.8. The data exhibits an oscillatory behaviour for $T < 200$ ns, where, with increasing magnetic field, we observe a decrease in amplitude and an increase in frequency. This complex structure is captured by our model, represented by the solid orange curves and can be understood by considering the nuclear spin spectra filtered through the Hahn-echo sequence.

5.3 Model of Hahn-echo visibility

Through the Hahn-echo sequence we protect the spin coherence by filtering the Overhauser-field noise spectrum [166]. Therefore, we can use the obtained data to learn more about the underlying dynamics of the nuclear spin bath; we can use the Hahn-echo measurement as a spectroscopic tool to probe the nuclear spin dynamics. We can reproduce the general behaviour observed in our measurements by calculations of the nuclear spectra and subsequent application of a Hahn-echo filter function. Our approach follows the work of Cywinsky *et al.* [166].

5.3.1 Nuclear spectra

The dominating contribution to the nuclear noise spectrum in our samples is the Larmor precession of the nuclear spin bath which is altered by the quadrupolar coupling to inhomogeneous strain-induced electric-field gradients. For the calculation of the nuclear spectra we assume an ensemble of non-interacting nuclear spins and calculate the quantum evolution of a single nucleus considering a Hamiltonian that only contains the Zeeman and quadrupolar

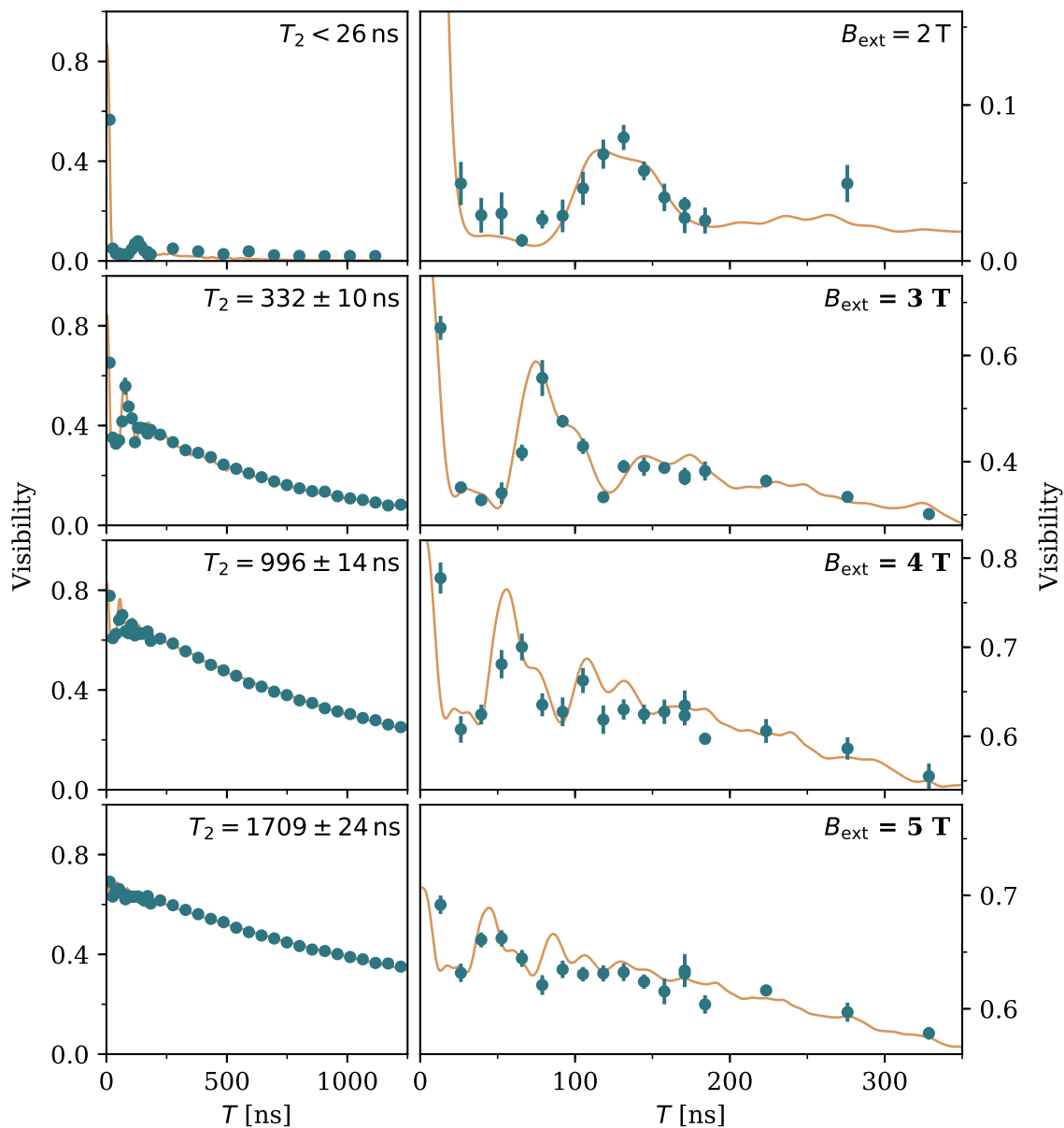


Fig. 5.8 **Hahn-echo visibility** Extracted visibilities (blue points) for different inter-pulse delays, T , and increasing magnetic field (top to bottom). The values are extracted from the measurement without initial spin inversion and error bars represent standard deviation of the mean. The coherence times are extracted from the exponential visibility decay. A zoom into the first 350 ns is given on the right-hand-side. The solid curves (orange) are the result of modelling the Hahn-echo sequence as a spectral filter for the nuclear spectra.

Electron Coherence

interactions. The single-spin picture is then generalised by sampling a Gaussian probability distribution of the quadrupolar energies and orientations, which accounts for the inhomogeneous spread of strain-induced electric field gradients in our samples. In a last step, we sum over the 4 different isotopes: Ga⁶⁹, Ga⁷¹, As⁷⁵, and In¹¹⁵.

The Zeeman energies of the nuclei differ significantly from the electron and we can thus decouple their dynamics. In this semi-classical picture the electron precesses around the magnetic field given by the vector sum of the external magnetic field and the Overhauser field [167]:

$$B_{\text{tot}} = |B_{\text{tot}}| = \sqrt{\left(B_{\text{ext}} + B_{\text{OH}}^{\parallel}\right)^2 + \left(B_{\text{OH}}^{\perp}\right)^2}, \quad (5.2)$$

where we split the Overhauser field into components parallel, $B_{\text{OH}}^{\parallel}$, and perpendicular, B_{OH}^{\perp} , to the external magnetic field, B_{ext} . We are working in a regime where we can safely assume $B_{\text{ext}} \gg B_{\text{OH}}$ allowing us to approximate B_{tot} by:

$$B_{\text{tot}} \approx B_{\text{ext}} + B_{\text{OH}}^{\parallel} + \frac{\left(B_{\text{OH}}^{\perp}\right)^2}{2B_{\text{ext}}}. \quad (5.3)$$

Thus, the energy-level splitting couples to $B_{\text{OH}}^{\parallel}$ and $\left(B_{\text{OH}}^{\perp}\right)^2$, and their dynamics can lead to dephasing of the electron spin. Assuming that the two Overhauser-field components are independent we can treat them separately and the final Hahn-echo decay will be the product of the two independent decays.

Therefore, we can decompose the spectrum into an on-axis and a transverse component and consider their effect separately. A third component is given by a constant, zero-frequency term, the origin of the suppressed coherence in the FID measurement and effectively filtered by the Hahn-echo sequence. The calculated spectra shown in Fig. 5.9 are based on parameters derived from atomistic calculations by Bulutay *et al.* [106, 168] with an indium concentration of 0.5. The two components of the spectrum show distinctive features which are broadened due to the inhomogeneous distribution of electric-field gradients. The inset in the left panel shows an example of the contributions of the nuclear spin species to the noise spectra. Here, we show the data for on-axis Overhauser-field fluctuations in a 2 Tesla external magnetic field. Overall, indium dominates the nuclear spin dynamics owing to its large spin quantum number, followed by arsenic which contributes the majority of atoms to the quantum dot, whereas the gallium isotopes play an insignificant role.

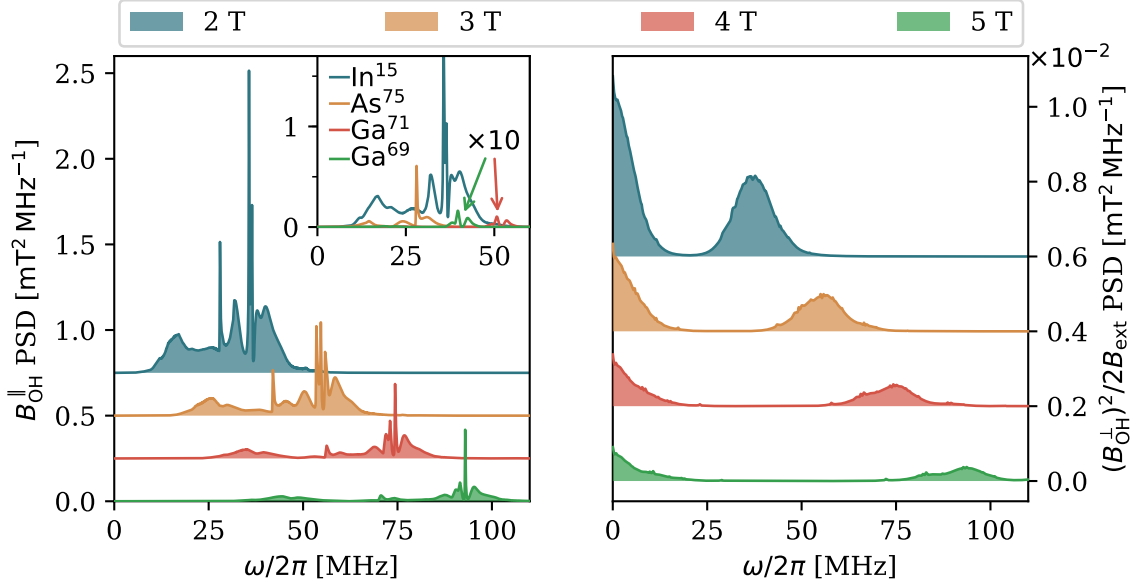


Fig. 5.9 **Nuclear spin noise spectra** Power spectral density (PSD) of the nuclear spin noise decomposed into the linearly-coupled, parallel (left panel) and quadratically-coupled, perpendicular (right panel) components. The inset in the left panel shows the contributions of the four isotopes to $B_{\text{OH}}^{\parallel}$ at a 2 T magnetic field.

$B_{\text{OH}}^{\parallel}$

The linearly-coupled Overhauser-field component arises due to the large inhomogeneous strain profile inherent to InGaAs quantum dots. Crucially, the tilt between the external magnetic field orientation and the effective quadrupolar-field axis enables parallel Overhauser-field components in the hyperfine interaction. The strain leads to a quadrupolar coupling strength which is equivalent to a ~ 1 T magnetic field and thus dominates at low external magnetic fields. For external fields ≤ 2 T the strong inhomogeneous broadening restrains the large amplitude term from any relevant rephasing. However, as we increase the magnetic field, the Zeeman-interaction term starts to dominate the nuclear dynamics, resulting in a reduced amplitude of the parallel component. This explains the strong pickup of coherence between 2 and 3 Tesla, where we also observe a partial rephasing, resulting in the oscillations observed at short times T in our visibility-decay measurements. As we go to higher fields, the frequency of the oscillations increases accompanied by a reduction of the amplitude due to the decreasing relative strength of the parallel component.

$$B_{\text{OH}}^{\perp}$$

The quadratically-coupled Overhauser-field component arises from the relative precession of the nuclei owing to different Larmor frequencies and is two orders of magnitudes weaker than the on axis noise. A multiplication in the time domain is identical to a convolution in the frequency domain and thus, we can represent the quadratic coupling by an auto-convolution in the spectral domain. Owing to the large spread of quadrupolar energies the convolution results in a broad-frequency shoulder continuously spread from $0 \sim 10$ MHz. This feature causes a loss of coherence without any revival and is responsible for the exponential decay, limiting the coherence at high external magnetic fields. Therefore, the inhomogeneity of the electric-field gradients limits the electron-spin coherence to the microsecond regime, determined by the Overhauser-field strength. The coupling scales inversely with the external magnetic field which causes a reduction of the amplitude with increasing field and results in a linear increase of coherence time.

5.3.2 Delay-dependent Hahn-echo visibility

Above, we have discussed qualitatively the nuclear-noise spectra and their effect on the electron-spin coherence. In a next step, we calculate the dependence of the Hahn-echo visibility on the inter-pulse delay, T , based on these spectra and following a filter-function approach [166]. For this approach, we assume that both Overhauser-field components can be treated as Gaussian noise sources. In general, this is not given for the quadratically coupled component [169]. However, in the case of InGaAs quantum dots we can justify this approach since the correlation time of the noise is much shorter than T [170].

In order to get visibility decays that are comparable to our measurements we require Overhauser field standard deviations of 40 mT and 28 mT for the parallel and perpendicular components, respectively, which agrees with the value of 33 mT extracted earlier from the FID decay. We also introduce a field-dependent scaling factor for the maximum visibility at $T = 0$ to account for our imperfect rotations. The visibility decay extracted from filtering the spectra is given by the solid curves in Fig. 5.8. The model clearly captures the behaviour of our measurement data showing that the time-dependent electron spin coherence can indeed be explained by only considering the Zeeman and quadrupolar interactions of the nuclei.

As mentioned earlier, the final visibility decay is the product of the two contributions derived separately for each spectrum. In Fig. 5.10 we show the Hahn-echo decay divided into the two contributions for all measured fields. The curves illustrate the effect each component has on the electron spin coherence. Here, we can also clearly see the reduced initial visibility to take into account due to our limited rotation fidelity.

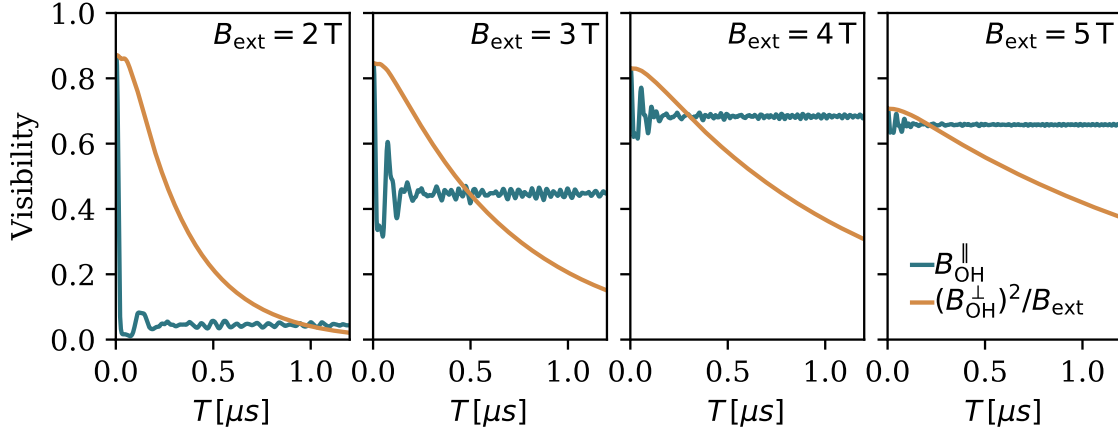


Fig. 5.10 **Hahn-echo decay components** The Hahn-echo decay is separated into the two Overhauser field contributions. The parallel component leads to a smooth, exponential decay (orange curve), whereas the transverse component results in oscillations of visibility which are strongly suppressed with increasing magnetic field. The visibility at $T = 0$ is reduced as a result of imperfect rotations.

Using the same parameters as for the curves describing our measurements we can calculate the nuclear-noise spectra for a wide range of fields and extract the corresponding Hahn-echo visibilities. At higher external magnetic fields we find that the visibility decay approaches a single exponential and the short-time oscillations are completely suppressed. The coherence time follows the expected linear increase with a gradient of about $0.7 \mu\text{sT}^{-1}$, reaching more than $5 \mu\text{s}$ at 10 T. This behaviour is confirmed by a measurement of a different quantum dot at $B_{\text{ext}} = 7 \text{ T}$, where we find $T_2 = 2.70 \pm 0.04 \mu\text{s}$.

5.4 Discussion of results

The introduction of an efficient way to strongly suppress the build-up of nuclear polarisation allowed us to measure the full FID of the electron spin, decaying with $T_2^* = 1.93 \pm 0.03 \text{ ns}$. Our scheme allows for a significantly reduced measurement time compared to the repeated removal of nuclear polarisation, which is an inherently slow process. Simultaneously to our work other groups have investigated different ways to study the electron spin coherence in a polarisation-free environment [55, 154].

Furthermore, the new technique enabled us to extend the spin coherence to the microsecond regime through employment of a Hahn-echo sequence - a regime in which heralded spin-spin entanglement could be realised. The extracted visibilities show a non-trivial dependence on the external magnetic field and we can use the measurements to gain insight

into the evolution of the electron spin in the presence of a nuclear spin bath. We find that the coherence is intrinsically limited by quadrupolar coupling of the nuclear spins to the inhomogeneous electric-field gradients. These gradients are inherent to the growth of InGaAs quantum dots and lead to an irreversible loss of coherence through broadening of the nuclear noise spectra. Bechtold *et al.* have reported similar results [154], however the pick-up of coherence already takes place at fields of 1-2 T. Together with the lower wavelength (~ 940 nm) this points to a sample with lower Indium concentration and thus lower strain. A more quantitative comparison is frustrated by the fact that they only show normalised data.

The linear increase of T_2 we observe has also been reported by Press *et al.* for external fields of 2-4 T [95], however their data suggest a saturation of coherence at higher fields. The measurement of the coherence time at high fields is very sensitive to experimental imperfection and accidental spin pumping during the free evolution of the electron mimics a reduced lifetime T_1 , which would otherwise only be expected to play a role for fields $\gtrsim 10$ T [143, 144]. This could potentially explain the saturation at lower fields.

Experiments in electrostatically defined GaAs quantum dots have observed similar signatures as well, however the impact of quadrupolar broadening in these systems is limited [167, 171]. They benefit from the absence of indium and the deficiency of growth induced strain. In combination with the larger nuclear bath these characteristics allow for coherence times close to 1 ms [172].

One strategy to extend the coherence time beyond the limit of a simple Hahn echo experiment is the implementation of more complex, multi-pulse decoupling schemes. Such schemes have been successfully realised in electrostatically defined quantum dots [167, 172], NV centres in diamond [173, 174] or phosphorus donors in silicon [175]. These dynamic decoupling (DD) schemes rely on refocussing of the spin evolution, analogous to the Hahn-echo experiment and thus require inter-pulse spacings that are shorter than the typical dephasing time of the noise source [176]. The correlation time in our system is about 50 ns due to the spectrally broad nuclear spin dynamics. An implementation of a periodic dynamic decoupling (PDD) pulse sequence at $B_{\text{ext}} = 1.5$ T with up to 9 π pulses and an inter-pulse delay of 6.5 ns enabled us to push the coherence time from ~ 20 ns to more than 65 ns. However, further decoupling from the underlying nuclear spin noise is limited due to pulse imperfections. While improvements of the rotation pulse fidelity can be achieved through compound pulses (Sec. 2.3.3), the number of rotations will ultimately be limited by acoustic-phonon enabled excitonic dephasing [99].

Since the inhomogeneous broadening is directly related to the strain-driven assembly of our quantum dots, new growth methods and different materials could potentially lead to longer coherence times. This could for example be achieved by a system like II-VI quantum

dots, which benefit from the absence of quadrupolar nuclear moments [177], or through strain-free growth processes [178, 179]. In fact, optically active GaAs/AlGaAs quantum dots grown by strain-free droplet epitaxy have already shown notably different nuclear dynamics [180].

Changing the sample structure and composition of course presents a drastic step and will be accompanied with other difficulties such as different optical properties. There is one more promising route: a single heavy-hole spin in an InGaAs quantum dot. In principle, it should allow for longer coherence times owing to its p -like symmetry, which results in a vanishing amplitude of the wavefunction at the location of the nuclei and a reduced hyperfine interaction [51, 52]. In the next chapter we will study the coherence of a single hole spin in our samples and show superior performance in terms of coherence.

Chapter 6

Hole Coherence

"What we observe is not nature itself, but nature exposed to our method of questioning."

- Werner Heisenberg, [181]

In this chapter we study the coherence properties of a single hole spin as a promising alternative to the electron. Preliminary measurements [54, 182] and theoretical predictions [51] point towards high potential for a more coherent ground state which is beneficial for the implementation of a quantum network.

In the first section we show how we can use our n^+ -doped samples to study the spin of a single hole and take a brief look at the properties of holes with respect to their wavelength relative to the X^0 transition. In the remainder of this chapter we focus on the coherence properties of a single hole spin and the underlying noise spectrum, which we study with respect to the external magnetic field and different decoupling techniques.

This work has been done in close collaboration with Claire Le Gall, who started the work on holes together with me and later focussed on the modelling and theoretical analysis of the results, as well as Robert Stockill who joined me in the laboratory for the coherence measurements presented in this chapter. Most of this work has been submitted for publication [183].

6.1 Initial study of holes in our samples

In the absence of electrically clean p -doped samples our experiments have so far been based on the electron spin in InGaAs quantum dots. This work presents the first study of hole spins in our laboratory and we start with an initial investigation of the characteristics relevant for

our experiments. The experiments in this section are all performed without an externally applied magnetic field.

6.1.1 Photocreation of holes

The sample used in this chapter is based on the structure introduced in Sec. 2.2.1 and is identical to the ones used in the earlier chapters (3 - 5). This sample has been designed and fabricated to be able to deterministically load and host single electron spins by including a heavily n -doped layer providing a reservoir of free electrons. Similar designs incorporating a p -doped layer to provide an excess of holes often suffer from an increase in electrical noise compared to the n -doped samples. This effect is amplified by the electric-field dependent g -factor of the hole [184, 185], which leads to charge-noise induced spin dephasing [182]. Therefore, we rely on our electrically clean n -doped samples which can be optically loaded with a single hole spin. We note that recently there have been promising results on electrically cleaner p -doped samples which allow for deterministic charging through the applied gate voltage [54].

The PL spectra presented in the introduction (Fig. 2.6) show emission for the positively charged exciton, indicating that the quantum dot can host a single hole. However, with a negatively charged reservoir we need to optically create the hole, a process known as photocreation. The process is illustrated in Fig. 6.1 including the relevant energy levels and transitions for the measurements in Voigt geometry performed in this chapter. We choose a gate voltage corresponding to the charging plateau of the X^+ observed in PL and drive the X^0 transition for ~ 20 ns (orange arrow). Owing to the applied DC bias the electron tunnels out nearly instantaneously, leaving behind a single hole (grey arrow).

After successful initialisation of the hole charge we can perform experiments in the same manner as for the electron, where we selectively drive one transition of the Λ -system (light red arrow) to read out and initialise the spin state through the spontaneous decay of the excited state which again has a branching ratio of 50% resulting in on average 2 photons per readout (blue arrows). As before, rotations within the ground-state manifold are realised using red-detuned ps-laser pulses (dark red arrow) [94].

An open question was, how well we can drive the transition of the neutral exciton far away from its charge stability region and if we need to work close to the edge of the X^+ charging plateau in order to efficiently generate holes. Therefore, we measure the saturation of the X^+ count rate depending on the X^0 -drive power. For the measurements presented in Fig. 6.2 we fix the power of the X^+ drive to $\sim 18 \times P_{\text{sat}}^{X^0}$, where $P_{\text{sat}}^{X^0}$ denotes the X^0 saturation power measured at a gate voltage $V_g = 50.9$ mV (grey data) - well within the charging plateau of the neutral exciton. The high power ensures that we are saturating the transition of the positive

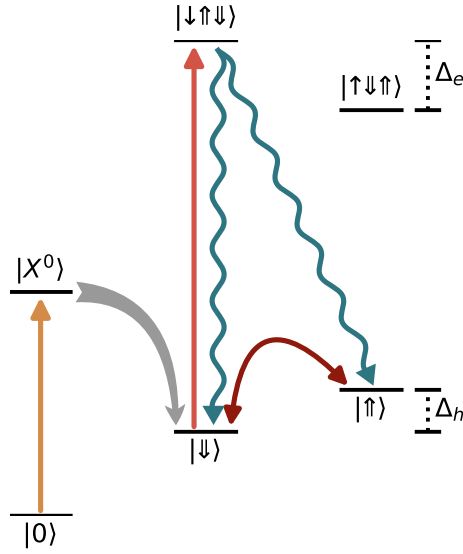


Fig. 6.1 **Photocreation of holes** Energy level scheme for X^0 and X^+ in Voigt geometry illustrating the process of photocreating a hole: The DC bias of the sample is chosen such that the electron of the neutral exciton created by a laser pulse on the X^0 transition (orange arrow) tunnels out nearly instantaneously leaving behind a single hole spin (grey arrow). Experiments are then carried out using the readout and initialisation laser (light red arrow) as well as the red-detuned rotation laser (dark red arrow).

trion, while we measure the corresponding fluorescence for different X^0 -drive powers. We repeat the measurements at different gate voltages, representing different positions within the charging plateau. The X^0 transition shows fluorescence down to $V_g = 43$ mV and therefore lower gate voltages correspond to an increase in the distance to the charge stability region of the neutral exciton. The solid curves are fits of the saturation function to the data and the extracted saturation powers are given in the inset. The data show, that, despite the slight increase of P_{sat} with reduced gate voltage, we can efficiently initialise the hole charge across the whole charging plateau of the positive trion. Further, the amount of X^0 power needed to saturate the count rate from the X^+ transition is below the saturation power of the X^0 transition across the whole range of gate voltages. Thus, the average lifetime of the hole charge is exceeding the excited state lifetime. However, the difference in power lies within an order of magnitude, motivating further investigations of the charge lifetime in time-resolved measurements.

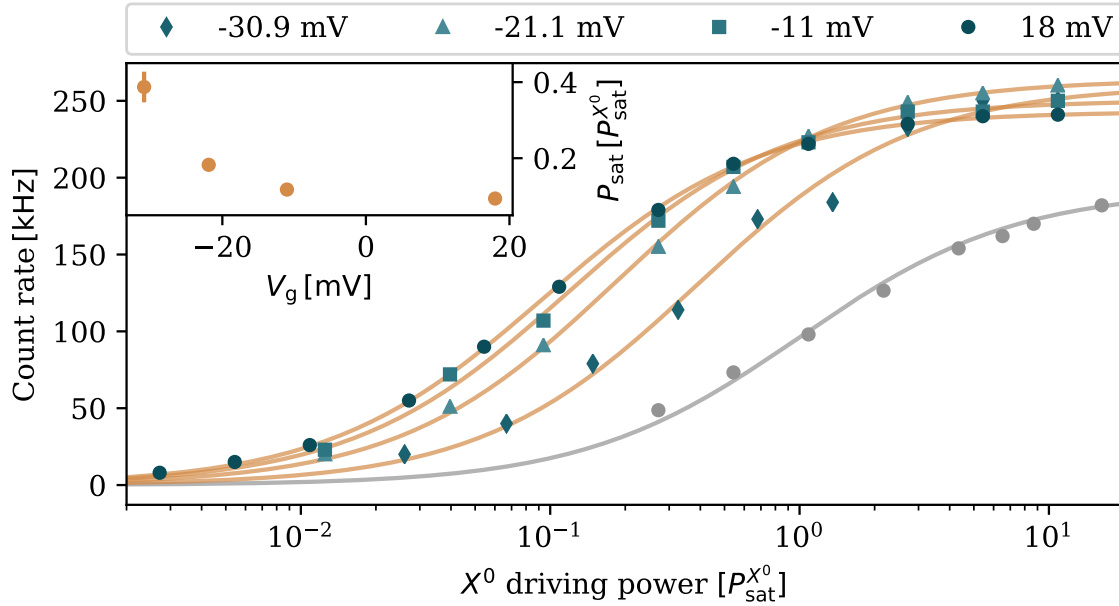


Fig. 6.2 **Gate-voltage dependent saturation of hole occupation** Count rate of the X^+ transition as a function of the photocreation-laser power, resonant with the X^0 transition, measured for different positions on the charging plateau. The X^+ transition is driven at $\sim 18 \times P_{\text{sat}}^{X^+}$ and the charging plateau of the X^0 transition ends at ~ 43 mV. The inset shows the saturation power for the different measurements. Powers are measured relative to the saturation of the X^0 transition $P_{\text{sat}}^{X^0}$ measured at 50.9 mV, shown in grey. Error bars represent ± 1 standard deviation.

6.1.2 Charge lifetimes

The energy of the positive trion with respect to the neutral exciton varies strongly across different quantum dots and we can find both red and blue detuned transitions. Therefore, we investigate the charge lifetime of the hole, T_1^{Charge} , through time-resolved measurement for a range of different quantum dots.

For these measurements, we apply a constant drive on the X^+ transition and we measure the decay of fluorescence following a 20 ns pulse on the neutral exciton transition to load the quantum dot with a single hole spin. We then fit the exponential decay of the fluorescence signal to extract the $1/e$ value. A range of measurements for four different quantum dots is presented in Fig. 6.3.

A first result is that T_1^{charge} strongly depends on the power of the drive on the X^+ transition: The lifetime increases for a decrease in power which is specified relative to the saturation power of the transition. In other words, the measurements indicate that the lifetime is linked to the excited state population, which we confirm through a measurement where we keep the

drive power fixed and detune the quantum dot by changing the gate voltage. We measure an increase in lifetime with detuning of the quantum dot transition confirming that it is indeed the excited state population and not the laser itself that causes the loss of charges.

These observations can be explained by Auger processes [186–188], where an electron-hole pair recombines non-radiatively by transferring the energy to a third charge in the form of kinetic energy. In the case of the X^+ the energy would be transferred to the second hole in the trion state which would leave the quantum dot due to the additional momentum, resulting in an empty quantum dot. This process is especially relevant and well studied for collidal quantum dots [189–191] and has recently also been studied in InGaAs quantum dots [192].

A second observation is a correlation of lifetime and detuning from the X^0 transition. The data can be approximated by:

$$T_1^{\text{Charge}}(P) = \frac{A}{1 + P c^{-1}} + T_\infty \quad (6.1)$$

shown as solid curves in Fig. 6.3 and we can extract the asymptotic behaviour: $T_1^{\text{Charge}}(P \rightarrow \infty) = T_\infty$ and $T_1^{\text{Charge}}(P = 0) = A + T_\infty$. The extracted values are shown in the inset for the corresponding detuning of the X^+ transition from the neutral exciton, where $T_1^{\text{Charge}}(P = 0)$ and $T_1^{\text{Charge}}(P \rightarrow \infty)$ are represented by filled circles and triangles, respectively. A possible reason could be the stronger confinement of the exciton leading to lower energies of the X^+ transition and a more stable excited state.

We note, that we have seen a quantum dot with a red-detuned X^+ transition which was particularly noisy and showed lifetimes similar to the ones observed for the blue detuned quantum dot shown here. However, based on the noise we assume that there was a nearby charge trap, which influenced the quantum dot characteristics.

The charge-lifetime measurements performed here, show that the holes in our sample will be suitable for spin-coherence studies. For these measurements, excited state population mainly occurs during the spin-initialisation and readout, which requires on average the absorption of two-photons. Thus, charge loss through the Auger process will be negligible. Moreover, we choose to work with quantum dots which are red-detuned from the X^0 transition to work with more stable excited states.

6.1.3 Phonon-assisted processes

In a last step of the initial characterisation of hole spins in our sample, we examined the RF on the spectrometer, mainly driven by the fact that we observed X^+ emission for blue-detuned transitions even in the absence of photocreation. In general, X^0 and X^+ are typically $\gtrsim 250$ GHz apart, compared to $k_B T \sim 100$ GHz at 5 K. The process of phonon absorption

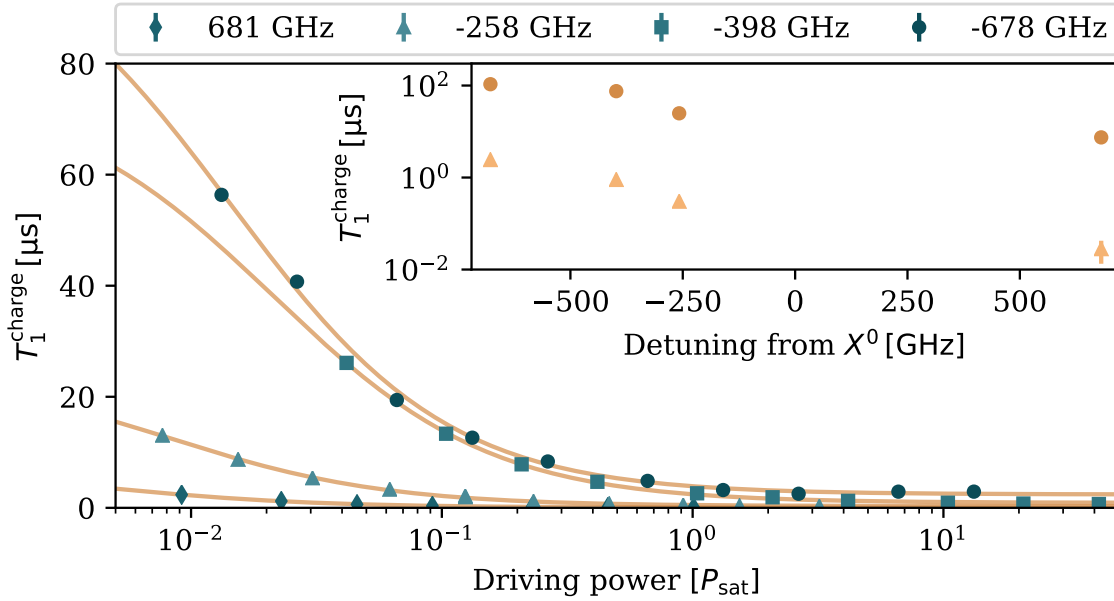


Fig. 6.3 **Power-dependent charge lifetime** Power dependent charge lifetime for four quantum dots with different detuning of the X^+ transition from the neutral exciton. The inset shows asymptotic values of T_1^{Charge} where filled circles (triangles) represent zero (infinite) drive strength. Errorbars represent ± 1 standard deviation.

is directly proportional to the phonon occupation number, n , which is given by the Bose-Einstein distribution, whereas phonon emission is proportional to $n + 1$. Thus, at these temperatures, phonon emission is the dominant process which is also evidenced in the highly asymmetric phonon sideband [142, 193, 194].

Figure 6.4 shows spectra for measurements on a quantum dot with blue- (left panel) and red-detuned (right panel) transition of the positive trion. The spectra are recorded driving either the X^0 or the X^+ transitions as well as both transitions while keeping the drive strength constant. The measurements are corrected for the laser background by subtracting a reference measurement where the quantum dot is tuned off resonance.

For the measurement of the quantum dot with blue-detuned X^+ transition (left panel) we observe emission at both frequencies when only driving the X^+ transition (blue). This process is enabled by phonon-assisted excitation of the X^0 transition leading to emission at the corresponding frequency as well as the creation of holes which allow for emission at the X^+ frequency. In the case where we only drive the X^0 transition we only observe emission at the corresponding frequency since any hole that is created will be trapped in the ground state for microseconds and phonon absorption is unlikely due to the combination of the strong

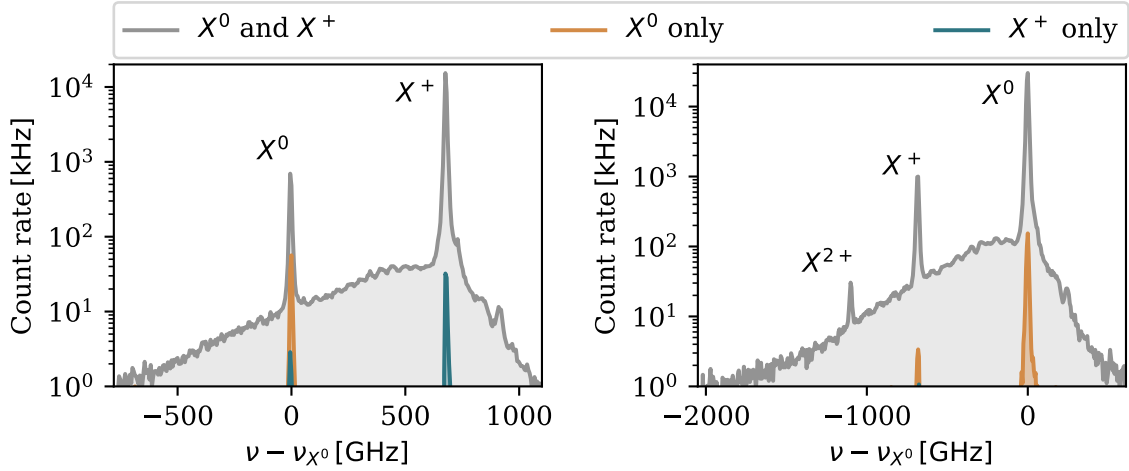


Fig. 6.4 **Resonance fluorescence spectra** Spectra of the quantum dot emission for resonantly driving the X^0 and X^+ transitions both individually and together. The left (right) panel shows the spectra of a quantum dot with a blue-detuned (red-detuned) X^+ transition, where the x-axis is given by the frequency relative to the X^0 transition.

blue shift and the low temperature. If we drive both transitions we recover emission at the two transition frequencies as well as a spectrally broad phonon sideband.

In contrast, for the quantum dot with red-detuned X^+ transition (right panel), we do not observe any emission if we only drive the transition of the positive trion as there is no hole to populate the ground state and driving of the X^0 transition would require absorption of phonons which again is strongly suppressed at the required frequency. However, we observe phonon-assisted emission at the X^+ frequency while only driving the X^0 transition. Driving both transitions, we again observe emission corresponding to the two driven transitions as well as emission at the X^{2+} transition frequency on top of the broad phonon sideband.

In our experiments we use a holographic grating to filter the emission spectrum and only collect photons at the X^+ frequency. For our spin-coherence measurements, we pulse the hole photocreation in order to minimise the background contribution of phonon-assisted emission from the X^0 transition at the X^+ frequency.

6.2 Inhomogeneous dephasing time

The importance of the inhomogeneous dephasing time T_2^* for the quality of spin-photon entanglement is apparent in the entanglement experiment presented in Chapter 3. As in most cases, it is not so much the exact value that can be achieved, but the relative scaling of T_2^* with respect to the other time scales involved in spin-photon entanglement. We have seen in

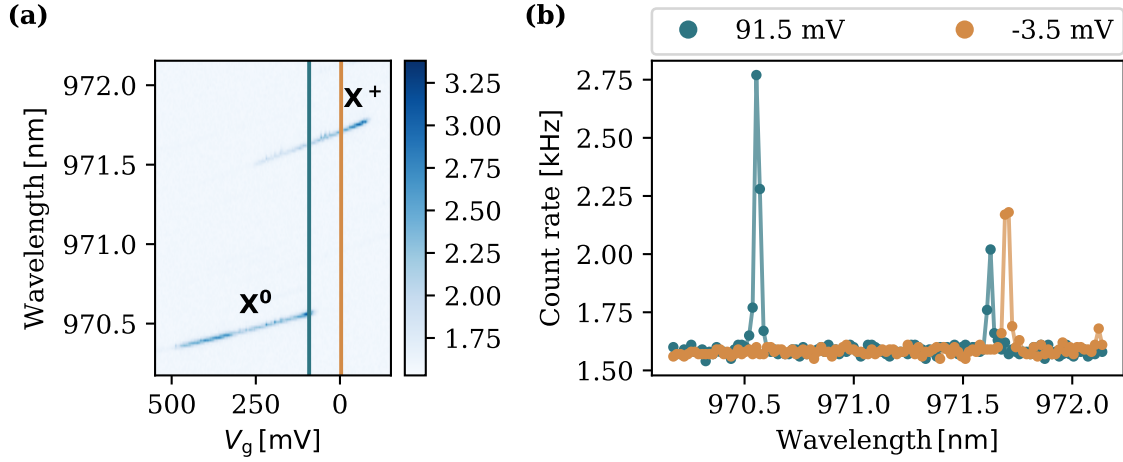


Fig. 6.5 **Photoluminescence spectrum** (a) Two-dimensional PL map of X^0 and X^+ transition for the studied quantum dot. The figure is a zoom in of the data presented in Fig. 2.6. (b) PL spectra for different gate voltages corresponding to the lines shown in (b).

Chapter 5 that in the case of the electron T_2^* is on the same order of magnitude as the optical lifetime $\Gamma^{-1} \approx 0.7$ ns, which characterises the spin-photon state transfer. This is one of the key areas where the hole spin is thought to be superior to the electron and initial indirect measurements through CPT support this claim with indications of $T_2^* \geq 100$ ns [54, 182]. Direct transient measurements of the free induction decay, however, could only reach T_2^* of up to 26 ns [53, 55, 94, 195]. The dominating mechanism limiting those dephasing times has been suggested to either be nuclear spin noise or electric charge fluctuations [54, 94, 182, 195], showing that the understanding of the governing mechanism is still lacking. Here, we study the dephasing of the hole spin with respect to the external magnetic field, allowing us to identify a cross-over from nuclear spin to electrical noise dominated dephasing.

6.2.1 Experimental method

Coherent control of the holes works in exactly the same way as for the electron [94] and thus the experimental setup is analogous to the work presented in Chapter 5. However, we have to optically reload the quantum dot once the charge is lost by introducing a low power laser pulse resonant with the X^0 transition. In our experiments, we typically apply such a charge reinitialisation pulse every 20 repetitions of the measurement sequence to ensure that we have a hole present for most of the time.

The PL spectra of the quantum dot used for the remainder of this chapter is presented in Fig. 6.5 (a), where we present a two dimensional PL map of the relevant transitions. In Fig. 6.5 (b) we present two PL spectra corresponding to different gate voltages indicated by the

vertical lines in (a). For gate voltages around 90 mV we can observe both transitions due to the non-resonant charge creation. However, during our experiments we work at gate voltages just below zero to ensure that we have a stable charging configuration. Depending on the exact external magnetic field we drive the X^+ resonantly at ~ 971.6 nm, while the optical initialisation of the hole is typically around 970.4 nm.

Contrary to the common assumption that the hyperfine interaction with the nuclei can be neglected for the hole spin we do observe signatures of feedback between the nuclear spin environment and the hole spin in our measurements of Ramsey interference. We therefore use the technique introduced for the electron (Sec. 5.1.3) to prevent nuclear polarisation through alternating initial spin states. As depicted in Fig. 6.6 (a), the spin inversion is achieved by an additional π rotation after the spin repumping for every other measurement. The effect of this measurement sequence is presented in Figure 6.6 (b) and (c), where we show exemplary Ramsey fringes for measurements at 4 Tesla starting at 0 ns and 13.14 ns, respectively. Initially, we measure the Ramsey interference fringes without any effort to prevent nuclear polarisation (i.e. no spin inversion) represented by the orange data. Similar to the electron, we recover non-sinusoidal signals particularly evident for the longer delay (Fig. 6.6 (c)), which approaches a square wave. Through implementation of the measurement sequence with alternating initial spin states we recover the sinusoidal oscillations in the measurement signal, demonstrated by the blue data which represent the signal from the non-inverted part of the sequence.

It is important to note, that the delay of 13 ns presented in Fig. 6.6 (c) is an order of magnitude longer than the dephasing time of the electron. Therefore, while we do get feedback between the hole and the nuclear spin bath, it is much weaker than for the electron where we already get significant feedback for hundreds of picoseconds (Sec. 5.1.2). However, the increase in T_2^* necessitates measurements for much longer delays, hence suppressing the build-up of nuclear spin polarisation is still important here.

Owing to the imperfect spin rotation the measured signal still deviates from a clean sinusoidal oscillation as can be seen in Fig. 6.6 (c) and with increasing delays and correspondingly decreasing visibility it becomes difficult to reliably extract the visibility through fitting of a sinusoidal function. In fact, for long delays the signal tends towards the extrema of the Ramsey fringes similar to the square wave behaviour of the non-protected measurement (orange) in Fig. 6.6 (c). Therefore, the measurement only gives reliable data for the maximum or the minimum of the Ramsey fringes and we rely on the extraction of the Ramsey decay envelope based on the measured extrema. Further, we subtract the mean of the data to account for fluctuations in the count rate caused by intensity fluctuations or slight changes in the background suppression.

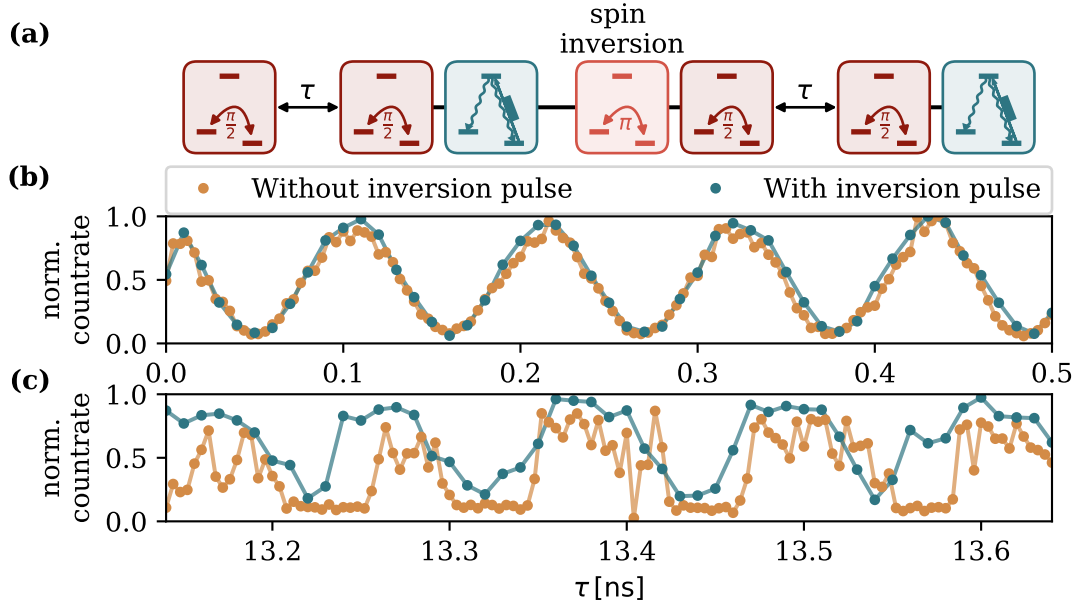


Fig. 6.6 **Hole spin Ramsey** (a) Schematic of the pulse sequence including a spin inversion for every other measurement. (b) and (c) Measurements of Ramsey interference at $B_{\text{ext}} = 4\text{ T}$ with (blue) and without (orange) alternating initial spin state for delays of $0 - 0.5\text{ ns}$ and $13.14 - 13.64\text{ ns}$, respectively.

6.2.2 Magnetic-field-dependent inhomogeneous dephasing time

Figure 6.7 shows the decay of Ramsey-interference fringes measured for magnetic fields in the range of $1\text{ T} \leq B_{\text{ext}} \leq 8\text{ T}$. In order to extract the dephasing time T_2^* the data are fitted with a decay function, $V(\tau) = a + b \times \exp((-\tau/T_2^*)^2)$, represented by the solid curves. The constant a is included to account for an offset between two datasets of opposite initial spin states caused by the imperfect spin inversion. This offset leads to non-zero values at long delays which do not correspond to coherence. In general, this contribution is small and does not hinder us in extracting the dephasing time. The top right panel shows an exemplary measurement trace used to extract the height of the Ramsey interference fringes for $B_{\text{ext}} = 3\text{ T}$ and $\tau \sim 26.5\text{ ns}$.

A summary of the extracted dephasing times is given in Fig. 6.8, showing an order of magnitude improvement of T_2^* compared to the electron across the whole range of external magnetic fields [161, 196] (see also Chapter 5). Initially, we observe an increase of T_2^* with the external field for values up to $B_{\text{ext}} = 4\text{ T}$, where it peaks at $T_2^* = 70 \pm 7\text{ ns}$. Subsequently, we measure a decay of T_2^* proportional to $1/B_{\text{ext}}$ which is indicated by the dotted curve in Fig. 6.8. This shows that the dephasing time at higher fields is dominated by electrical noise induced inhomogeneous dephasing, which has been suggested by Houel *et al.* [182]. The

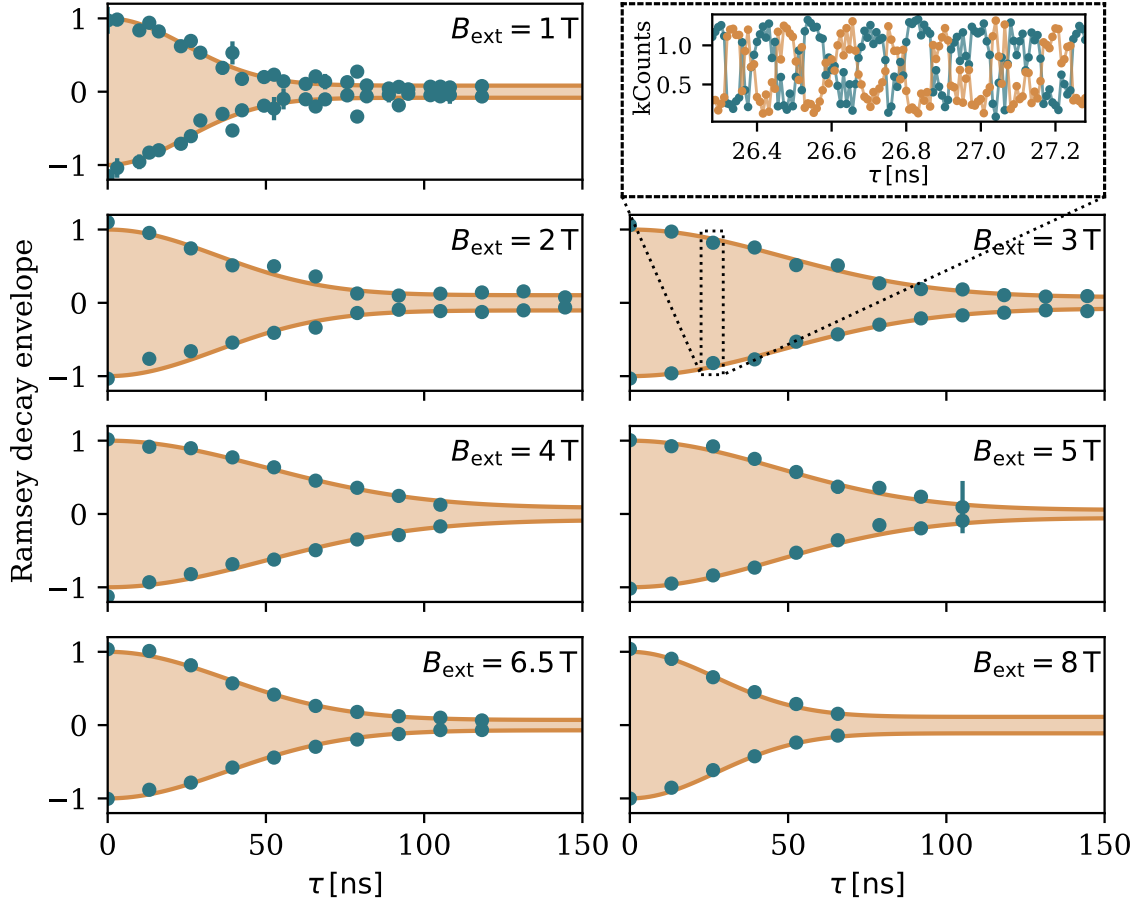


Fig. 6.7 **Ramsey interference decay for different magnetic fields** Measurements of the Ramsay interference decay envelope for external magnetic fields of 1 T to 8 T as indicated in the top right corner of each panel. The solid curves are fits to the data to extract the inhomogeneous decay time. Error bars represent ± 1 standard deviation. The top right corner shows the data used to determine the Ramsey fringe height at $\tau \sim 26.5$ ns and $B_{\text{ext}} = 3$ T

underlying mechanism can be understood by considering the energy fluctuations that can be caused by the charge noise. The electric field F_z applied along the growth axis shifts the exact position of the hole wavefunction within the quantum dot. This leads to a change of the in-plane hole g-factor, g_h^x , due to a gradient in the indium concentration [197], which is measured to scale linearly with the applied electric field, $g_h^x \propto F_z$ [184, 185]. Therefore, electrical noise δF_z in the sample directly affects the ground-state Zeeman splitting:

$$\delta E_Z^{\text{elec}} = \frac{\partial g_h^x}{\partial F_z} \delta F_z \mu_B B_{\text{ext}}. \quad (6.2)$$

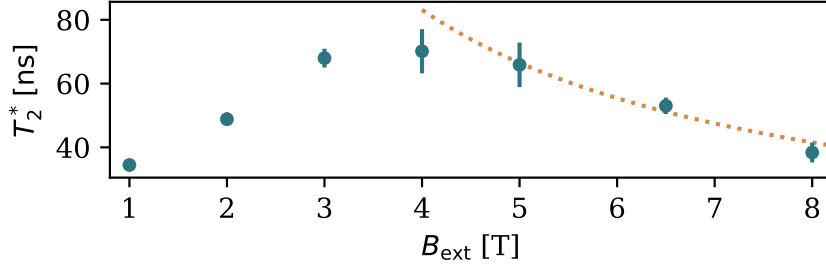


Fig. 6.8 **Magnetic-field-dependent inhomogeneous dephasing time** Summary of the inhomogeneous dephasing times extracted from the Ramsey decay envelopes. The dashed curve indicates a $1/B_{\text{ext}}$ dependence and error bars represent ± 1 standard deviation.

The inhomogeneous dephasing time is inversely proportional to those energy fluctuations and we find that $T_2^* \propto 1/(\delta F_z B_{\text{ext}})$. We note that we can safely neglect spin-orbit interactions, which could limit T_2 and thus T_2^* through T_1 [198], due to the slow spin relaxation of about $20 \mu\text{s}$ measured in our experiment. This value is comparable to the hole spin relaxation measured in an ensemble of self-assembled InGaAs quantum dots [199].

In the low field regime the dephasing time T_2^* scales linearly with the external magnetic field. This behaviour has been predicted for pure heavy-hole spins as a direct result of the long-range dipole-dipole coupling between the hole spin and the z -component of the surrounding nuclear spins [51, 104]. However, due to strain and geometric anisotropy we do not have a pure heavy hole (i.e. $\beta > 0$). In general, the hole spin experiences a magnetic field given by $\mathbf{B} = \mathbf{B}_{\text{ext}} + \mathbf{B}^{\text{nuc}}$ leading to a Zeeman ground-state splitting of $E_Z = g_h \mu_B \|\mathbf{B}\|$. If we now consider the effect of nuclear spin fluctuations δB^{nuc} on the ground-state splitting we find:

$$\delta E_Z^{\text{nuc}} \approx \mu_B g_h \delta B_{x,h}^{\text{nuc}} + \frac{\sqrt{3} \mu_B g_h}{4\beta B_{\text{ext}}} (\delta B_{z,h}^{\text{nuc}})^2. \quad (6.3)$$

Here, $\delta B_{x,e}^{\text{nuc}}$ and $\delta B_{z,h}^{\text{nuc}}$ denote the effective fields due to the nuclear spin fluctuations along the external magnetic field and the growth axis, affecting the ground-state splitting to first and second order, respectively. Therefore, the linear increase of T_2^* with the external magnetic field should only occur if the second-order term dominates.

6.2.3 Electron FID in the same QD

In order to get an estimate of the nuclear-field amplitudes for the hole, we load an electron into the same quantum dot and measure a free induction decay at 2T. Analogous to the measurement presented in Sec. 5.1.4, this allows us to determine the three-dimensional standard deviation of the effective magnetic field given by Eqn. 5.1.

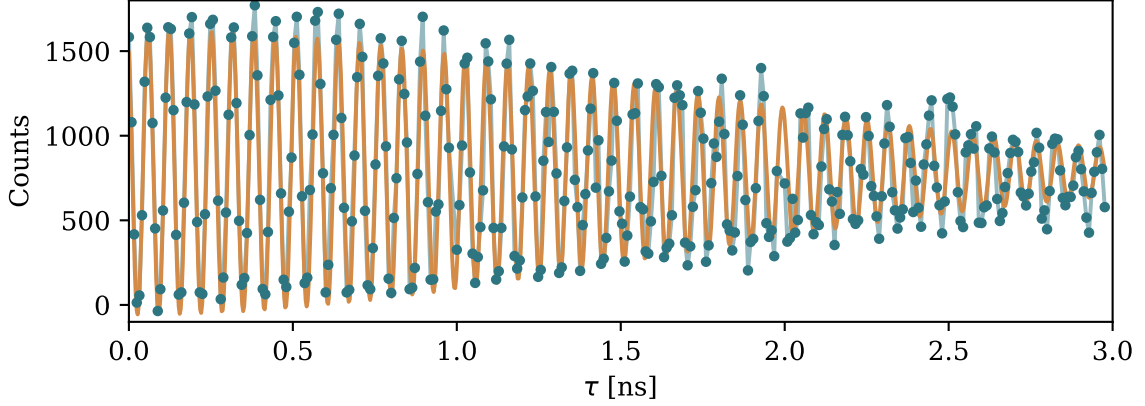


Fig. 6.9 **Electron FID** Free induction decay for the electron spin in the same quantum dot. Orange curve presents a fit to the data and we extract $T_2^* = 2.24 \pm 0.07$ ns.

Here, we combine the technique of alternating initial spin states with modulation of the gate voltage to depolarise the nuclear spin bath using the cotunneling of the electron [64]. The measurement of the FID is presented in Fig. 6.9 and together with a fit of the data to a sine curve with Gaussian decay envelope (orange curve). We extract a dephasing time of 2.24 ± 0.07 ns and estimate $g_e = 0.55$ from the measured Larmor frequency $\omega_L = 2\pi \times 15.506 \pm 0.005$ GHz. Based on these values we find the three dimensional Overhauser field fluctuations for the electron: $\sigma_{\text{OH}} = \sqrt{6} \frac{\hbar}{g_e \mu_B T_2^*} = 22.6 \pm 0.7$ mT.

In order to get estimates for $\delta B_{x,h}^{\text{nuc}}$ and $\delta B_{z,h}^{\text{nuc}}$, we assume a ten-fold reduction of the hyperfine coupling constants for the hole compared to the electron [52] and thus the hyperfine energy fluctuations for the hole are given by:

$$\delta B_{z,h}^{\text{nuc}} = \frac{g_e}{10g_h} \delta B_{z,e}^{\text{nuc}} \quad \text{and} \quad \delta B_{x,h}^{\text{nuc}} = \frac{2\beta}{\sqrt{3}} \delta B_{z,h}^{\text{nuc}}, \quad (6.4)$$

where $\delta B_{z,h}^{\text{nuc}} = \sigma_{\text{OH}}/\sqrt{3}$. The light-hole mixing, β , can be estimated from the in-plane hole g-factor, g_h^x , which we extract from measuring the Larmor frequency to be $g_h^x = 0.165$. The relation of the in-plane g-factor to the hole g-factor is given by:

$$g_h^x = \frac{2}{\sqrt{3(1+\beta^2)}} \beta g_h. \quad (6.5)$$

We do not have a measurement of g_h for this quantum dot, however we can assume $g_h = 1.6$ based on earlier measurements on our samples. Moreover, the exact value for the nuclear field fluctuations is secondary and a choice of $1 \leq g_h \leq 2$ would result in similar values. Based on these assumptions, we infer $\beta \approx 0.09$ and thus $\delta B_z^{\text{nuc}} \approx 0.45$ mT and $\delta B_x^{\text{nuc}} \approx 0.05$ mT. Similar values have been estimated using hole-depolarisation measurements [200, 201].

Therefore, the fluctuations along the x -axis should dominate resulting in a magnetic-field independent dephasing time, in clear contrast to our observations. A possible explanation for the linear increase observed here is a more complex hyperfine interaction between the hole spin and the nuclear bath, which includes coherent noncollinear interactions which induce precession of the nuclear spins [202].

6.3 Coherence time

We now decouple the hole spin from the quasi-static noise through the implementation of a Hahn-echo measurement, analogous to the measurement performed for the electron (Sec. 5.2). The improvement of T_2^* already approaches the regime where heralded entanglement becomes possible and the following experiments will show how far we can extend the coherence with a simple refocussing pulse.

6.3.1 Experimental method

For the implementation of the Hahn-echo sequence we can again draw upon the previous experiment on the electron and use the same pulse sequence for the decoupling from correlated noise sources. The only addition is our weak pulse on the X^0 transition for the photocreation of the hole which we apply for every 20th repetition of the sequence. The pulse sequence is summarised in Fig. 6.10 (a), including the spin-state inversion which is provided by an additional π pulse applied for every other repetition of the measurement. The delay T between the two pulses is fixed for every measurement and we scan the position of the central refocussing pulse by $\tau \ll T_2^*$. As a result, the measurement signal oscillates at twice the Larmor frequency and we can extract the visibility directly through fitting a sine curve to the data. An example is given in Fig. 6.10 (b), for $B_{\text{ext}} = 1$ T and $T = 26.28$ ns. Here, we recover visibilities of $96 \pm 3\%$ ($V = 87 \pm 3\%$) for the counts corresponding to a run of the measurement sequence without (with) the initial π pulse. The visibility for the inverted spin state is reduced due to the imperfect π rotation and we draw all our visibilities in the following only from the signal without the spin-inversion pulse. The significantly reduced nuclear feedback compared to the Ramsey measurements is explained by the reduced overall phase accumulated by the hole spin due to the decoupling sequence.

The spin lifetime in our system is about $20 \mu\text{s}$ independent of the externally applied magnetic field, leading to non-negligible spin relaxation over the course of a measurement. Previous observations of slow hole spin relaxation can be explained considering spin-orbit-mediated phonon scattering [199]. However, the magnetic-field-independent spin relaxation

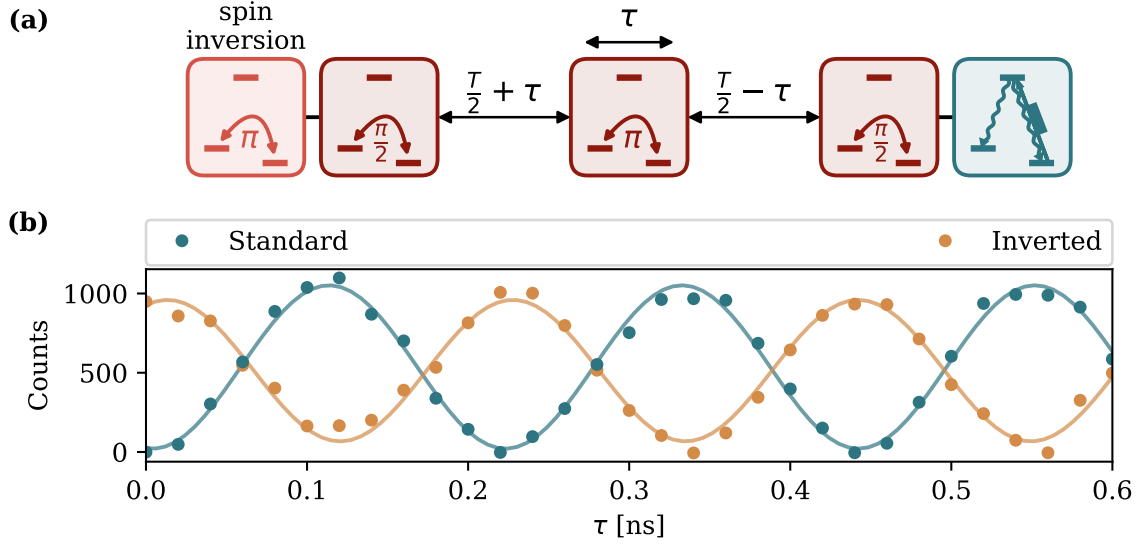


Fig. 6.10 **Hahn-echo sequence and visibility** (a) Schematic of the Hahn-echo pulse sequence including the spin inversion, which is applied every other repetition of the sequence. (b) Exemplary measurement at $B_{\text{ext}} = 1 \text{ T}$ and $T = 26.28 \text{ ns}$. Solid curves are fits to the data and we extract $V = 96 \pm 3\%$ and $V = 87 \pm 3\%$ for the data without (blue) and with (orange) the additional π pulse.

observed here points towards a more complex mechanism, potentially involving two-phonon processes which lead to a suppression of the magnetic field dependence [203]. In our experiment we factor out the contribution of the spin relaxation by keeping the duration between the spin initialisation and readout constant. As a consequence the initial visibility, V_0 , deviates from unity, which we take into account when fitting the data.

6.3.2 Hahn-echo visibility decay

We record the visibility decay of the Hahn-echo signal with increasing T across the same range of external magnetic fields as for the Ramsey experiments. Figure 6.11 (a) shows four exemplary measurements at external fields of 1 T, 3 T, 5 T and 8 T, where the data points represent the average of the extracted visibilities for each pulse separation T .

For measurements at $B_{\text{ext}} \geq 3 \text{ T}$ the coherence time T_2 is extracted by fitting the data with a visibility decay function, $V(T) = V_0 \exp[-(T/T_2)^{1.48}]$, indicated by the solid curves¹. We use the initial visibility V_0 to normalise the data in order to account for pulse infidelities and spin relaxation and observe a reduction of T_2 with increasing magnetic field. In contrast,

¹The exact value of the exponent is based on an analysis of the scaling of dynamic decoupling presented in Sec. 6.5.2.

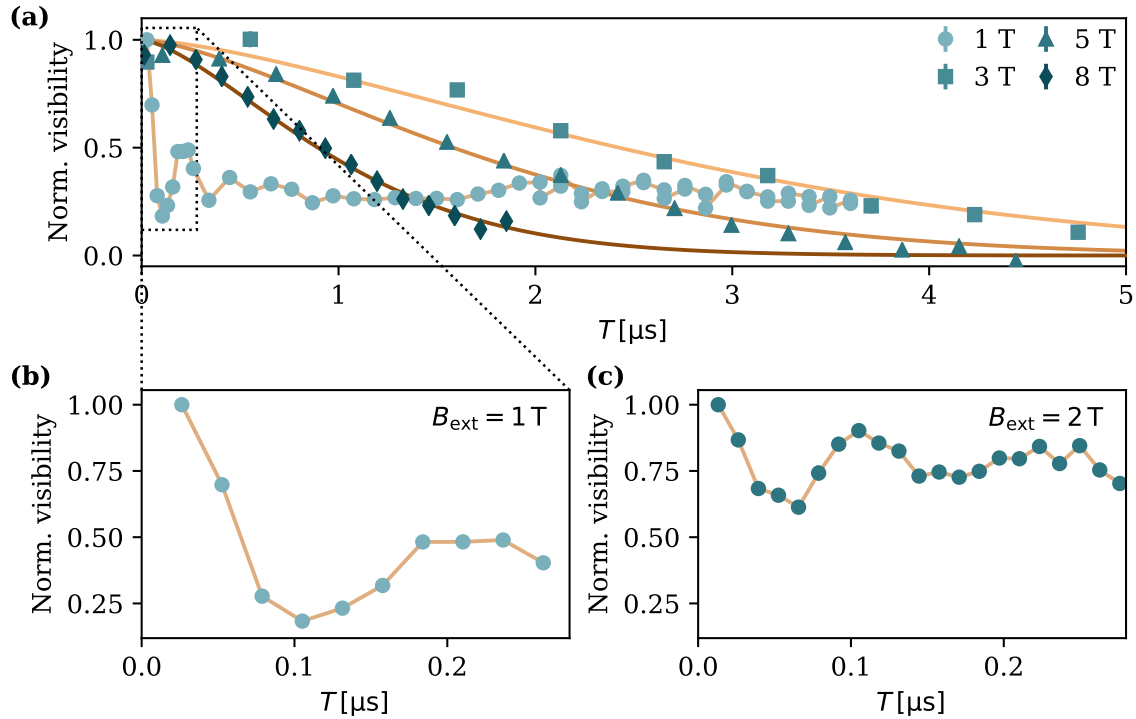


Fig. 6.11 **Hahn-echo visibility** (a) Exemplary Hahn-echo visibility measurements at different external magnetic fields (blue symbols). The orange curves are fits to the data to extract the coherence time, except for $B_{\text{ext}} = 1 \text{ T}$, where the curve only serves as a guide to the eye. Error bars represent ± 1 standard deviation. (b) Zoom in of the first $0.28 \mu\text{s}$ of the 1 T data revealing a sharp drop and revival of coherence. (c) Hahn-echo visibility at 2 T for the same range as (b), showing similar behaviour.

measurements taken at lower fields ($B_{\text{ext}} \leq 2 \text{ T}$) show a strong deviation from a single exponential decay. We observe structure in the Hahn-echo visibility presented in Fig. 6.11 (b) and (c) where the initial 280 ns of the data are shown. Here, the solid lines only serve as guide to the eye. We can clearly see a sharp decay and revival of coherence similar to the behaviour seen for the electron (see Section 5.2.2).

The striking similarity of the observed structure to the one observed for the electron is further confirmed by measurements of the electron Hahn echo in the same quantum dot. Figure 6.12 shows the Hahn-echo visibilities for electron and hole spin in the studied quantum dot at $B_{\text{ext}} = 2 \text{ T}$. As discussed earlier those oscillations can be attributed to the interactions with the precessing nuclear spins in the quantum dot. At low external magnetic fields the first-order coupling dominates and the strain-induced quadrupolar shifts of the nuclei lead to significant high-frequency noise centred around the Zeeman splitting of the nuclear species, resulting in modulation of the echo signal at short delays. The reduced suppression of

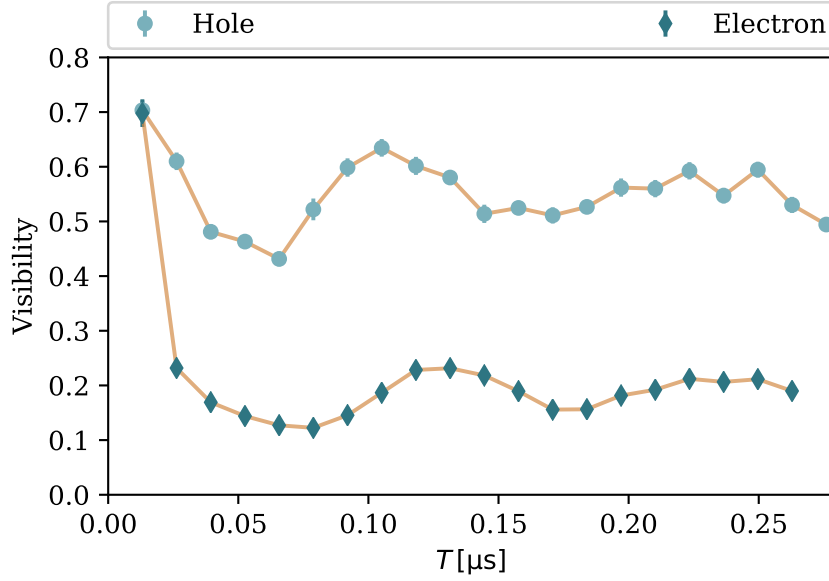


Fig. 6.12 **Hahn-echo comparison** Measurements of the Hahn-echo visibility for an electron and a hole in the same quantum dot at $B_{\text{ext}} = 2\text{ T}$. The data for the hole is reproduced from Fig. 6.11 (c). Error bars represent ± 1 standard deviation.

the visibility of the hole is evidence of the weaker coupling to the nuclear environment. Furthermore, we observe a slight increase of the frequency of the oscillations for the hole spin, which may be due to the smaller hole wavefunction resulting in interactions with an altered nuclear ensemble. These results show that, despite the strong heavy-hole character of the pseudospin in our quantum dot, nuclear fluctuations along the external magnetic field axis still clearly dominate the hole dynamics at low external magnetic fields.

A comparison of the coherence times across the whole range of external magnetic fields extracted from the fits is shown in Fig. 6.13. For $B_{\text{ext}} \leq 2\text{ T}$ we extract the time where the visibility falls below $1/e$ for the first time, as we cannot attribute a single decay to the measured visibility. The extracted coherence times for higher fields ($B_{\text{ext}} \geq 3\text{ T}$) show a decay with increasing magnetic field and a fit to the data gives $T_2(B_{\text{ext}}) \propto 1/B_{\text{ext}}^{0.99 \pm 0.03}$, indicated by the dashed orange curve. Analogous to the behaviour seen in the Ramsey measurements at high fields, this decay indicates a linear increase of the coupling to electrical noise with the external magnetic field. At low magnetic fields this coupling should be negligible and indeed the tail of the 1 T and 2 T data shows very slow decays of coherence after the initial drop due to the interaction with the nuclear spin environment (see Fig. 6.11).

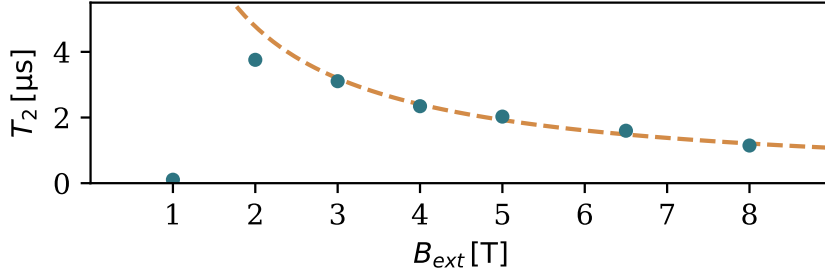


Fig. 6.13 **Magnetic-field-dependent coherence time** Summary of the coherence times extracted from the decay of Hahn-echo visibility across the full range of external magnetic fields. For $B_{\text{ext}} \geq 3$ T the values are obtained from fits to the data and error bars represent ± 1 standard deviation. For $B_{\text{ext}} \leq 2$ T we show the time where the visibility drops below $1/e$ for the first time. The dashed curve indicates a decay $\propto 1/B_{\text{ext}}^{0.99 \pm 0.03}$ for $B_{\text{ext}} \geq 3$ T.

6.4 Measurement of the electrical noise

The Hahn-echo data shows that we cannot completely decouple the hole spin from the underlying noise and that the coherence is ultimately still limited by electrical noise for external magnetic fields beyond 2 T. In this section, we determine the underlying noise spectrum through an independent measurement and show that it is in good agreement with our observed Hahn-echo measurements.

6.4.1 Intensity autocorrelation

In order to gain further understanding about the electrical noise present in our system, we measure the intensity $I(t)$ of the light scattered by the neutral exciton. Over time, the intensity fluctuates due to electrical noise which detunes the quantum dot from the resonant laser drive through the Stark effect, as schematically shown in the inset of Fig. 6.14 (a). Therefore, we can gain insight into the electrical noise properties in the vicinity of our quantum dot through calculation of either the Fourier transform [204] or the normalised autocorrelation function [205] of the recorded intensity:

$$g(\Delta t) = \frac{\langle I(\Delta t)I(0) \rangle}{\langle I \rangle^2} - 1. \quad (6.6)$$

Here, we follow the latter approach and the calculated autocorrelation function is shown in Fig. 6.14 (a). The autocorrelation data presents an average over the signal obtained for slightly varying laser detunings from the optical transition of the neutral exciton. The X^0

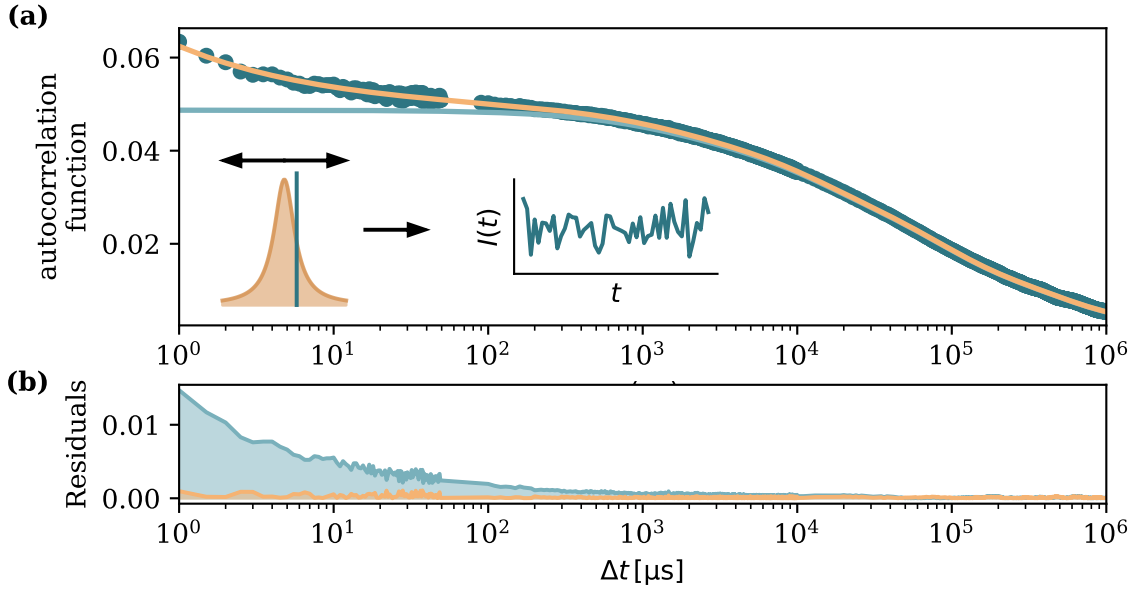


Fig. 6.14 **Normalised autocorrelation function of X^0 intensity fluctuations** (a) Auto correlation function extracted from the intensity fluctuation of the neutral exciton measured at $\sim 0.1 \times I_{\text{sat}}$. The orange curve represents a fit to the data including four exponential decays and a $1/(\Delta t)^{1-\lambda}$ component, whereas the light blue curve represents only the contribution of the four exponential functions. The insert depicts how electrical noise leads to intensity fluctuations, resulting in the bunching of the autocorrelation function. (b) Residuals of the two curves in (a) with respect to the measured autocorrelation function.

transition is driven at low excitation power, corresponding to about $0.1 \times I_{\text{sat}}$ and the gate voltage is chosen, such that we are well within the X^0 plateau..

The data is best captured by the fit given by the orange curve, which includes four exponential decays and a $1/\Delta t$ -like component:

$$g(\Delta t) = A_0 + A_1 e^{-\frac{\Delta t}{\tau_1}} + A_2 e^{-\frac{\Delta t}{\tau_2}} + A_3 e^{-\frac{\Delta t}{\tau_3}} + A_4 e^{-\frac{\Delta t}{\tau_4}} + \frac{A_5}{(\Delta t)^{1-\lambda}}, \quad (6.7)$$

with the parameters summarised in Tab. 6.1. The main contribution to the noise can be attributed to two-level fluctuators (TLF) which lead to the exponential decays over a range of different time scales [204, 206]. These contributions are highlighted by the blue curve, where we have excluded the $1/\Delta t$ -like component. The TLF contribute significantly to the dephasing time T_2^* of the hole spin, however they have relatively slow switching times ($\gtrsim 1$ ms) and can therefore be suppressed efficiently using a Hahn-echo sequence. However, the residuals presented in Fig. 6.14 (b) show that especially for $\Delta t < 1$ ms, corresponding to the lower boundary for typical switching times of the TLF, the noise spectrum cannot

i	TLF		$1/f^\lambda$	
	$A_i [10^{-4}]$	$\tau_i [\text{ms}]$	$A_5 [10^{-4}]$	λ
0	35.5 ± 0.7		137.3 ± 1.0	0.56 ± 0.01
1	101.8 ± 1.4	9.6 ± 0.2		
2	139.0 ± 0.9	464.8 ± 8.7		
3	167.5 ± 1.2	65.5 ± 1.1		
4	41.2 ± 0.8	1.22 ± 0.04		

Table 6.1 **Fitting parameters for the autocorrelation data** Summary of the parameters obtained from fitting the autocorrelation data with the function given in Eqn. 6.7.

originate purely from TLF. This is in good agreement with the Hahn-echo measurements where we do not fully decouple the hole spin from the underlying noise source.

Including the $1/\tau$ -like component in addition to the exponential decays enables us to fully capture the behaviour of the autocorrelation data even for small values of τ (orange curve). The additional $1/(\Delta t)^{1-\lambda}$ component can be related to a $1/f^\lambda$ noise spectrum for $\lambda < 1$ [207] and we find that $\lambda = 0.56 \pm 0.01$. This leads to the high frequency contributions in the noise spectrum of our quantum dot which limit the performance of the Hahn-echo sequence or, more precisely, the coherence of the hole spin. Similar results have been observed before, but the exact origin is yet to be understood [182, 204, 208].

6.5 Further extension of coherence

The implementation of Hahn echo only protects the coherence against quasi-static noise and therefore does not protect the spin against the $1/f$ noise observed here. However, protection against $1/f$ -type noise sources can be achieved through more elaborate multipulse decoupling sequences, which lead to filter-functions that also reduce the impact of noise at finite frequencies. By now, there are a variety of decoupling sequences available [166, 209] and in the following we will implement the first suggested version of dynamic decoupling.

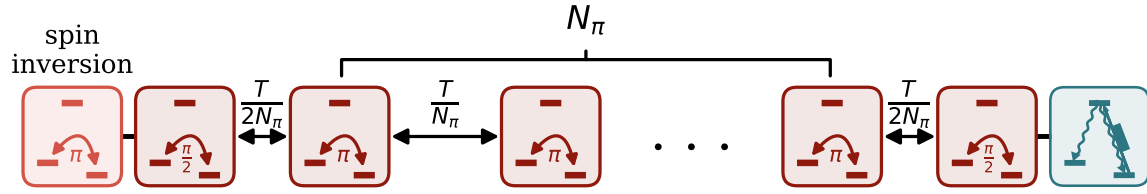


Fig. 6.15 **Dynamic decoupling pulse sequence** Schematic of the CP dynamic decoupling sequence. The N_π rotation pulses are evenly spaced with a separation of T/N_π and surrounded by the two $\pi/2$ pulses which are separated T . The spin inversion is again applied for every other repetition of the pulse sequence.

6.5.1 Experimental method

The experiment presents a natural extension of the Hahn-echo sequence as we add more refocussing pulses between the two $\pi/2$ pulses that project the spin population to the equatorial plane of the Bloch sphere. The pulse sequence used in this work, schematically shown in Fig. 6.15, is based on the initial proposal of Carr and Purcell (CP) [210]. It incorporates a total number of N_π refocussing pulses which are evenly spaced with a separation of T/N_π and encapsulated by the two $\pi/2$ rotations which are separated in time by T . For $N_\pi = 1$ this sequence corresponds to the Hahn-echo sequence used earlier. The initial spin inversion is again applied for every other run of the pulse sequence, realising an alternating initial spin state for the suppression of nuclear polarisation.

Owing to the increasing complexity, both in terms of the number of pulses as well as the changing inter-pulse spacing with changing T , we now use an AWG to generate the voltage pulses used for pulse picking the rotation pulses. The clock for the AWG is derived from the mode-locked laser, which also triggers the start of the measurement sequence to ensure synchronisation. The voltage pulses for the EOMs deriving the laser pulses from the CW sources are still generated by digital delay generators which receive a trigger signal from the AWG. Finally, the AWG also provides a reference signal for the time tagger which is correlated with the detection events in order to separately extract the readouts for the two initial spin states.

With increasing number of pulses we enter a region where the experimental performance starts to be limited by the pulse infidelities which reduce the visibility we recover. Therefore, we change to composite pulses in order to improve our rotation fidelities (Sec. 2.3.3). As a direct consequence, we can no longer sweep the relative delay of the pulses in order to recover oscillations of the count rates, since the delay stage is needed to tune the exact distance between the two pulses that form our composite rotation. Therefore, we have to rely on a different method to extract the visibility: we ensure that we recover the maximum count

Hole Coherence

rate for the ROI that corresponds to the non-inverted initial spin state (C_{\max}) and consequently we get the minimal count rate for the ROI of the inverted spin state (C_{\min}). The visibility is then given by:

$$V = \frac{C_{\max} - C_{\min}}{C_{\max} + C_{\min} - 2C_{\text{BGD}}}, \quad (6.8)$$

where we get an estimate for C_{BGD} from the residual level of fluorescence at the end of the readout and initialisation pulse.

6.5.2 Scaling of dynamic decoupling with N_{π}

The aim is to protect the hole spin coherence from the high frequency electrical noise that starts to dominate for fields exceeding 2 T (Fig. 6.12) and we thus choose to work at $B_{\text{ext}} = 5$ T where we expect that the coherence is completely governed by electrical noise processes. We successively increase the number of refocussing pulses, N_{π} , from 1 to 10 and measure the full visibility decay for each step.

A summary of all measurements is presented in Fig. 6.16 where we show the bare visibilities recovered from our measurements (blue and grey points). This measurement presents an extension of the Hahn-echo sequence and consequently the decay is also described by $V(T) = V_0 \exp[-(T/T_2^{\text{DD}})^{\alpha}]$. The solid curves represent fits to the blue data points, where $\alpha = 1.48$ as for the Hahn-echo measurements. The choice of α is motivated below. We note, that the grey data points are excluded from the fit since we observe strongly reduced visibilities for the first point, corresponding to $T/N_{\pi} = 26.28$ ns, especially for higher N_{π} . We believe that this reduction is due to a technical issue which we attribute to electrical pulse interference at these short pulse-picking delays, but the exact origin is still unclear.

Determining the exponent α

It is difficult to determine the shape of the visibility decay through direct fits to the data. If we choose to leave α as a fitting parameter we obtain the data presented in Fig. 6.17, where we summarise the extracted coherence time, T_2^{DD} , and the corresponding exponent for fits to the data presented in Fig. 6.16. The fitted exponent varies from 1.55 to 3.84, rendering it impossible to extract a reasonable value for α .

In order to obtain a better estimate of α we follow the approach of J. Medford *et al.* [211], relying on the scaling of coherence with the number of π pulses which is directly related to the underlying noise source and thus the exponent of the decay.

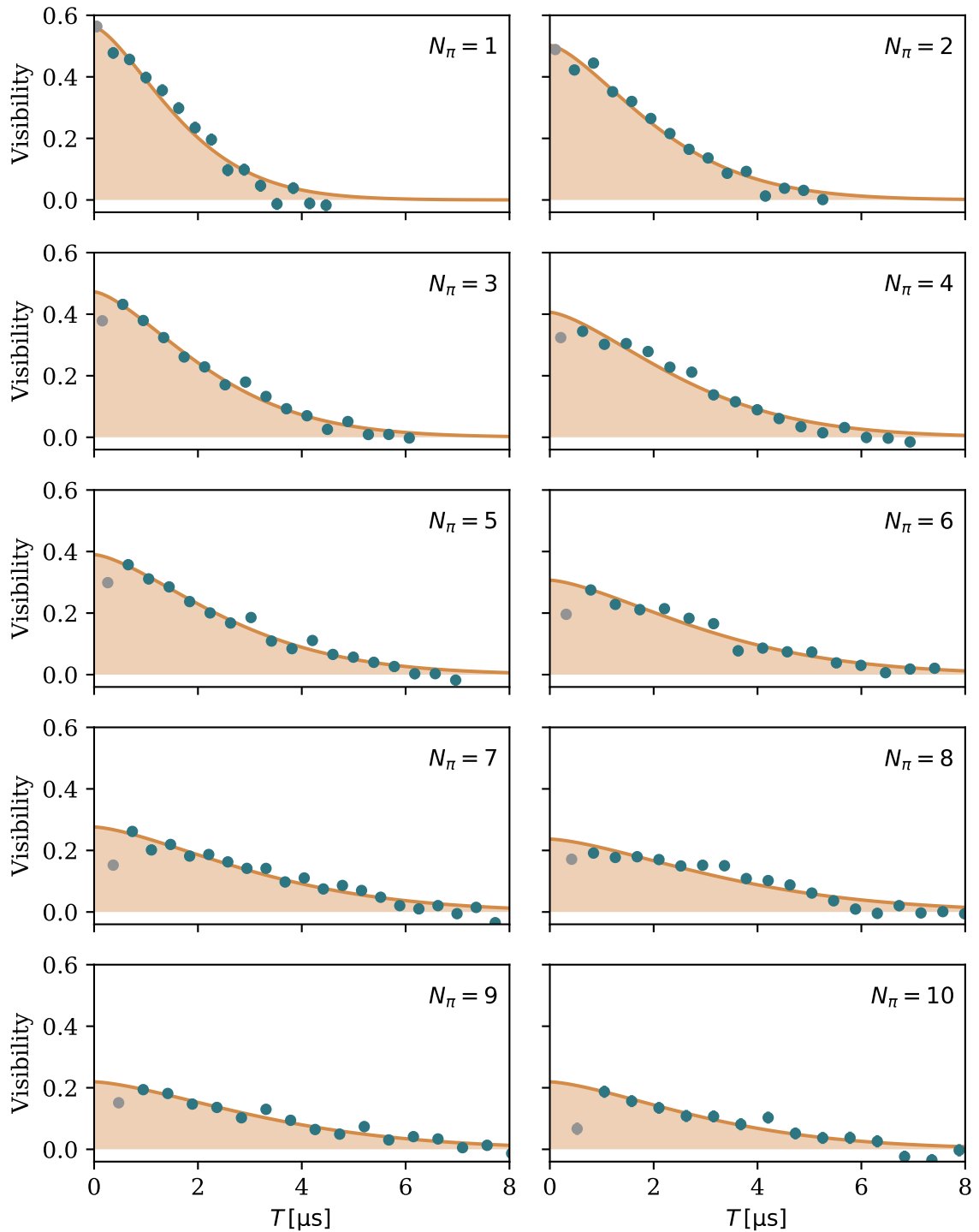


Fig. 6.16 **Dynamic decoupling visibilities** Summary of the extracted visibilities for measurements with 1 to 10 refocussing pulses as indicated in the top right corner (blue and grey points). Error bars represent ± 1 standard deviation and solid curves show fits to the blue data points used to extract the coherence time.

Hole Coherence

This can best be understood by looking at the time-dependent coherence of a qubit described by the coherence function $W(T)$, which is given by the ratio of the coherence at time T and the initial coherence [212] and, assuming Gaussian noise, can be expressed as:

$$W(T) = e^{-\chi(T)}, \quad (6.9)$$

where $\chi(T)$ is called attenuation function, which is given by [166]:

$$\chi(T) = \int_0^\infty \frac{d\omega}{\pi} S(\omega) \frac{F(\omega T)}{\omega^2}. \quad (6.10)$$

Here, $S(\omega)$ denotes the spectral density of the noise and $F(\omega T)$ is the filter function that describes the influence of the decoupling scheme on the decoherence². For a classical $1/f^\lambda$ noise spectrum, $S(\omega) = C\omega^{-\lambda}$, we thus find:

$$\begin{aligned} \chi^{(\lambda)}(T) &= C \int_0^\infty \frac{d\omega}{\pi} \frac{F(\omega T)}{\omega^{\lambda+2}} \\ &= CT^{\lambda+1} \int_0^\infty \frac{dx}{\pi} \frac{F(x)}{x^{\lambda+2}}. \end{aligned} \quad (6.11)$$

Therefore, the exponent of the noise spectrum is directly related to the exponent, α , of the visibility decay function, $V(T)$, through:

$$\alpha = \lambda + 1. \quad (6.12)$$

For the CP decoupling sequence implemented in our experiment the filter consists of periodically spaced, narrow peaks and we can approximate $\chi(T)$ as [170]:

$$\chi(T) \approx \frac{CT^{\lambda+1}}{\pi^2(2\pi N_\pi)^\lambda} \sum_{k=1}^{\infty} \frac{1}{(k - \frac{1}{2})^{\lambda+2}} \equiv \left(\frac{T}{T_2^{\text{DD}}} \right)^\alpha. \quad (6.13)$$

Therefore, the scaling of coherence with the number of pulses is described by:

$$T_2^{\text{DD}} \propto N_\pi^\gamma, \quad \text{with} \quad \gamma = \frac{\lambda}{\alpha} = \frac{\alpha - 1}{\alpha}, \quad (6.14)$$

where we have used Eqn. 6.12. In the following we will use this relation to accurately determine α .

In a first step, we repeatedly fit the data for different values of α across a range of $1.4 \leq \alpha \leq 3.2$ and extract the corresponding coherence times for each N_π shown in Fig. 6.18

²This filter-function approach was also used in the model for describing the Hahn-Echo data of the electron (Sec. 5.3).

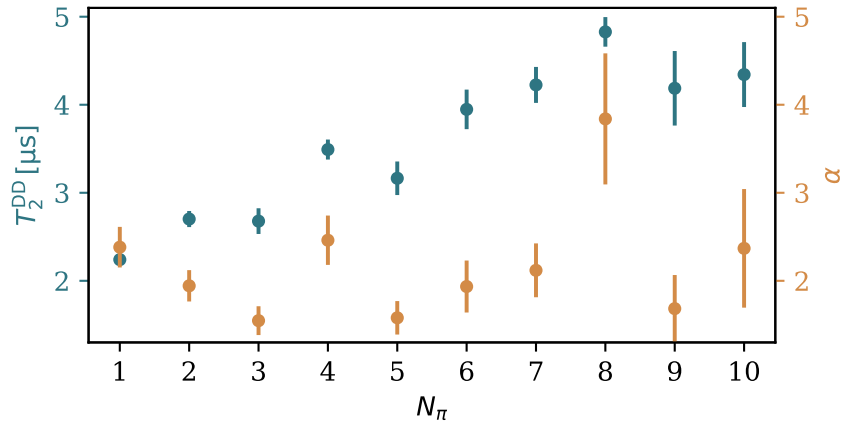


Fig. 6.17 T_2^{DD} with α as fitting parameter Dynamic decoupling coherence times (blue) extracted from fits where α (orange) is left as a free fitting parameter. Error bars represent ± 1 standard deviation.

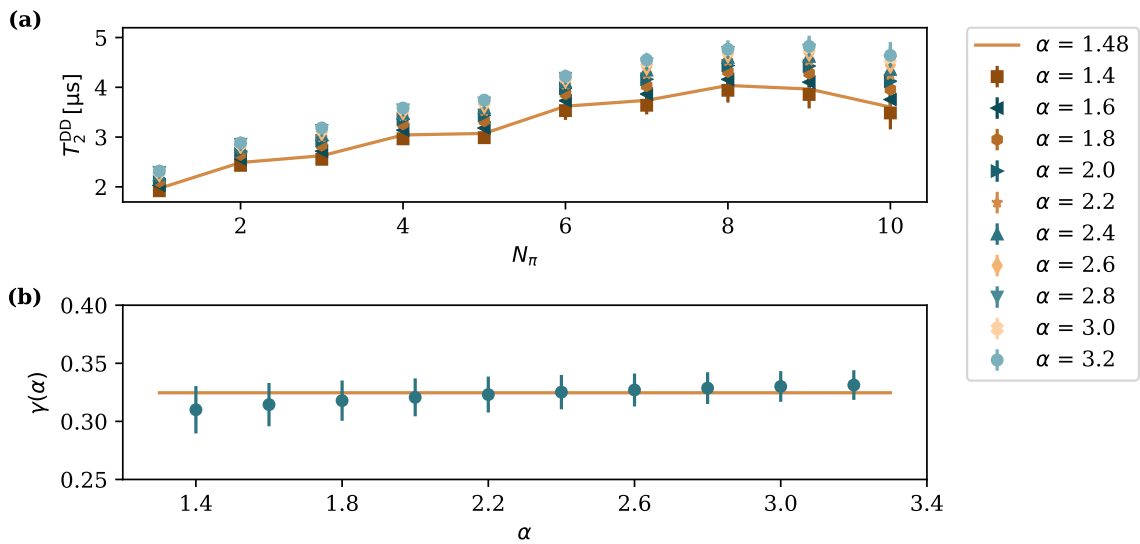


Fig. 6.18 **Determination of the exponent α** (a) Extracted T_2^{DD} with fixed $\alpha \in [1.4, 3.2]$ for the data presented in Fig. 6.16. (b) Scaling of coherence extracted for the different values of α . The solid lines shows the weighted average leading to $\gamma = 0.325 \pm 0.005$. Error bars represent ± 1 standard deviation.

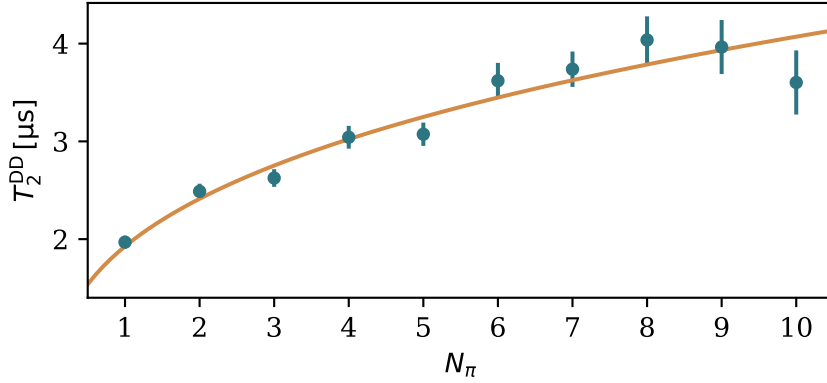


Fig. 6.19 **Scaling of coherence with N_π** Extracted coherence times from fits to the visibility decay data with $\alpha = 1.48$ shown as solid curves in Fig. 6.16. The solid curve shows the scaling with $\gamma = 0.325$ and error bars represent ± 1 standard deviation.

(a). While we observe a dependence of T_2^{DD} on the choice of α , the scaling of coherence with N_π appears to be independent of the choice of α . In a second step, we extract the scaling, γ through fitting the data with $T_2^{\text{DD}}(N_\pi) = T_2(N_\pi)^\gamma$ for each value of α . The extracted scaling factors $\gamma(\alpha)$ are shown in Fig. 6.18 (b) and the solid line corresponds to the weighted average of $\gamma = 0.325 \pm 0.005$. Since the scaling is insensitive to the choice of α , we can use this method to get a more accurate estimate of the exponent using Eqn. 6.14 and we find $\alpha = 1.48 \pm 0.01$. This result motivated the choice of α for the analysis of the visibility decay in Hahn-echo and dynamic-decoupling experiments.

Effectiveness of dynamic decoupling

Figure 6.19 summarises the extracted coherence times with $\alpha = 1.48$ from the fits shown in Fig. 6.16 alongside the scaling of $\gamma = 0.325$ extracted earlier. The increase of coherence with N_π also allows us to check if we are effectively decoupling our system from the underlying noise source. Based on the electrical noise measurement we expect the noise spectrum to follow a $1/f^\lambda$ dependence with $\lambda = 0.56 \pm 0.01$. Using the relation of α and λ (Eqn. 6.12) in combination with Eqn. 6.14 we can also directly relate λ to the scaling: $\gamma = \lambda/(1 + \lambda)$. Therefore, we would expect a scaling of $\gamma = 0.36 \pm 0.01$ based on the autocorrelation data and the assumption that the coherence is solely limited by the $1/f^\lambda$ noise. Our measured value of $\gamma = 0.325 \pm 0.005$ is in reasonable agreement with the theoretical prediction, showing that we successfully decouple our system, reaching $T_2^{\text{DD}} = 4.0 \pm 0.2 \mu\text{s}$ for $N_\pi = 8$.

In our measurement T_2^{DD} shows no further improvement for $N_\pi \geq 9$ which we attribute to pulse infidelities, leading to very low visibilities. At this point the interference with fluctu-

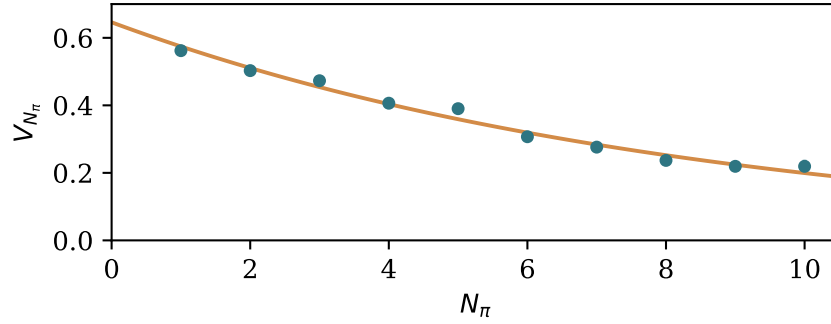


Fig. 6.20 **Reduction of visibility with N_π** Initial visibility extracted from the fits to the dynamic-decoupling visibility decay (blue). The solid curve represents a fit of $V_{N_\pi} = V_0 (V_1)^{N_\pi}$ to the data revealing $V_0 = 0.65 \pm 0.01$ and $V_1 = 0.89 \pm 0.01$. Error bars represent ± 1 standard deviation.

ations of the background signal can become relevant and potentially lead to an underestimate of the coherence. Thus, the observed scaling provides only a lower bound due to the reduction of coherence for high number of pulses.

Rotation fidelity

One of the major limitations to our experiment is the loss of visibility due to imperfect rotations, preventing reliable decoupling of the hole spin for $N_\pi \geq 9$. The use of composite pulses should correct for the tilted rotation axis, but the process is still limited by excitation-induced dephasing due to coupling to acoustic phonons [99].

We use the initial visibility for the different number of π pulses which we obtain from the fits to the dynamic decoupling data to determine our pulse fidelity. The extracted values are shown in Fig. 6.20. We can approximate the decrease of visibility by a power law $V_{N_\pi} = V_0 (V_1)^{N_\pi}$ and a fit to the data reveals $V_0 = 0.65 \pm 0.01$ and $V_1 = 0.89 \pm 0.01$. Therefore, the fidelity of the rotation is slightly lower than what we measured for the electron (Sec. 3.4), but still sufficient for the multipulse decoupling scheme demonstrated here. The reduced initial visibility can be attributed to two contributions: On the one hand, we still have two $\pi/2$ pulses in the case of $N_\pi = 0$, which also have sub-unity fidelity and on the other hand we are limited by relaxation of the hole-spin population during the $9.5 \mu\text{s}$ window between spin initialisation and readout.

6.5.3 Periodic dynamic decoupling

The CP pulse sequence we employ to decouple the spin presents only one possible decoupling sequence and there are more sophisticated decoupling sequences which rely on rotations around different axis [213, 214], recursive concatenation of pulses [215] and aperiodic spacings of the decoupling pulses [216].

Using the optical rotation pulses our rotation axis is fixed to the axis of the optical access and a choice of rotation axis would require precise control of the individual delays of the pulses, which is beyond the scope of our experimental setup. Therefore, we can only vary the delay between the pulses. Here, we implement a slightly different decoupling sequence where the the pulses are all evenly spaced with a separation of $T/(N_\pi + 1)$ as shown in Fig. 6.21 (a). We note, that this sequences requires an odd number of π pulses in order to achieve refocussing of the dephased spin state at $t = T$ [212]. This method is known as periodic dynamic decoupling (PDD) and even though it appears to be very similar to the CP sequence used earlier, it does lead to a different filter function for the underlying noise spectrum [166]. In general, PDD is expected to perform worse than CP owing to the fact that the latter sequence results in a better refocussing of the coherence after the final π pulse [166]; the spacing between the final π pulse and the $\pi/2$ pulses is a factor $1 + 1/N_\pi$ longer for PDD. However, in a best case scenario it can potentially outperform a CP sequence for very small pulse spacings [209].

The measured visibilities for up to 9 π pulses are given in Fig. 6.21 (b). The solid curves represent fits to the blue data points where we fix the exponent to $\alpha_{\text{CP}} = 1.48$. Here we rely on the fact, that the spin is experiencing the same noise spectrum as before, which should result in the same decay shape [212]. The extracted coherence times, T_2^{PDD} , are given by the blue points in Fig. 6.22 (a) with a maximum of $T_2^{\text{PDD}} = 3.8 \pm 0.2 \mu\text{s}$ for $N_\pi = 9$. The increase of coherence with N_π follows a scaling of $\gamma = 0.28 \pm 0.02$ which is weaker than the scaling we obtained for CP ($\gamma_{\text{CP}} = 0.325 \pm 0.005$), indicating a weaker performance of PDD.

Figure 6.22 (b) summarises the initial visibilities from the fits and we extract $V_0 = 0.69 \pm 0.01$ and $V_1 = 0.878 \pm 0.004$ which further supports the values obtained earlier. The difference of V_0 can be attributed to different length of the pulse sequence.

6.6 Discussion of Results

The initial study of hole spins revealed some basic properties that have to be taken into account for experiments using holes generated through photocreation. Our measurements indicate that there is a benefit to choosing quantum dots where the X^+ transition is red-detuned from the neutral exciton as they show longer charge lifetimes and thus require less

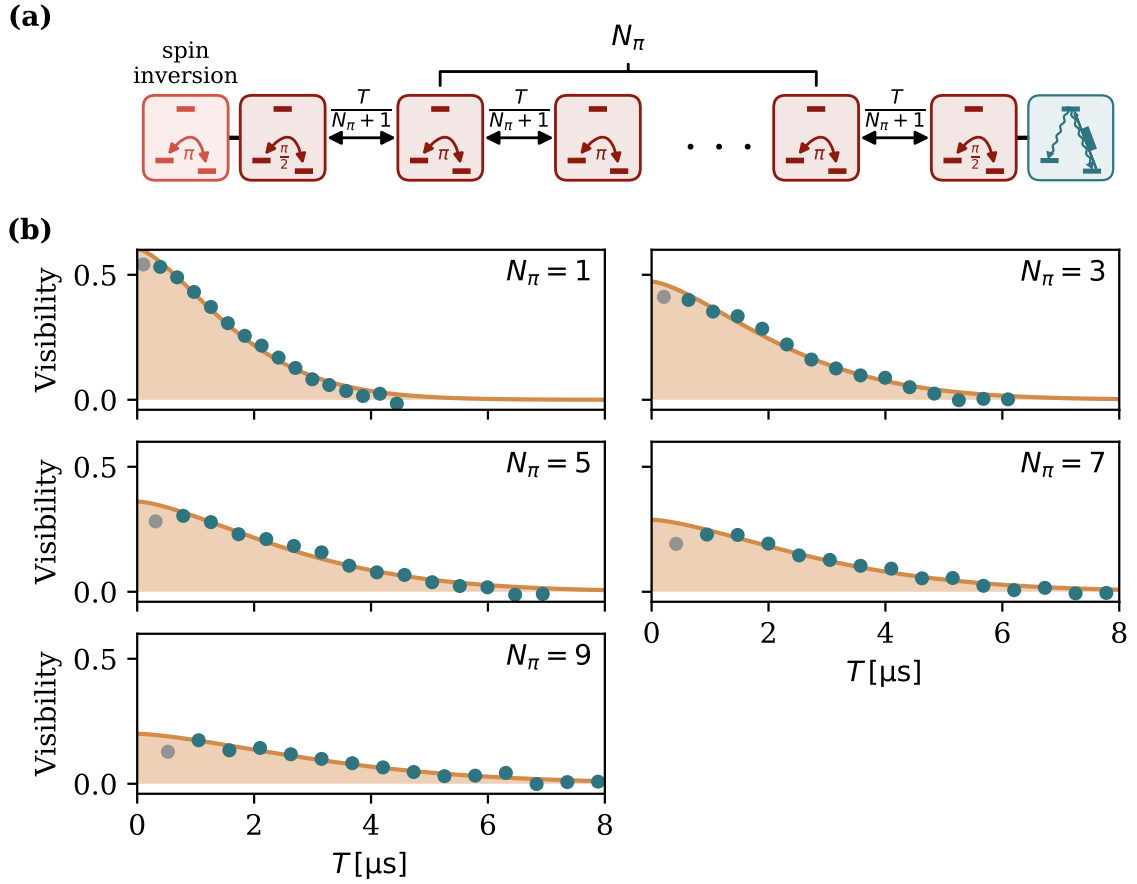


Fig. 6.21 **Periodic dynamic decoupling** (a) Pulse sequence for PDD where all pulses are evenly spaced by $T/(N_\pi + 1)$. (b) Extracted visibilities for increasing N_π as indicated in the top right corner (blue and grey points). Solid curves are fits to the blue data points with $\alpha_{\text{CP}} = 1.48$. Error bars represent ± 1 standard deviation.

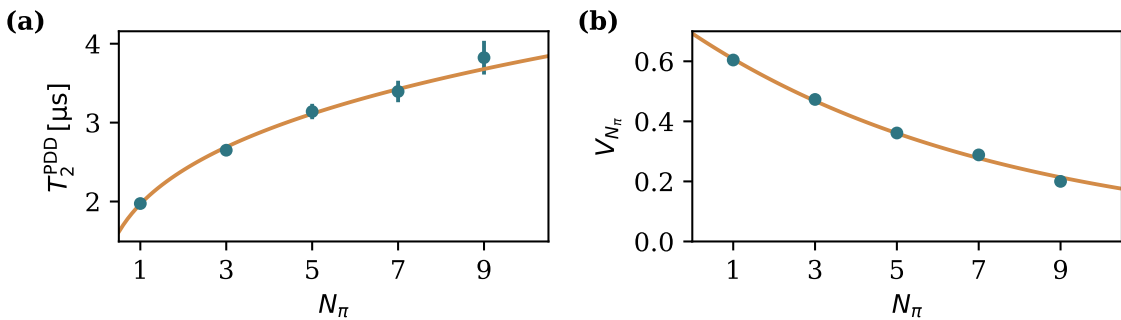


Fig. 6.22 **Scaling of coherence and visibility with N_π for PDD** (a) Extracted coherence times from fits to the visibility decay of PDD measurements. We extract a scaling of $\gamma = 0.28 \pm 0.02$ from the fit to the blue data (solid curve). (b) Error bars represent ± 1 standard deviation.

frequent photocreation. Ultimately, advances in sample fabrication will render the use of photocreation redundant due to the availability of electrically clean p -doped samples [54], which reduces the technical overhead needed to create the single hole spin.

The data presented in this chapter is the first study of hole coherence over a wide range of external magnetic fields, showing a crossover from nuclear to electrically dominated decoherence with increasing external magnetic field. The dephasing time shows a linear increase for low fields that is not explained by common theory [51, 104] and instead supports a recent prediction of a stronger and more complex hyperfine interaction [202]. For the Hahn-echo measurements we observe similar signatures to the measurements for the electron, showing that despite the relatively small hh - lh mixing the coherence at low fields is still limited by the quadrupolar coupling of the nuclei to the inhomogeneous electric-field gradients. The measurements are further supported by loading an electron into the same quantum dot allowing for a direct comparison at $B_{\text{ext}} = 2 \text{ T}$.

For higher fields, both T_2 and T_2^* are limited by electrical noise through the electric-field sensitive g -factor. We examine the underlying noise spectrum through measurements of the autocorrelation function of intensity fluctuation on the neutral exciton transition, revealing a $1/f$ -type contribution which is extrinsic to the quantum dot. Further measurements with a terminated gate³ show that the electrical noise is not caused by our instruments and further understanding of the origin of this noise is needed to prolong the coherence times of this system.

The dephasing times are an order of magnitude higher than for the electron [161, 196] (see also Chapter 5) which allows for a theoretical improvement of the fidelity of spin-photon entanglement by nearly two orders of magnitude and allows for heralding during the spin-spin entanglement presented in Chapter 3.

Finally, we present the first realisation of dynamic decoupling in these systems enabling us to measure coherence times of up to $T_2^{\text{DD}} = 4.0 \pm 0.2 \mu\text{s}$. The measured scaling with the number of pulses is in good agreement with the noise spectrum measured through the autocorrelations and the extension of coherence is only limited by the fidelities of our rotations.

Together with the dephasing measurements this study presents the longest coherence times measured in these systems through direct transient measurements and further confirms the potential of the hole spin as a resource for quantum information processing and specifically as spin-photon interface for efficient network architectures.

³The charging plateau of the X^+ spans across $V_g = 0 \text{ V}$, enabling us to perform measurements with a terminated gate.

Chapter 7

Conclusion

"Remember to look up at the stars and not down at your feet. Try to make sense of what you see and wonder about what makes the universe exist. Be curious. And however difficult life may seem, there is always something you can do, and succeed at. It matters that you don't just give up"

- Stephen Hawking, [217]

In this thesis we have presented experimental work towards the implementation of quantum networks based on semiconductor quantum dots, including the successful realisation of an elementary unit cell of such a network and further studies with a focus on the coherence properties of the charge carriers.

In Chapter 3 we have demonstrated spin-spin entanglement for electrons in two spatially separated quantum-dot samples. This proof-of-principle realisation of a quantum network relies on a probabilistic single-photon detection scheme and showed the potential of quantum dots for high-frequency generation of entanglement. Moreover, we show full control over the phase of the entangled state, which has so far only been realised for entanglement of ions within the same trap [138].

In order to realise a fault-tolerant extension to a network of multiple nodes we need to be able to store the entanglement and ensure its generation and distribution at rates which are faster than the storage time. The implementation of state-of-the-art light-collection efficiencies would already enable us to improve the entanglement rate beyond 100 kHz [114, 218], which, in combination with improved dephasing times, would allow us to reach rates comparable to the inverse coherence time - an important step towards fault tolerant scalability [219]. Promising routes for the storage of already established entanglement during repeated attempts to further extend the network are the use of stacked QD molecules [220] or potential hybrid systems as for example the coupling to electrostatically defined quantum dots [221].

Conclusion

The experiment is limited by the short dephasing time T_2^* of the electron spin which reduces the fidelity and prevents us from utilising the full Raman photon. Furthermore, it necessitates to read out the spin before the measurement of the projecting photon hindering heralding of the entanglement generation. The effect of a short T_2^* on the order of the radiative lifetime of the excited state is also clearly visible in the further investigation of the photon indistinguishability in Chapter 4.

These results show the importance of a good understanding of the limitations to coherence in InGaAs quantum dots on our way towards a scalable quantum network which motivated our efforts in understanding and extending the available coherence in these systems.

In Chapter 5 we studied the coherence of the electron and identified the coupling of the nuclear spins to the inhomogeneous strain field as the limiting factor for the coherence time. These results serve as motivation for the investigation of quantum dots based on growth methods with reduced strain and materials with a reduced nuclear bath. The Hahn-echo measurements show that a single refocussing pulse would already enable a heralded version of the entanglement. However, this would not affect the finite distinguishability introduced by spin dephasing and increases the demands on the entanglement sequence. Another possible route could be to extend the coherence through narrowing of the nuclear bath which has recently been shown as a promising route for the extension of coherence [155].

An interesting alternative to the electron is the hole spin, which has been used to demonstrate quantum correlations between distant quantum dots [115] and showed potential for longer coherence times [51, 54]. Our work discussed in Chapter 6 shows through direct transient measurements, that the hole spin, contrary to common belief, still significantly couples to the nuclear bath at lower fields where the coherence is limited due to the nuclear-bath dynamics, whereas the coherence for higher fields is dominated by electrical noise. The dephasing time of the hole spin exceeds the electron by an order of magnitude and, in combination with comparable coherence times, establishes the hole spin as superior spin-photon interface. Furthermore, the electrically dominated coherence time of the hole spin enabled the first successful implementation of dynamic decoupling in these systems, showing the potential of extending the lifetime of information or entanglement stored in the spin state.

An interesting objective for future experiments is the implementation of so called linear or measurement-based quantum computing [222], which presents an alternative approach to the well known circuit-based quantum computing. For the former, the computation is realised by performing single-photon measurements on a multi-photon entangled state, also known as cluster state [223]. Owing to the destructive nature of the computation process this method is also known as one-way quantum computing. First realisations of linear quantum computation have been shown using parametric down-conversion [224, 225]. Due to the high-quality

single photons quantum dots have been proposed as promising candidates for cluster-state generation [226] and recently, a one-dimensional cluster state was successfully generated using the dark exciton of a quantum dot [227]. The proposal relies on using the precession of the spin in an external magnetic field along x to implement spin rotations in the $z - y$ plane. Thus, this method requires a spin precession which is much slower than the excited state decay, but faster than the spin dephasing. For the bright states of the negative trion these conditions for the involved timescales are not readily met as the splitting of the electron is typically at least on the order of the decay rate of the excited state due to the external field which is required to suppress the Overhauser field fluctuations. While the decay rate can be increased through cavity-induced Purcell enhancement [228], the hole spin experiences less splitting of the ground-state due to the smaller g -factor and thus provides a promising route towards the realisation of cluster states.

In combination with the spin-spin entanglement presented in this work we could generate multi-dimensional cluster states through mapping of the entanglement onto the photonic state [229]. Recently, there have also been new studies suggesting a different method for generating cluster states by using Raman photons [230] and the creation of two-dimensional cluster states using quantum dot molecules [231]. Finally, the generation of cluster states is also relevant to the field of quantum communications through the realisation of all-photonic quantum repeaters [232].

Up to today there are a number of different physical systems being explored for the purpose of quantum information processing and communication as well as quantum metrology. While InGaAs quantum dots have become a central resource for high-purity single-photon sources, our work shows the strong potential as a fast and efficient resource for entanglement distribution. Moreover, the combination of efficient spin-spin entanglement and high-quality single-photon sources render quantum dots a prime candidate for the realisation of linear quantum computing.

Appendix A

Python library

In this appendix we briefly discuss some of the core functionality of the python library which is the foundation for the data acquisition and analysis. Even though some of the functions are specifically designed for the entanglement experiment, parts of the library can and have been used for other experiments. Especially the capability of recording timestamps and calculating histograms or two channel correlations are often very useful tools for other experiments.

We decided to realise experimental control and analysis in a single programming environment and chose Python 3.6 based on the availability of a wide range of open source packages and experience of using python in other projects. For the implementation of the Entanglement module we rely on a number of readily available packages, including:

- NumPy: Fundamental package for numerical computations in Python
- os: Enables interactions with the operating system such as creating new directories
- time: & datetime: Both providing time-related functions
- struct: Used for decoding binary data
- multiprocessing: Allows to use subprocesses and thus use of all available CPUs

The packages are imported at the beginning of the module and we refer to NumPy as np in following code examples.

The current module (Entanglement_v6b.py) contains 14 functions and > 1300 lines of code. Here, we aim to highlight a few of the more important functions and focus some crucial points. We note that the code presented here sometimes only provides the part of the code necessary to discuss the core functionality.

A.1 Measurement and compression of data

The measurements are run through a small executable file written in C which is run as a subprocess through the python interface setting the right parameters and saving a settings file. The data is then prepared for the analysis using a combination of three functions. First, we need to decode the binary files and convert the data into a format that can efficiently be processed in the python environment, which is done by the `ReadBinary` function presented in Listing A.1. The function requires the `filename` as well as its `directory` and `length` as input arguments to be able to open the corresponding file (line 2). There is an optional argument `opt` to allow to only read in the first (`opt=1`) or second (`opt=2`) half of the file. This option is needed if the filesize results in an array that exceeds the capability of the memory allocated for the program. The function then basically creates an empty array of unsigned 64-bit integers of the dimension $\text{length} \times 2$ (line 5) or $\text{length}/2 \times 2$ (lines 8,14), where we make sure to cover the case of an odd total length (lines 10-13). In a final step we read in the binary file 10 bytes at a time and decode it into the timestamp and corresponding channel which are saved in one row of the array which is then returned by the function.

```
1 def ReadBinary(directory , filename , length , opt = 0):
2     f = open(directory + '\\ ' + filename , 'rb')
3     if opt == 0:
4         ran = length
5         dta = np.empty((length , 2) , 'uint64')
6     elif opt == 1:
7         ran = int(length/2)
8         dta = np.empty((ran , 2) , 'uint64')
9     elif opt == 2:
10        if length%2 == 0:
11            ran = int(length/2)
12        else:
13            ran = int(length/2) + 1
14        dta = np.empty((ran , 2) , 'uint64')
15        f.seek(int(length/2)*10)
16    for i in range(ran):
17        dta[i] = struct.unpack('<QH' , f.read(10))
18    f.close()
19    return dta
```

Listing A.1 `ReadBinary(...)`

The decoded data is then passed on to the function `splitData` (Listing A.2) which splits it into five one-dimensional arrays according to the input channel the events were registered on (lines 3-7). This way, we only need to keep the timestamp as the channel number is now

A.1 Measurement and compression of data

decoded in the array itself and after a check that the conversion was successful, i.e. that the overall number of events is maintained, the function returns the 5 arrays containing the timestamps (lines 8,9).

```
1 def splitData(dta):
2     length = len(dta)
3     chan1 = (np.compress(dta[:,1]==1,dta,axis=0))[:,0]
4     chan2 = (np.compress(dta[:,1]==2,dta,axis=0))[:,0]
5     chan3 = (np.compress(dta[:,1]==3,dta,axis=0))[:,0]
6     chan4 = (np.compress(dta[:,1]==4,dta,axis=0))[:,0]
7     chan5 = (np.compress(dta[:,1]==5,dta,axis=0))[:,0]
8     if (len(chan1) + len(chan2) + len(chan3) + len(chan4) + len(chan5)) ==
9         length:
10        return chan1, chan2, chan3, chan4, chan5
11    raise ValueError('Length of channel lists is not equal to length of
12        initial data.')
```

Listing A.2 **splitData(...)**

In a final step the `saveChan` function shown in Listing A.3 saves the data in a compressed `.npz` file which contains a zipped archive of files corresponding to the individual arrays. Apart from the arrays containing the data and the directory we want to save to, the function also requires the filename of the initial binary file, which contains the data and a measurement prefix used to structure the saving of our data. In the case where the file is processed in two parts we can then concatenate the final arrays and save them again into one file. Similarly the library contains a function to read the compressed file and extract the arrays needed for further processing.

```
1 def saveChan(filename, chan1, chan2, chan3, chan4, chan5, directory):
2     date = filename[:10]
3     prefix = filename[18:-4]
4     directory = directory + '\\'+ date + '\\'+ prefix
5     if not os.path.exists(directory):
6         os.makedirs(directory)
7     os.chdir(directory)
8     np.savez_compressed(filename[:-4], chan1 = chan1, chan2 = chan2, chan3
9         = chan3,
10        chan4 = chan4, chan5 = chan5)
```

Listing A.3 **saveChan(...)**

The whole process of decoding, splitting and saving the data takes less than the actual measurement time, typically ~ 45 s, and therefore provides a constant time offset to the actual data analysis. However, the reduction of information stored in the arrays and the use

of compressed files allows us to reduce the file size to $\sim 1/3$ of its original size rendering further processing and data management more efficient.

A.2 Clock-Channel correlations

A first check of the measurement is often performed by visualising it in a histogram which also allows to define basic parameters like the position of the relevant ROIs or the accumulated delay between the channels due to different path length from the point of emission all the way to the TDC. To obtain the relative timing information we need to correlate the events on each detection channel with the reference clock provided by the experiment and usually measured on the first channel.

```
1 def corrClockChan(chanClock, chanCounts, directory, filename):
2
3     ...
4
5     clock = np.array_split(clock, clock.shape[0]//1000000)
6     for i in range(len(clock)-1):
7         cStart = np.take(clock[i], 0)
8         lastClock = np.take(clock[i+1],0)
9         dataTMP = data[np.searchsorted(data, cStart):np.searchsorted(data,
10                                lastClock)]
11         for c in clock[i][1:]:
12             dataTMP[np.searchsorted(dataTMP, cStart):np.searchsorted(dataTMP, np
13                                .uint64(c))] -=cStart
14             cStart=c
15         dataTMP[np.searchsorted(dataTMP, cStart):] -=cStart
16
17     ...
18
19     return (data*81)
```

Listing A.4 **corrClockChan(...)**

The correlation function `corrClockChan` thus needs the `filename`, `directory` and the channel numbers of the clock (`chanClock`) and the measured events (`chanCounts`). After loading the data and extracting the two relevant arrays, the function will delete any events that happened before the first clock, before starting to the relative timing of the events. The core functionality is shown in Listings A.4: The clock array is split into smaller arrays (line 5) in order to increase the efficiency of accessing the data and we then loop through the arrays (line 6) and modify the data in-place by creating a view of the array (line 9). We then simply

search the data array for all events within two events on the clock channel and subtract the corresponding clock (line 11). Here, we make use of the fact that the arrays are sorted to significantly increase the speed of the search function. Moreover, the search function will convert all input parameter to one data type, which we avoid by making sure all our variables are unsigned 64-bit integers, preventing a reduction of processing time by three orders of magnitude. After processing the data after the final clock and checking that the data does not contain events at times longer than one clock cycle we return the data in picoseconds (line 18).

A.3 Two-photon correlations

Often we are interested in calculating correlations between two channels registering single photon event. Examples are $g^2(\tau)$ or HOM measurements presented in the last chapter. The function `corr_g2` requires a number of input parameters used to load the data for the two channels as well as the reference timestamps on the clock channel. The data is then corrected for any relative offset determined by the histograms of the data and we first have to extract all counts that are in the corresponding ROI, typically a short window after the excitation of the system. The principal process of identifying the counts within a given ROI is highlighted in the Listing A.5. Initially we create an array of zeros with dimensions identical to the array containing the data (line 1). We then loop through all timestamps contained in the data of the channel and find the last clock signal that registered before the event (line 4) and calculate the relative position within one experimental run (line 5). Here, `expcycle_length` denotes the period of the experimental sequence in number of bins. Finally we check if the event `e` is within the beginning (`start_roi`) and end (`lim`) of the ROI and replace the next zero in the `counts` array with the corresponding timestamp (lines 6-8). If the event lies outside of the ROI we shorten the `counts` array by one entry (line 10).

```

1 counts = np.zeros((len(dta),), np.uint64)
2 h = 0
3 for i in dta:
4     c = clock[np.searchsorted(clock, i, side = 'right')-1]
5     e = (i-c)%expcycle_length
6     if e >= start_roi and e <= lim:
7         counts[h] = i
8         h+=1
9     else:
10        counts = counts[:-1]
```

Listing A.5 Identifying events within a ROI

The process of correlating the events within the ROIs in time is shown in Listing A.6, where we highlight the working principal without considering the limiting cases for events at the beginning and end of the arrays. We start with creating an empty array with the maximally required size to save the time difference of events (line 1). Subsequently, we loop through the events of the first channel (`counts_1`) and find the position `p` of closest entry in the array of the second channel (`counts_2`). The time difference to the closest 2 events is then calculated and saved to the corresponding array (line 5), where `n` is an input parameter of the function. The final array is returned by the function and we can calculate a histogram of the data to find the correlation function.

```
1 times = np.empty(len(counts_1)*n*2, np.int64)
2 f=0
3 for i in counts_1:
4     p = np.searchsorted(counts_2, i)
5     times[f:f+2*n] = i-counts_2[p-n:p+n]
6     f+=(2*n)
```

Listing A.6 Extract time difference of events

A.4 Extraction of three photon coincidences

The heart of the module is of course the function that extracts the three-photon coincidences which evidence the creation of entanglement in our experiment. Similar to the two-photon correlations we first need to load all the data and correct it for the relative delays extracted from the histograms before we can start processing the data.

For the processing we have to first identify if an event corresponds to any ROI and separate them accordingly. The principal is similar to before, but this time we have nine different ROIs: 4 readout basis per quantum dot and the entanglement ROI. However, initially we do not need to distinguish between the four readout bases and we therefore have only 3 ROIs. There are more counts in the two readout ROIs than in the ROI of the entanglement pulse and we thus start by checking if an event corresponds to either of the two readouts in order to minimise the time until the correct ROI is identified. Furthermore, Raman photons corresponding to the successful generation of entanglement are only measured in transmission and events in the two channels corresponding to the reflection of the etalon are not relevant for the entanglement ROI.

Once we have extracted all relevant counts from the four channels we check for each event in the entanglement ROI if we successfully measured a photon in the subsequent readout measurements of the two quantum dots. For each three-photon event that fulfils

A.5 Graphical user interface

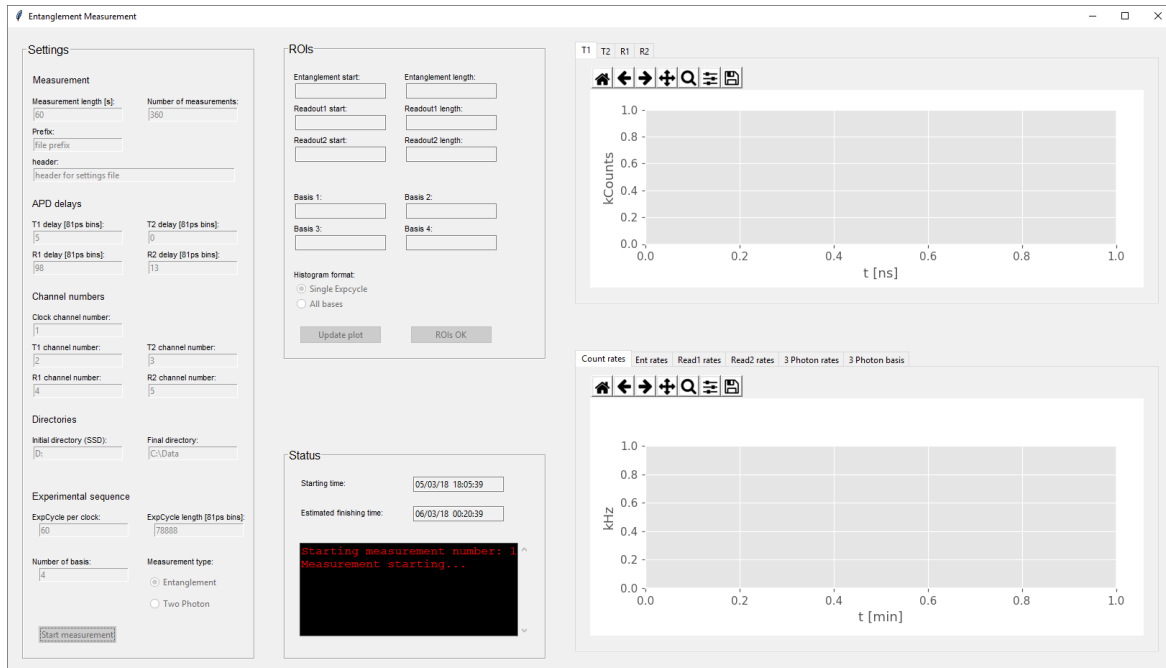


Fig. A.1 **Graphical user interface** Screenshot of the graphical user interface used for the entanglement measurement.

all criteria we extract the corresponding readout basis which is returned by the function alongside the timestamps of all three photons and the channel they were registered on as well as the corresponding timestamp of the clock. Furthermore, the function also returns the corresponding count rates measured within the ROIs, which provide a measure for the correct running of the experiment.

The analysis of one file typically takes about 70 to 80s which is longer than the measurement itself, but close enough to be able to efficiently analyse the data using 2 CPUs.

A.5 Graphical user interface

Based on the library described here, we have implemented a graphical user interface shown in Fig. A.1, which combined the measurement, compression and analysis of the data. The program can be used to set all measurement parameters and automatically calculates a histogram of the first measurement which is shown in the top right corner of the interface and can be used to set the ROIs for the analysis of the data. The count rates and extracted three-photon events are then shown in the lower right corner of the interface and can be used to monitor the correct running of the program. The status window shows updates about the progress of all processes and also provides information of the duration of each step.

Python library

The program uses multiprocessing to make efficient use of the available computing power and realise close-to real-time analysis of the data. During the running of the experiment 1 CPU is designated for the measurement itself in order to ensure no data loss and a second CPU is used to decode and compress the binary files. The remaining 2 CPUs each analyse the data and we can therefore ensure that the data is analysed about 2 minutes after finishing the measurement.

References

1. Feynman, R. P. Simulating physics with computers. *International Journal of Theoretical Physics* **21**, 467–488 (1982).
2. Turing, A. M. On Computable Numbers, with an Application to the Entscheidungsproblem. *Proceedings of the London Mathematical Society* **s2-42**, 230–265 (1937).
3. Riordan, M., Hoddeson, L. & Herring, C. The invention of the transistor. *Reviews of Modern Physics* **71**, S336–S345 (1999).
4. Deutsch, D. Quantum Theory, the Church-Turing Principle and the Universal Quantum Computer. *Proceedings of the Royal Society A: Mathematical, Physical and Engineering Sciences* **400**, 97–117 (1985).
5. Deutsch, D & Jozsa, R. Rapid Solution of Problems by Quantum Computation. *Proceedings of the Royal Society A: Mathematical, Physical and Engineering Sciences* **439**, 553–558 (1992).
6. Grover, L. K. *A fast quantum mechanical algorithm for database search* in *Proceedings of the twenty-eighth annual ACM symposium on Theory of computing - STOC '96* (ACM Press, New York, New York, USA, 1996), 212–219.
7. Shor, P. W. Polynomial-Time Algorithms for Prime Factorization and Discrete Logarithms on a Quantum Computer. *SIAM Journal on Computing* **26**, 1484–1509 (1997).
8. *The development of the number field sieve* (eds Lenstra, A. K. & Lenstra, H. W. J.) (Springer Berlin Heidelberg, Berlin, Heidelberg, 1993).
9. Rivest, R. L., Shamir, a. & Adleman, L. A method for obtaining digital signatures and public-key cryptosystems. *Communications of the ACM* **21**, 120–126 (1978).
10. Bennett, C. & Brassard, G. Quantum cryptography: Public key distribution and coin tossing. *Proceedings of IEEE International ...* (1984).
11. Ekert, A. K. Quantum cryptography based on Bell's theorem. *Physical Review Letters* **67**, 661–663 (1991).
12. Bennett, C. & Wiesner, S. Communication via one- and two-particle operators on Einstein-Podolsky-Rosen states. *Physical Review Letters* **69**, 2881–2884 (1992).
13. Bennett, C., Brassard, G. & Crépeau, C. Teleporting an unknown quantum state via dual classical and Einstein-Podolsky-Rosen channels. *Physical Review Letters* **70**, 1895–1899 (1993).
14. Haffner, H, Roos, C & Blatt, R. Quantum computing with trapped ions. *Physics Reports* **469**, 155–203 (2008).
15. Monroe, C & Kim, J. Scaling the Ion Trap Quantum Processor. *Science* **339**, 1164–1169 (2013).

References

16. Kok, P., Nemoto, K., Ralph, T. C., Dowling, J. P. & Milburn, G. J. Linear optical quantum computing with photonic qubits. *Reviews of Modern Physics* **79**, 135–174 (2007).
17. Jones, J. a. Quantum computing with NMR. *Progress in nuclear magnetic resonance spectroscopy* **59**, 91–120 (2011).
18. Wendin, G. Quantum information processing with superconducting circuits: a review. *Reports on Progress in Physics* **80**, 106001 (2017).
19. Doherty, M. W. *et al.* The nitrogen-vacancy colour centre in diamond. *Physics Reports* **528**, 1–45 (2013).
20. Childress, L. & Hanson, R. Diamond NV centers for quantum computing and quantum networks. *MRS Bulletin* **38**, 134–138 (2013).
21. Kloeffel, C. & Loss, D. Prospects for Spin-Based Quantum Computing in Quantum Dots. *Annual Review of Condensed Matter Physics* **4**, 51–81 (2013).
22. DiVincenzo, D. P. The Physical Implementation of Quantum Computation. *Fortschritte der Physik* **48**, 771–783 (2000).
23. Nielsen, M. A. & Chuang, I. L. *Quantum Computation and Quantum Information* (Cambridge University Press, Cambridge, 2010).
24. Gisin, N. & Thew, R. Quantum communication. *Nature Photonics* **1**, 165–171 (2007).
25. Georgescu, I. M., Ashhab, S. & Nori, F. Quantum simulation. *Reviews of Modern Physics* **86**, 153–185 (2014).
26. Degen, C. L., Reinhard, F. & Cappellaro, P. Quantum sensing. *Reviews of Modern Physics* **89**, 035002 (2017).
27. Warburton, R. J. Single spins in self-assembled quantum dots. *en. Nature Materials* **12**, 483–493 (2013).
28. De Greve, K. *et al.* Quantum-dot spin–photon entanglement via frequency downconversion to telecom wavelength. *Nature* **491**, 421–425 (2012).
29. Gao, W. B., Fallahi, P., Togan, E, Miguel-Sanchez, J & Imamoglu, a. Observation of entanglement between a quantum dot spin and a single photon. *Nature* **491**, 426–30 (2012).
30. Schaibley, J. R. *et al.* Demonstration of Quantum Entanglement between a Single Electron Spin Confined to an InAs Quantum Dot and a Photon. *Physical Review Letters* **110**, 167401 (2013).
31. Kimble, H. J. The quantum internet. *Nature* **453**, 1023–30 (2008).
32. Al-Khuzheyri, R. *et al.* Resonance fluorescence from a telecom-wavelength quantum dot. *Applied Physics Letters* **109**, 163104 (2016).
33. Fitzsimons, J. F. Private quantum computation: an introduction to blind quantum computing and related protocols. *npj Quantum Information* **3**, 23 (2017).
34. Einstein, A. Physics and reality. *Journal of the Franklin Institute* **221**, 349–382 (1936).
35. Xiu, F. *et al.* Electric-field-controlled ferromagnetism in high-Curie-temperature Mn_{0.05}Ge_{0.95} quantum dots. *Nature Materials* **9**, 337–344 (2010).

36. Gao, X., Cui, Y., Levenson, R. M., Chung, L. W. & Nie, S. In vivo cancer targeting and imaging with semiconductor quantum dots. *Nature Biotechnology* **22**, 969–976 (2004).
37. Courtney, C. M. *et al.* Photoexcited quantum dots for killing multidrug-resistant bacteria. *Nature Materials* **15**, 529–534 (2016).
38. Kim, T. H. *et al.* Full-colour quantum dot displays fabricated by transfer printing. *Nature Photonics* **5**, 176–182 (2011).
39. Coe-Sullivan, S., Liu, W., Allen, P. & Steckel, J. S. Quantum Dots for LED Downconversion in Display Applications. *ECS Journal of Solid State Science and Technology* **2**, R3026–R3030 (2012).
40. Loss, D. & DiVincenzo, D. P. Quantum computation with quantum dots. *Physical Review A* **57**, 120–126 (1998).
41. Imamoglu, A. *et al.* Quantum Information Processing Using Quantum Dot Spins and Cavity QED. *Physical Review Letters* **83**, 4204–4207 (1999).
42. Golovach, V. N. & Loss, D. Electron spins in artificial atoms and molecules for quantum computing. *Semiconductor Science and Technology* **17**, 355–366 (2002).
43. Calarco, T., Datta, A., Fedichev, P., Pazy, E. & Zoller, P. Spin-based all-optical quantum computation with quantum dots: Understanding and suppressing decoherence. *Physical Review A* **68**, 012310 (2003).
44. Lodahl, P., Mahmoodian, S. & Stobbe, S. Interfacing single photons and single quantum dots with photonic nanostructures. *Reviews of Modern Physics* **87**, 347–400 (2015).
45. Vamivakas, A. N. & Atatüre, M. Photons and (artificial) atoms: an overview of optical spectroscopy techniques on quantum dots. *Contemporary Physics* **51**, 17–36 (2010).
46. Bayer, M. *et al.* Fine structure of neutral and charged excitons in self-assembled In(Ga)As/(Al)GaAs quantum dots. *Physical Review B* **65**, 195315 (2002).
47. Ellis, D. J. P. *et al.* Control of fine-structure splitting of individual InAs quantum dots by rapid thermal annealing. *Applied Physics Letters* **90**, 23–26 (2007).
48. Atatüre, M. Quantum-Dot Spin-State Preparation with Near-Unity Fidelity. *Science* **312**, 551–553 (2006).
49. Emary, C., Xu, X., Steel, D. G., Saikin, S. & Sham, L. J. Fast Initialization of the Spin State of an Electron in a Quantum Dot in the Voigt Configuration. *Physical Review Letters* **98**, 047401 (2007).
50. Xu, X. *et al.* Fast Spin State Initialization in a Singly Charged InAs-GaAs Quantum Dot by Optical Cooling. *Physical Review Letters* **99**, 097401 (2007).
51. Fischer, J., Coish, W. A., Bulaev, D. V. & Loss, D. Spin decoherence of a heavy hole coupled to nuclear spins in a quantum dot. *Physical Review B* **78**, 155329 (2008).
52. Fallahi, P., Yılmaz, S. T. & Imamoglu, A. Measurement of a Heavy-Hole Hyperfine Interaction in InGaAs Quantum Dots Using Resonance Fluorescence. *Physical Review Letters* **105**, 257402 (2010).
53. Greilich, A., Carter, S. G., Kim, D., Bracker, A. S. & Gammon, D. Optical control of one and two hole spins in interacting quantum dots. *Nature Photonics* **5**, 702–708 (2011).

References

54. Prechtel, J. H. *et al.* Decoupling a hole spin qubit from the nuclear spins. *Nature Materials* **15**, 981–986 (2016).
55. Sun, Z., Delteil, A., Faelt, S. & Imamoğlu, A. Measurement of spin coherence using Raman scattering. *Physical Review B* **93**, 241302 (2016).
56. Cho, A. & Arthur, J. Molecular beam epitaxy. *Progress in Solid State Chemistry* **10**, 157–191 (1975).
57. Neave, J. H., Dobson, P. J., Harris, J. J., Dawson, P. & Joyce, B. A. Silicon doping of MBE-grown GaAs films. *Applied Physics A Solids and Surfaces* **32**, 195–200 (1983).
58. Drexler, H, Leonard, D, Hansen, W, Kotthaus, J. P. & Petroff, P. M. Spectroscopy of Quantum Levels in Charge-Tunable InGaAs Quantum Dots. *Physical Review Letters* **73**, 2252–2255 (1994).
59. Warburton, R. J. *et al.* Giant permanent dipole moments of excitons in semiconductor nanostructures. *Physical Review B* **65**, 113303 (2002).
60. Borri, P. *et al.* Ultralong Dephasing Time in InGaAs Quantum Dots. *Physical Review Letters* **87**, 157401 (2001).
61. Kuhlmann, A. V. *et al.* A dark-field microscope for background-free detection of resonance fluorescence from single semiconductor quantum dots operating in a set-and-forget mode. *Review of Scientific Instruments* **84**, 073905 (2013).
62. Smith, J. M. *et al.* Voltage Control of the Spin Dynamics of an Exciton in a Semiconductor Quantum Dot. *Physical Review Letters* **94**, 197402 (2005).
63. Dreiser, J, Atatüre, M, Galland, C & Müller, T. Optical investigations of quantum dot spin dynamics as a function of external electric and magnetic fields. *Physical Review B* **77**, 75317 (2008).
64. Latta, C., Srivastava, A. & Imamoğlu, A. Hyperfine Interaction-Dominated Dynamics of Nuclear Spins in Self-Assembled InGaAs Quantum Dots. *Physical Review Letters* **107**, 167401 (2011).
65. Mollow, B. R. Power Spectrum of Light Scattered by Two-Level Systems. *Physical Review* **188**, 1969–1975 (1969).
66. Autler, S. H. & Townes, C. H. Stark Effect in Rapidly Varying Fields. *Physical Review* **100**, 703–722 (1955).
67. Schabert, A., Keil, R. & Toschek, P. E. Dynamic stark effect of an optical line observed by cross-saturated absorption. *Applied Physics* **6**, 181–184 (1975).
68. Xu, X. *et al.* Coherent Optical Spectroscopy of a Strongly Driven Quantum Dot. *Science* **317**, 929–932 (2007).
69. Wu, F. Y., Grove, R. E. & Ezekiel, S. Investigation of the Spectrum of Resonance Fluorescence Induced by a Monochromatic Field. *Physical Review Letters* **35**, 1426–1429 (1975).
70. Flagg, E. B. *et al.* Resonantly driven coherent oscillations in a solid-state quantum emitter. *Nature Physics* **5**, 203–207 (2009).
71. Vamivakas, A. N., Zhao, Y., Lu, C. Y. & Atatüre, M. Spin-resolved quantum-dot resonance fluorescence. *Nature Physics* **5**, 198–202 (2009).
72. Foot, C. J. *Atomic Physics* (Oxford University Press, 2005).

73. Loudon, R. *The Quantum Theory of Light* (Oxford University Press, 1973).
74. Konthasinghe, K. *et al.* Coherent versus incoherent light scattering from a quantum dot. *Physical Review B* **85**, 235315 (2012).
75. Matthiesen, C., Vamivakas, A. N. & Atatüre, M. Subnatural Linewidth Single Photons from a Quantum Dot. *Physical Review Letters* **108**, 093602 (2012).
76. Matthiesen, C. *et al.* Phase-locked indistinguishable photons with synthesized waveforms from a solid-state source. *Nature Communications* **4**, 1600 (2013).
77. Kimble, H. J., Dagenais, M. & Mandel, L. Photon Antibunching in Resonance Fluorescence. *Physical Review Letters* **39**, 691–695 (1977).
78. Fleischhauer, M., Imamoglu, A. & Marangos, J. P. Electromagnetically induced transparency: Optics in coherent media. *Reviews of Modern Physics* **77**, 633–673 (2005).
79. Gray, H. R., Whitley, R. M. & Stroud, C. R. Coherent trapping of atomic populations. *Optics Letters* **3**, 218 (1978).
80. Xu, X. *et al.* Coherent Population Trapping of an Electron Spin in a Single Negatively Charged Quantum Dot. *Nature Physics* **4**, 692–695 (2008).
81. Harris, S. E., Field, J. E. & Imamoglu, A. Nonlinear optical processes using electromagnetically induced transparency. *Phys. Rev. Lett.* **64**, 1107–1110 (1990).
82. Hau, L. V., Harris, S. E., Dutton, Z. & Behroozi, C. H. Light speed reduction to 17 metres per second in an ultracold atomic gas. *Nature* **397**, 594–598 (1999).
83. Phillips, D., Fleischhauer, a., Mair, a., Walsworth, R. & Lukin, M. Storage of Light in Atomic Vapor. *Physical Review Letters* **86**, 783–786 (2001).
84. Gaubatz, U., Rudecki, P., Schiemann, S. & Bergmann, K. Population transfer between molecular vibrational levels by stimulated Raman scattering with partially overlapping laser fields. A new concept and experimental results. *The Journal of Chemical Physics* **92**, 5363–5376 (1990).
85. Vitanov, N. V., Rangelov, A. A., Shore, B. W. & Bergmann, K. Stimulated Raman adiabatic passage in physics, chemistry, and beyond. *Reviews of Modern Physics* **89**, 015006 (2017).
86. Koppens, F. H. L. *et al.* Driven coherent oscillations of a single electron spin in a quantum dot. *Nature* **442**, 766–771 (2006).
87. Nowack, K. C., Koppens, F. H. L., Nazarov, Y. V. & Vandersypen, L. M. K. Coherent Control of a Single Electron Spin with Electric Fields. *Science* **318**, 1430–1433 (2007).
88. Chen, P., Piermarocchi, C., Sham, L. J., Gammon, D. & Steel, D. G. Theory of quantum optical control of a single spin in a quantum dot. *Physical Review B* **69**, 075320 (2004).
89. Combescot, M. & Betbeder-Matibet, O. Theory of spin precession monitored by laser pulse. *Solid State Communications* **132**, 129–134 (2004).
90. Pryor, C. E. & Flatté, M. E. Predicted ultrafast single-qubit operations in semiconductor quantum dots. *Applied Physics Letters* **88**, 233108 (2006).
91. Economou, S. E., Sham, L. J., Wu, Y. & Steel, D. G. Proposal for optical U(1) rotations of electron spin trapped in a quantum dot. *Physical Review B* **74**, 205415 (2006).

References

92. Clark, S. M., Fu, K.-M. C., Ladd, T. D. & Yamamoto, Y. Quantum Computers Based on Electron Spins Controlled by Ultrafast Off-Resonant Single Optical Pulses. *Physical Review Letters* **99**, 040501 (2007).
93. Press, D. *et al.* Ultrafast optical spin echo in a single quantum dot. *Nature Photonics* **4**, 367–370 (2010).
94. De Greve, K. *et al.* Ultrafast coherent control and suppressed nuclear feedback of a single quantum dot hole qubit. *Nature Physics* **7**, 872–878 (2011).
95. Press, D., Ladd, T. D., Zhang, B. & Yamamoto, Y. Complete quantum control of a single quantum dot spin using ultrafast optical pulses. *Nature* **456**, 218–221 (2008).
96. Berezovsky, J, Mikkelsen, M. H., Stoltz, N. G., Coldren, L & Awschalom, D. D. Picosecond coherent optical manipulation of a single electron spin in a quantum dot. *Science* **320**, 349–352 (2008).
97. Ardelt, P.-L. *et al.* Dissipative preparation of the exciton and biexciton in self-assembled quantum dots on picosecond time scales. *Physical Review B* **90**, 241404 (2014).
98. Quilter, J. H. *et al.* Phonon-Assisted Population Inversion of a Single InGaAs/GaAs Quantum Dot by Pulsed Laser Excitation. *Physical Review Letters* **114**, 137401 (2015).
99. Ramsay, A. J. *et al.* Damping of Exciton Rabi Rotations by Acoustic Phonons in Optically Excited InGaAs/GaAs Quantum Dots. *Physical Review Letters* **104**, 017402 (2010).
100. Levitt, M. H. Composite pulses. *Progress in Nuclear Magnetic Resonance Spectroscopy* **18**, 61–122 (1986).
101. Mizrahi, J. *et al.* Quantum control of qubits and atomic motion using ultrafast laser pulses. *Applied Physics B* **114**, 45–61 (2014).
102. Yang, W. & Sham, L. J. General theory of feedback control of a nuclear spin ensemble in quantum dots. *Physical Review B* **88**, 235304 (2013).
103. Urbaszek, B. *et al.* Nuclear spin physics in quantum dots: An optical investigation. *Reviews of Modern Physics* **85**, 79–133 (2013).
104. Testelin, C., Bernardot, F., Eble, B. & Chamarro, M. Hole–spin dephasing time associated with hyperfine interaction in quantum dots. *Physical Review B* **79**, 195440 (2009).
105. Merkulov, I. a., Efros, A. L. & Rosen, M. Electron spin relaxation by nuclei in semiconductor quantum dots. *Physical Review B* **65**, 205309 (2002).
106. Bulutay, C. Quadrupolar spectra of nuclear spins in strained $\text{In}_x\text{Ga}_{(1-x)}\text{As}$ quantum dots. *Physical Review B* **85**, 115313 (2012).
107. Högele, A. *et al.* Dynamic Nuclear Spin Polarization in the Resonant Laser Excitation of an InGaAs Quantum Dot. *Physical Review Letters* **108**, 197403 (2012).
108. Huang, C.-W. & Hu, X. Theoretical study of nuclear spin polarization and depolarization in self-assembled quantum dots. *Physical Review B* **81**, 205304 (2010).
109. Latta, C. *et al.* Confluence of resonant laser excitation and bidirectional quantum-dot nuclear-spin polarization. *Nature Physics* **5**, 758–763 (2009).

110. Chekhovich, E. A., Hopkinson, M., Skolnick, M. S. & Tartakovskii, A. I. Suppression of nuclear spin bath fluctuations in self-assembled quantum dots induced by inhomogeneous strain. *Nature Communications* **6**, 1–7 (2015).
111. Waeber, A. M. *et al.* Few-second-long correlation times in a quantum dot nuclear spin bath probed by frequency-comb nuclear magnetic resonance spectroscopy. *Nature Physics* **12**, 688–693 (2016).
112. Schulte, C. H. H. *et al.* Quadrature squeezed photons from a two-level system. *Nature* **525**, 222–225 (2015).
113. Senellart, P., Solomon, G. & White, A. High-performance semiconductor quantum-dot single-photon sources. *Nature Nanotechnology* **12**, 1026–1039 (2017).
114. Somaschi, N. *et al.* Near-optimal single-photon sources in the solid state. *Nature Photonics* **10**, 340–345 (2016).
115. Delteil, A. *et al.* Generation of heralded entanglement between distant hole spins. *Nature Physics* **12**, 218–223 (2016).
116. Stockill, R. *et al.* Phase-Tuned Entangled State Generation between Distant Spin Qubits. *Physical Review Letters* **119**, 010503 (2017).
117. Gywat, O., Krenner, H. J. & Berezovsky, J. *Spins in Optically Active Quantum Dots* (ed Rafailov, E. U.) (Wiley-VCH Verlag GmbH & Co. KGaA, Weinheim, Germany, 2009).
118. *Quantum Dots* (ed Tartakovskii, A.) (Cambridge University Press, Cambridge, 2012).
119. Schrödinger, E. Discussion of Probability Relations between Separated Systems. *Mathematical Proceedings of the Cambridge Philosophical Society* **31**, 555–563 (1935).
120. Zanardi, P., Zalka, C. & Faoro, L. Entangling power of quantum evolutions. *Physical Review A* **62**, 030301 (2000).
121. Dür, W., Vidal, G., Cirac, J. I., Linden, N. & Popescu, S. Entanglement Capabilities of Nonlocal Hamiltonians. *Physical Review Letters* **87**, 137901 (2001).
122. Turchette, Q. A. *et al.* Deterministic Entanglement of Two Trapped Ions. *Physical Review Letters* **81**, 3631–3634 (1998).
123. Sackett, C. A. *et al.* Experimental entanglement of four particles. *Nature* **404**, 256–259 (2000).
124. Steffen, M. *et al.* Measurement of the Entanglement of Two Superconducting Qubits via State Tomography. *Science* **313**, 1423–1425 (2006).
125. Matsukevich, D. N. *et al.* Entanglement of Remote Atomic Qubits. *Physical Review Letters* **96**, 030405 (2006).
126. Ritter, S. *et al.* An elementary quantum network of single atoms in optical cavities. *Nature* **484**, 195–200 (2012).
127. Kurpiers, P. *et al.* Deterministic Quantum State Transfer and Generation of Remote Entanglement using Microwave Photons. arXiv: 1712.08593 (2017).
128. Briegel, H., Dür, W., Cirac, J. & Zoller, P. Quantum repeaters: The role of imperfect local operations in quantum communication. *Physical Review Letters* **81**, 5932–5935 (1998).

References

129. Ding, X. *et al.* On-Demand Single Photons with High Extraction Efficiency and Near-Unity Indistinguishability from a Resonantly Driven Quantum Dot in a Micropillar. *Physical Review Letters* **116**, 020401 (2016).
130. Dousse, A. *et al.* Controlled Light-Matter Coupling for a Single Quantum Dot Embedded in a Pillar Microcavity Using Far-Field Optical Lithography. *Physical Review Letters* **101**, 267404 (2008).
131. Cabrillo, C., Cirac, J. I., García-Fernández, P. & Zoller, P. Creation of entangled states of distant atoms by interference. *Physical Review A* **59**, 1025–1033 (1999).
132. Duan, L.-M. & Kimble, H. J. Efficient Engineering of Multiatom Entanglement through Single-Photon Detections. *Physical Review Letters* **90**, 253601 (2003).
133. Barrett, S. D. & Kok, P. Efficient high-fidelity quantum computation using matter qubits and linear optics. *Physical Review A* **71**, 060310 (2005).
134. Moehring, D. L. *et al.* Entanglement of single-atom quantum bits at a distance. *Nature* **449**, 68–71 (2007).
135. Hofmann, J. *et al.* Heralded Entanglement Between Widely Separated Atoms. *Science* **337**, 72–75 (2012).
136. Hensen, B. *et al.* Loophole-free Bell inequality violation using electron spins separated by 1.3 kilometres. *Nature*, 1–5 (2015).
137. Narla, A. *et al.* Robust Concurrent Remote Entanglement Between Two Superconducting Qubits. *Physical Review X* **6**, 031036 (2016).
138. Slodička, L. *et al.* Atom-Atom Entanglement by Single-Photon Detection. *Physical Review Letters* **110**, 083603 (2013).
139. Hong, C. K., Ou, Z. Y. & Mandel, L. Measurement of subpicosecond time intervals between two photons by interference. *Physical Review Letters* **59**, 2044–2046 (1987).
140. Vittorini, G., Hucul, D., Inlek, I. V., Crocker, C. & Monroe, C. Entanglement of distinguishable quantum memories. *Physical Review A* **90**, 040302 (2014).
141. Besombes, L., Kheng, K., Marsal, L. & Mariette, H. Acoustic phonon broadening mechanism in single quantum dot emission. *Physical Review B* **63**, 155307 (2001).
142. Favero, I. *et al.* Acoustic phonon sidebands in the emission line of single InAs/GaAs quantum dots. *Physical Review B* **68**, 233301 (2003).
143. Lu, C.-Y. *et al.* Direct measurement of spin dynamics in InAs/GaAs quantum dots using time-resolved resonance fluorescence. *Physical Review B* **81**, 035332 (2010).
144. Kroutvar, M. *et al.* Optically programmable electron spin memory using semiconductor quantum dots. *Nature* **432**, 81–84 (2004).
145. Flagg, E. *et al.* Interference of Single Photons from Two Separate Semiconductor Quantum Dots. *Physical Review Letters* **104**, 137401 (2010).
146. Benyoucef, M., Wang, L., Rastelli, A. & Schmidt, O. G. Toward quantum interference of photons from independent quantum dots. *Applied Physics Letters* **95**, 261908 (2009).
147. Thoma, A. *et al.* Exploring Dephasing of a Solid-State Quantum Emitter via Time- and Temperature-Dependent Hong-Ou-Mandel Experiments. *Physical Review Letters* **116**, 033601 (2016).

148. Gschrey, M. *et al.* Highly indistinguishable photons from deterministic quantum-dot microlenses utilizing three-dimensional in situ electron-beam lithography. *Nature Communications* **6**, 7662 (2015).
149. Patel, R. B. *et al.* Two-photon interference of the emission from electrically tunable remote quantum dots. *Nature Photonics* **4**, 632–635 (2010).
150. Maunz, P. *et al.* Heralded Quantum Gate between Remote Quantum Memories. *Physical Review Letters* **102**, 250502 (2009).
151. Hucul, D. *et al.* Modular entanglement of atomic qubits using photons and phonons. *Nature Physics* **11**, 37–42 (2014).
152. Bernien, H. *et al.* Heralded entanglement between solid-state qubits separated by three metres. *Nature* **497**, 86–90 (2013).
153. Pfaff, W. *et al.* Unconditional quantum teleportation between distant solid-state quantum bits. *Science* **345**, 532–535 (2014).
154. Bechtold, A. *et al.* Three-stage decoherence dynamics of an electron spin qubit in an optically active quantum dot. *Nature Physics* **11**, 1005–1008 (2015).
155. Éthier-Majcher, G. *et al.* Improving a Solid-State Qubit through an Engineered Mesoscopic Environment. *Physical Review Letters* **119**, 130503 (2017).
156. Campbell, L. & Garnett, W. *The Life of James Clerk Maxwell* (Cambridge University Press, Cambridge, 2010).
157. Lettow, R. *et al.* Quantum Interference of Tunably Indistinguishable Photons from Remote Organic Molecules. *Physical Review Letters* **104**, 123605 (2010).
158. Legero, T., Wilk, T., Kuhn, A. & Rempe, G. Time-resolved two-photon quantum interference. *Applied Physics B: Lasers and Optics* **77**, 797–802 (2003).
159. Woolley, M. J., Lang, C., Eichler, C., Wallraff, A. & Blais, A. Signatures of Hong–Ou–Mandel interference at microwave frequencies. *New Journal of Physics* **15**, 105025 (2013).
160. Heilbron, J. L. *The dilemmas of an upright man: Max Planck and the fortunes of German science* (Harvard University Press, 2000).
161. Stockill, R. *et al.* Quantum dot spin coherence governed by a strained nuclear environment. *Nature Communications* **7**, 12745 (2016).
162. Ladd, T. D. *et al.* Pulsed Nuclear Pumping and Spin Diffusion in a Single Charged Quantum Dot. *Physical Review Letters* **105**, 107401 (2010).
163. Cherbunin, R. V. *et al.* Dynamics of the nuclear spin polarization by optically oriented electrons in a (In,Ga)As/GaAs quantum dot ensemble. *Physical Review B - Condensed Matter and Materials Physics* **80**, 1–8 (2009).
164. Hansom, J. *et al.* Environment-assisted quantum control of a solid-state spin via coherent dark states. *Nature Physics* **10**, 725–730 (2014).
165. Hahn, E. L. Spin Echoes. *Physical Review* **80**, 580–594 (1950).
166. Cywiński, Ł., Lutchyn, R. M., Nave, C. P. & Das Sarma, S. How to enhance dephasing time in superconducting qubits. *Physical Review B - Condensed Matter and Materials Physics* **77**, 1–11 (2008).

References

167. Bluhm, H. *et al.* Dephasing time of GaAs electron-spin qubits coupled to a nuclear bath exceeding 200 μ s. *Nature Physics* **7**, 109–113 (2011).
168. Bulutay, C., Chekhovich, E. A. & Tartakovskii, A. I. Nuclear magnetic resonance inverse spectra of InGaAs quantum dots: Atomistic level structural information. *Physical Review B* **90**, 205425 (2014).
169. Neder, I. *et al.* Semiclassical model for the dephasing of a two-electron spin qubit coupled to a coherently evolving nuclear spin bath. *Physical Review B - Condensed Matter and Materials Physics* **84**, 1–13 (2011).
170. Cywiński, Ł. Dynamical-decoupling noise spectroscopy at an optimal working point of a qubit. *Physical Review A* **90**, 042307 (2014).
171. Botzem, T. *et al.* Quadrupolar and anisotropy effects on dephasing in two-electron spin qubits in GaAs. *Nature Communications* **7**, 11170 (2016).
172. Malinowski, F. K. *et al.* Notch filtering the nuclear environment of a spin qubit. *Nature Nanotechnology* **12**, 16–20 (2016).
173. Ryan, C. A., Hodges, J. S. & Cory, D. G. Robust Decoupling Techniques to Extend Quantum Coherence in Diamond. *Physical Review Letters* **105**, 200402 (2010).
174. Knowles, H. S., Kara, D. M. & Atatüre, M. Observing bulk diamond spin coherence in high-purity nanodiamonds. *Nature Materials* **13**, 21–25 (2014).
175. Muhonen, J. T. *et al.* Storing quantum information for 30 seconds in a nanoelectronic device. *Nature Nanotechnology* **9**, 986–991 (2014).
176. Viola, L. & Lloyd, S. Dynamical suppression of decoherence in two-state quantum systems. *Physical Review A* **58**, 2733–2744 (1998).
177. Le Gall, C., Brunetti, A., Boukari, H. & Besombes, L. Electron-nuclei spin dynamics in II-VI semiconductor quantum dots. *Physical Review B* **85**, 195312 (2012).
178. Keizer, J. G. *et al.* Atomic scale analysis of self assembled GaAs/AlGaAs quantum dots grown by droplet epitaxy. *Applied Physics Letters* **96**, 062101 (2010).
179. Jahn, J.-P. *et al.* An artificial Rb atom in a semiconductor with lifetime-limited linewidth. *Physical Review B* **92**, 245439 (2015).
180. Sallen, G. *et al.* Nuclear magnetization in gallium arsenide quantum dots at zero magnetic field. *Nature Communications* **5**, 3268 (2014).
181. Heisenberg, W. *Physics and Philosophy: The Revolution in Modern Science* 3rd (Penguin Classics, 2000).
182. Houel, J. *et al.* High Resolution Coherent Population Trapping on a Single Hole Spin in a Semiconductor Quantum Dot. *Physical Review Letters* **112**, 107401 (2014).
183. Huthmacher, L. *et al.* Coherence of a dynamically decoupled quantum-dot hole spin. arXiv: 1711.09169 (2017).
184. Bennett, A. J. *et al.* Voltage tunability of single-spin states in a quantum dot. *Nature Communications* **4**, 1522 (2013).
185. Prechtel, J. H. *et al.* Electrically tunable hole g factor of an optically active quantum dot for fast spin rotations. *Physical Review B* **91**, 165304 (2015).
186. Efros, A. & Rosen, M. Random Telegraph Signal in the Photoluminescence Intensity of a Single Quantum Dot. *Physical Review Letters* **78**, 1110–1113 (1997).

187. Klimov, V. I., Mikhailovsky, A. A., McBranch, D. W., Leatherdale, C. A. & Bawendi, M. G. Quantization of multiple auger rates in semiconductor quantum dots. *Science* **287**, 1011–1013 (2000).
188. Park, Y. S., Bae, W. K., Pietryga, J. M. & Klimov, V. I. Auger recombination of biexcitons and negative and positive trions in individual quantum dots. *ACS Nano* **8**, 7288–7296 (2014).
189. Klimov, V. I. *et al.* Optical Gain and Stimulated Emission in Nanocrystal Quantum Dots. *Science* **290**, 314–317 (2000).
190. Jha, P. P. & Guyot-Sionnest, P. Trion decay in colloidal quantum dots. *ACS Nano* **3**, 1011–1015 (2009).
191. Cohn, A. W., Rinehart, J. D., Schimpf, A. M., Weaver, A. L. & Gamelin, D. R. Size dependence of negative trion auger recombination in photodoped cdse nanocrystals. *Nano Letters* **14**, 353–358 (2014).
192. Kurzmann, A., Ludwig, A., Wieck, A. D., Lorke, A. & Geller, M. Auger Recombination in Self-Assembled Quantum Dots: Quenching and Broadening of the Charged Exciton Transition. *Nano Letters* **16**, 3367–3372 (2016).
193. Duke, C. B. & Mahan, G. D. Phonon-Broadened Impurity Spectra. I. Density of States. *Physical Review* **139**, A1965–A1982 (1965).
194. Urbaszek, B. *et al.* Temperature-dependent linewidth of charged excitons in semiconductor quantum dots: Strongly broadened ground state transitions due to acoustic phonon scattering. *Physical Review B - Condensed Matter and Materials Physics* **69**, 1–6 (2004).
195. Godden, T. M. *et al.* Coherent Optical Control of the Spin of a Single Hole in an InAs/GaAs Quantum Dot. *Physical Review Letters* **108**, 017402 (2012).
196. Bechtold, A. *et al.* Three-stage decoherence dynamics of an electron spin qubit in an optically active quantum dot. *Nature Physics* **11**, 1005–1008 (2015).
197. Salis, G. *et al.* Electrical control of spin coherence in semiconductor nanostructures. *Nature* **414**, 619–622 (2001).
198. Bulaev, D. V. & Loss, D. Spin relaxation and decoherence of holes in quantum dots. *Physical Review Letters* **95**, 1–4 (2005).
199. Heiss, D. *et al.* Observation of extremely slow hole spin relaxation in self-assembled quantum dots. *Physical Review B* **76**, 241306 (2007).
200. Eble, B. *et al.* Hole–Nuclear Spin Interaction in Quantum Dots. *Physical Review Letters* **102**, 146601 (2009).
201. Dahbashi, R. *et al.* Measurement of heavy-hole spin dephasing in (InGa)As quantum dots. *Applied Physics Letters* **100**, 031906 (2012).
202. Ribeiro, H., Maier, F. & Loss, D. Inhibition of dynamic nuclear polarization by heavy-hole noncollinear hyperfine interactions. *Physical Review B - Condensed Matter and Materials Physics* **92**, 1–9 (2015).
203. Trif, M., Simon, P. & Loss, D. Relaxation of Hole Spins in Quantum Dots via Two-Phonon Processes. *Physical Review Letters* **103**, 106601 (2009).

References

204. Kuhlmann, A. V. *et al.* Charge noise and spin noise in a semiconductor quantum device. *Nature Physics* **9**, 570–575 (2013).
205. Stanley, M. J. *et al.* Dynamics of a mesoscopic nuclear spin ensemble interacting with an optically driven electron spin. *Physical Review B* **90**, 195305 (2014).
206. Machlup, S. Noise in semiconductors: Spectrum of a two-parameter random signal. *Journal of Applied Physics* **25**, 341–343 (1954).
207. Keshner, M. $1/f$ noise. *Proceedings of the IEEE* **70**, 212–218 (1982).
208. Dial, O. E. *et al.* Charge Noise Spectroscopy Using Coherent Exchange Oscillations in a Singlet-Triplet Qubit. *Physical Review Letters* **110**, 146804 (2013).
209. Zhang, W. *et al.* Long-time electron spin storage via dynamical suppression of hyperfine-induced decoherence in a quantum dot. *Physical Review B* **77**, 125336 (2008).
210. Carr, H. & Purcell, E. Effects of Diffusion on Free Precession in Nuclear Magnetic Resonance Experiments. *Physical Review* **94**, 630–638 (1954).
211. Medford, J. *et al.* Scaling of Dynamical Decoupling for Spin Qubits. *Physical Review Letters* **108**, 086802 (2012).
212. Szańkowski, P., Ramon, G., Krzywda, J., Kwiatkowski, D. & Cywiński, Ł. Environmental noise spectroscopy with qubits subjected to dynamical decoupling. *Journal of Physics: Condensed Matter* **29**, 333001 (2017).
213. Meiboom, S. & Gill, D. Modified Spin-Echo Method for Measuring Nuclear Relaxation Times. *Review of Scientific Instruments* **29**, 688–691 (1958).
214. Maudsley, A. Modified Carr-Purcell-Meiboom-Gill sequence for NMR fourier imaging applications. *Journal of Magnetic Resonance (1969)* **69**, 488–491 (1986).
215. Khodjasteh, K. & Lidar, D. A. Fault-Tolerant Quantum Dynamical Decoupling. *Physical Review Letters* **95**, 180501 (2005).
216. Uhrig, G. S. Keeping a Quantum Bit Alive by Optimized π -Pulse Sequences. *Physical Review Letters* **98**, 100504 (2007).
217. Jha, A. Stephen Hawking marks 70th birthday with speech to leading cosmologists. *The Guardian* (2012). URL: <https://www.theguardian.com/science/2012/jan/08/stephen-hawking-70-cambridge-speech> (accessed May 2018).
218. Wang, H. *et al.* Near-Transform-Limited Single Photons from an Efficient Solid-State Quantum Emitter. *Physical Review Letters* **116**, 213601 (2016).
219. Monroe, C. *et al.* Large-scale modular quantum-computer architecture with atomic memory and photonic interconnects. *Physical Review A* **89**, 022317 (2014).
220. Kim, D., Carter, S. G., Greulich, A., Bracker, A. S. & Gammon, D. Ultrafast optical control of entanglement between two quantum-dot spins. *Nature Physics* **7**, 223–229 (2011).
221. Kim, D. *et al.* Optically Loaded Semiconductor Quantum Memory Register. *Physical Review Applied* **5**, 024014 (2016).
222. Raussendorf, R. & Briegel, H. J. A One-Way Quantum Computer. *Physical Review Letters* **86**, 5188–5191 (2001).

-
223. Briegel, H. J. & Raussendorf, R. Persistent Entanglement in Arrays of Interacting Particles. *Physical Review Letters* **86**, 910–913 (2001).
 224. Walther, P *et al.* Experimental one-way quantum computing. *Nature* **434**, 169–76 (2005).
 225. Prevedel, R. *et al.* High-speed linear optics quantum computing using active feed-forward. *Nature* **445**, 65–9 (2007).
 226. Lindner, N. & Rudolph, T. Proposal for Pulsed On-Demand Sources of Photonic Cluster State Strings. *Physical Review Letters* **103**, 113602 (2009).
 227. Schwartz, I. *et al.* Deterministic generation of a cluster state of entangled photons. *Science* **354**, 434–437 (2016).
 228. Gérard, J. M. *et al.* Enhanced spontaneous emission by quantum boxes in a monolithic optical microcavity. *Physical Review Letters* **81**, 1110–1113 (1998).
 229. Economou, S. E., Lindner, N. & Rudolph, T. Optically Generated 2-Dimensional Photonic Cluster State from Coupled Quantum Dots. *Physical Review Letters* **105**, 093601 (2010).
 230. Scerri, D., Malein, R. N. E., Gerardot, B. D. & Gauger, E. M. Frequency-encoded linear cluster states with coherent Raman photons. arXiv: 1802.02859 (2018).
 231. Gimeno-Segovia, M., Rudolph, T. & Economou, S. E. Deterministic generation of large-scale entangled photonic cluster state from interacting solid state emitters. arXiv: 1801.02599 (2018).
 232. Buterakos, D., Barnes, E. & Economou, S. E. Deterministic Generation of All-Photonic Quantum Repeaters from Solid-State Emitters. *Physical Review X* **7**, 041023 (2017).

